*Clays and Clay Minerals*, Vol. 61, No. 1, 1–10, 2013.

# INFLUENCE OF CATIONS ON AGGREGATION RATES IN Mg-MONTMORILLONITE

AL. KATZ[1], MIN XU[2], JEFFREY C. STEINER[3], ADRIANNA TRUSIAK[3], ALEXANDRA ALIMOVA[4], PAUL GOTTLIEB[4], AND KARIN BLOCK[3,*]

[1] Department of Physics, City College of New York, New York, NY 10031, USA
[2] Department of Physics, Fairfield University, Fairfield, CT 06824, USA
[3] Department of Earth and Atmospheric Science, City College of New York, New York, NY 10031, USA
[4] Sophie Davis School of Biomedical Education, City College of New York, New York, NY 10031, USA

**Abstract**—Critical-zone reactions involve inorganic and biogenic colloids in a cation-rich environment. The present research defines the rates and structure of purified Mg-montmorillonite aggregates formed in the presence of monovalent ($K^+$) and divalent ($Ca^{2+}$, $Mg^{2+}$) cations using light-extinction measurements. Time evolution of turbidity was employed to determine early-stage aggregation rates. Turbidity spectra were used to measure the fractal dimension at later stages. The power law dependence of the stability ratios on cation concentration was found to vary with the reciprocal of the valence rather than the predicted reciprocal of valence-squared, indicating that the platelet structure may be a factor influencing aggregation rates. The critical coagulation concentrations (CCC) (3 mM for $CaCl_2$, 4 mM for $MgCl_2$, and 70 mM for KCl) were obtained from the stability ratios. At a later time and above a minimal cation concentration, turbidity reached a quasi-stable state, indicating the formation of large aggregates. Under this condition, an approximate turbidity forward-scattering correction factor was applied and the fractal dimension was determined from the extinction spectra. For the divalent cations, the fractal dimensions were $1.65 \pm 0.3$ for $Ca^{2+}$ and $1.75 \pm 0.3$ for $Mg^{2+}$ and independent of cation concentrations above the CCC. For the monovalent cation, the fractal dimension increased with $K^+$ concentration from 1.35 to 1.95, indicating a transition to a face-to-face geometry from either an edge-to-edge or edge-to-face orientation.

**Key Words**—Aggregation Rates, Critical Coagulation Concentration, Fractal Dimension, Montmorillonite, Smectite, Stability Ratio, Turbidity.

## INTRODUCTION

The aggregation of colloidal clay particles is of widespread interest to industry and terrestrial ecology. Remediation applications often depend on manipulating conditions that lead to clay aggregation and aggregate stability (Kornilovich *et al.*, 2005; Ravera *et al.*, 2006). In the critical zone and in ecologic setting, clays play an important role in the interaction of inorganic nutrients, RNA, and proteins with dissolved organic compounds, soil clots, and other components of natural systems (Lagaly, 2006). The ubiquity of dissolved cations in the environment is a pivotal factor to understanding the aggregation rate, specific structure, and overall cohesiveness of aggregates and, therefore, dictates sequestration rates of suspended and dissolved species into sediment beds.

During aggregation, colloidal particles form a mass fractal structure (Meakin, 1983) at a rate determined by the potential barrier between particles. In the DLVO model (Derjaguin and Landau, 1941; Verwey and Overbeek, 1948), the potential is the sum of the attractive van der Waals potential and the repulsive Coulomb potential. The Coulomb potential, $\Psi$, decreases exponentially with distance, $x$, from the platelets, *i.e.* $\Psi \propto \exp(-\kappa x)$, where $\kappa$ is the Debye-Hückel parameter and $1/\kappa$ is a measure of the double layer thickness (Hunter, 1993). The thickness of the electrical double layer is inversely proportional to the cation valence and the square root of the cation concentration (Luckham and Rossi, 1999). In distilled water or at low electrolyte concentrations, the charged double layer extends for several tens of nanometers and the energy barrier is much greater than $k_BT$ where $k_B$ is the Boltzmann constant and T is the absolute temperature. In order to aggregate, particles must overcome this energy barrier and, therefore, multiple collisions are necessary for particle adhesion. This regime is referred to as reaction limited colloidal aggregation (RLCA) or slow aggregation. At elevated cation concentration the double layer thickness decreases causing the potential barrier to also decrease, thus augmenting the probability of particle cohesion. At sufficiently high cation concentrations, the energy barrier disappears and every collision results in particle adhesion. This is the diffusion limited colloidal aggregation (DLCA) or fast aggregation regime. The concentration at which the energy barrier disappears is referred to as the critical coagulation concentration (CCC). The Schulze-Hardy rule predicts that the CCC varies with the valence of the coagulating ion raised to the sixth power (Hunter, 1993).

Smectites are highly reactive, expandable, negatively charged, hydrous 2:1 layered phyllosilicates; mont-

* E-mail address of corresponding author:
kblock@ccny.cuny.edu
DOI: 10.1346/CCMN.2013.0610101

morillonite is the common dioctahedral smectite (aluminous) clay mineral. While the theory for clustering within colloids is well understood, aggregate formation within clay minerals is less well defined and the derivation of accurate aggregation rates remains a challenge. In fact, van Oss *et al.* (1990) applied electrophoresis measurements to determine that DLVO theory does not adequately describe the flocculation of a smectite in NaCl solution and that polar forces must be included to explain the data for smectite. Individual clay-mineral platelets are conceptually assumed to be disk shaped with diameters of several hundred nm and thicknesses up to 5 nm (Plaschke *et al.*, 2001; Tournassat *et al.*, 2003; Ploehn and Liu, 2006). Platelet edges have a pH-dependent positive charge while the faces are negatively charged. This distribution of charge influences the structure of the aggregates and makes aggregation rates strongly dependent on cation valence and concentration. Three modes of smectite flocculation are possible (van Olphen, 1977; Keren and Sparks, 1995; Luckham and Rossi, 1999): (1) edge-to-face (E-F) aggregates in which the edge of a platelet associates with the face plane of another platelet; (2) face-to-face (F-F) aggregates formed by the association of parallel planes of platelets; and (3) edge-to-edge (E-E) aggregates formed by association of platelets along their edges. E-F aggregation occurs at lower cation concentration while at greater cation concentration F-F aggregation dominates (Stawiński *et al.*, 1990; Keren and Sparks, 1995).

The aggregation kinetics and the role of electrolytes and/or pH in aggregation have been investigated for different clay minerals, including kaolinite, smectite, and illite (Ferreiro and Helmy, 1974; Novich and Ring, 1984; Goldberg and Glaubig, 1987; Stawiński *et al.*, 1990; Goldberg *et al.*, 1991; Pierre and Ma, 1999; Derrendinger and Sposito, 2000; Tawari *et al.*, 2001; Lagaly and Ziesmer, 2003; Berka and Rice, 2004, 2005; Morris and Żbik, 2009; Nasser and James, 2009). In each of the studies listed, some aspect of CCC, fractal dimension, and sticking probability has been examined, though these studies have not applied turbidity measurements to ascertain aggregation rates and aggregate mass fractal dimension. In natural systems where clay minerals are suspended in complex solutions containing salts, organic compounds, and microbes, aggregation kinetics may have significant implications for carbon storage and pollutant transport (e.g. von Wachenfeldt *et al.*, 2009; Bouchelaghem and Jozja, 2009). Time-resolved optical measurements allow one to probe the dynamics of clay colloidal stability for different environmental scenarios. Turbidity measurements provide information as to aggregate size, fractal dimension, and aggregation rates.

In the work presented here, the influence of $Ca^{2+}$, $Mg^{2+}$, and $K^{+}$ cations on smectite flocculation were investigated over two time frames. At an early time, flocs were much smaller than optical wavelengths ($kr \ll 1$, where $k = 2\pi/\lambda$ is the optical wavenumber and $r$ is the aggregate radius) and forward scattering can be ignored ($\gamma \approx 0$, in equation 5). In this situation, the turbidity $\tau \propto N$, where $N$ is the number of primary particles per aggregate (Berry and Wills, 1986) and is also linear in time, leading to estimates for aggregation rates from the slope of $d\tau/dt$. At later times, when flocs were large ($kr \gg 1$), the forward scattering correction factor lent itself to an approximation which allowed the fractal dimension to be extracted from the wavelength dependence of the turbidity.

## MATERIALS AND METHODS

### *Accofloc® montmorillonite*

A high-purity Na-montmorillonite (referred to by the commercial name 'Accofloc®' and with the chemical formula: $(Na,Ca)_{0.33}(Al_{1.67}Mg_{0.33})Si_4O_{10}(OH)_2n(H_2O)$; American Colloid Company, Arlington Heights, Illinois, USA) was processed as described below to obtain <0.2 μm clay particles and made homoionic with $Mg^{2+}$ using the cation substitution technique described by Moore and Reynolds (1997). The Accofloc® was initially washed in 5% sodium hypochlorite (bleach) to remove organic contaminants and then triple washed in distilled water to rinse out the bleach. Large particles and non-clay minerals were removed by centrifugation at 3600 rpm (2700 g) for 20 min. This process resulted in the elimination of particles >0.2 μm (Moore and Reynolds, 1997; Środoń, 2006) and the supernatant comprising the <0.2 μm size fraction was collected for further optical analysis. The purified clay mineral was suspended in 0.1 M $MgCl_2$ overnight and centrifuged at 1300 rpm for 30 min and rinsed in distilled water 8–10 times. Two drops of $AgNO_3$ were added to the suspension after the rinses to verify that all chloride had been removed. The suspension was then autoclaved to ensure sterility. The concentration (w/v) of the stock suspension was 3.1 g/L in the $MgCl_2$ and $CaCl_2$ experiments and 2.2 g/L in the KCl experiments, as determined by light extinction and confirmed by drying and weighing. Visual inspection of the Accofloc® suspension confirmed the absence of noticeable aggregation during storage.

### *Light-extinction measurements*

Light-extinction measurements were performed by first preparing suspensions of KCl, $CaCl_2$, and $MgCl_2$ in distilled water. Salt concentrations ranged from 0.2 mM to 1000 mM. Two mL of salt solution was placed in a 1 cm path-length quartz cuvette and the transmission integrated for 60 s to provide a reference signal. Next, 0.5 mL of Accofloc® suspension was added to the cuvette and the post-mixing transmission measured over a time period of 3000 s. This procedure resulted in a five-fold dilution of the Accofloc® and a 0.8-fold

dilution of the salt solution. The Accofloc® concentration was sufficiently dilute so as to be in the single scattering region. Addition of the salts had no significant effect on the pH, which remained neutral. Specimens were illuminated by a halogen lamp coupled to an optical fiber. The transmitted light was collected by a second fiber coupled to a spectrometer (Ocean Optics) and computer. A 1 mm aperture was placed on the collection fiber coupler which was located 5 cm from the sample. This geometry limited the collection solid angle to 0.001 sr (steradian). A magnetic stirrer was used to prevent settling of the clay mineral aggregates during data collection. Experiments were performed at room temperature (20°C) and at pH = 7. Spectra were integrated for 1 s intervals and each spectrum was saved separately. Spectra were analyzed in the 420 to 950 nm range, a region in which the Accofloc® optical absorption was negligible and light extinction was due entirely to scattering. The lack of structure in the extinction spectrum of Accofloc® in distilled water (not shown) confirmed that absorption is negligible at the wavelengths used in the data analysis (Banin and Lahav, 1968).

## RESULTS AND DISCUSSION

### *Turbidity and aggregation*

The early stages of clay mineral aggregation can be described by a bimolecular reaction process in which the kinetics is dominated by joining of individual particles (García-García *et al.*, 2006, 2007): $N' + N' \rightarrow N_2'$. The rate equation can be written as:

$$\frac{dN'(t)}{dt} = -KN'^2(t) \quad (1)$$

where $N'(t)$ is the particle concentration and $K$ is the aggregation rate per particle concentration. Integration of equation 1 gives:

$$\frac{1}{N'(t)} = \frac{1}{N'_0} + Kt \quad (2)$$

where $N'_0$ is the density of particles at $t = 0$. The average number of primary particles in an aggregate is $N = N'_0/N'(t)$ and thus

$$N(t) = 1 + KN'_0 t \quad (3)$$

From equation 3, in this early growth region, aggregate growth is linear in time (Puertas and Nieves, 1997; Kobayashi and Ishibashi, 2011).

Colloidal aggregates form a mass fractal structure in which the number of primary particles per aggregate is proportional to $r^{D_f}$ where $D_f$ is the fractal dimension of the aggregate and $r$ is the aggregate radius of gyration. In the DLCA regime, aggregates have a fractal dimension in the range of 1.7 to 1.9, while in the RLCA regime, the fractal dimension ranges from 2.1 to 2.3 (Lin *et al.*, 1989, 1990a, 1990b). Static light scattering techniques are frequently employed for measuring $D_f$ (Sorensen, 2001). Recently, broadband light scattering was demonstrated to be useful in the investigation of $D_f(t)$ with ~1 s time resolution (Alimova *et al.*, 2009). Both aggregate size and fractal dimension could be obtained from the spectral dependence of the turbidity in light-extinction measurements. The advantage of turbidity measurements over angle-resolved scattering spectroscopy is the potential to determine the aggregate size and related growth rates as well as the fractal dimensions of aggregates. The turbidity ($\tau$) for a system of colloidal aggregates was given by (M. Xu, in prep.):

$$\tau = N'NLc_0k^4a^6\frac{2N}{(D_f-1)(D_f-2)}\frac{1}{(kr)^2}\left[1-(1+(kr)^2)^{1-D_f/2}\cos\left((D_f-2)\arctan(kr)\right)\right] \quad (4)$$

where $L$ is the optical path length; $c_0k^4a^6$ is the scattering cross-section of a single platelet; $a$ is the effective primary particle radius; $D_f$ is the fractal dimension of the aggregate; and $r$ is the radius of the aggregate. Note that $N'N$ is the number density of clay platelets and is a constant for each individual experiment.

The large extent of forward scattered light from clay mineral aggregates requires a correction to the Beer-Lambert law (Spinrad *et al.*, 1978; Wind and Szymanski, 2002). The correction factor depends on the aggregate size as larger particles exhibit greater forward scattering. The turbidity correction factor, $\gamma$, is given by equation 5, below, where $I_s$ is the total scattered light intensity and $\theta$ is the beam divergence. The relationship between the true transmitted intensity, $I_T$, and the measured transmitted intensity, $I_M$, is given by:

$$I_T = \frac{I_M - \gamma I_0}{1-\gamma} \quad (6)$$

where $I_o$ is the source intensity. The turbidity corrected for forward scattering is given by:

$$\tau = \ln\left(\frac{I_T}{I_0}\right) = \ln\left(\frac{\frac{I_M}{I_0}-\gamma}{1-\gamma}\right) \quad (7)$$

$$\gamma = \frac{I_s(\theta)}{I_s} = \frac{1-\left[1+(kr)^2\sin^2(\theta/2)\right]^{1-D_f/2}\cos\left[(D_f-2)\arctan(kr\sin(\theta/2))\right]}{1-\left(1+(kr)^2\right)^{1-D_f/2}\cos\left((D_f-2)\arctan(kr)\right)} \quad (5)$$

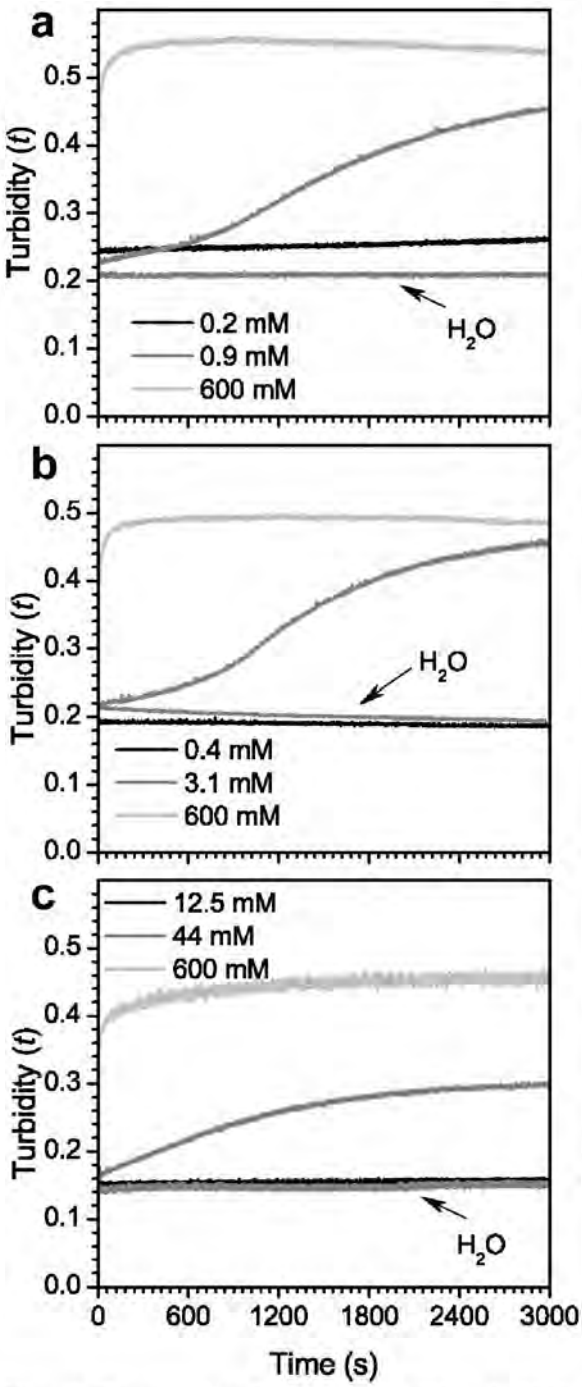


Figure 1. Changes in Accofloc® turbidity at 650 nm for 3000 s after addition of low, medium, and high concentrations of (a) $CaCl_2$, (b) $MgCl_2$, and (c) KCl. The turbidity value for Mg-montmorillonite in distilled water is shown.

*Turbidity: three cases*

Coagulation with three cation species, $Ca^{2+}$, $Mg^{2+}$, and $K^+$, was investigated. The coagulation dynamics in all experiments was divided into temporal subsets reflective of different aggregation states, *i.e.* linear growth and quasi-stable end point. Turbidity plots at $\lambda$ = 650 nm for typical low, medium, and high concentrations of $CaCl_2$, $MgCl_2$, and KCl (Figure 1a–c) for 3000 s illustrate the transformations between the linear and rapid growth regions. The case of Mg-montmorillonite in distilled water is shown in Figure 1a.

For each cationic species, measurements fell into three groups: non-aggregating, slow-aggregating, and rapid aggregating. Turbidity increased for all the studied concentrations except over the lowest concentration ranges, indicative of growth in aggregate size. The time-evolution patterns of the turbidity exhibited one of three different configurations. In the lower cation concentration range (<0.2 mM $CaCl_2$; <0.4 mM $MgCl_2$; <12 mM KCl), $\tau$ remained constant over the 3000 s duration of the experiments, indicating a lack of aggregation. At slightly greater concentrations (second configuration), $\tau$ increased linearly over a period of several minutes to tens of minutes, after which $\tau$ increased more rapidly. At still more elevated concentrations, $\tau(t)$ exhibited linear behavior for a short interval after which $\tau$ rapidly approached its near-final (3000 s) value.

*Early time/linear region*

The brief duration of the linear growth region was considered an obstacle to turbidity measurements of aggregate growth rates (Puertas and Nieves, 1997). In the present exercise a wide range of cation concentrations was explored to provide an extended coverage of the linear growth region. During the initial post-mixing phase, aggregates produced were small ($kr << 1$) and $N$ grew linearly with time (equation 3), leading to a linear increase in turbidity. The duration of this 'linear' region decreased as the cation concentration increased (Figure 2). The slope of the growth parameter, $\tau(t)$, over the linear period varied with both cation concentration and valence; increasing concentration drives the slope upscale until it reaches a saturation point. The linear region slope is plotted in Figure 3. Note that the slope of $\tau(t)$ is proportional to the aggregation rate and, therefore, proportional to the probability of particles adhering upon collision. This linear region behavior is consistent with the DLVO model. At reduced cation concentration, the diffuse layer of charge is thick and the potential barrier is substantially greater than $k_BT$. In this situation, aggregation is in the RLCA regime and aggregate growth rate is slow. At greater cation concentration, the double layer thickness was decreased, reducing the potential barrier height and resulting in an increased probability of platelets overcoming the barrier and adhering. Elevated cation concentration lowered the potential barrier, resulting in an increased sticking probability. At the CCC, the repulsive barrier is zero and every collision results in particle adhesion, *i.e.* the DLCA regime. Further increase in cation concentration above the CCC does not favor increased aggregation

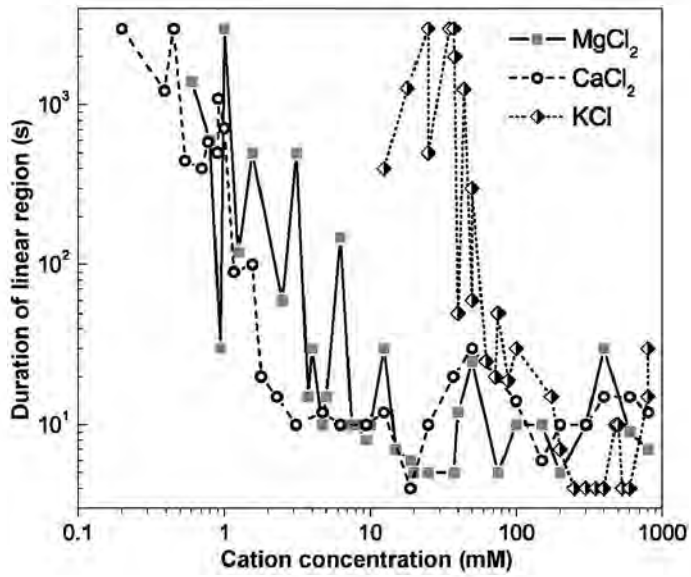


Figure 2. Duration of linear region.

rates. A CCC of 3 mM for $CaCl_2$, 4 mM for $MgCl_2$, and 70 mM for KCl was observed (Figure 3), in reasonable agreement with the Schulze-Hardy rule.

The stability ratio (W) was defined as the ratio of the number of total collisions to the number of collisions resulting in adhesion (Hunter, 1993). The ratio is equal to the reciprocal of the aggregation rate after normalizing the rate such that for concentrations greater than the CCC, the rate is unity. At the lowest concentrations for which aggregation was observed, the stability ratio was ~$10^4$ (Figure 4). A linear fit to the log-log data at concentrations below the CCC yielded slopes of $-3.2\pm0.7$ for $CaCl_2$, $-3.3\pm0.4$ for $MgCl_2$, and $-6.7\pm1.7$ for KCl. The resulting monovalent to divalent slope ratio of ~2 indicates that the stability ratio varies as $1/z$ rather than the $1/z^2$ model proposed by Reerink and Overbeek (1954), where $z$ represents cation valence. Experimental slope results frequently fail to follow the predicted $1/z^2$ relationship (Elimelech *et al.*, 1998). The observed $1/z$ dependence appears to be a result of the non-spherical shape and the unique charge distribution found in clay platelets. These factors may result in

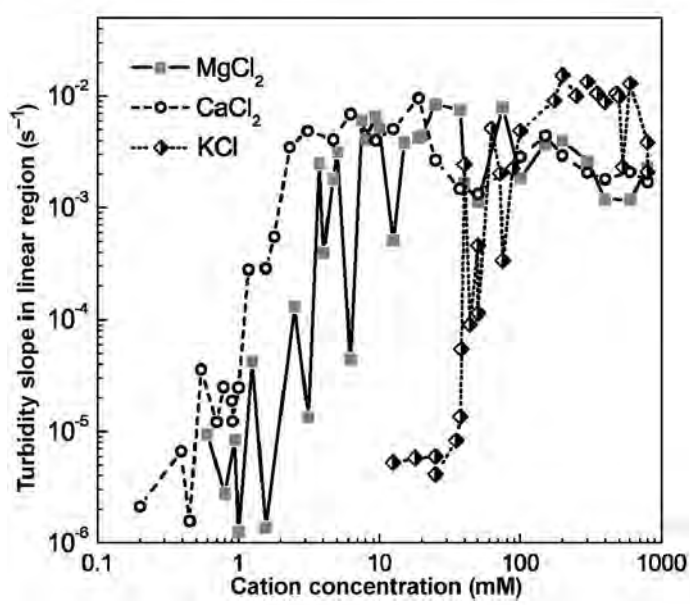


Figure 3. Slope of turbidity in linear growth region.

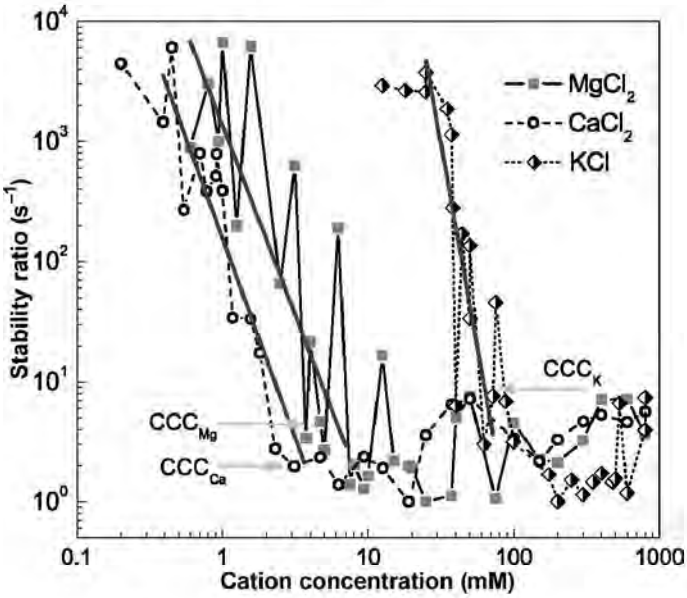


Figure 4. Stability ratios, CCC, are indicated.

different potential barriers for F-F, E-F, or E-E platelet associations. Czigany *et al.* (2005) also observed a departure from the $1/z^2$ model in montmorillonite, though the ratio of the stability slope in NaCl to $CaCl_2$ calculated by those authors was 0.5.

*Later time/larger aggregates*

For the three cations, the linear region transitioned ultimately into an equilibration interval characterized by a turbidity which is generally stable for most cation concentrations. That the turbidity remained relatively constant for the higher concentrations does not necessary imply that aggregate growth had discontinued. In the limit of large aggregate size, $\tau$ becomes approximately independent of $r$ for $D_f < 2$ but increases as $\tau \propto r^{2-D_f}$ for $D_f > 2$. Thus, a constant turbidity can be used as an indicator that $D_f < 2$, *i.e.* aggregation is in the DLCA. This case allows the appropriate approximations of turbidity and forward scattering factors to be applied to the analysis of fractal dimension. From equation 4, in the limit $kr >> 1$, and $D_f < 2$ (DLCA), $\tau \propto k^{4-D_f}$ can be shown. For $D_f > 2$, $\tau$ becomes proportional to $k^2$; therefore, the fractal dimension can be extracted more readily from the turbidity spectrum for DLCA than for RLCA. The slopes of $\tau(k)$ at 3000 s (not corrected for forward scattering) for all studied cation concentrations are shown in Figure 5. At the greater cation concentrations (*i.e.* DLCA) the slope is <2, while for lower concentrations (*i.e.* RLCA) the slope is >2, demonstrating the necessity to correct the turbidity for forward scattering. For $kr >> 1$ and $D_f < 2$, the forward scattering correction factor was approximated as $\gamma \approx (\sin\theta/2)^{2-D_f}$ to simplify the correction to the turbidity. Under this assumption, $D_f$ can be calculated directly from the turbidity. The fractal dimension for cation concentrations that satisfy these conditions are shown in Figures 6a–c. All concentrations above the CCC were characterized by $D_f < 2$. For cation levels at some degree below the CCC, $D_f < 2$. This indicates that although multiple collisions are needed for particle adhesion, the mass fractal dimension of the aggregate is more consistent with DLCA than RLCA. For the DLCA datasets, the $Ca^{2+}$ and $Mg^{2+}$ groups correspond to fractal dimensions of 1.65±0.3 and 1.75±0.3, respectively, except for the lowest concentrations. In contrast, the fractal dimension for the $K^+$-aggregated Mg-montmorillonite increased consistently from 1.35 to 1.95. This can be a consequence of a preponderance of the more loosely packed E-F and E-E associations in the aggregates at lower KCl concentrations, while the aggregates in the divalent cation suspensions were predominantly F-F associations. The differences in fractal characteristics between the monovalent and divalent cations can also be related to the effects of the cations on tactoid structure (Schramm and Kwak, 1982; Whalley and Mullins, 1991). Similar results were found by Tombácz and Szekeres (2004), who observed that montmorillonite formed E-F aggregates at concentrations above 25 mM NaCl and F-F aggregates above 100 mM NaCl at pH 4.

Notably, turbidity reached a maximum in tandem with concentration for the monovalent system whereas for the divalent system the turbidity maximum occurred at mid-level concentrations (Figure 7). This may be a consequence of increased water viscosity at very high cation concentrations and subsequent effects on aggregation. For the divalent cations at concentrations greater than the CCC, $D_f$ is independent of cation concentration

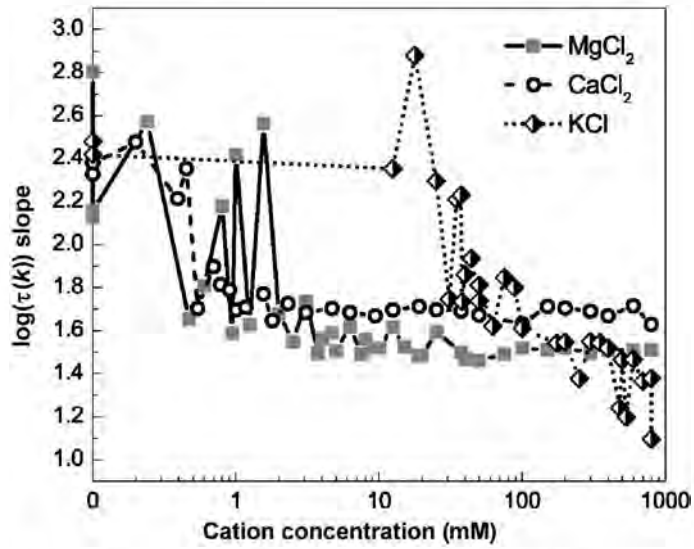


Figure 5. Slope of log–log plot of $\tau(k)$ at 3000 s. $\tau$ is not corrected for forward scattering.

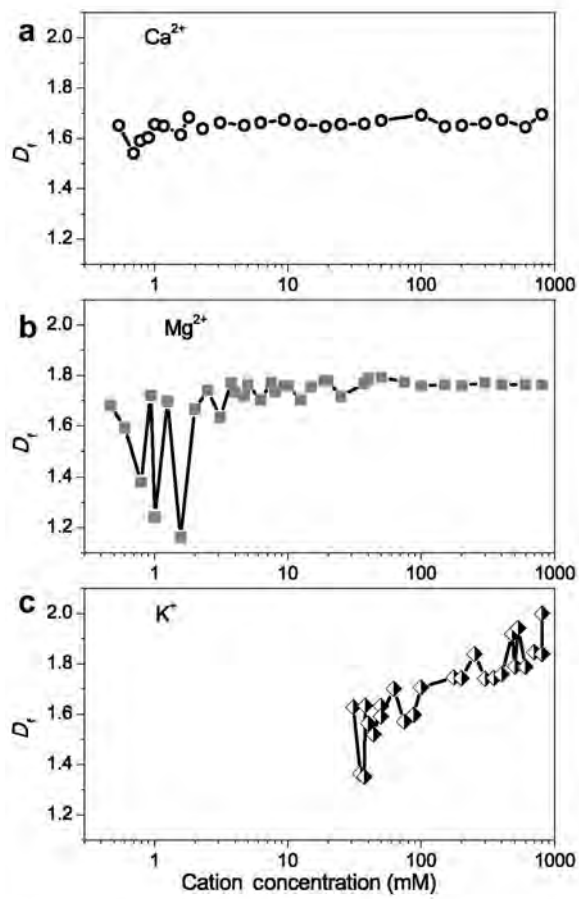


Figure 6. Aggregate fractal dimension as a function of cation concentration at $t = 3000$ s for (a) $Ca^{2+}$, (b) $Mg^{2+}$, and (c) $K^{+}$.

and, therefore, from equation 4, the greater turbidity associated with mid-level concentration of divalent cations implies that aggregate size is greater at mid-concentration. This is in contrast to the monovalent cation in which the largest aggregates occur at elevated $K^{+}$ concentrations.

An unusual feature of KCl aggregation relates to differences in the temporal location of the maximum turbidity. For the mid-level concentrations (100–500 mM), $\tau_{max}$ occurs at an early time (<10 min) but for high-level concentrations (>500 mM), $\tau_{max}$ is found at the end of the experiment (50 min, Figure 8). This may indicate that at mid-level $K^{+}$ concentrations, either the flocs exhibit a degree of partial disaggregation or a decrease in $D_f$ over time, a result not observed in divalent experiments.

## CONCLUSION

An improved understanding of the conditions necessary for the consolidation of cohesive smectite aggregates is of great importance to environmental and industrial concerns. The baseline for the conditions where flocculation is induced has been established here through an analysis of turbidity measurements in the linear growth region. These values were employed to determine relative aggregation rates, the relevant stability ratios for aggregate growth, and a working definition for the CCC range.

A key finding of this investigation pertains to a comparison of the stability ratio of the log-log slope for the divalent cations relative to the monovalent case which shows that smectite aggregation rates differ substantially from those implied by DLVO theory. This indicates that the impact of plate-like geometry in a natural system produces a condition that is less sensitive

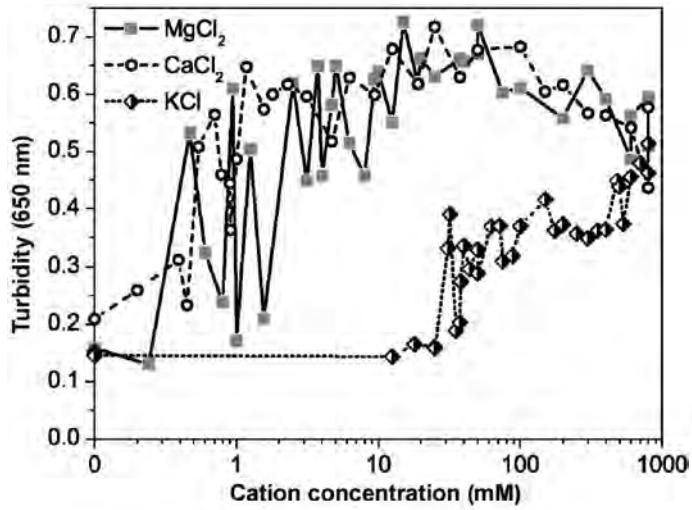


Figure 7. Turbidity at 3000 s after addition of cations.

to cation valence than in idealized experiments conducted with spherical primary particles. The DLVO theory was also found (Missana and Adell, 2000) to be unable to accurately predict clay colloidal stability, a result of pH-dependent charge distribution and the role of edge-to-face effects in aggregation.

The CCC is considered the boundary condition that separates rapid from slow aggregation rates where the rapid condition corresponds to DLCA and the slow condition to RLCA. This data set demonstrates that for a range of concentrations below the CCC the DLCA regime prevails. This is expected to hold true for different homoionic clay minerals ($Na^+$, $K^+$, or $Ca^{2+}$), although variation in surface charge may result in a different CCC value. Greater fractal dimension at greater cation concentration indicates more F-F associations, while lower cation concentration appears to favor E-F and E-E platelet associations. The greater effectiveness of divalent cations on aggregation has a bearing on the coalescence of particulate aggregates in systems with significant variations in the flux of dissolved species, such as estuaries and lacustrine environments and in areas subject to upward migrations of water through pore solutions.

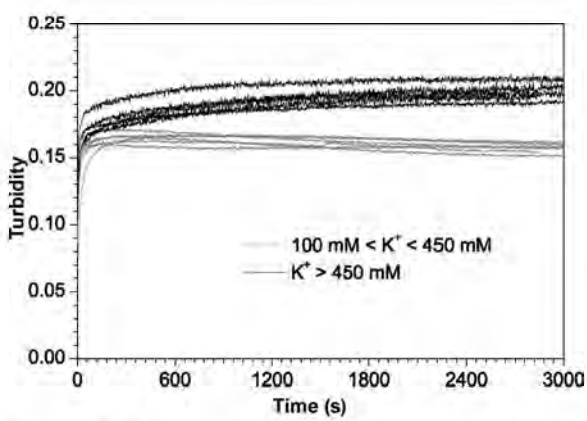


Figure 8. Turbidity at mid- and high-level concentrations of $K^+$.

## ACKNOWLEDGMENTS

The present work was supported in part by a City Seed grant #93370-09 from the City College of New York, PSC-CUNY Award #64577-00 42, and an NIH Research Centers in Minority Institutions (NIH/NCRR/RCMI) CCNY/Grant G12-RR03060.

## REFERENCES

Alimova, A., Katz, A., Orozco, J., Wei, H., Gottlieb, P., Rudolph, E., Steiner, J.C., and Xu, M. (2009) Time evolution of smectite fractal dimension measured by broadband light scattering. *Journal of Optics A: Pure and Applied Optics*, **11**, 105706.

Banin, A. and Lahav, N. (1968) Optical study of particle size of montmorillonite with various adsorbed cations. *Nature*, **217**, 1146–1147.

Berka, M. and Rice, J.A. (2004) Absolute aggregation rate constants in aggregation of kaolinite measured by simultaneous static and dynamic light scattering. *Langmuir*, **20**, 6152–6157.

Berka, M. and Rice, J.A. (2005) Relation between aggregation kinetics and the structure of kaolinite aggregates. *Langmuir*, **21**, 1223–1229.

Berry, M.V. and Wills, H.H. (1986) Optics of fractal clusters such as smoke. *Optica Acta*, **33**, 577–591.

Bouchelaghem, F. and Jozja, N. (2009) Multi-scale study of permeability evolution of a bentonite clay owing to pollutant transport: Part I. Model derivation. *Engineering Geology*, **108**, 119–132.

Czigany, S., Flury, M., and Harsh, J.B. (2005) Colloid stability in vadose zone Hanford sediments. *Environmental Science & Technology*, **39**, 1506–1512.

Derjaguin, B. and Landau, L. (1941) Theory of the stability of strongly charged lyophobic sols and of the adhesion of strongly charged particles in solution of electrolytes. *Acta Physicochimica*, **14**, 633–662.

Derrendinger, L. and Sposito, G. (2000) Flocculation kinetics and cluster morphology in illite/NaCl suspensions. *Journal of Colloid and Interface Science*, **222**, 1–11.

Elimelech, M., Gregory, J., Jia, X., and Williams, R. (1998) *Particle Deposition and Aggregation: Measurement, Modelling and Simulation*. Butterworth-Heinemann, London.

Ferreiro, E.A. and Helmy, A.K. (1974) Flocculation of Na-montmorillonite by electrolytes. *Clays and Clay Minerals*, **10**, 203–213.

García-García, S., Jonsson, M., and Wold, S. (2006) Temperature effect on the stability of bentonite colloids in water. *Journal of Colloid and Interface Science*, **298**, 694–705.

García-García, S., Wold, S., and Jonsson, M. (2007) Kinetic determination of critical coagulation concentrations for sodium- and calcium-montmorillonite colloids in NaCl and $CaCl_2$ aqueous solutions. *Journal of Colloid and Interface Science*, **315**, 512–519.

Goldberg, S., Forster, H.S., and Heick, E.L. (1991) Flocculation of illite/kaolinite and illite/montmorillonite mixtures as affected by sodium adsorption ratio and pH. *Clays and Clay Minerals*, **39**, 375–380.

Goldberg, S. and Glaubig, R.A. (1987) Effect of saturating cation, pH, and aluminum and iron oxide on the flocculation of kaolinite and montmorillonite. *Clays and Clay Minerals*, **35**, 220–227.

Hunter, R.J. (1993) *Introduction to Modern Colloid Science*. Oxford University Press, New York, 344 pp.

Keren, R. and Sparks, D.L. (1995) The role of edge surfaces in flocculation of 2:1 clay minerals. *Soil Science Society of America Journal*, **59**, 430–435.

Kobayashi, M. and Ishibashi, D. (2011) Absolute rate of turbulent coagulation from turbidity measurement. *Colloid & Polymer Science*, **289**, 831–836.

Kornilovich, B., Mishchuk, N., Abbruzzese, K., Pshinko, G., and Klishchenko, R. (2005) Enhanced electrokinetic remediation of metals-contaminated clay. *Colloids and Surfaces A: Physicochemical and Engineering Aspects*, **265**, 114–123.

Lagaly, G. (2006) Colloid Clay Science. Pp. 141–246 in: *Handbook of Clay Science*, **1** (F. Bergaya, B.K.G. Theng, and G. Lagaly, editors). Elsevier, Amsterdam.

Lagaly, G. and Ziesmer, S. (2003) Colloid chemistry of clay minerals: the coagulation of montmorillonite dispersions. *Advances in Colloid and Interface Science*, **100–102**, 105–128.

Lin, M.Y., Lindsay, H.M., Weitz, D.A., Ball, R.C., Klein, R., and Meakin, P. (1989) Universality in colloid aggregation. *Nature*, **339**, 360–362.

Lin, M.Y., Lindsay, H.M., Weitz, D.A., Ball, R.C., Klein, R., and Meakin, P. (1990a) Universal reaction-limited colloid aggregation. *Physical Review A*, **41**, 2005–2030.

Lin, M.Y., Lindsay, H.M., Weitz, D.A., Klein, R., Ball, R.C., and Meakin, P. (1990b) Universal diffusion-limited colloid aggregation. *Journal of Physics: Condensed Matter*, **2**, 3093–3113.

Luckham, P.F. and Rossi, S. (1999) The colloidal and rheological properties of bentonite suspensions. *Advances in Colloid and Interface Science*, **82**, 43–92.

Meakin, P. (1983) Formation of fractal clusters and networks by irreversible diffusion-limited aggregation. *Physical Review Letters*, **51**, 1119–1122.

Missana, T. and Adell, A. (2000) On the applicability of DLVO theory to the prediction of clay colloids stability. *Journal of Colloid and Interface Science*, **230**, 150–156.

Moore, D. and Reynolds, R.C., Jr. (1997) *X-ray Diffraction and the Identification and Analysis of Clay Minerals*, 2nd edition. Oxford University Press, New York.

Morris, G.E. and Żbik, M.S. (2009) Smectite suspension structural behaviour. *International Journal of Mineral Processing*, **93**, 20–25.

Nasser, M.S. and James, A.E. (2009) The effect of electrolyte concentration and pH on the flocculation and rheological behaviour of kaolinite suspensions. *Journal of Engineering Science and Technology*, **4**, 430–446.

Novich, B.E. and Ring, T.A. (1984) Colloid stability of clays using photon correlation spectroscopy. *Clays and Clay Minerals*, **32**, 400–406.

Pierre, A.C. and Ma, K. (1999) DLVO theory and clay aggregate architectures formed with $AlCl_3$. *Journal of the European Ceramic Society*, **19**, 1615–1622.

Plaschke, M., Schäfer, T., Bundschuh, T., Ngo Manh, T., Knopp, R., Geckeis, H., and Kim, J.I. (2001) Size characterization of bentonite colloids by different methods. *Analytical Chemistry*, **73**, 4338–4347.

Ploehn, H.J. and Liu, C. (2006) Quantitative analysis of montmorillonite platelet size by atomic force microscopy. *Industrial & Engineering Chemistry Research*, **45**, 7025–7034.

Puertas, A.M. and Nieves, F.J.d.l. (1997) A new method for calculating kinetic constants within the Rayleigh – Gans – Debye approximation from turbidity measurements. *Journal of Physics: Condensed Matter*, **9**, 3313.

Ravera, M., Ciccarelli, C., Gastaldi, D., Rinaudo, C., Castelli, C., and Osella, D. (2006) An experiment in the electrokinetic removal of copper from soil contaminated by the brass industry. *Chemosphere*, **63**, 950–955.

Reerink, H. and Overbeek, J.T.G. (1954) The rate of coagulation as a measure of the stability of silver iodide sols. *Discussions of the Faraday Society*, **18**, 74–84.

Schramm, L.L. and Kwak, J.C.T. (1982) Influence of exchangeable cation composition on the size and shape of montmorillonite particles in dilute suspension. *Clays and Clay Minerals*, **30**, 40–48.

Sorensen, C.M. (2001) Light scattering by fractal aggregates: a review. *Aerosol Science & Technology*, **35**, 648–687.

Spinrad, R.W., Zaneveld, J.R.V., and Pak, H. (1978) Volume scattering function of suspended particulate matter at near-forward angles: a comparison of experimental and theoretical values. *Applied Optics*, **17**, 1125–1130.

Środoń, J. (2006) Identification and quantitative analysis of clay minerals. Pp. 765–788 in: *Handbook of Clay Science*, **1** (F. Bergaya, B.K.G. Theng, and G. Lagaly, editors) Elsevier, Amsterdam.

Stawiński, J., Wierzchoś, J., and Garcia-Gonzalez, M.T. (1990) Influence of calcium and sodium concentration on the microstructure of bentonite and kaolin. *Clays and Clay Minerals*, **38**, 617–622.

Tawari, S.L., Koch, D.L., and Cohen, C. (2001) Electrical double-layer effects on the Brownian diffusivity and aggregation rate of Laponite clay particles. *Journal of Colloid and Interface Science*, **240**, 54–66.

Tombácz, E. and Szekeres, M. (2004) Colloidal behavior of aqueous montmorillonite suspensions: the specific role of pH in the presence of indifferent electrolytes. *Applied Clay Science*, **27**, 75–94.

Tournassat, C., Neaman, A., Villiéras, F., Bosbach, D., and Charlet, L. (2003) Nanomorphology of montmorillonite particles: Estimation of the clay edge sorption site density by low-pressure gas adsorption and AFM observations. *American Mineralogist*, **88**, 1989–1995.

van Olphen, H. (1977) *Introduction to Clay Colloid Chemistry*. Wiley-Interscience Publication, John Wiley & Sons, New York.

van Oss, C.J., Giese, R.F., and Costanzo, P.M. (1990) DLVO and non-DLVO interactions in hectorite. *Clays and Clay Minerals*, **38**, 151–159.

Verwey, E.J.W. and Overbeek, J.T.G. (1948) *Theory of the Stability of Lyophobic Colloids*. Elsevier Publishing, New York.

von Wachenfeldt, E., Bastviken, D., and Tranvik, L.J. (2009) Microbially induced flocculation of allochthonous dissolved organic carbon in lakes. *Limnology and Oceanography*, **54**, 1811–1818.

Whalley, W.R. and Mullins, C.E. (1991) Effect of saturating cation on tactoid size distribution in bentonite suspensions. *Clay Minerals*, **26**, 11–17.

Wind, L. and Szymanski, W.W. (2002) Quantification of scattering corrections to the Beer-Lambert law for transmittance measurements in turbid media. *Measurement Science and Technology*, **13**, 270.

(*Received 12 July 2012; revised 19 December 2012; Ms. 691; AE: S. Wold*)

*Clays and Clay Minerals*, Vol. 61, No. 1, 11–25, 2013.

# THE EFFECT OF ANTIMONATE, ARSENATE, AND PHOSPHATE ON THE TRANSFORMATION OF FERRIHYDRITE TO GOETHITE, HEMATITE, FEROXYHYTE, AND TRIPUHYITE

RALPH MICHAEL BOLANZ[1,*], ULRICH BLÄSS[1], SONIA ACKERMANN[1], VALERIAN CIOBOTĂ[2], PETRA RÖSCH[2], NICOLAE TARCEA[3], JÜRGEN POPP[2,3], AND JURAJ MAJZLAN[1]

[1] Institute of Geoscience, Friedrich-Schiller-University, Jena, Germany
[2] Institute of Physical Chemistry, Friedrich-Schiller-University, Jena, Germany
[3] Institute of Photonic Technology, Jena, Germany

**Abstract**—Iron oxides, typical constituents of many soils, represent a natural immobilization mechanism for toxic elements. Most iron oxides are formed during the transformation of poorly crystalline ferrihydrite to more crystalline iron phases. The present study examined the impact of well known contaminants, such as P(V), As(V), and Sb(V), on the ferrihydrite transformation and investigated the transformation products with a set of bulk and nano-resolution methods. Irrespective of the pH, P(V) and As(V) favor the formation of hematite ($\alpha$-$Fe_2O_3$) over goethite ($\alpha$-FeOOH) and retard these transformations at high concentrations. Sb(V), on the other hand, favors the formation of goethite, feroxyhyte ($\delta'$-FeOOH), and tripuhyite ($FeSbO_4$) depending on pH and Sb(V) concentration. The elemental composition of the transformation products analyzed by inductively coupled plasma optical emission spectroscopy show high loadings of Sb(V) with molar Sb:Fe ratios of 0.12, whereas the molar P:Fe and As:Fe ratios do not exceed 0.03 and 0.06, respectively. The structural similarity of feroxyhyte and hematite was resolved by detailed electron diffraction studies, and feroxyhyte was positively identified in a number of the samples examined. These results indicate that, compared to P(V) and As(V), Sb(V) can be incorporated into the structure of certain iron oxides through Fe(III)-Sb(V) substitution, coupled with other substitutions. However, the outcome of the ferrihydrite transformation (hematite, goethite, feroxyhyte, or tripuhyite) depends on the Sb(V) concentration, pH, and temperature.

**Key Words**—Antimony, Arsenic, Ferrihydrite, Feroxyhyte, Goethite, Hematite, Iron Oxides, Phosphorous, Transformation, Tripuhyite.

## INTRODUCTION

Iron oxides are omnipresent constituents of most soils and count as important sinks for heavy metals and toxic elements (*e.g.* Ackermann *et al.*, 2009). Amongst the iron oxides, poorly crystalline 2-line ferrihydrite (referred to hereafter as ferrihydrite) is the initial secondary iron oxide formed during the weathering of primary iron minerals (Loan *et al.*, 2005). Ferrihydrite is generally considered to be an intermediate step in the formation of well crystallized iron oxides, such as goethite ($\alpha$-FeOOH) and hematite ($\alpha$-$Fe_2O_3$) (Cudennec and Lecerf, 2006). The outcome of the ferrihydrite transformation depends on temperature, pH, and abundance of foreign ions (*e.g.* Cornell *et al.*, 1987; Nagano *et al.*, 1994; Paige *et al.*, 1996, 1997; Shaw *et al.*, 2005; Cudennec and Lecerf, 2006; Das *et al.*, 2011a, 2011b). The most common products of the ferrihydrite transformation are goethite and hematite (Cornell and Schwertmann, 2003). Near or at the surface of the Earth both goethite and hematite are the two most stable iron oxides (Cornell and Schwertmann, 2003; Das *et al.*, 2011b). Although goethite and hematite can be formed simultaneously by ferrihydrite transformation (Das *et al.*, 2011b), conditions which are favorable for goethite are unfavorable for hematite and *vice versa* (Schwertmann and Murad, 1983). The transformation of ferrihydrite to goethite is thought to be a process in which ferrihydrite dissolves and goethite is formed by nucleation/crystallization from bulk solution (Schwertmann and Murad, 1983; Blesa and Matijevic, 1989; Cornell and Schwertmann, 2003). Hematite, on the other hand, is formed topotactically through atomic solid-solid rearrangement within the ferrihydrite matrix (Schwertmann and Murad, 1983; Johnston and Lewis, 1983; Cudennec and Lecerf, 2006; Cornell and Schwertmann, 2003). Because of these two different competing formation mechanisms (Schwertmann and Fischer, 1966), one could speculate that any parameter which leads to the stabilization of ferrihydrite favors the formation of hematite, whereas any parameter leading to the dissolution of ferrihydrite favors goethite formation. The first of these parameters is temperature. Elevated temperatures result in the aggregation of ferrihydrite particles (Fischer and Schwertmann, 1975) and lead to dehydration, which favors the formation of hematite (Cornell and Schwertmann, 2003; Cudennec and Lecerf,

* E-mail address of corresponding author:
ralph.bolanz@uni-jena.de
DOI: 10.1346/CCMN.2013.0610102

2006). The second parameter is pH. At room temperature, ferrihydrite is least soluble at pH 7–8 (Schwertmann and Murad, 1983), where goethite formation has its minimum and hematite is favored. Conversely, goethite formation from ferrihydrite has its maximum at pH 12 in alkaline media and pH 4 in acidic media at room temperature (Schwertmann and Murad, 1983). The third notable parameter is the abundance of foreign ions during the transformation process, which can affect the transformation rate and cause variations in the transformation products (for summaries see Jambor and Dutrizac (1998) and Cornell and Schwertmann (2003)).

The focus of the present study was the transformation of ferrihydrite in the presence of P(V), As(V), and Sb(V). In aqueous solution, P(V) and As(V) are both coordinated tetrahedrally by four oxygen atoms and show, at pH 4–12, the same species ($H_2P/AsO_4^-$, $HP/AsO_4^{2-}$, and $P/AsO_4^{3-}$) (Guan *et al.*, 2009). Sb(V), however, displays from pH 4–12 only one dominant species, $Sb(OH_6)^-$ (Filella *et al.*, 2002). In the presence of phosphate, the solubility (Majzlan, 2011) and consequently the transformation rate of ferrihydrite is reduced (Paige *et al.*, 1997), and aggregation of colloidal iron oxide particles is observed (Ile *et al.*, 1996), which leads to a preferred formation of hematite (Paige *et al.*, 1997). Like phosphate, arsenate favors the aggregation of ferrihydrite, decreases the transformation rate, and promotes the formation of hematite over goethite (Paige *et al.*, 1996).

P(V), As(V), and Sb(V) may occur together in Sb mine tailings and compete for the same adsorption sites on the surfaces of the more abundant minerals, especially ferrihydrite or its transformation products, goethite and hematite. The present study, therefore, examined the transformation of ferrihydrite into other, more crystalline iron oxides in the presence of antimonate, and compared the results with those for phosphate- and arsenate-doped ferrihydrite, transformed under the same conditions. To the authors' knowledge, no comparable transformation experiments have ever been performed with antimonate. The newly formed products were characterized using an array of bulk and nano-resolution methods.

## MATERIALS AND METHODS

Two-line ferrihydrite was synthesized after Schwertmann and Cornell (2000). A mass of 10.1 g $Fe(NO_3)_3 \cdot 9H_2O$ (Alfa Aesar, Ward Hill, Massachusetts, USA) was dissolved in 200 mL of deionized water and transformed into 2-line ferrihydrite by adding 45 mL of 5 M potassium hydroxide (Merck, Darmstadt, Germany) solution under constant stirring. The suspension was adjusted to 490 mL with deionized water, resulting in an end-point pH of ~13. The suspension was then adjusted to 500 mL with deionized water. The resulting brown aggregates (flocs) settled after a few minutes in suspension and showed a dry weight of ~7 g (air-dried). This ferrihydrite slurry was immediately adjusted to the desired pH (4, 7, or 12) by adding nitric acid (65%) (J.T. Baker, Center Valley, Pennsylvania, USA) and doped with pre-selected volumes of a 15 mM solution of potassium hexahydroxoantimonate (Merck, Darmstadt, Germany) for Sb(V), arsenic pentoxide (Alfa Aesar, Ward Hill, Massachusetts, USA) for As(V), and potassium dihydrogen phosphate (Merck, Darmstadt, Germany) for P(V). Previous studies indicated that nitrate does not significantly interfere with the adsorption of P(V), As(V), and Sb(V) onto amorphous $Fe(OH)_3$ (Álvarez-Benedí *et al.*, 2005; Tighe *et al.*, 2005). The ferrihydrite synthesized was, therefore, unwashed in order to maintain the calculated Fe concentration and, thus, to keep the Fe to P/As/Sb ratio constant. The volumes of the doping solutions were calculated to arrive at the P(V)/As(V)/Sb(V) molarity of 0 mM, 0.225 mM, 0.750 mM, 2.250 mM, and 6.000 mM after adjusting to 500 mL with deionized water. After bringing the volume to ~490 mL, the pH was checked and adjusted again if necessary by adding nitric acid (65%) or 5 M potassium hydroxide solution and the volume finally brought to 500 mL with deionized water. The samples were then stored at 70°C for up to 16 days and sample aliquots were taken every second day, washed, air-dried, and sealed in glass vials. The synthesis of ferrihydrite involved high pH conditions under which Si may be mobilized into the aqueous solutions. For this reason polyethylene (PE) containers were used exclusively during this work, rather than glassware.

A second series of ferrihydrite samples was synthesized as described above. In this series, ferrihydrite was doped at pH 4 in smaller concentration steps with molar Sb:Fe ratios of 0.000–0.080 in steps of 0.005, 0.090, 0.100, and 0.300; 0.300–0.500 in steps of 0.025, and 0.500–1.000 in steps of 0.100. The doped ferrihydrite was again incubated for 16 days at 70°C, washed, air-dried, and sealed in glass vials.

Several reference compounds were synthesized for Raman spectroscopy measurements. The hematite ($\alpha$-$Fe_2O_3$) reference was synthesized by transforming 2-line ferrihydrite at pH 4 and 70°C in aqueous solution for 16 days. The sample was washed, air-dried, and sealed in a glass vial. Pure feroxyhyte ($\delta'$-FeOOH) was synthesized after Schwertmann and Cornell (2000). A mass of 5.96 g $FeCl_2 \cdot 4H_2O$ was dissolved in 300 mL of deionized water and adjusted to pH 8 with 5 M NaOH solution. 40 mL of $H_2O_2$ (30%) was added quickly and the pH was again adjusted to 8. The product was washed, air-dried, and sealed in glass vials. Tripuhyite reference 1 was synthesized using a modified version of the Diemar *et al.* (2009) recipe. A solution of 0.1 M $Fe_2(SO_4)_3 \cdot H_2O$ (Sigma-Aldrich) was mixed with a 0.1 M $KSb(OH)_6$ (Merck, Darmstadt, Germany) solution at a ratio of 1:2.

The brown precipitate was refluxed for three days at 100°C, washed, air-dried, and sealed in a glass vial. Tripuhyite reference 2 was synthesized using a modified version of the Martinelli *et al.* (2004) recipe. Hematite, synthesized as described above, was mixed with $Sb_2O_5$ (Alfa Aesar, Ward Hill, Massachusetts, USA) and heated in a sintered corundum crucible for 24 h at 600°C, followed by 48 h at 900°C and cooled over 12 h to 25°C. Immediately after the synthesis, tripuhyite was washed, air-dried, and sealed in a glass vial. All reference compounds were analyzed and checked for impurities by X-ray diffraction (XRD).

The pH was measured with a pH100 pH meter (VWR, Radnor, Pennsylvania, USA), which was calibrated with a pH 6.86 (HANNA Instruments, Woonsocket, Rhode Island, USA) and a pH 4.00 buffer solution (HANNA Instruments, Woonsocket, Rhode Island, USA) according to the calibration procedure.

Elemental composition (P, As, Sb, and Fe) was determined by inductively-coupled plasma optical emission spectrometry (ICP-OES) using a Quadrupol-ICP-MS X SeriesII (ThermoFisher Scientific, Bremen, Germany) with a charge-coupled device (CCD) detector.

Powder XRD patterns were collected using a Bruker D8 Advance DaVinci diffractometer (Karlsruhe, Germany), employing CuK$\alpha$ radiation ($\lambda$ = 1.54058 Å). The patterns were collected at room temperature between 5 and 90°2θ, with a step size of 0.02°2θ and a collection time of 1 s/step. The proportions of the phases in the samples were extracted from the XRD patterns. To check the procedure, a standard was prepared containing 25 wt.% ferrihydrite, 25 wt.% goethite, 25 wt.% hematite, and 25 wt.% feroxyhyte. In order to quantify the area (intensity) of the following reflections, the program *Fityk* 0.9.8 (Wojdyr, 2010) was used: ferrihydrite 33.90°2θ, goethite 21.37°2θ (101), hematite 24.15°2θ (012), and feroxyhyte 35.13°2θ (100). The intensities obtained were normalized for hematite and feroxyhyte to 100% and all the intensities were weighted by $I/I_{cor}$ values, taken from the Crystallography Open Database (COD) (Downs and Hall-Wallace, 2003; Gražulis *et al.* 2009, 2012); ferrihydrite 1.03 (COD 9012761), goethite 2.92 (COD 9002158), hematite 4.82 (COD 1011267), and feroxyhyte 2.27 (COD 1008762). This method enabled the quantification of all phases in the samples with an inaccuracy of <5 wt.% for the standard prepared. The incorporation of elements heavier than iron (*e.g.* As, Sb) into the iron oxides can affect the XRD peak intensities, and must be taken into account.

The morphology and grain size for goethite and hematite were examined by scanning electron microscopy (SEM) using a Carl Zeiss ULTRA PLUS FE-SEM (Oberkochen, Germany) operating at 20 kV with an Inlens SE-detector. Several milligrams of air-dried sample were distributed over a conductive carbon pad with adhesive properties (PLANO, Wetzlar, Germany). As all the samples studied were <1 μm across, the samples were not coated with carbon which could have masked the morphological characteristics.

Morphological characteristics, grain size, and electron diffraction of feroxyhyte samples were studied by transmission electron microscopy (TEM) using a LEO922 OMEGA instrument (Carl Zeiss, Oberkochen, Germany) operating at 200 kV with an in-column Omega filter and energy dispersive X-ray (EDX) detector. The feroxyhyte sample was suspended in ethanol, placed on a Lacey copper grid, and air dried to prepare it for analysis.

The specific surface area of selected transformation products was determined using the Brunauer-Emmet-Teller (BET) method (Brunauer *et al.*, 1938) with a Quantachrome Autosorb (Odelzhausen, Germany) automated gas sorption system. About 0.2 g of the sample was outgassed at 70°C for 2–7 h and measured using evaporated liquid $N_2$ as the adsorbate gas.

Raman analyses of the iron oxides were performed using a commercial micro-Raman setup (HR LabRam inverse system, Jobin Yvon Horiba) (Kyoto, Japan). Raman scattering was excited by a frequency doubled Nd:YAG laser at a wavelength of 532 nm with a laser power of ~20 μW incident on the sample. The low laser power was selected to prevent alteration of the sample. The laser beam was focused on the sample by means of a Leica PLFluoar ×100/0.75 microscope objective lens down to a spot diameter of ~0.7 μm. The dispersive spectrometer had an entrance slit of 100 μm, a focal length of 800 mm, and was equipped with a grating of 300 lines/mm. The Raman scattered light was detected by a Peltier-cooled CCD detector. The integration times for one Raman spectrum ranged from 60 to 1000 s.

## RESULTS

### *Morphology and surface area*

The ferrihydrite samples synthesized had a specific surface area of 252 $m^2/g$, in good agreement with other studies (Hansen *et al.*, 1994; Larsen and Postma, 2001). Goethite synthesized at pH 12 consisted of acicular crystals 250–1750 nm long and 80–200 nm in diameter with a specific surface area of 25 $m^2/g$, whereas hematite synthesized at pH 4 displayed rhombohedral crystals with a particle size of 35–260 nm and a specific surface area of 30 $m^2/g$. These values are consistent with the literature (Cornell and Schwertmann, 2003). Feroxyhyte samples formed at pH 4 and Sb(V) concentrations of 6 mM exhibited rhombohedral crystals with a size of 10–30 nm and a specific surface area of 94 $m^2/g$, which is less than the given values for Sb-free feroxyhyte of 140–240 $m^2/g$ (Carlson and Schwertmann, 1980).

### *Products of transformation experiments (XRD, Raman spectroscopy, and TEM)*

In the transformation experiments (summarized in Figure 1) the phases produced in the runs were color-

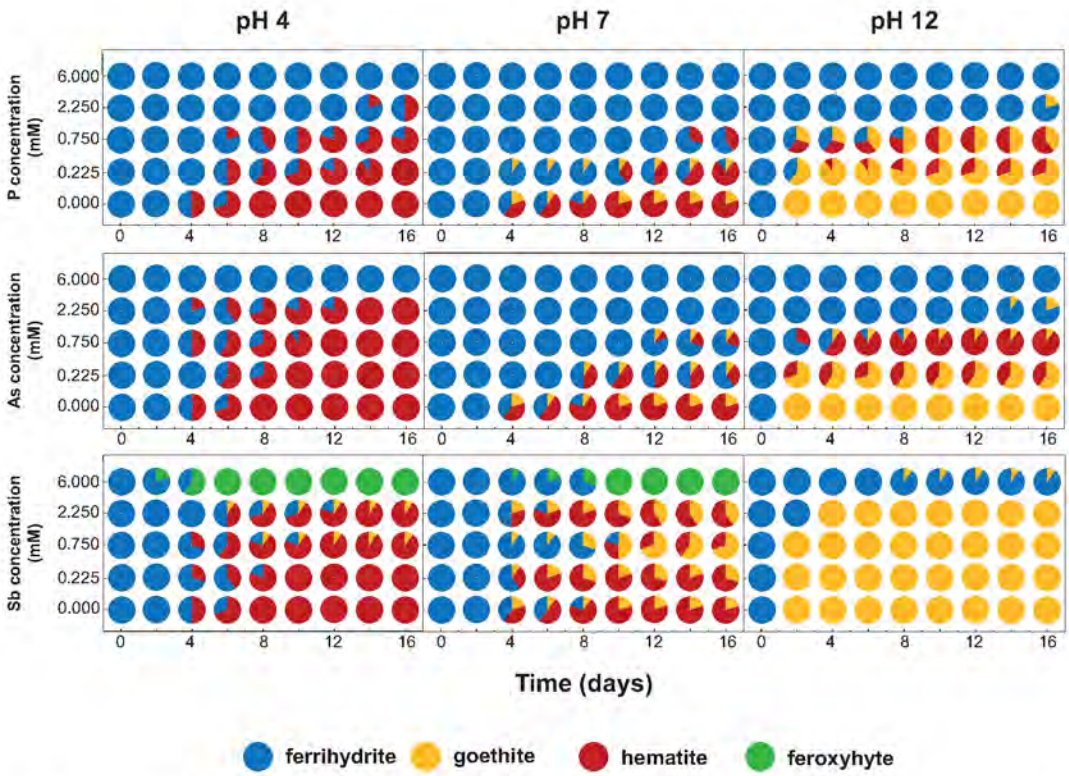


Figure 1. Iron oxide speciation and quantification for P-, As-, and Sb-doped ferrihydrite and subsequently formed transformation products.

coded and the pie charts show the quantitative proportions of the phases. The results were sorted according to the two principal variables used in the runs, starting pH of the solution and the molarity of a pentavalent cation, either P(V), As(V), or Sb(V). Temperature was kept constant at 70°C in all runs.

Under acidic conditions (pH 4), in the absence of P(V), As(V), or Sb(V), and at 70°C, ferrihydrite transformed completely to hematite within 8 days (Figure 1), an expected result, considering the preferred formation of hematite at elevated temperatures (Cornell and Schwertmann, 2003, p. 389). In the presence of P(V) and As(V), the transformation rate generally declined with increasing concentrations, to a complete inhibition at 6.00 mM P(V) or As(V). The presence of Sb(V), however, led to a more complex transformation behavior. At low Sb(V) concentrations (0.225 mM), the transformation to hematite was slightly retarded. With increasing Sb(V) concentrations, goethite appeared in addition to hematite and the transformation rate was diminished. At 6.00 mM Sb(V), surprisingly, the transformation rate suddenly increased with feroxyhyte as the only crystalline transformation product after 6 days.

At neutral pH (7), the transformation of pure ferrihydrite took 12 days and yielded a mixture of 70 wt.% hematite and 30 wt.% goethite. P(V) and As(V) retarded the transformation process significantly and caused a complete inhibition at concentrations of 2.25 mM and above. In the presence of Sb(V), the transformation was again not only affected by retardation but, just as at pH 4, the presence of Sb(V) seemed to favor goethite, but in the presence of 6.00 mM Sb(V) the ferrihydrite was converted almost completely to feroxyhyte with traces of hematite (the latter detected only by Raman spectroscopy).

Under alkaline conditions (pH 12) and in the absence of 'foreign' ions, ferrihydrite transformed almost completely within 2 days to goethite, with traces of hematite (detected by Raman spectroscopy). No changes in composition were observed until day 16, when the experiment was terminated. These observations are consistent with the results of Schwertmann and Murad (1983), Nagano *et al.* (1994), and Cudennec and Lecerf (2006).

P(V) and As(V) favored hematite formation over goethite, and retarded the transformation process significantly at concentrations of 2.25 mM. At concentrations of 6.00 mM only traces of hematite were detected by Raman spectroscopy. In the presence of Sb(V), ferrihydrite transformed almost undisturbed to goethite. Only at concentrations of 6.00 mM Sb(V) was a retarding effect observed. The main transformation product was goethite with traces of hematite (detected by Raman spectroscopy).

Table 1. Iron oxide speciation by Raman spectroscopy from selected ferrihydrite transformation products. fh: ferrihydrite, goe: goethite, hem: hematite, and fx: feroxyhyte. The asterisk marks components occurring in trace amounts which were not detected by XRD.

| Additive | Concentration | pH4 | pH7 | pH12 |
|---|---|---|---|---|
| $P^{5-}$ | high (6. mM) | fh/hem* | fh | fh/hem* |
| | low (0.75 mM) | fh/hem | fh/hem | goe/hem |
| | free (0 mM) | hem | goe/hem | goe/hem* |
| $As^{5-}$ | high (6 mM) | fh/hem* | fh | fh/hem* |
| | low (0.75 mM) | fh/hem | fh/goe/hem | goe/hem |
| | free (0 mM) | hem | goe/hem | goe/hem* |
| $Sb^{5-}$ | high (6 mM) | fx | fx/hem* | fh/goe/hem* |
| | low (0.75 mM) | goe/hem | goe/hem | goe |
| | free (0 mM) | hem | goe/hem | goe/hem* |

Raman spectroscopy is a powerful tool for mineral identification (Dörfer *et al.*, 2010; Ciobotă *et al.*, 2012), especially for iron oxides (Hanesch, 2009). For this reason, selected samples were analyzed by Raman spectroscopy. The Raman spectra (summarized in Table 1) confirmed the XRD measurements and complemented them by identifying iron oxide species occurring in trace amounts only.

Because of the poor crystallinity of feroxyhyte, this phase was also characterized by TEM. Several selected-area electron diffraction (SAED) patterns of single feroxyhyte crystals were collected (Figure 2). Feroxyhyte formed rhombohedral crystals 10–30 nm across and with sharp diffraction spots. Despite the sensitivity of feroxyhyte (fx) to the electron beam and its small size, one crystal was tilted carefully by up to ~18° along the $[110]_{fx}$ axis from the $[1\bar{1}1]_{fx}$ zone to the $[2\bar{2}1]_{fx}$ zone. These measurements confirmed the 3D consistency with the feroxyhyte lattice.

*Chemical composition of the transformation products (ICP-OES)*

The elemental composition of all 405 runs (shown in Figure 1) is summarized in Figure 3. A direct comparison between the different loadings (P(V), As(V), Sb(V)) is complex, considering that different anions lead to different ratios amongst the transformation products and retard the transformation at different rates.

At pH 12 and concentrations of up to 0.750 mM, P(V) and As(V) led to goethite + hematite mixtures which were free of untransformed ferrihydrite. At 0.750 mM, molar P:Fe and As:Fe ratios of 0.0024 and 0.0068, respectively, were observed. Higher P(V) and As(V) concentrations (2.250–6.000 mM) led to ferrihydrite as the dominant phase, showing significantly larger molar P:Fe and As:Fe ratios of 0.012 and 0.024, respectively. In the presence of Sb(V), pure goethite was even formed at concentrations of 2.250 mM. These goethite samples showed molar Sb:Fe ratios of 0.034. At Sb(V) concentrations of 6.000 mM,

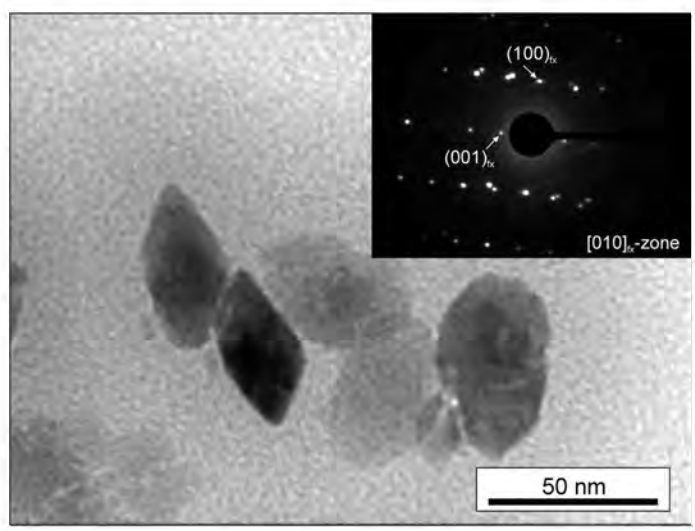


Figure 2. Bright-field TEM image and corresponding selected area electron diffraction pattern (inset) of that area showing the rhombohedral shape and the sharp diffraction spots of feroxyhyte.

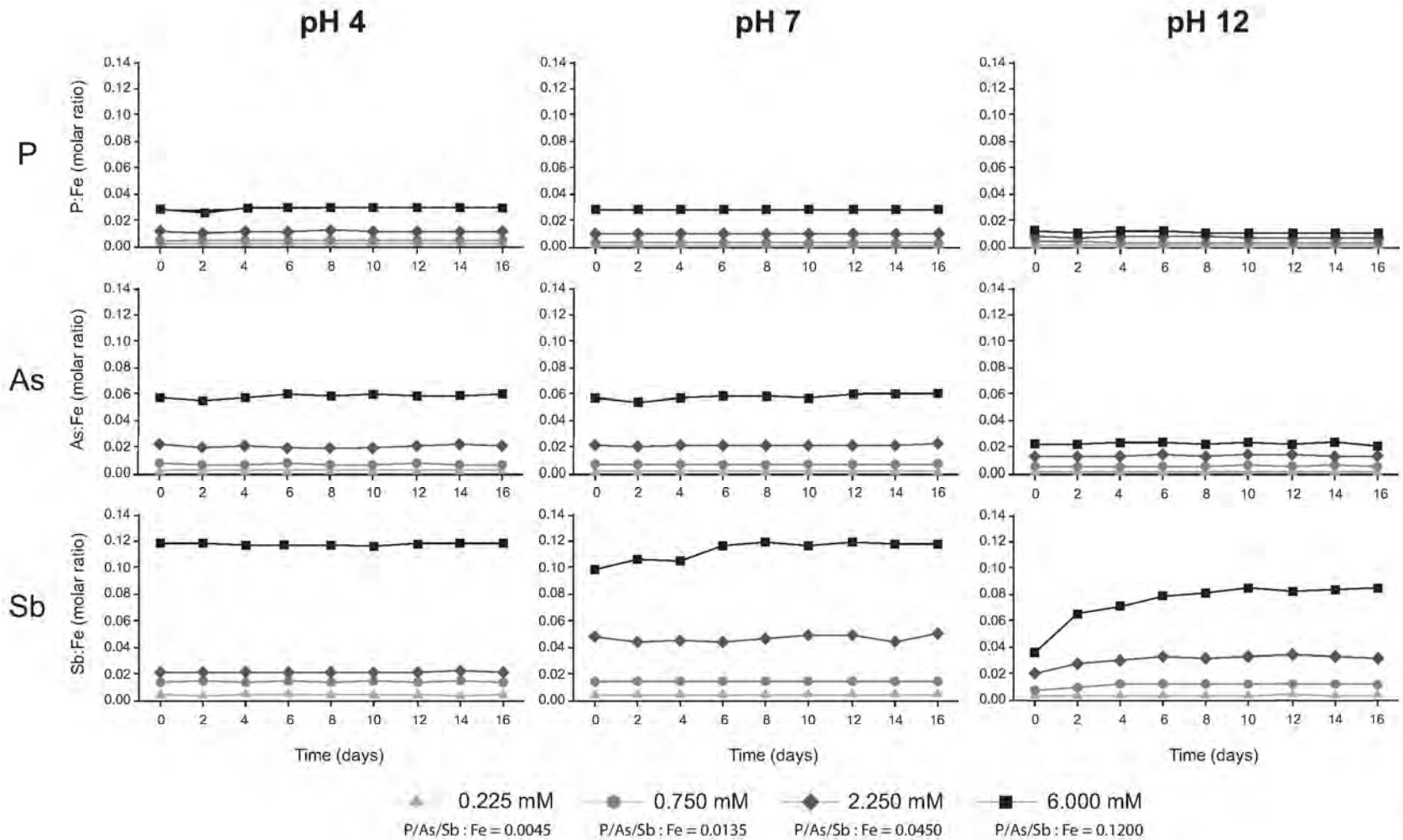


Figure 3. Chemical composition of the transformation products given as molar ratios of P, As, and Sb *vs.* Fe. The molar starting ratios of P/As/Sb:Fe are given for each concentration step.

goethite formed but ferrihydrite remained as the dominant phase until day 16, when the experiment was terminated. The goethite + ferrihydrite mixtures displayed molar Sb:Fe ratios of 0.085.

At pH 7, neither P(V)- nor As(V)-doped ferrihydrite transformed completely. Samples doped with P(V) revealed a maximum molar P:Fe ratio of 0.028, whereas As(V)-doped samples showed a maximum molar As:Fe ratio of 0.060. Ferrihydrite doped with Sb(V), however, displayed a maximum molar Sb:Fe ratio of 0.052 (at 2.25 mM) for the goethite + hematite mixtures and 0.121 (at 6.00 mM) for feroxyhyte.

At pH 4, P(V) and As(V) revealed the highest concentrations in untransformed ferrihydrite (at 6.00 mM) with molar P:Fe and As:Fe ratios of 0.029 and 0.060, respectively. Again, the highest Sb(V) concentrations were found in feroxyhyte with molar Sb:Fe ratios of 0.120. Surprisingly, the goethite + hematite mixtures (formed at 2.25 mM Sb) contained not only less Sb(V) than in similar mixtures formed at pH 7, but also less than in goethite formed at pH 12.

*Transformations at increasing Sb:Fe ratios*

During the ferrihydrite transformations at pH 4 and 7, an increase in goethite abundance and the formation of feroxyhyte was observed. In order to investigate these two changes in transformation products and to evaluate the stability of feroxyhyte at even higher Sb:Fe ratios, a second experiment at smaller concentration steps was performed. The conditions of temperature at 70°C and 16 days of transformation time were maintained for all samples. Selected XRD patterns of the experiment are shown in Figure 4.

In the absence of Sb(V) (molar Sb:Fe ratio of 0.000) and pH 4, hematite was the only transformation product. With increasing Sb(V) concentrations, the formation of goethite (goe) was indicated by a growing (101) peak at 21.15°2θ. The increase in intensity of the $(101)_{goe}$ peak was coupled with an increase of its full width at half maximum value (FWHM), and hence, a decrease in the crystallinity of goethite. Hematite was also affected by increasing Sb(V) concentrations, showing decreasing intensities and an increasing FWHM of its peaks. However, the peaks ascribed to hematite did not decrease equally in intensity. From the dominant hematite peaks, (102), (104), and (024) decreased strongly in intensity, whereas (110), (113), (116), and (300) decreased far less. Simultaneously, the hematite peaks (006) and (226) increased in intensity. The remaining peaks at a molar Sb:Fe ratio of 0.300 correspond well with the feroxyhyte peaks {100}, {002}, {101}, {102}, {110}, and {202}.

With further increasing Sb(V) concentrations, the FWHM of the feroxyhyte peaks increased. At molar Sb:Fe ratios of 0.600–1.000, the only crystalline ferrihydrite transformation product was the iron antimonate, tripuhyite ($FeSbO_4$).

As both feroxyhyte and tripuhyite are poorly crystalline transformation products, the XRD results were confirmed by Raman spectroscopy (selected spectra are shown in Figure 5). Sample pH4Sb6.000 was the product of ferrihydrite transformed at pH 4, 70°C, and Sb(V) concentrations of 6.000 mM, with an aging time of 16 days. The Raman spectrum confirmed feroxyhyte as the only transformation product with impurities of $KNO_3$ from the ferrihydrite synthesis. Sample pH7Sb6.000 was formed under the same conditions, but at pH 7 instead of pH 4. In this case feroxyhyte was accompanied by traces of hematite and again some minor $KNO_3$ impurities. At a molar Sb:Fe ratio of 0.600 (sample pH4Sb:Fe0.600), no feroxyhyte was formed but tripuhyite instead. This tripuhyite was poorly crystalline, which reduced the quality of the Raman spectrum considerably. In comparison to tripuhyite reference 1, synthesized following the method of Diemar *et al.* (2009), only minor similarities could be observed with sample pH4Sb:Fe0.600, *i.e.* mainly the band at ~620 $cm^{-1}$. Tripuhyite reference 2, synthesized following the method of Martinelli *et al.* (2004), was in better agreement with the sample. However, the bands at ~740 $cm^{-1}$ and ~500 $cm^{-1}$ were not distinctive, and the band at ~420 $cm^{-1}$ was missing. Furthermore, both tripuhyite reference compounds were clearly identified by XRD, although the Raman spectra showed only minor similarities between them (see Figure 5). The Raman spectra of feroxyhyte, therefore, agree well with the XRD results. The Raman spectra of tripuhyite, however, showed considerable differences between the sample (pH4Fe:Sb0.600) and the reference compounds (prepared using two different methods), and also between the reference compounds themselves. The poor crystallinity of the nano-sized tripuhyite in sample pH4Fe:Sb0.600 could lead to phonon-confinement effects, often observed in nano-sized crystallites (*e.g.* Georgescu *et al.*, 2012), causing the observed band shifts in the Raman spectrum.

## DISCUSSION

*Maximum adsorption capacities*

With the measured specific surface area of the transformation products and the necessary surface area for the adsorption of P(V), As(V), and Sb(V) complexes taken from the literature, maximum adsorption capacities for a simple adsorption model could be calculated.

The specific surface area of ferrihydrite should be handled with care, because it is highly variable and can fluctuate between 100 and 700 $m^2/g$ (Cornell and Schwertmann, 2003). Considering that the structure and chemical formula is still under debate (Michel *et al.*, 2007; Jambor and Dutrizac, 1998), adsorption calculations for ferrihydrite bear a significant uncertainty. The area required for the adsorption of one phosphate ion to the ferrihydrite surface varies between 0.33 and 0.62 $nm^2$ (Ryden *et al.*, 1977; Borggaard *et al.*, 2005; Gimsing and

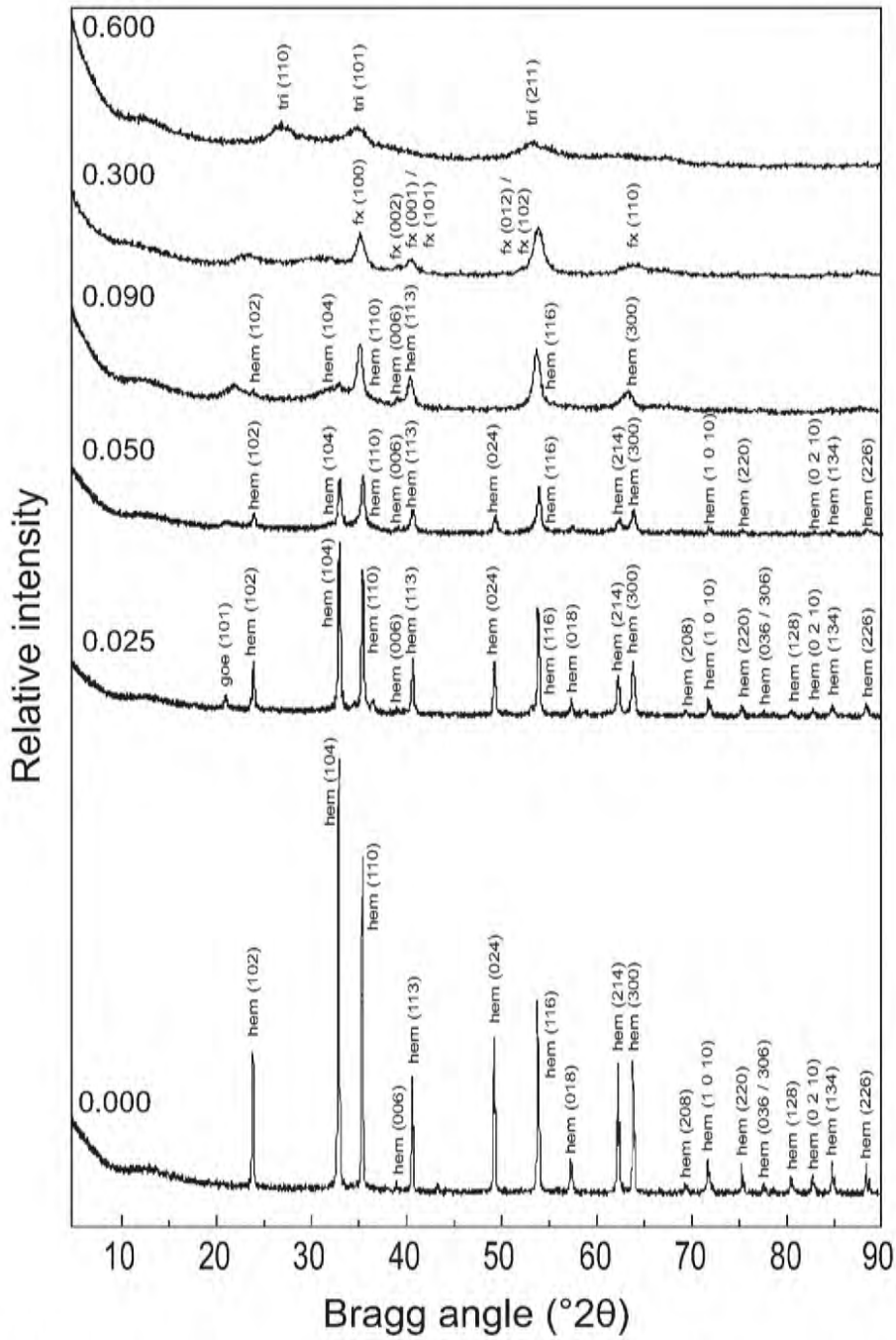


Figure 4. Ferrihydrite transformation in the presence of increasing Sb(V) concentrations. The numbers in front of each pattern indicate the molar Sb:Fe ratio. hem: hematite, goe: goethite, fx: feroxyhyte, tri: tripuhyite. All experiments were performed at pH 4 and with an aging time of 16 days.

Borggaard, 2007; Arai and Sparks, 2001) and for arsenate 0.40 $nm^2$ (Zhu *et al.*, 2011). These values led to a calculated maximum adsorption capacity for phosphate and arsenate of 39.27 (5.03 $\mu mol/m^2$) and 78.44 mg/g (4.18 $\mu mol/m^2$), respectively. To the authors' knowledge, no information about the area taken by one antimonate ion at the surface of ferrihydrite is available.

For goethite, the reported areas for an adsorbed phosphate ion are 0.61–0.66 $nm^2$ (Atkinson *et al.*, 1972; Barrow *et al.*, 1981; Torrent *et al.*, 1990; Borggaard *et al.*, 2005); those for an arsenate ion, 0.65–1.11 $nm^2$ (Salazar-Camacho and Villalobos, 2010; Wainipee *et al.*, 2010; Mamindy-Pajany *et al.*, 2011); and for an antimonate ion, 0.417 $nm^2$ (Leuz *et al.*, 2006). These

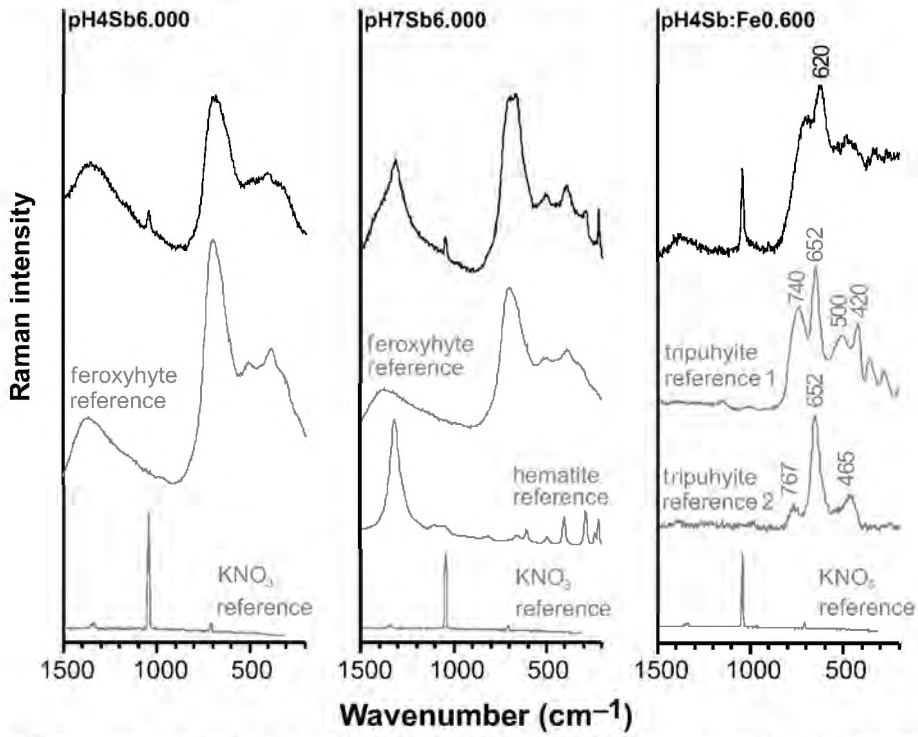


Figure 5. Selected Raman spectra of ferrihydrite transformations at increased Sb(V) concentrations. Sample 1 was transformed at pH 4, 70°C, and Sb(V) concentration of 6.000 mM with an aging time of 16 days. Sample 2 was transformed under the same conditions, but pH 7 instead of pH 4. Sample 3 was transformed at a Sb:Fe molar ratio of 0.600 at pH 4, 70°C, and 16 days of aging.

values led to a maximum adsorption capacity of goethite for P(V) of 2.11 mg/g (2.72 μmol/m$^2$), As(V) 4.79 mg/g (2.55 μmol/m$^2$), and Sb(V) 12.03 mg/g (3.95 μmol/m$^2$). Hematite is more complex with regard to its adsorption capacity as both morphology and grain size are very dependent on the synthesis conditions (Cornell and Schwertmann, 2003) and, therefore, adsorption capacity varies (Barron *et al.*, 1988; Torrent *et al.*, 1994). The area required for an adsorbed phosphate ion is between 0.40 and 0.61 nm$^2$ (Barron *et al.*, 1988; Colombo *et al.*, 1994; Torrent *et al.*, 1994; Gimsing and Borggaard, 2007); for an arsenate ion, 0.37 nm$^2$ (Mamindy-Pajany *et al.*, 2011); and for an antimonate ion, 0.780 nm$^2$ (Ambe, 1987). For hematite, maximum adsorption capacities for P(V) of 3.86 mg/g (4.15 μmol/m$^2$), As(V) 10.10 mg/g (4.49 μmol/m$^2$), and Sb(V) 7.78 mg/g (2.13 μmol/m$^2$) were reached. To the authors' knowledge, no comparable information for feroxyhyte is available.

The chemical composition of the transformation products indicates that the P(V) and As(V) contents were all below the calculated maximum adsorption capacities, except for hematite, which contained up to 27.35 mg As/g. For Sb(V), the highest concentrations occurred in feroxyhyte with 142.56 mg of Sb/g, followed by ferrihydrite with 110.30 mg of Sb/g. Unfortunately, no comparable literature values are available for Sb(V) adsorption for both minerals. Goethite contained 44.39 mg of Sb/g, significantly more than the calculated maximum adsorption capacity, whereas pure hematite was only present in a low-Sb(V) environment, remaining below the calculated adsorption capacity at 7.01 mg of Sb/g.

Considering the calculated maximum adsorption capacities, the Sb(V) loadings in the goethite samples are considerably greater than expected from a simple adsorption system. One could, therefore, speculate that Sb(V) is not only adsorbed to the surface of the goethite crystals but incorporated into their structure.

The validity of these calculated maximum adsorption capacities must be considered as a rough approximation. This model assumes a complete mononuclear, monodentate coverage of the whole specific surface area, not taking reactive adsorption sites, crystal morphology, or shielding of other ions into account. Furthermore, the adsorption to ferrihydrite, still without a widely accepted crystal structure or chemical composition, is poorly understood. The aggregates formed by ferrihydrite and the size of the single particles may have a significant impact on the adsorption behavior and, therefore, on the adsorption capacity. Hematite, on the other hand, has a well defined crystal structure and chemical composition, though the size of the crystallites and their habit depends heavily on the formation conditions. For ferrihydrite and hematite, therefore, adsorption densities from the literature may be insufficient for the calculation of maximum adsorption capacities. Adsorption capacities calculated from literature values are summarized graphically in Figure 6.

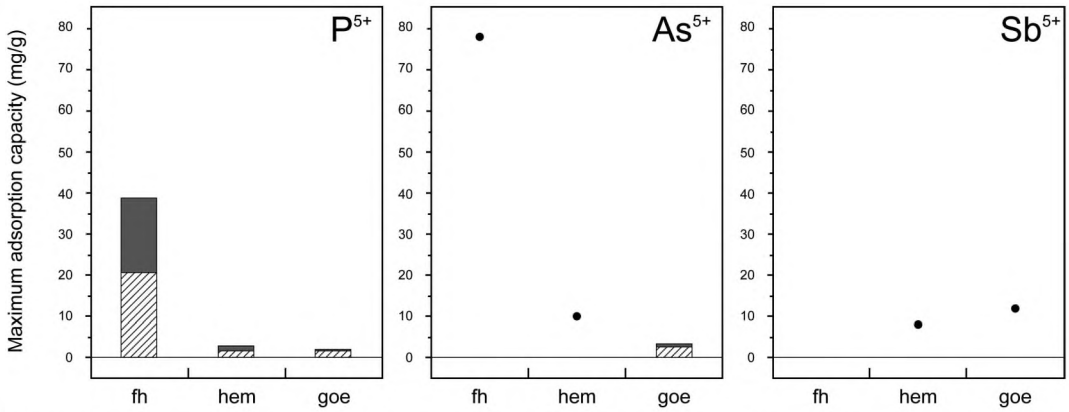


Figure 6. Graphical summary of the maximum adsorption capacities calculated from different literature values. The striped bars show the adsorption capacity that can be reached by every cited literature value. The gray bars indicate the uncertainty for the maximum adsorption capacity calculated from literature values. Dots indicate that only one literature value was available. fh: ferrihydrite, hem: hematite, goe: goethite.

*Feroxyhyte or hematite*

At increasing Sb(V) concentrations, the XRD patterns showed an apparent transition between hematite ($\alpha$-$Fe_2O_3$) and feroxyhyte ($\delta'$-FeOOH). The six indicative peaks of feroxyhyte (100), (002), (011/101), (012/102), (110), and (022/202), which can be seen in the powder XRD patterns, share the same 2$\theta$ positions as the hematite peaks (110), (113), (116), (300), (006), and (226), respectively. A problem arises when hematite and feroxyhyte coexist, because the powder XRD pattern is a linear combination of the patterns of both minerals, with a complete overlap of the feroxyhyte peaks with hematite peaks.

Therefore, all electron diffraction patterns of feroxyhyte were also cross-checked for indexing with a hematite (space group $R\bar{3}c$) model. The results showed that the lattice of feroxyhyte coincides completely with the lattice of hematite. All feroxyhyte indices can, therefore, be converted to hematite indices by a transformation of the lattice basis. The relation of the two lattices is given by the following transformation matrix:

$$\bar{h}_{\text{hem}} = \bar{h}_{\text{fx}} \cdot \mathbf{P} \qquad \text{with } \mathbf{P} = \begin{pmatrix} 1 & 1 & 0 \\ \bar{1} & 2 & 0 \\ 0 & 0 & 3 \end{pmatrix} \qquad (1)$$

The unit-cell volume of hematite is nine times larger than that of feroxyhyte. Hence, several reflections of hematite should be extinct for feroxyhyte. Due to the fact that the *c* axis of hematite is three times larger, only hematite reflections with $l = 3n$ are present for feroxyhyte. In addition, the *c*-glide plane of hematite causes a further extinction rule for hematite of $l = 6n$ for (00*l*), which is not valid for feroxyhyte. Therefore, only these extinction rules provide an opportunity for unambiguous identification of feroxyhyte. All reflections of powder electron diffraction patterns show only *d* spacings characteristic of feroxyhyte, and also an electron diffraction pattern along the $[010]_{\text{fx}}$ zone clearly violates the extinction of $l = 6n$ for hematite (hem) (see Figure 2). The diffraction spot $(003)_{\text{hem}}$ is weak but clearly present and cannot be an effect of double diffraction. During tilting of the crystal from the $[301]_{\text{hem}}$ zone to the $[601]_{\text{hem}}$ zone, which corresponds to $[1\bar{1}1]_{\text{fx}}$ and $[2\bar{2}1]_{\text{fx}}$ of feroxyhyte, a zone axis of $[401]_{\text{hem}}$ should be clearly visible in the case of hematite, because it contains the $(10\bar{4})$ diffraction spot, one of the strongest reflections of hematite. The absence of this additional zone axis provides evidence for the presence of feroxyhyte (Figure 7).

The atomic structure of hematite is characterized by hexagonally close-packed layers of oxygen, in which 2/3 of the octahedral sites are filled by ferric iron in an ordered manner. In contrast, the unit cell of feroxyhyte corresponds to a primitive cell setting of a close-packed oxygen arrangement, which does not allow an ordered occupancy of any of the octahedral sites. Therefore, feroxyhyte (after the model of Patrat *et al.*, 1983) can be considered as completely disordered hematite, which of course contains some (OH) groups for charge balance. Whether the OH groups are disordered, as in the structural model of feroxyhyte of Patrat *et al.* (1983), or ordered into basal layers, as in the $Fe(OH)_2$-structure type (Parise *et al.*, 2000; Cornell and Schwertmann, 2003), is still not known.

The formation of feroxyhyte occurs in this study only at certain, relatively high Sb(V) concentrations. The necessity of having higher Sb(V) concentrations together with the rapid formation of feroxyhyte indicates a nucleation/crystallization from bulk solution, rather than a solid-state formation of feroxyhyte from hematite by cation disorder. This is supported by considering that Sb-doped hematite remains stable for more than 16 days at 70°C in aqueous solution without any signs of a transformation to feroxyhyte. The observed apparent

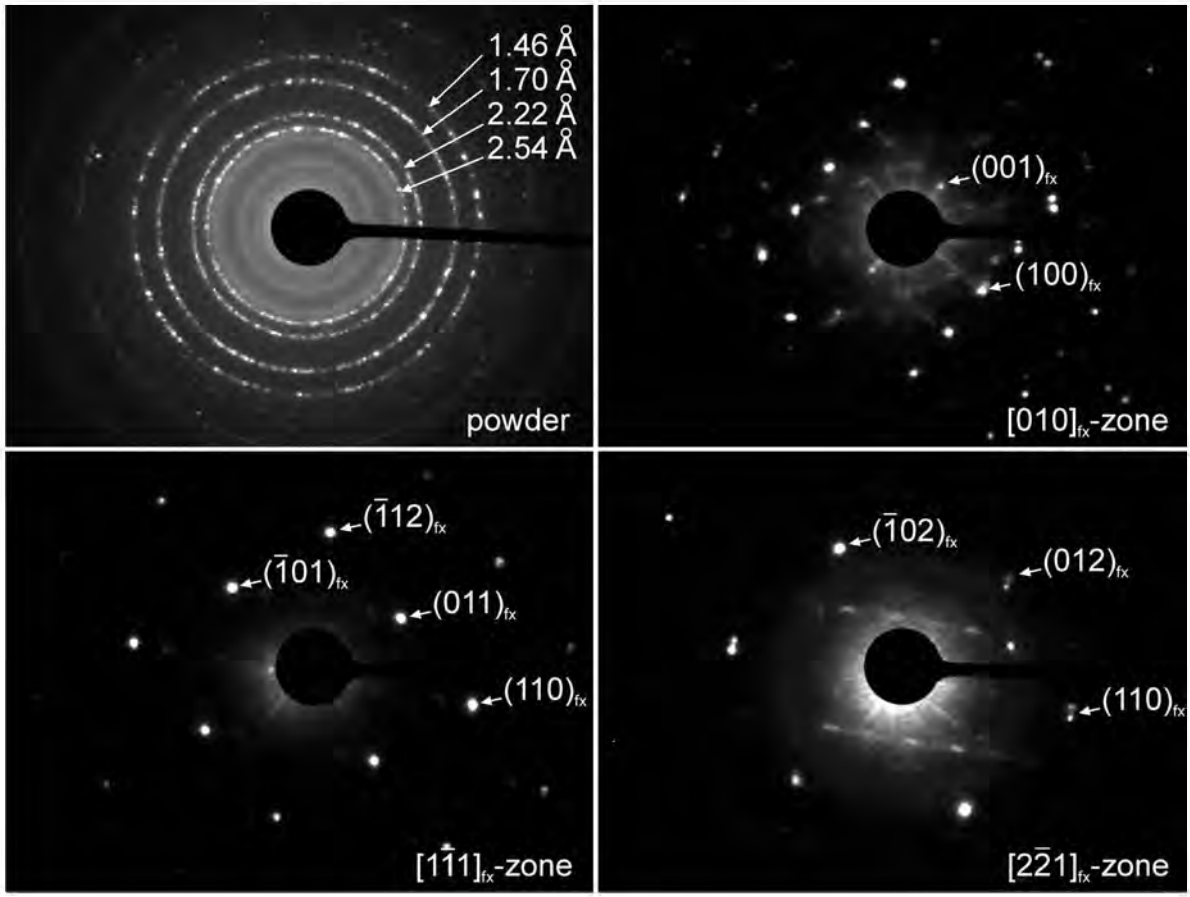


Figure 7. Selected electron diffraction pattern of feroxyhyte. The powder pattern shows the four dominant diffraction lines of feroxyhyte, whereas additional lines of hematite are clearly absent. In the [010] zone pattern, the (001) reflection of feroxyhyte is clearly visible but should be extinct for hematite. The [1$\bar{1}$1] and [2$\bar{2}$1] zone pattern belong to the same crystal tilted by ~18° along the [110] axis.

transition between hematite and feroxyhyte in the XRD patterns is, therefore, considered to be a decreasing hematite signal at increasing Sb(V) concentrations, combined with an increasing feroxyhyte signal, and not a solid-state transformation.

*Adsorption or structural incorporation of P(V), As(V), and Sb(V)*

During the transformation experiments, P(V) and As(V) showed similar behaviors, consistent with the literature (Das *et al.*, 2011a; Shaw *et al.*, 2005). The formation of hematite was favored over goethite and, at high concentrations of both anions, the transformation was retarded or inhibited. Except for the As(V) adsorption to hematite, the P(V) and As(V) concentrations in the solid transformation product remained below the calculated adsorption capacities, in agreement with previous adsorption studies (Atkinson *et al.*, 1972; Ryden *et al.*, 1977; Barrow *et al.*, 1981; Barron *et al.*, 1988; Torrent *et al.*, 1990; Colombo *et al.*, 1994; Torrent *et al.*, 1994; Arai and Sparks, 2001; Borggaard *et al.*, 2005; Gimsing and Borggaard, 2007; Salazar-Camacho and Villalobos, 2010; Wainipee *et al.*, 2010; Mamindy-Pajany *et al.*, 2011; Zhu *et al.*, 2011).

Transformations in the presence of Sb(V), however, differed strongly from those with P(V) and As(V). During the transformation experiments with Sb(V), goethite was favored over hematite. At higher Sb(V) concentrations, feroxyhyte replaced goethite and hematite. In addition, the solid transformation products feroxyhyte and goethite showed extraordinarily high concentrations of Sb(V).

As most studies deal with the adsorption of contaminants to the surfaces of iron oxides rather than with their structural incorporation, the possibility of a pure adsorption system should be examined. P(V), As(V), and Sb(V) occur in aqueous solution typically as anionic complexes. Between pH 4 and 12, three different pH-dependent species of P(V) and As(V) were distinguished. At pH 4, the dominant species was $H_2(P,As)O_4^-$; at pH 7, $H(P,As)O_4^{2-}$; and at pH 12, $(P,As)O_4^{3-}$. For Sb(V), only one dominant species, $Sb(OH)_6^-$, was

observed over the whole pH range of 4–12 (Brintzinger, 1948; Pitman *et al.*, 1957; Filella *et al.*, 2002). In order to attract and, therefore, adsorb an anionic complex, a positively charged surface was needed, and thus the pH of the solution must have been lower than the point of zero charge (PZC) of the mineral. Feroxyhyte, formed at pH 4 and 7, had a PZC of ~7.5–8 (Borggaard, 1983, Parida *et al.*, 1997). This means that feroxyhyte, under certain conditions, is close to the point of zero charge, but anionic complexes are already attracted by the surface and adsorption is possible. In the experiments carried out, feroxyhyte showed molar Sb:Fe ratios of up to 0.12 (145 mg Sb/g). Can a pure adsorption system explain such high concentrations sufficiently? Unfortunately, no adsorption capacities for feroxyhyte are available in the literature. Under the assumption that one Fe-octahedron on the feroxyhyte surface exposes an area of 0.149 $nm^2$, as at the goethite (001) face, and a mononuclear monodentate binding of the Sb-octahedra, a maximum of 127 mg Sb/g can be adsorbed to the feroxyhyte surface, which is less than in the feroxyhyte samples. This calculation is based on the specific surface area of the feroxyhyte samples and the chemical surface properties of goethite. As the feroxyhyte structure is still under debate (Drits *et al.*, 1993; Manceau and Drits, 1993) and the occupancy of Fe on the octahedral sites is unclear, the goethite model was considered as a better basis for a rough estimate.

Goethite, on the other hand, which was formed in the experiments at pH 12, showed molar Sb:Fe ratios of 0.03 (44 mg of Sb/g). Considering that the adsorption capacity for goethite calculated after Leuz *et al.* (2006) is ~12 mg of Sb/g, a pure adsorption system is again unlikely. The PZC for goethite is also ~7.2–9.0 (Atkinson *et al.*, 1967; Borggaard, 1983; Gaboriaud and Ehrhardt, 2003; Walsch and Dultz, 2010; Cristiano *et al.*, 2011), which means that at pH 12 the surface of goethite is negatively charged and repels anionic complexes such as $Sb(OH)_6^-$. These findings suggest that mechanisms other than or in addition to pure adsorption take place during the transformation experiments in the presence of Sb(V). These are probably incorporation, but surface precipitation cannot be excluded.

### *Possible model for the observed findings*

The high concentrations of Sb(V) in some of the runs can be explained by adsorption, surface precipitation, or incorporation. As discussed above, the adsorption capacities are insufficient to explain the 'foreign ion' uptake, especially in the case of goethite and feroxyhyte. Surface precipitation is possible, but no evidence for additional phases could be detected by Raman spectroscopy. Therefore, incorporation of Sb(V) into the structures of goethite and feroxyhyte seems to be the most viable explanation for the observations.

Sb(V) is usually coordinated octahedrally in the field of oxygen anions. The ionic radius of Sb(V) is 0.60 Å, very similar to that of 0.55 Å for Fe(III) (Shannon, 1976). In terms of ionic radii, the substitution of Sb(V) for Fe(III) should be easy. Of course, such heterovalent substitution must be coupled with the exchange of other

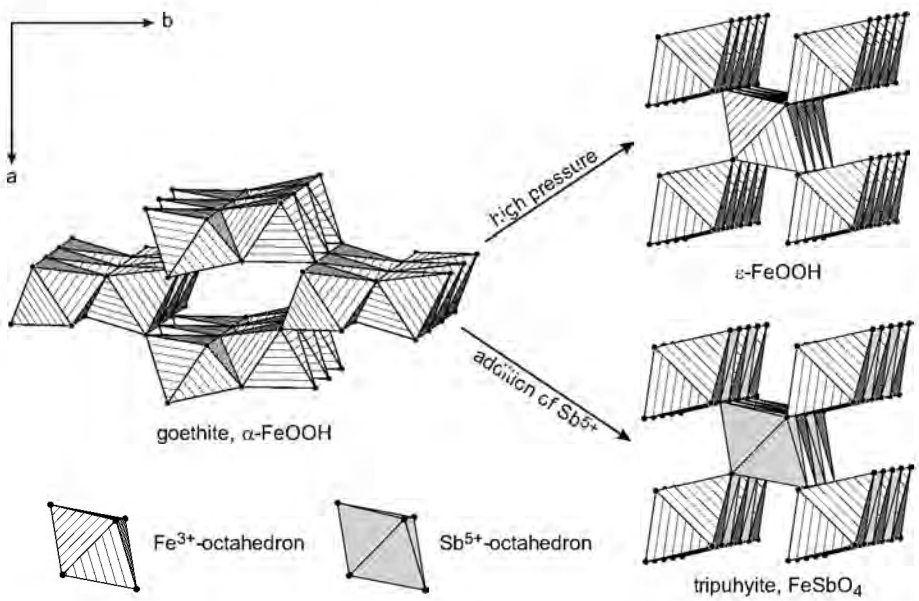


Figure 8. (Left) Structure of goethite (α-FeOOH) consisting of double octahedral chains (*Pbnm* setting). In a high-pressure environment, the tunnels which run parallel to the octahedral chains collapse, forming the denser high-pressure phase ε-FeOOH (upper right). During the Sb(V) → Fe(III) substitution, these tunnels could also collapse, forming the denser tripuhyite structure (lower right). Both ε-FeOOH and tripuhyite are isostructural with rutile.

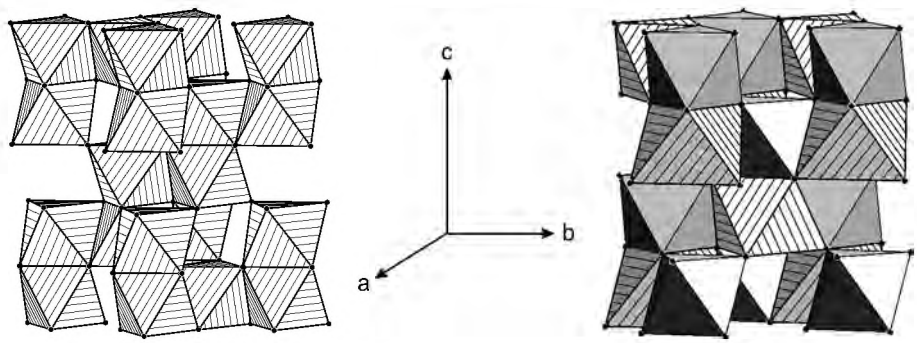


Figure 9. Structures similar to that of hematite (left) can incorporate pentavalent ions. These pentavalent ions cannot occur in close contact with each other because of the strong electrostatic repulsion. In $LiNbO_3$, a superstructure of hematite, the presence of Nb(V) face-sharing octahedra is avoided by monovalent $Li^+$ octahedra in between, reducing the electrostatic repulsion.

ions. One possibility is the loss of hydrogen concomitant with this substitution:

$$Fe(III) + 2H^+ = Sb(V) \quad (2)$$

Such a mechanism could operate in goethite or feroxyhyte. Here, the loss of some of the H atoms may not be critical to the preservation of the entire structure.

First, the structure of goethite is considered. Goethite consists of [001] double octahedral chains (in the *Pbnm* setting) (Figure 8). The octahedral units in the structure of goethite have the composition $Fe(III)O_3(OH)_3$. The H atoms occupy positions in the tunnels between the double chains. The Fe(III)-Sb(V) substitution would change the composition of the octahedra to $Sb(V)O_5(OH)$ and leave two H positions in the tunnels vacant. The crystal structure of goethite could probably tolerate a certain degree of Sb(V) substitution but would probably collapse if a significant portion of the tunnels remained empty. This mechanism could operate in goethite and account for the Sb(V) incorporation, based on the following crystal-chemical arguments.

The collapse of the tunnels between the double chains in goethite leads to a denser structure with single octahedral chains. Such a structure belongs to the high-pressure polymorph ε-FeOOH (Pernet *et al.*, 1975; Suzuki, 2010) (Figure 8). This phase is isostructural with rutile. Interestingly, tripuhyite, $FeSbO_4$, also has a rutile-type structure (Berlepsch *et al.*, 2003) (Figure 8). Hence, the Fe(III)-Sb(V) substitution in goethite leads to a withdrawal of H atoms, collapse of the tunnels, and a gradual conversion of goethite to tripuhyite on the atomic scale. This transformation from double to single chains can also account for the observation that the crystallinity of goethite worsens with increasing Sb load.

In hematite, coupling of the Fe(III)-Sb(V) with H loss is limited or excluded. Structures derived from that of hematite are capable of incorporating pentavalent cations. The best example is $LiNbO_3$, a superstructure of the hematite structure (Figure 9), with the substitution of 2 Fe(III) for $Li^+ + Nb(V)$. The cations in $LiNbO_3$ are ordered in such a way as to avoid the presence of two Nb(V) ions in two face-sharing octahedra because such an arrangement would lead to a strong electrostatic repulsion. By analogy, by forcing Sb(V) into the structure of hematite, the Fe(III)–Sb(V) repulsion in two neighboring face-sharing octahedra would be too strong. The substitution of 2 Fe(III) for $H^+ + Sb(V)$ seems implausible.

The only way to store a larger amount of Sb(V) in a hematite-related structure is to disorder the cations such that no octahedra share a face with other octahedra. Such octahedra could then be occupied by Sb(V). The disordered variant of the hematite structure is feroxyhyte, δ′-FeOOH, a phase observed in a number of runs.

The presence of tripuhyite in antimony mine tailings was reported in previous studies (Majzlan, 2011; Mitsunobu *et al.*, 2011) though feroxyhyte was not. One possible reason for this is the poor crystallinity as well as the small crystal size of feroxyhyte and the fact that the XRD peaks of hematite and feroxyhyte overlap completely. Feroxyhyte could be identified erroneously as poorly crystalline hematite or hematite could mask the presence of feroxyhyte.

## ACKNOWLEDGMENTS

The authors are grateful to Hannes Herzel for his help during the iron oxide syntheses. Thanks also to Dirk Merten, Ines Kamp, Maria Wierzbicka-Wieczorek, and Arkadiusz Wieczorek for their help with ICP-OES, XRD, and SEM, and to Anna Schmidt and Beate Truckenbrodt (all Jena) for BET measurements. In addition, the authors are grateful to two anonymous reviewers and the Editors for their comments and suggestions. This research was funded by the Deutsche Forschungsgemeinschaft (DFG) Research Training Group GRK 1257/1.

## REFERENCES

Ackermann, S., Gieré, R., Newville, M., and Majzlan, J. (2009) Antimony sinks in the weathering crust of bullets from Swiss shooting ranges. *Science of the Total Environment*, **407**, 1669–1682.

Álvarez-Benedí, J., Bolado, S., Cancillo, I., Calvo, C., and García-Sinovas, D. (2005) Adsorption-desorption of arsenate in three Spanish soils. *Vadose Zone Journal*, **4**, 282–290.

Ambe, S. (1987) Adsorption kinetics of antimony(V) ions onto $\alpha$-$Fe_2O_3$ surfaces from an aqueous solution. *Langmuir*, **3**, 489–493.

Arai, Y. and Sparks, D.L. (2001) ATR-FTIR Spectroscopic investigation on phosphate adsorption mechanisms at the ferrihydrite-water interface. *Journal of Colloid and Interface Science*, **241**, 317–326.

Atkinson, R.J., Quirk, J.P., and Posner, A.M. (1972) Kinetics of isotropic-exchange of phosphate at alpha-FeOOH-aqueous solution interface. *Journal of Inorganic and Nuclear Chemistry*, **34**, 2201–2211.

Atkinson, R.J., Posner, A.M., and Quirk, J.P. (1967) Adsorption of potential-determining ions at the ferric oxide-aqueous electrolyte interface. *The Journal of Physical Chemistry*, **71**, 3, 550–558.

Barron, V., Herruzo, M., and Torrent, J. (1988) Phosphate adsorption by aluminous hematite of different shapes. *Soil Science Society of America Journal*, **52**, 3, 647–651.

Barrow, N.J., Madrid, L., and Posner, A.M. (1981) A partial model for the rate of adsorption and desorption of phosphate by goethite. *Journal of Soil Science*, **32**, 3, 399–407.

Berlepsch, P., Armbruster, T., and Brugger, J. (2003) Tripuhyite, $FeSbO_4$, revisited. *Mineralogical Magazine*, **67**, 31–46.

Blesa, M.A. and Matijevic, E. (1989) Phase-transformations of iron-oxides, oxyhydroxides, and hydrous oxides in aqueous-media. *Advances in Colloid and Interface Science*, **29**, 173–221.

Borggaard, O.K. (1983) Effect of surface-area and mineralogy of iron-oxides on their surface-charge and anion-adsorption properties. *Clays and Clay Minerals*, **31**, 230–232.

Borggaard, O.K., Raben-Lange, B., Gimsing, A.L., and Strobel, B.W. (2005) Influence of humic substances on phosphate adsorption by aluminium and iron oxides. *Geoderma*, **127**, 270–279.

Brintzinger, H. (1948) Die Antimonat-, Antimonit-, Germanat- und Aluminat-Ioden im gelössten Zustand. *Zeitschrift für Anorganische und Allgemeine Chemie*, **256**, 98–102.

Brunauer, S., Emmett, P.H., and Teller, E. (1938) Adsorption of gases in multimolecular layers. *Journal of the American Chemical Society*, **60**, 308–319.

Carlson, L. and Schwertmann, U. (1980) Natural occurrence of feroxyhyte (δ'-FeOOH). *Clays and Clay Minerals*, **28**, 272–280.

Ciobotă, V., Salama, W., Tarcea, N., Rösch, P., Aref, M.E., Gaupp, R., and Popp, J. (2012) Identification of minerals and organic materials in Middle Eocene ironstones from the Bahariya Depression in the Western Desert of Egypt by means of micro-Raman spectroscopy. *Journal of Raman Spectroscopy* **43**, 405–410.

Colombo, C., Barrón, V., and Torrent, J. (1994) Phosphate adsorption and desorption in relation to morphology and crystal properties of synthetic hematites. *Geochimica et Cosmochimica Acta*, **58**, 1261–1269.

Cornell, R.M. and Schwertmann, U. (2003) *The Iron Oxides, Properties, Reactions, Occurrences, and Uses*. Wiley-VCH Verlag, Weinheim, Germany.

Cornell, R.M., Giovanoli, R., and Schindler, P.W. (1987) Effect of silicate species on the transformation of ferrihydrite into goethite and hematite in alkaline media. *Clays and Clay Minerals*, **35**, 21–28.

Cristiano, E., Hu, Y.-J., Siegfried, M., Kaplan, D., and Nitsche, H. (2011) A comparison of point of zero charge measurements methodology. *Clays and Clay Minerals*, **59**, 107–115.

Cudennec, Y. and Lecerf, A. (2006) The transformation of ferrihydrite into goethite or hematite, revisited. *Journal of Solid State Chemistry*, **179**, 716–722.

Das, S., Hendry, J., and Essilfie-Dughan, J. (2011a) Effects of adsorbed arsenate on the rate of transformation of 2-line ferrihydrite at pH 10. *Environmental Science & Technology*, **45**, 5557–5563.

Das, S., Hendry, J., and Essilfie-Dughan, J. (2011b) Transformation of two-line ferrihydrite to goethite and hematite as a function of pH and temperature. *Environmental Science & Technology*, **45**, 268–275.

Diemar, G.A., Filella, M., Leverett, P., and Williams, P.A. (2009) Dispersion of antimony from oxidizing ore deposits. *Pure and Applied Chemistry*, **81**, 1547–1553.

Dörfer, T., Schumacher, W., Tarcea, N., Schmitt, M., and Popp, J. (2010) Quantitative mineral analysis using Raman spectroscopy and chemometric techniques. *Journal of Raman Spectroscopy* **41**, 684–689.

Downs, R. T. and Hall-Wallace, M. (2003) "The American Mineralogist Crystal Structure Database". *American Mineralogist*, **88**, 247–250.

Drits, V.A., Sakharov, B.A., and Manceau, A. (1993) Structure of feroxyhyte as determined by simulation of X-ray diffraction curves. *Clay Minerals*, **28**, 209–222.

Filella, M., Belzile, N., and Chen, Y.-W. (2002) Antimony in the environment: a review focused on natural waters – II. Relevant solution chemistry. *Earth-Science Reviews*, **59**, 265–285.

Fischer, W.R. and Schwertmann, U. (1975) The formation of hematite from amorphous iron(III) hydroxide. *Clays and Clay Minerals*, **23**, 33–37.

Gaboriaud, F. and Ehrhardt, J.-J. (2003) Effects of different crystal faces on the surface charge of colloidal goethite (α-FeOOH) particles: an experimental and modeling study. *Geochimica et Cosmochimica Acta*, **67**, 967–983.

Georgescu, D., Baia, L., Ersen, O., Baia, M., and Simon, S. (2012) Experimental assessment of the phonon confinement in $TiO_2$ anatase nanocrystallites by Raman spectroscopy. *Journal of Raman Spectroscopy*, **43**, 876–883.

Gimsing, A.L. and Borggaard, O.K. (2007) Phosphate and glyphosate adsorption by hematite and ferrihydrite and comparison with other variable-charge minerals. *Clays and Clay Minerals*, **55**, 108–114.

Grazulis, S., Chateigner, D., Downs, R. T., Yokochi, A. T., Quirós, M., Lutterotti, L., Manakova, E., Butkus, J., Moeck, P., and Le Bail, A. (2009) "Crystallography Open Database – an open-access collection of crystal structures". *Journal of Applied Crystallography*, **42**, 726–729.

Gražulis, S., Daškevič, A., Merkys, A., Chateigner, D., Lutterotti, L., Quirós, M., Serebryanaya, N.R., Moeck, P., Downs, R.T., and LeBail, A. (2012) "Crystallography Open Database (COD): an open-access collection of crystal structures and platform for world-wide collaboration". *Nucleic Acids Research*, **40**, D420–D427.

Guan, X., Dong, H., Ma, J., and Jiang, L. (2009) Removal of arsenic from water: Effects of competing anions on As(III) removal in $KMnO_4$-Fe(II) process. *Water Research*, **43**, 3891–3899.

Hanesch, M. (2009) Raman spectroscopy of iron oxides and (oxy)hydroxides at low laser power and possible applications in environmental magnetic studies. *Geophysical Journal International*, **177**, 941–948.

Hansen, H.C.B., Raben-Lange, R., Raulund-Rasmussen, K., and Borggaard, O.K. (1994) Monosilicate adsorption by ferrihydrite and goethite at pH 3–6. *Soil Science*, **158**, 40–46.

He, Q.H., Leppard, G.G., Paige, C.R., and Snodgrass, W.J. (1996) Transmission electron microscopy of a phosphate effect on the colloid structure of iron hydroxide. *Water Research*, **30**, 1345–1352.

Jambor, J.L. and Dutrizac, J.E. (1998) Occurrence and constitution of natural and synthetic ferrihydrite, a widespread iron oxyhydroxide. *Chemical Review*, **98**, 2549–2585.

Johnston, J.H. and Lewis, D.G. (1983) A detailed study of the transformation of ferrihydrite to hematite in an aqueous medium at 92°C. *Geochimica et Cosmochimica Acta*, **47**, 1823–1831.

Larsen, O. and Postma, D. (2001) Kinetics of reductive bulk dissolution of lepidocrocite, ferrihydrite, and goethite. *Geochimica et Cosmochimica Acta*, **65**, 1367–1379.

Leuz, A-K., Mönch, H., and Johnson, C.A. (2006) Sorption of Sb(III) and Sb(V) to goethite: Influence on Sb(III) oxidation and mobilization. *Environmental Science & Technology*, **40**, 7277–7282.

Loan, M., Parkinson, G.M., and Richmond, W.R. (2005) The effect of zinc sulfide on phase transformations of ferrihydrite. *American Mineralogist*, **90**, 258–261.

Majzlan, J. (2011) Thermodynamic stabilization of hydrous ferric oxide by adsorption of phosphate and arsenate. *Environmental Science & Technology*, **45**, 4726–4732.

Majzlan, J., Lalinska, B., Chovan, M., Bläss, U., Brecht, B., Göttlicher, J., Steininger, R., Hug, K., Ziegler, S., and Gescher, J. (2011) A mineralogical, geochemical, and microbiogical assessment of the antimony- and arsenic-rich neutral mine drainage tailings near Pezinok, Slovakia. *American Mineralogist*, **96**, 1–13.

Mamindy-Pajany, Y., Hurel, C., Marmier, N., and Roméo, M. (2011) Arsenic (V) adsorption from aqueous solution onto goethite, hematite, magnetite and zero-valent iron: Effects of pH, concentration and reversibility. *Desalination*, **281**, 93–99.

Manceau, A. and Drits, V.A. (1993) Local-structure of ferrihydrite and feroxyhyte by EXAFS spectroscopy. *Clay Minerals*, **28**, 165–184.

Martinelli, A., Ferretti, M., Basso, R., Cabella, R., Lucchetti, G., Marescotti, P., and Buscaglia, V. (2004) Solid state miscibility in the pseudo-binary $TiO_2$–$(FeSb)O_4$ system at 1373 K. *Zeitschrift für Kristallographie*, **219**, 487–493.

Michel, M.F., Ehm, L., Antao, S.M., Lee, P.L., Chupas, P.J., Liu, G., Strongin, D.R, Schoonen, M.A.A, Phillips, B.L., and Parise, J.B. (2007) The structure of ferrihydrite, a nanocrystalline material. *Science*, **316**, 5832, 1726–1729.

Mitsunobu, S., Takahashi, Y., Utsunomiya, S., Marcus, M.A., Terada, Y., Iwamura, T., and Sakata, M. (2011) Identification and characterization of nanosized tripuhyite in soil near Sb mine tailings. *American Mineralogist*, **96**, 7, 1171–1181.

Nagano, T., Nakashima, S., Nakayama, S., and Senoo, M. (1994) The use of color to quantify the effect of pH and temperature on the crystallization kinetics of goethite under highly alkaline conditions. *Clays and Clay Minerals*, **42**, 226–234.

Paige, C.R., Snodgrass, W.J., Nicholson, R.V., and Scharer, J.M. (1996) The crystallization of arsenate-contaminated iron hydroxide solids at high pH. *Water Environment Research*, **68**, 981–987.

Paige, C.R., Snodgrass, W.J., Nicholson, R.V., Scharer, J.M., and He, Q.H. (1997) The effect of phosphate on the transformation of ferrihydrite into crystalline products in alkaline media. *Water, Air, and Soil Pollution*, **97**, 397–412.

Parida, K.M., Gorai, B., Das, N.N., and Rao, S. B. (1997) Studies on ferric oxide hydroxides. III. Adsorption of selenite ($SeO_3^{2-}$) on different forms of iron oxyhydroxides. *Journal of Colloid and Interface Science*, **185**, 355–362.

Parise, J.B., Marshall, W.G., Smith, R.I., Lutz, H.D., and Moller, H. (2000) The nuclear and magnetic structure of "white rust"-Fe(OH0.86D0.14)2. *American Mineralogist*, **85**, 189–193.

Patrat, G., de Bergevin, F., Pernet, M., and Joubert, J. (1983) Structure locale de delta-Fe O O H. *Acta Crystallographica B*, **39**, 165–170.

Pernet, M., Joubert, J.C., and Berthet-Colominas, C. (1975) Etude par diffraction neutronique de la forme haute pression de FeOOH. *Solid State Communications*, **17**, 1505–1510.

Pitman, A.L., Pourbaix, M., and de Zoubov, N. (1957) Potential-pH diagram of the antimony-water system. Its applications to properties of the metal, its compounds, its corrosion, and antimony electrodes. *Journal of the Electrochemical Society*, **104**, 594–600.

Ryden, J.C., McLaughlin, J.R., and Syers, J.K. (1977) Mechanisms of phosphate sorption by soil and hydrous ferric oxide gel. *Journal of Soil Science*, **28**, 72–92.

Salazar-Camacho, C. and Villalobos, M. (2010) Goethite surface reactivity: III. Unifying arsenate adsorption behavior through a variable crystal face-site density model. *Geochimica et Cosmochimica Acta*, **74**, 2257–2280.

Schwertmann, U. and Cornell, R.M. (2000) *Iron Oxides in the Laboratory: Preparation and Characterization*, 2nd edition. Wiley-VCH Verlag, Weinheim, Germany.

Schwertmann, U. and Fischer, W.R. (1966) Zur Bildung von α-FeOOH und α-$Fe_2O_3$ aus amorphem Eisen(III)-hydroxid III. *Zeitschrift für Anorganische und Allgemeine Chemie*, **346**, 137–142.

Schwertmann, U. and Murad, E. (1983) Effect of pH on the formation of goethite and hematite from ferrihydrite. *Clays and Clay Minerals*, **31**, 277–284.

Shannon, R.D. (1976) Revised effective ionic radii and systematic studies of interatomic distances in halides and chalcogenides. *Acta Crystallographica A*, **32**, 751–767.

Shaw, S., Pepper, S.E., Bryan, N.D., and Livens, F.R. (2005) The kinetics and mechanisms of goethite and hematite crystallization under alkaline conditions, and in the presence of phosphate. *American Mineralogist*, **90**, 1852–1860.

Suzuki, A. (2010) High-pressure X-ray diffraction study of ε-FeOOH. *Physics and Chemistry of Minerals*, **37**, 153–157.

Tighe, M., Lockwood P., and Wilson, S. (2005) Adsorption of antimony(V) by floodplain soils, amorphous iron(III) hydroxide and humic acid. *Journal of Environmental Monitoring*, **7**, 1177–1185.

Torrent, J., Barrón, V., and Schwertmann, U. (1990) Phosphate adsorption and desorption by goethites differing in crystal morphology. *Soil Science Society of America Journal*, **54**, 1007–1012.

Torrent, J., Schwertmann, U., and Barrón, V. (1994) Phosphate sorption by natural hematites. *European Journal of Soil Science*, **45**, 45–51.

Wainipee, W., Weiss, D.J., Sephton, M.A., Coles, B.J., Unsworth, C., and Court, R. (2010) The effect of cruide oil on arsenate adsorption on goethite. *Water Research*, **44**, 5673–5683.

Walsch, J. and Dultz, S. (2010) Effects of pH, Ca- and $SO_4$-concentration on surface charge and colloidal stability of goethite and hematite – consequences for the adsorption of anionic organic substances. *Clay Minerals*, **45**, 1–13.

Wojdyr, M. (2010) Fityk: a general-purpose peak fitting program. *Journal of Applied Crystallography*, **43**,1126–1128. (reprint)

Zhu, J., Pigna, M., Cozzolino, V., Caporale, A.G., and Violante, A. (2011) Sorption of arsenite and arsenate on ferrihydrite: Effect of organic and inorganic ligands. *Journal of Hazardous Materials*, **189**, 564–571.

(*Received 20 July 2012; revised 24 January 2013; Ms. 695; AE: H. He*)

*Clays and Clay Minerals*, Vol. 61, No. 1, 26–33, 2013.

# STRUCTURE AND PHOTOLUMINESCENCE OF COMPOSITES BASED ON CdS ENCLOSED IN MAGADIITE

YUFENG CHEN*, GENSHENG YU, FEI LI, AND JUNCHAO WEI

Department of Chemistry, Nanchang University, Jiangxi 330031, P.R. China

**Abstract**—In order to extend the application of magadiite to optical fields (rather than the usual focus on adsorption, catalysis, ion exchange, *etc.*), a magadiite-CdS (Mag-CdS) composite was synthesized from Na-magadiite by ion exchange. Various techniques were used to characterize the composite. X-ray diffraction results indicated that the Mag-CdS composite retained the host magadiite structure in spite of decrease in the intensity of the X-ray diffraction peak of the host magadiite. The analytical results confirmed the formation of the Mag-CdS composite, along with the modification of the optical properties of CdS by the host magadiite.

**Key Words**—CdS Nanoparticles, Composites, Magadiite, Photoluminescence.

## INTRODUCTION

Magadiite ($Na_2Si_{14}O_{29}\cdot xH_2O$) belongs to the family of layered Na silicates which includes makatite, kanemite, kenyaite, and octosilicate. It was first described by Eugster (1967) who found it, together with kenyaite, in lake beds at Lake Magadi, Kenya. Recent studies of magadiite have focused mainly on adsorption (Guerra *et al.*, 2010), cation exchange (Bi *et al.*, 2012), intercalation (Zhen and Pinnavaia, 2003), and modification and organization of guest species (Supronowicz *et al.*, 2012; Macedo *et al.*, 2007; Díaz *et al.*, 2007), *etc.* The modification or organization of guest molecules into Na-magadiite layered hosts offers a variety of applications, such as adsorbents (Nunes *et al.*, 2011), catalysts (Park *et al.*, 2009), cation exchangers, molecular sieves (Sun *et al.*, 2009), luminescent materials (Mizukami *et al.*, 2002; Ogawa *et al.*, 2010), optical recording materials (Ogawa and Kuroda, 1995), and separation media (Centi and Perathoner, 2008).

Nanoparticle CdS is a representative of the II–VI group semiconductors with extensive applications in electro-luminescence devices, photocatalysis, and biological sensors (Sun *et al.*, 2008; Rayevska *et al.*, 2010; Xu *et al.*, 2012; Freeman *et al.*, 2007). Because of the aggregation of CdS nanoparticles and the potential for oxidation, attempts have been made to improve the stability of the CdS nanoparticles by incorporating them into organic polymers (Li *et al.*, 2005) or inorganic materials (Rosa-Fox *et al.*, 2003; Kryukov *et al.*, 1998; Chang *et al.*, 1994). Though much attention has been focused on CdS nanoparticles capped by organic molecules or enclosed in a polymer matrix, which not only maintains the optical properties of the CdS but effectively protects the CdS from environmental perturbation (Rosa-Fox *et al.*, 2003; Kryukov *et al.*, 1998), CdS nanoparticles embedded in inorganic host materials are still worthy of study because of the greater stability of the inorganic compared with the organic materials in some special applications. Several studies of the optical properties of CdS revealed that major luminescence effects were associated with the incorporation in host materials (Shen *et al.*, 2008; Jyothy *et al.*, 2009). For this reason, magadiite, which has a layered structure, is thermally stable, and is resistant to common acids, bases, and oxidants, was selected here to enclose the CdS nanoparticles to form a CdS/magadiite composite. A ZnO-magadiite composite was synthesized (Ozawa *et al.*, 2009) using magadiite and $Zn(NO_3)_2$ as reactants, and the size of ZnO particles as a function of heat-treatment temperatures was investigated. Here, a composite based on CdS nanoparticles enclosed in magadiite was prepared using magadiite and $Cd(NH_3)_4^{2+}$ as reactants in a basic medium that facilitated ion exchange. The optical properties of the composite were investigated. The results indicated that the optical properties of CdS nanoparticles incorporated in magadiite were quite different from those of pure CdS particles. The Mag-CdS composite should be more resistant to acids than pure CdS particles and more thermally stable than CdS composites enclosed in organic polymers. The Mag-CdS composite is, therefore, a possible candidate for use as an electro-luminescent material.

## EXPERIMENTAL

Na-magadiite was synthesized by reaction of the $SiO_2$–NaOH–$Na_2CO_3$ system under hydrothermal conditions (Kwon *et al.*, 2005). At 150°C, the reaction was carried out in a sealed, Teflon-lined autoclave with a silica gel solution (14 mL of $H_2SiO_3$ and 127 mL of $H_2O$), NaOH

* E-mail address of corresponding author:
yfchen@ncu.edu.cn
DOI: 10.1346/CCMN.2013.0610103

(0.510 g), and $Na_2CO_3$ (2.690 g) as the reactants. After reaction for 96 h, the product was filtered, washed with deionized water, and dried at 40°C for 12 h. The Na-magadiite sample obtained was labeled 'Mag'. To introduce CdS nanoparticles into the interlayer space of Mag, a two-step process was used. At first, the ion-exchange method was adopted, *i.e.* Mag (1.027 g) was added to $Cd(NH_3)_4^{2+}$ aqueous solution (0.2 M, 100.0 mL ) which was prepared by reaction of $CdCl_2{\cdot}5/2H_2O$ with concentrated $NH_3$ solution, and stirred for 3 days at room temperature. The pH of the mixed suspension was 12.0; hydrolysis of $Cd(NH_3)_4^{2+}$ could be avoided at this pH (Bases and Mesmer, 1976). A portion of the sediment from the mixed suspension was then filtered, washed, and dried at 40°C for 12 h. The dried product was labeled as Mag-Cd. The remainder of the sediment was filtered, washed, and dispersed quickly (~2–3 min) into deionized water (100 mL) to form a new suspension in order to remove excess $Cd(NH_3)_4^{2+}$ (which can react with $Na_2S$ to form CdS outside the magadiite) (Vorokh *et al.*, 2008). Finally, $Na_2S$ (0.1 M, 20 mL) solution was added gradually to the new suspension and stirred continuously. The Mag-CdS composite was obtained after the precipitate was filtered, washed, and dried at 40°C for 12 h.

The pure CdS particles were prepared by the same method as mentioned above, *i.e.* $Na_2S$ solution (0.1 M, 20 mL) was added to $Cd(NH_3)_4^{2+}$ solution (0.2 M, 25 mL), and stirred continuously. The CdS precipitate was filtered, washed, and dried at 40°C for 12 h.

An environmental scanning electron microscope equipped with energy dispersive X-ray analysis (SEM-EDX XL30 ESEM FEG, Philips, Genesis 2000, The Netherlands) was used for morphological analysis of the surface structure and the compositional analysis of the samples for Na, Cd, Si, O, and S, with an accelerating voltage of 20 kV for EDX microanalysis. H elemental analysis was performed using a CHN Element Analyzer (Elementar Vario EL, Hanau, Germany). Powder X-ray diffraction (XRD) patterns were measured on a Bruker D8 Focus diffractometer using CuKα radiation (Bruker, Karlsruhe Germany). All the samples were scanned in the range 2–70°2θ at a scan rate 2°2θ/min. Fourier-transform infrared (FTIR) spectra were recorded using a Shimadzu IR Prestige-21 FTIR spectrometer (Shimadzu Company, Chiyoda-ku, Tokyo, Japan). Samples were prepared using the standard KBr disc method.

Thermogravimetric (TG) and differential thermal analysis (DTA) data were collected using a synchronous thermal analyzer (STA-200, Dazhan, Jiangsu, China), in a dynamic atmosphere using dry $N_2$ purge gas, with heating from room temperature up to 800°C at a rate of 10°C/min. The optical properties were characterized using photo-luminescent spectra (FL, F-7000, Hitachi Limited Corporation, Chiyoda, Tokyo Japan) and UV-vis trans-mission spectroscopy (U-4100 Spectrophoto-meter, Hitachi Limited Corporation, Chiyoda, Tokyo, Japan). Transmission electron microscopy (TEM) (JEM-2010, JEOL Company, Akishima, Tokyo, Japan) was used to examine the morphologies and estimate the sizes of the CdS nanoparticles enclosed in the magadiite.

## RESULTS AND DISCUSSION

The chemical composition of the Na-magadiite prepared here was obtained by combining the results of CHN elemental analysis, SEM-EDX compositional analyses (Figures 1 and 2), and TG analyses (Figure 3). The SEM-EDX compositional analyses of Mag and Mag-CdS (Figure 1, Table 1) revealed the molar ratio of Na:Si:O to be 1.0:7.0:18.1 for the Mag, and the morphological changes of the samples on the basis of SEM images (Figure 2). According to the thermogravimetric curve, Na-magadiite lost 9.2% of its total weight as water below 145°C, which was mainly due to interlayer water (Aline and Alexandre, 2009). In light of the EDX analysis, CHN element analysis, and weight loss, as well as the charge-balance principle, an empirical composition for the Na-magadiite prepared was estimated to be $Na_{1.0}Si_{7.0}O_{13.0}(OH)_3{\cdot}xH_2O$ ($x$ = 2.14), which compared favorably with the approximate composition of $NaSi_7O_{13}(OH)_3{\cdot}3H_2O$ suggested by previous workers (Eugster, 1967; Schwieger and Lagaly, 2004; McAtee *et al.*, 1968). By the same method, the molar ratio of Na:Cd:Si:S:O presented in the Mag-CdS composite was estimated to be

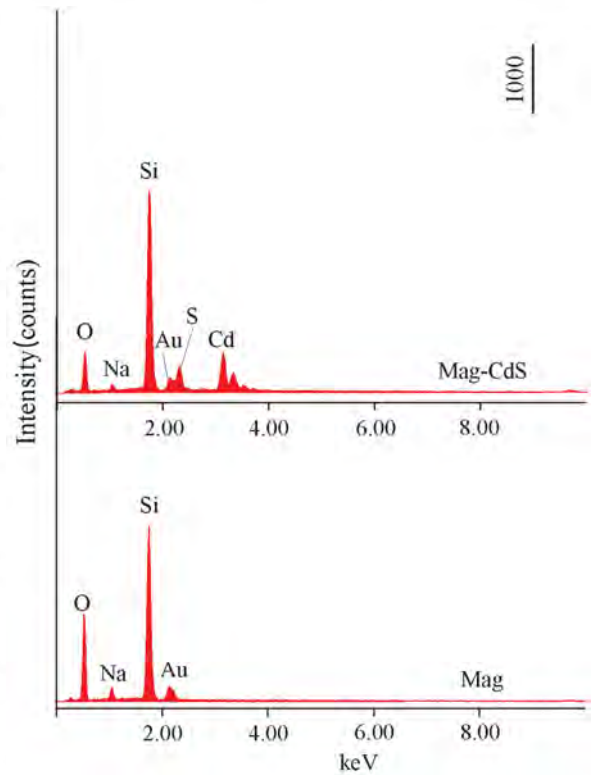


Figure 1. SEM-EDX results of Mag and Mag-CdS.

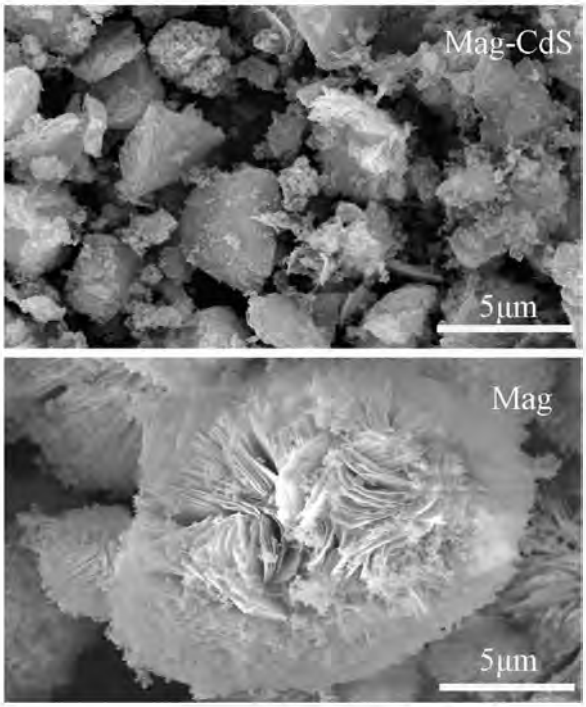


Figure 2. SEM images of Mag and Mag-CdS.

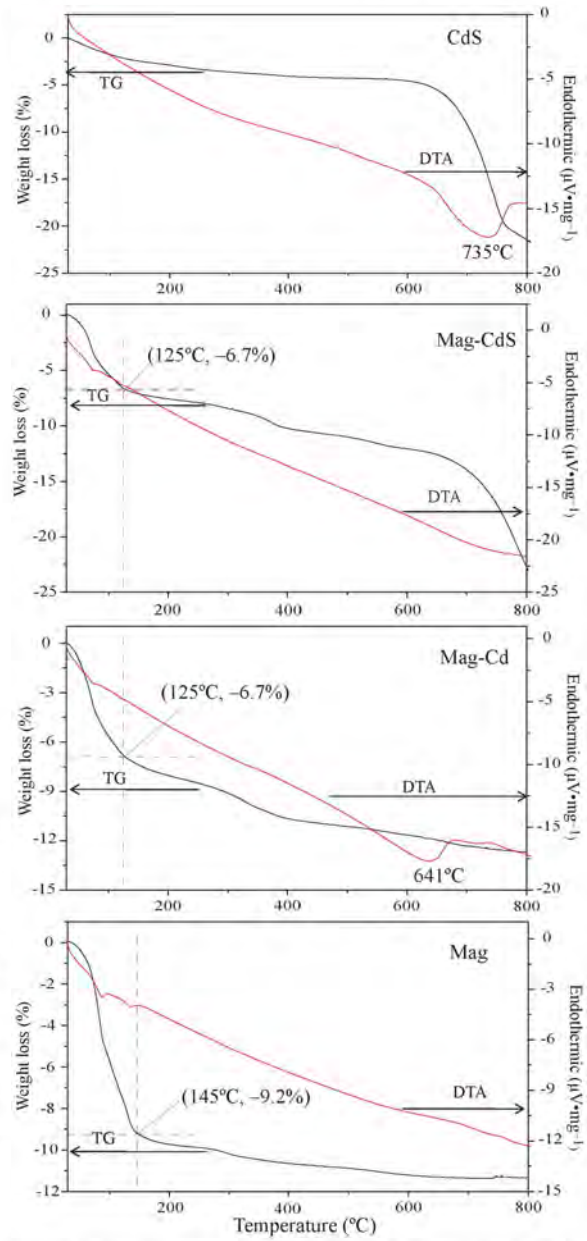


Figure 3. TG-DTA curves of Mag, Mag-Cd, Mag-CdS, and CdS.

0.28:0.82:7.0:0.46:17.87. The molar ratio of Cd:S (0.82:0.46) in the composite was not close to the expected value of 1:1, indicating excess Cd(II). The excess Cd(II) would compensate for layer charge. Allowing for the charge balance between the layers and interlayer guests, the empirical composition of the composite was estimated to be $Na_{0.28}Cd_{0.36}Si_{7.0}O_{13.0}(OH)_3 \cdot (CdS)_{0.46} \cdot xH_2O$ ($x$ = 1.87). The Au signal detected was attributed to Au electroplate.

X-ray diffraction patterns of Mag showed a $d_{001}$ reflection corresponding to a basal spacing of 15.6 Å (Figure 4). This interlayer spacing was in agreement with values in the literature (Schwieger and Lagaly, 2004). Based on the XRD data for the Mag sample and taking into account information provided by Schwieger and Lagaly (2004), all the reflections could be indexed as shown in Figure 4. The cell parameters of Mag were refined as $a$ = 7.272(3) Å, $b$ = 7.297(2) Å, $c$ = 15.684(6) Å, and β = 96.6(5)°, which values were similar to those ($a$ = 7.25 Å, $b$ = 7.25 Å, $c$ = 15.69 Å, β = 96.8°) given by Schwieger and Lagaly (2004). After intercalation of $Cd(NH_3)_4^{2+}$ ions into magadiite, the reflections of the Mag-Cd (Figure 4) were less intense than those of the pure ions. However, as far as the positions of peaks were concerned, the intercalated samples still had peaks corresponding to Na-magadiite, indicating that the structure was unaffected by the introduction of $Cd(NH_3)_4]^{2+}$ ions. Moreover, the intercalation of $Cd(NH_3)_4^{2+}$ ions into magdiite resulted in no significant change in the basal spacing. In an earlier study on the intercalation of $[Pt(NH_3)_4]^{2+}$ and $Co(sep)^{3+}$ ions into Na-magadiite, no change was reported in the basal spacing either (Schwieger *et al.*, 2004; Daily and Pinnavaia, 1992). Moreover, when the loading of $[Pt(NH_3)_4]^{2+}$ or $Co(sep)^{3+}$ ions increased, the intensity of the 001 (5.6°2θ) peak decreased. Similarly, a remarkable difference in the intensity of the peak at 5.6°2θ was noted, the intensity of which decreased with intercalation of $Cd(NH_3)_4^{2+}$ into magadiite, while the peak position remained unchanged. The decrease in the intensity of the peak at 5.6°2θ suggested that $Cd(NH_3)_4^{2+}$ ions were intercalated within the interlayer spaces. After introduction of $S^{2-}$ to Mag-

Table 1. Chemical composition of Mag and Mag-CdS.

| Samples | Elements | Wt.% | Molar ratio (%) | Molar ratio/formula/weight loss |
|---|---|---|---|---|
| Mag | OK | 69.35 | 54.28 | Na:Si:O:H=1.0:7.0:18.1:7.3 |
| | NaK | 5.49 | 2.99 | $Na_{1.0}Si_{7.0}O_{13.0}(OH)_3{\cdot}xH_2O$ ($x$ = 2.14) |
| | SiK | 23.42 | 20.94 | |
| | H | 1.74 | 21.78 | $H_2O$ loss = 9.2% (~25–145°C) |
| Mag-CdS | OK | 56.77 | 53.87 | Na:Cd:Si:S:O:H = 0.28:0.82:7.0:0.46:17.87:6.74 |
| | NaK | 1.28 | 0.84 | $Na_{0.28}Cd_{0.36}Si_{7.0}O_{13.0}(OH)_3{\cdot}(CdS)_{0.46}{\cdot}xH_2O$ ($x$ = 1.87) |
| | SiK | 19.46 | 21.10 | |
| | SK | 2.92 | 1.39 | |
| | CdL | 18.23 | 2.48 | |
| | H | 1.34 | 20.32 | $H_2O$ loss = 6.7% (~25–125°C) |

Na, Cd, Si, S, and O analyzed by EDX; H obtained from CHN element analysis and TG.

Cd, the final product, Mag-CdS, also retained the layered structure of the host magadiite. Therefore, both the Mag-Cd and Mag-CdS had similar interlamellar basal spacings to those of the initial magadiite (15.6 Å), which may be attributed to two opposing effects: the increasing interlayer spacing caused by the introduction of $Cd(NH_3)_4^{2+}$ or CdS into the Mag and the decreasing interlayer spacing brought about by the loss of interlayer water. These two opposing effects occurred simultaneously, leading to invariable spacing. In addition, the XRD pattern of the pure CdS showed no obvious peaks, suggesting that it was amorphous. Reflections attributed to CdS were not observed in the XRD patterns of Mag-CdS. Therefore, the CdS enclosed in the magadiite may have been amorphous.

The thermal analyses of Mag, Mag-Cd, Mag-CdS, and CdS (Figure 3) suggested that the TG-DTA curves of Mag-Cd and Mag-CdS were very different from those of Mag and CdS. This expected difference may be associated with the use of the $Cd(NH_3)_4^{2+}$ cations or CdS nanoparticles were possibly inserted into the lamellar space. As shown in TG curves, Mag exhibited a rapid mass loss of 9.2% up to 145°C because of loss of interlayer water (Aline and Alexandre, 2009). After ion exchange with $Cd(NH_3)_4^{2+}$ at room temperature, the Mag may have lost some interlayer water molecules owing to intercalation of $Cd(NH_3)_4^{2+}$. So the mass loss up to 145°C for Mag-Cd was ~6.7%. Although the TG-DTA curves changed after the introduction of CdS nanoparticles to the Mag, the mass loss of 6.7% up to 145°C for the Mag-CdS composite persisted. Moreover, the TG-DTA curves of Mag-CdS composite were the same as those of Mag and CdS. These results confirmed the formation of the Mag-CdS composite.

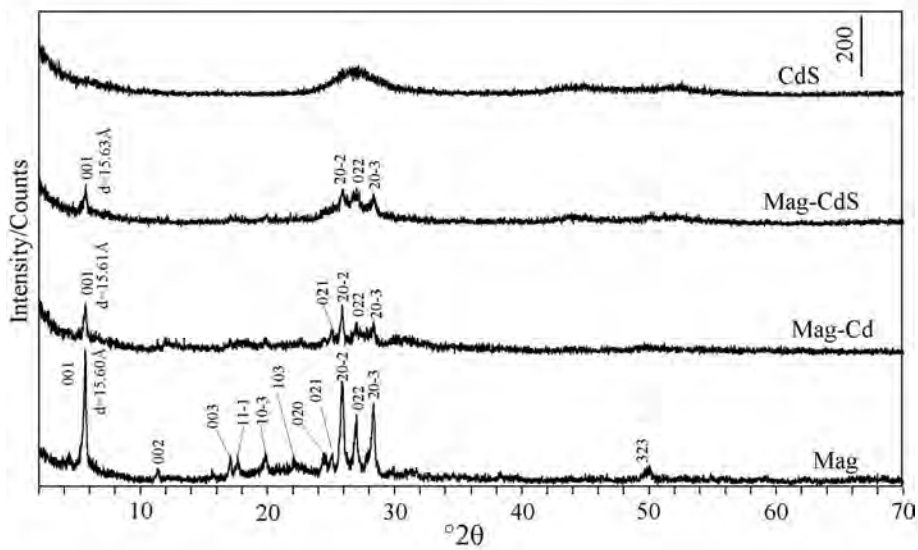


Figure 4. XRD patterns of Mag, Mag-Cd, Mag-CdS, and CdS.

Infrared spectra of Mag, Mag-Cd, Mag-CdS, and CdS (Figure 5) showed that, for Mag-Cd and Mag-CdS, all of the IR bands observed appeared at different frequencies from those in the Mag and CdS, with the exception of the bands at 3445 and 1635 $cm^{-1}$ which were attributed to the presence of the O–H stretching and bending modes of silanol groups and water molecules (distinguishing between them is difficult) (Motke *et al.*, 2002). For the Mag, the antisymmetric stretching modes of Si–O–Si bridges were observed at 1107 $cm^{-1}$ (Nunes *et al.*, 2011), while the band at 458 $cm^{-1}$ was associated with the very strong symmetric stretching vibrations of Si–O–Si bridges (Huang *et al.*, 1999). The vibrational mode near 782 $cm^{-1}$ was attributed to the mordenite bending mode of Si–O–Si mixed with Si–Si motion (Huang *et al.*, 1999; Laughlin and Joannopoulos, 1977). With respect to the IR spectra of the intermediate product, Mag-Cd, and the final product, Mag-CdS, distinct changes in the region 458–1107 $cm^{-1}$ were found. The band at 1107 $cm^{-1}$ shifted to 1083 $cm^{-1}$ and this was assigned to the stretching modes of terminal $Si–O^-$ bonds from *Q*3 units (Huang *et al.*, 1999). The bands between 663 and 446 $cm^{-1}$ were associated with the symmetric stretching vibrations of Si–O–Si bridges (Huang *et al.*, 1999). All these results suggested that the composite formed was based on the incorporation of CdS in the magadiite.

Photoluminescence (PL) measurements (Figure 6) were taken at room temperature. The PL excitation spectrum of the pure CdS detected at 556 nm (Figure 6I) showed a broad excitation band ranging from 445 to 340 nm. The emission spectra of the pure CdS were obtained under excitations at 320, 340, 350, 365, 370, and 445 nm (Figure 6II). A weak, high-energy peak at 470 nm and a broad peak centered at ~556 nm were observed in all the emission spectra of the CdS. The sources of the bands are the subject of some debate. Most researchers believe that the high-energy peak at 470 nm is due to near-band-edge emission while the strong, broad, and asymmetrical peak centered at ~556 nm is usually attributed to recombination of trapped charge carriers at surface defects due to either sulfur vacancies or cadmium vacancies (Zhao *et al.*, 2012; Rai and Bokatial, 2011). Some researchers consider, however, that the peak at ~556 nm corresponds to the band gap of CdS and the weak emission peak at 470 nm is attributed to a higher-level transition in CdS crystallites (Wang *et al.*, 2002; Wei *et al.*, 2005).

The emission spectra of the Mag-CdS composite (Figure 7) revealed a strong, broad peak centered at

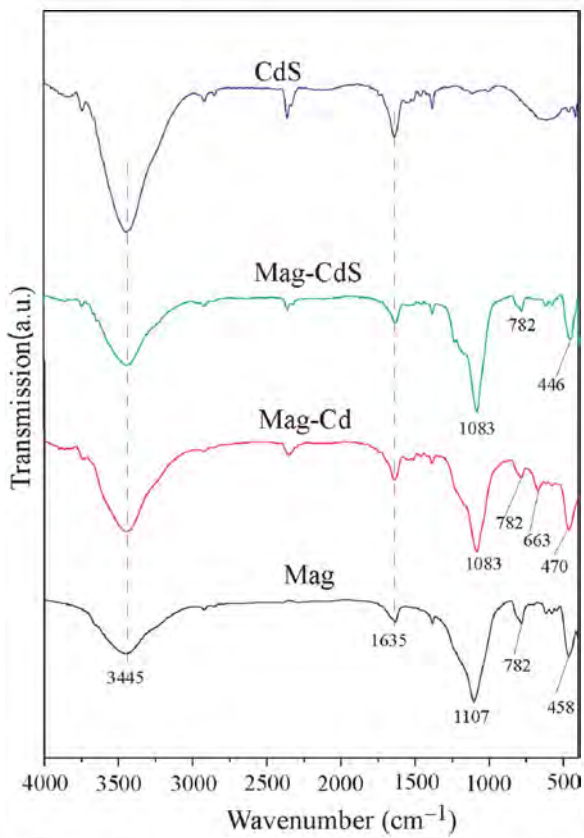


Figure 5. FTIR spectra of Mag, Mag-Cd, Mag-CdS, and CdS.

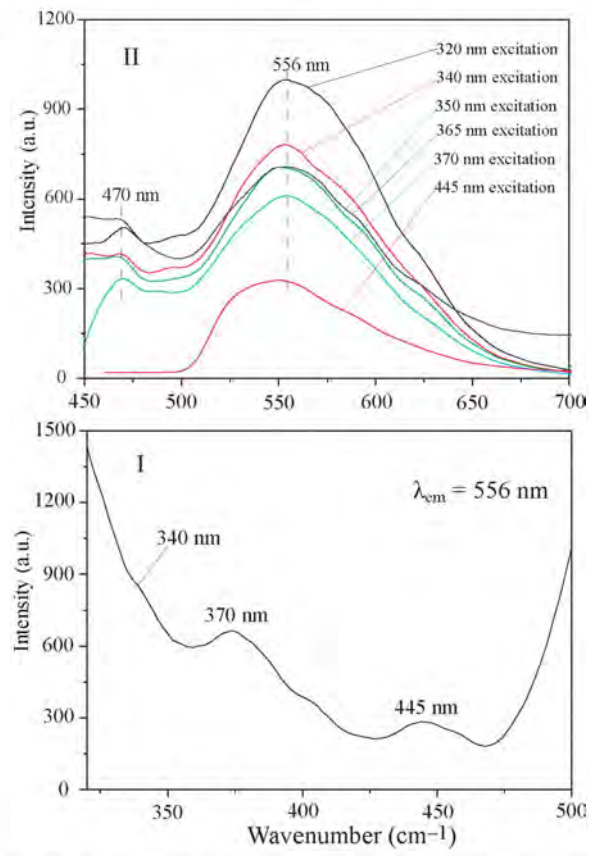


Figure 6. Excitation spectrum of CdS ($\lambda_{em}$ = 556 nm) and emission spectra of CdS under different excitation wavelengths.

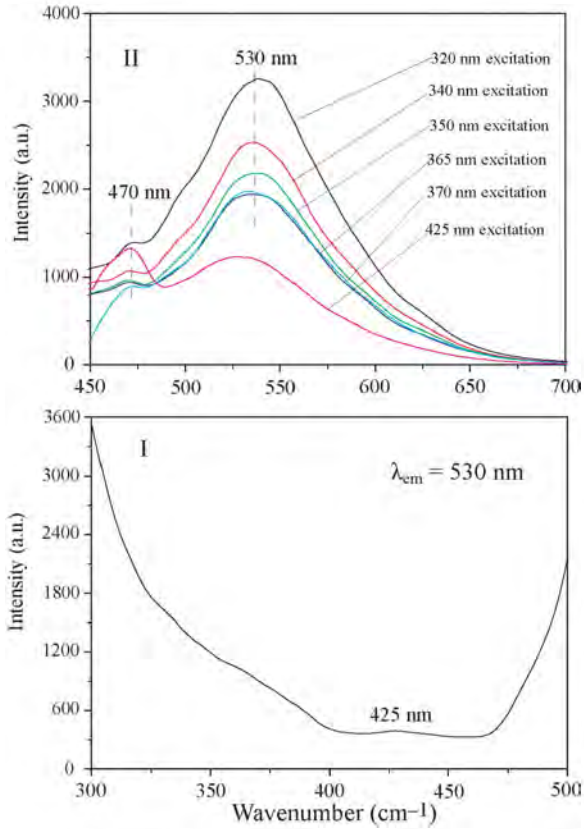


Figure 7. Excitation spectrum of CdS ($\lambda_{em}$ = 530 nm) and emission spectra of Mag-CdS under different excitation wavelengths.

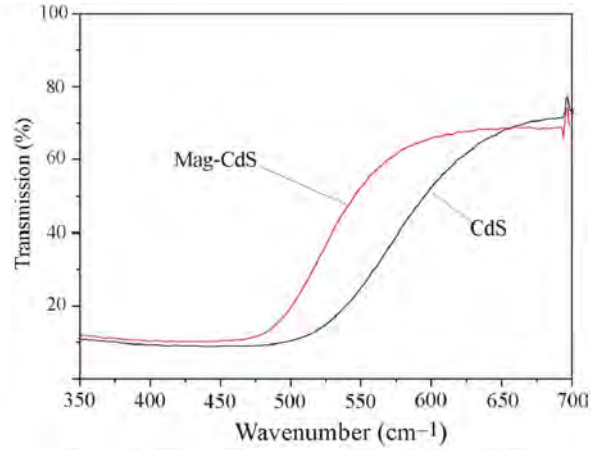


Figure 8. UV-visible spectra of Mag-CdS and CdS.

~530 nm and a weak peak at 470 nm under the excitations at 320, 340, 350, 365, 370, and 425 nm. The peak centered at 530 nm, which was associated with defect levels of interstitial sulfur (Vigil *et al.*, 1997; Blanco *et al.*, 1998), shifted by ~26 nm compared with that of the pure CdS (556 nm), while the peak at 470 nm did not shift. (In PL or UV-vis spectra, a 'red shift' implies the position of a peak moving to lower energy or longer wavelength; 'blue shift' implies the position of a peak moving to higher energy or shorter wavelength.) Notably, no red PL bands occurred in the Mag-CdS composites. These red PL bands have been found in other composites consisting of CdS nanoparticles and inorganic host materials (Rosa-Fox *et al.*, 2003; Guo *et a.l*, 2011; Kang *et al.*, 2008; Panda *et al.*, 2004), and thought to be related to the strain-related defects at the core/shell interface between CdS nanoparticles and inorganic host materials (Guo *et al.*, 2011). Various vacancies and interface defects between host materials and guests, however, often act as complicated luminescence centers and induce a wide variety of luminescence features for photon semiconductors (Cao *et al.*, 2005).

To understand the optical properties of the CdS nanoparticles before and after insertion into the Mag,

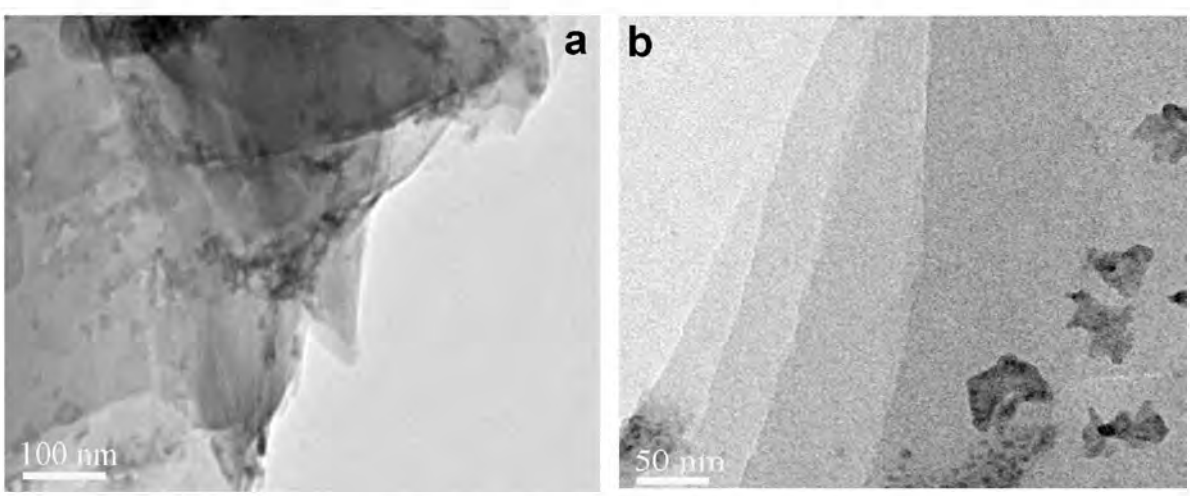


Figure 9. TEM observation of Mag-CdS at different magnifications.

UV-vis transmission spectra were recorded (Figure 8). The transmission band-edge of the Mag-CdS composite shifted to higher energy (2.4 eV, 525 nm) compared with that of the pure CdS particles (2.2 eV, 575 nm). The blue shift in the transmission spectra implied that the optical properties of CdS nanoparticles packed in the Mag may be modified by the host material.

To support these results, observation by TEM of the Mag-CdS composite (Figure 9) revealed a layered structure, with the sizes of particles in the Mag-CdS composites being <10 nm wide. Based on these results, the changed optical properties of CdS enclosed in Mag should be attributed largely to the effects of the host Mag on the CdS nanoparticles, such as size confinement effects or surface defects deactivation, *etc.*

## CONCLUSIONS

The structure and optical properties of the composite based on CdS nanoparticles enclosed in layered magadiite were investigated. The blue shifts present in the PL and UV-vis transmission spectra for the Mag-CdS composite confirmed that the magadiite may modify the optical properties of CdS. Observation by TEM confirmed incorporation of CdS nanoparticles into magadiite and estimated the sizes of the enclosed CdS nanoparticles to be <10 nm across. The changed optical properties of the CdS nanoparticles enclosed in the magadiite may be due to the effects of the host magadiite on the CdS nanoparticles (such as size-confinement effect). The composite based on CdS nanoparticles enclosed in magadiite should be more resistant to acids than the pure CdS, and be more thermally stable than the composites based on CdS nanoparticles enclosed in organic hosts. The composite presented here has potential applications in optical fields.

## ACKNOWLEDGMENTS

The present study was supported by the National Natural Science Foundation of China (Grant No.51162021).

## REFERENCES

Aline, O.M. and Alexandre, G.S.P. (2009) Effect of thermal dehydration and rehydration on Na-magadiite structure. *Journal of Colloid and Interface Science*, **330**, 392–398.

Bases, C.F. and Mesmer Jr., R.E. (1976) *The Hydrolysis of Cations*. John Wiley & Sons, Inc., New York, pp. 300–301.

Bi, Y.F., Blanchard, J., Lambert, J.F., Millot, Y., Casale, S., Zeng, S., Nie, H., and Li, D.D. (2012) Role of the Al source in the synthesis of aluminum magadiite. *Applied Clay Science*, **57**, 71–78.

Blanco, A., López, C., Mayoral, R., Míguez, H., Meseguer, F., Mifsud, A., and Herrero, J. (1998) CdS photoluminescence inhibition by a photonic structure. *Applied Physics Letters*, **73**, 1781–1783.

Cao, L.X., Huang, S.H., Lü, S.Z., and Lin, J.L. (2005) Effect of layer thickness on the luminescence properties of ZnS/CdS/ZnS quantum dot quantum well. *Journal of Colloid Interface & Science*, **284**, 516–520.

Centi, G. and Perathoner, S. (2008) Catalysis by layered materials: A review. *Microporous and Mesoporous Materials*, **107**, 3–15.

Chang, S.Y., Liu, L., and Asher, S.A. (1994) Creation of templated complex topological morphologies in colloidal silica. *Journal of the American Chemistry Society*, **116**, 6745–6747.

Daily, J.S. and Pinnavaia, T.J. (1992) Intercalative reaction of a cobalt (III) cage complex, Co(sep) 3+, with magadiite, a layered sodium silicate. *Journal of Inclusion Phenomena and Molecular Recognition in Chemistry*, **13**, 47–61.

Díaz, U., Cantín, Á., and Corma, A. (2007) Novel layered organic-inorganic hybrid materials with bridged silsesquioxanes as pillars. *Chemistry of Materials*, **19**, 3686–3693.

Eugster, H.B. (1967) Hydrous sodium silicate from lake Magadi, Kenya: precursors for bedded chert. *Science*, **157**, 1177–1180.

Freeman, R., Gill, R., Beissenhirtz, M., and Willner, I. (2007) Self-assembly of semiconductor quantum-dots on electrodes for photoelectrochemical biosensing. *Photochemical and Photobiological Science*, **6**, 416–422.

Guerra, D.L., Ferrreira, J.N., Pereira, M.J., Viana, R.R., and Airoldi, C. (2010) Use of natural and modified magadiite as adsorbents to remove Th(IV), U(VI), and Eu(III) from aqueous media – thermodynamic and equilibrium study. *Clays and Clay Minerals*, **58**, 327–339.

Guo, L.M., Wang X.H., Zhong C.F., and Li, L.T. (2011) Synthesis and photoluminescence of CdS QDs in $ZrO_2$ nanotubes by sequential chemical bath deposition. *Journal of Physics D: Applied Physics*, **44**, 165403/1-5.

Huang, Y., Jiang, Z., and Schwieger,W. (1999) Vibrational spectroscopic studies of layered silicates. *Chemistry of Materials*, **11**, 1210–1217.

Jyothy, P.V., Amrutha, K.A., Xavier, J., and Unnikrishnan, N.V. (2009) Fluorescence characteristics of $Dy^{3+}$/CdS nanocrystals doped silica xerogel. *Journal of Physics and Chemistry of Solids*, **70**, 927–930.

Kang, S.Z., Cui, Z.Y., Xu, Z.Z., and Mu, J. (2008) Thermostability of photoluminescence of CdS nanoparticles loaded on silica spheres. *Colloids and Surfaces A: Physicochemical and Engineering Aspects*, **315**, 44–46.

Kryukov, A.I., Smirnova, N.P., Korzhak, A.V., Kuchmii, S.Ya., and Eremenko, A.M. (1998) CdS nanoparticles in porous silicate glasses: energy characteristics, photocatalytic activity, and the effect of siliver ion doping. *Theoretical and Experimental Chemistry*, **34**, 360–365.

Kwon, O.Y., Jeong, S.Y., Suh, J.K., and Lee, J.M. (1995) Hydrothermal synthesis of Na-magadiite and Na-kenyaite in the presence of carbonate. *Bulletin Korean Chemical Society*, **16**, 737–742.

Laughlin, R.B. and Joannopoulos, J.D. (1977) Phonons in amorphous silica. *Physical Review B*, **16**, 2942–2952.

Li, Y., Chun, E., Liu, Y., Pickett, N., Skabara, P.J., Cummins, S.S., Ryley, S., Sutherland, A.J., and O'Brien, P. (2005) Synthesis and characterization of CdS quantum dots in polystyrene microbeads. *Journal of Material Chemistry*, **15**, 1238–1243.

Macedo, T.S.R., Petrucelli, G.C., and Airoldi, C. (2007) Silicic acid magadiite as a host for n-alkyldiamine guest molecules and features related to the thermodynamics of intercalation. *Clays and Clay Minerals*, **55**, 151–159.

McAtee, J.L., House, R., and Eugster, H.P. (1968) Magadiite from Trinity County, California. *American Mineralogist*, **53**, 2061–2069.

Mizukami, N., Tsujimura, M., Kuroda, K., and Ogawa, M. (2002) Preparation and characteriza- tion of Eu-magadiite intercalation compounds. *Clays and Clay Minerals*, **50**, 799–806.

Motke, S.G., Yawale, S.P., and Yawale, S.S. (2002) Infrared

spectra of zinc doped lead borate glasses. *Bulletin of Material Science*, **25**, 75–78.

Nunes, A., Moura, A.O., and Prado, A.G.S. (2011) Calorimetric aspects of adsorption of pesticides 2,4-D, diuron and atrazine on a magadiite surface. *Journal of Thermal Analysis and Calorimetry*, **106**, 445–452.

Ogawa, M., Ide, Y., and Mizushima, M. (2010) Controlled spatial separation of Eu ions in layered silicates with different layer thickness. *Chemical Communications*, **46**, 2241–2243.

Ogawa, M. and Kuroda, K. (1995) Photofunctions of intercalation compounds. *Chemical Reviews*, **95**, 399–438.

Ozawa, K., Nakao, Y., Cheng, Z.X., Wang, D.F., Osada, M.R., Okada, R., Saeki, K., Itoh, H., and Iso, F. (2009) Fabrication of novel composites of ZnO-nanoparticles and magadiite. *Materials Letters*, **63**, 366–369.

Panda, S.K., Chakrabarti, S., Satpati, B., Satyam, P.V., and Chaudhuri, S. (2004) Optical and microstructural characterization of CdS–ZnO nanocomposite thin films prepared by sol–gel technique. *Journal of Physics D: Applied Physics*, **37**,628–635.

Park, K.W., Jung, J.H., Seo, H.J., and Kwon, O.Y. (2009) Mesoporous silica-pillared kenyaite and magadiite as catalytic support for partial oxidation of methane. *Microporous and Mesporous Materials*, **121**, 219–225.

Rai, S. and Bokatial, L. (2011) Effect of CdS nanoparticles on photoluminescence spectra of $Tb^{3+}$ in sol–gel-derived silica glasses. *Bulletin of Material Science*, **34**, 227–231.

Rayevska, O.E., Grodzyuk, G.Y., Dzhagan, V.M., Stroyuk, O.L., Kuchmiy, S.Y., Plyusnin, V.F., Grivin, V.P., and Valakh, M.Y. (2010) Synthesis and characterization of white-emitting CdS quantum dots stabilized with polyethylenimine. *Journal of Physical Chemistry C*, **114**, 22478–22486.

Rosa-Fox, N.D., Piñero, M., Litrán, R., and Esquivias, L. (2003) Photoluminescence from CdS quantum dots in silica gel. *Journal of Sol-Gel Science and Technology*, **26**, 947–951.

Schwieger, W. and Lagaly, G. (2004) Alkali silicates and crystalline silicic acids. Pp. 541–551 in: *Handbook of Layered Materials* (S.M. Auerbach, K.A. Carrado, and P.K. Dutta, editors). Marcel Dekker Inc, New York.

Schwieger, W., Selvam, T., Gravenhorst, O., Pfänder, N., Schlögl, R., and Mabande, G.T.P. (2004) Intercalation of $[Pt(NH_3)_4]2t$ ions into layered sodium silicate magadiite: a useful method to enhance their stabilisation in a highly dispersed state. *Journal of Physics and Chemistry of Solids*, **65**, 413–420.

Shen, S. and Guo, L. (2008) Growth of quantum-confined CdS nanoparticles inside Ti-MCM-41 as a visible light photocatalyst. *Materials Research Bulletin*, **43**, 437–446.

Sun, W.T., Yu, Y., Pan, H.Y., Gao, X.F., Chen, Q., and Peng, L.M. (2008) CdS quantum dots sensitized $TiO_2$ nanotube-array photoelectrodes. *Journal of the American Chemical Society*, **130**, 1124–1125.

Sun, X., King, J., and Anthony, J.L. (2009) Molecular sieve synthesis in the presence of tetra-alkylammonium and dialkylimidazolium molten salts. *Chemical Engineering Journal*, **147**, 2–5.

Supronowicz, W., Roessner, F., Schwieger, W., Meilikhov, M., and Esken, D. (2012) Synthesis and properties of Sn-containing magadiite. *Clays and Clay Minerals*, **60**, 254–264.

Vigil, O., Reich, I., García-Rocha, M., and Zelaya-Ańgel, O. (1997) Characterization of defect levels in chemically deposited CdS films in the cubic-to-hexagonal phase transition. *Journal of Vacuum Science & Technology A*, **15**, 2282–2286.

Vorokh, A.S., Kozhevnikov, N.S., Uritskaya, A.A., and Magerl, A. (2008) The synthesis of nucleus–shell $Cd(OH)_2$/CdS structures by chemical precipitation from aqueous solutions. *Russian Journal of Physical Chemistry A*, **82**, 1132–1139.

Wang, Y., Meng, G., Zhang, L., Liang, C., and Zhang, J. (2002) Catalytic growth of large-scale single-crystal CdS nanowires by physical evaporation and their photoluminescence. *Chemistry of Materials*, **14**, 1773–1777.

Wei, F., Li, G.C., and Zhang, Z.K. (2005) Synthesis of high quality CdS nanorods by solvo-thermal process and their photoluminescence. *Journal of Nanoparticle Research*, **7**, 685–689.

Xu, F., Yuan, Y.F., Han, H.J., Wu, D.P., Gao, Z.Y., and Jiang, K. (2012) Synthesis of ZnO/CdS hierarchical heterostructure with enhanced photocatalytic efficiency under nature sunlight. *CrystEngComm*, **14**, 3615–3622.

Zhao, P.Q., Xiong, S.J., Wu, X.L., and Chu, P.K. (2012) Photoluminescence induced by twinning interface in CdS nanocrystals. *Applied Physics Letters*, **100**, 171911/1-4.

Zhen, W. and Pinnavaia, T.J. (2003) Intercalation of poly(-propyleneoxide) amines (Jeffamines) in synthetic layered silicas derived from ilerite, magadiite, and kenyaite. *Journal of Material Chemistry*, **13**, 2127–2131.

(*Received 17 September 2012; revised 26 December 2012; Ms. 715; AE: S.M. Kuznicki*)

*Clays and Clay Minerals*, Vol. 61, No. 1, 34–56, 2013.

# WEATHERING OF ALMANDINE GARNET: INFLUENCE OF SECONDARY MINERALS ON THE RATE-DETERMINING STEP, AND IMPLICATIONS FOR REGOLITH-SCALE Al MOBILIZATION

JASON R. PRICE[1,*], DEBRA S. BRYAN-RICKETTS[2,3], DIANE ANDERSON[1,4], AND MICHAEL A. VELBEL[2]

[1] Department of Earth Sciences, P.O. Box 1002, Millersville University, Millersville, PA 17551-0302, USA
[2] Department of Geological Sciences, 206 Natural Science Building, Michigan State University, East Lansing, Michigan 48824-1115, USA
[3] Environmental Protection Division, Los Alamos National Laboratory, Box 1663, Los Alamos, NM 87544, USA
[4] Celerity, 4720 Gettysburg Rd., Suite 204, Mechanicsburg, PA 17055, USA

**Abstract**—Secondary surface layers form by replacement of almandine garnet during chemical weathering. This study tested the hypothesis that the kinetic role of almandine's weathering products, and the consequent relationships of primary-mineral surface texture and specific assemblages of secondary minerals, both vary with the solid-solution-controlled variations in Fe and Al contents of the specific almandine experiencing weathering.

Surface layers are protective (PSL) when the volume of the products formed by replacement is greater than or equal to the volume of the reactants replaced. Under such circumstances, reaction kinetics at the interface between the garnet and the replacing mineral are transport controlled and either transport of solvents or other reactants to, or products from, the dissolving mineral is rate limiting. Beneath PSLs, almandine garnet surfaces are smooth, rounded, and featureless. Surface layers are unprotective (USL) when the volume of the products formed by replacement is less than the volume of the reactants replaced. Under such circumstances, reaction kinetics at the interface between the garnet and the replacing mineral are interface controlled and the detachment of ions or molecules from the mineral surface is rate limiting. Almandine garnet surfaces beneath USLs exhibit crystallographically oriented etch pits. However, contrary to expectations, etch pits occur on almandine garnet grains beneath some layers consisting of mineral assemblages consistent with PSLs.

Based on the Pilling-Bedworth criterion, surface layers are more likely to be protective over a broad range of reactant-mineral compositions when they contain goethite, kaolinite, and pyrolusite. However, this combination requires specific ranges of Fe and Al content of the natural reacting almandine garnet. To form a PSL of goethite and kaolinite, an almandine garnet must have a minimum Al stoichiometric coefficient of ~3.75 a.p.f.u., and a minimum Fe stoichiometric coefficient of ~2.7 a.p.f.u.

Product minerals also influence the mobility of the least-mobile major rock-forming elements. A PSL consisting of goethite, gibbsite, and kaolinite yields excess Al for export during almandine garnet weathering. As the quantity of kaolinite present in the PSL decreases, the amounts of Al available for export increases.

**Key Words**—Almandine Garnet, Chemical Weathering, Coweeta Hydrologic Laboratory, Gibbsite, Goethite, Hematite, Kaolinite, Protective Surface Layers, Saprolite, Unprotective Surface Layers.

## INTRODUCTION

Weathering products are widely believed to exert an influence on the rates and mechanisms of primary-mineral weathering (Berner, 1978, 1981; Velbel, 1984a, 1993). However, specific examples of relationships between individual product minerals and distinctive alteration textures indicative of particular weathering mechanisms are not common. This is especially true when different weathering products are associated with different alteration textures. For example, denticulated (sawtooth, hacksaw, or 'cockscomb') terminations on naturally weathered pyroxenes and amphiboles appear identical regardless of whether the weathering product being formed is a 2:1 clay or an assemblage of hydroxides (*e.g.* Velbel, 1989, 2007; Velbel and Barker, 2008; Velbel *et al.*, 2009). These same textures also occur regardless of whether the environment of alteration is pedogenic or burial diagenetic (*e.g.* Berner *et al.*, 1980; Velbel, 2007).

Previous workers have reported almandine garnet weathering to various products, including gibbsite, goethite, and hematite (Embrechts and Stoops, 1982; Parisot *et al.*, 1983; Velbel, 1984a; Graham *et al.*, 1989a,b; Robertson and Butt, 1997). Additional studies have reported a great variety of garnet surface textures on both naturally weathered (Embrechts and Stoops, 1982; Parisot *et al.*, 1983; Velbel, 1984a, Ghabru *et al.*, 1989; Robertson and Butt, 1997) and diagenetically altered (Hansley, 1987; Salvino and Velbel, 1989) grains.

* E-mail address of corresponding author:
Jason.Price@millersville.edu
DOI: 10.1346/CCMN.2013.0610104

Velbel (1993) hypothesized that during subaerial weathering, the formation of surface layers composed of gibbsite and goethite should have different kinetic consequences and produce different dissolution and replacement textures than surface layers composed of gibbsite and hematite. A surface layer composed of gibbsite and goethite formed by replacement of almandine garnet is predicted to have a volume greater than the volume of the parent almandine garnet replaced (Velbel, 1993). In such a scenario the surface layer has negligible porosity. Negligible porosity requires that transport of soluble species to or from the almandine's surface is restricted to grain-boundary diffusion between product-mineral crystals or volume diffusion through the product-mineral crystal structures. Such a layer thereby inhibits continued garnet dissolution. Reaction kinetics in which the rate-determining process is diffusion of mobile reactant or product species through the medium surrounding the primary mineral are referred to as transport-controlled or transport-limited kinetics, and primary-mineral surfaces affected by transport-limited kinetics are smooth and rounded (Berner, 1978). Solid material through which diffusion is rate limiting is referred to as a protective surface layer (Velbel, 1993; abbreviated herein as PSL). Following previous work using the Pilling-Bedworth criterion, Velbel (1993) defined a surface layer as being protective when the volume of the product(s) formed by replacement of a primary mineral is greater than or equal to the volume of the reactant mineral replaced ($V_p/V_r \geqslant 1$). In contrast, a surface layer composed of gibbsite and hematite formed by replacement of almandine garnet will have a volume significantly less than the volume of the parent almandine garnet replaced (Velbel, 1993) ($V_p/V_r < 1$). In such a scenario the resulting high porosity in, and/or cracks and other voids through, the surface layer allow movement of solvent and solutes to and from the reacting almandine garnet surface. The surface layer has no restricting effect of solvent on solute transport, and does not protect the primary-mineral surface from access by mobile species. Reaction kinetics in which the rate-determining process is reaction at the interface (slower than diffusion of mobile reactant or product species through the medium surrounding the primary mineral) are referred to as surface-controlled or interface-limited kinetics. Primary-mineral surfaces affected by surface-controlled kinetics exhibit crystallographically controlled etch pits (Berner, 1978). A layer of products with these characteristics is referred to here as an unprotective surface layer (USL).

Four tests exist for distinguishing transport-limited from interface-limited kinetics (Berner, 1978) but three apply only to laboratory experiments. Examination of primary-mineral surfaces for smooth or pitted surfaces is the only one of the four tests that can be applied to naturally weathered mineral grains as well as experimental kinetic data (Velbel, 2004). Velbel (1993) tested the hypothesis that different combinations of secondary Fe- and Al-bearing minerals have different consequences for mineral–water reaction kinetics and primary-mineral surface textures. He found broad agreement between the product-reactant volume ratios ($V_p/V_r$) and textural observations. Specifically, of the major rock-forming silicates, only almandine garnet exhibited both kinetic mechanisms. The product-reactant volume ratios indicated that gibbsite-goethite layers which had been reported by previous workers (*e.g.* Velbel, 1984b, and references therein) formed PSLs over smooth almandine surfaces in saprolites beneath soils. In contrast, products were absent from etched surfaces in soils. Both phenomena had been reported by previous workers; *e.g.* Velbel, 1984b, and references therein. The amount (volume) of product that can be formed upon replacement of a primary mineral by its secondary weathering products depends on the abundances of product-forming elements in the primary mineral. Therefore, the product volume varies with compositional variations in the primary mineral due to elemental substitution in solid-solution. To date Velbel's (1993) hypothesis has not been extended beyond end-member compositions of natural almandine garnets.

The purpose of this study was to test the hypothesis that the kinetic role of almandine garnet's weathering products varies with the composition of the specific almandine experiencing weathering. This hypothesis is tested by calculating the product-reactant volume ratios for natural almandine garnets from Coweeta Hydrologic Laboratory (CHL) in western North Carolina, USA, using the Pilling-Bedworth criterion (Velbel, 1993). In support of this, the formation and nature of surface layers on naturally occurring almandine garnets, including observations of underlying garnet surface textures, are initially characterized. Second, the possible temporal changes in surface layer mineralogy are considered based on the surface textures of naturally weathered almandine garnets in the observational portion of the study. Finally, the possibility of exporting Al derived during almandine garnet surface layer formation, as a function of the different secondary minerals in the surface layer, is presented following work by Velbel *et al.* (2009). Aluminum budgets for the system are determined from the stoichiometric coefficients of Al and Fe in the parent almandine garnet and secondary PSL minerals. Production of PSLs and, subsequently, possible excess Al available for export is a function of the primary almandine garnet's Al and Fe stoichiometric coefficients, molar mass, and specific gravity.

## BACKGROUND

### *Previous work*

The rate-determining step of the hydrolysis of silicate minerals during chemical weathering may occur by one of three mechanisms: (1) transport control in which

either transport of solvents and/or other reactants to, or products from, the dissolving mineral is rate limiting; (2) reaction-, surface-, or interface-control whereby the detachment of ions or molecules from the mineral surface is rate limiting; or (3) a combination of transport- and interface-control (Berner, 1978, 1981; Blum and Lasaga, 1987; Schott and Petit, 1987; Velbel, 2004). In pure transport-controlled dissolution, ions are detached so rapidly from the surface of a crystal that they become concentrated in the solution adjacent to the mineral surface (Berner, 1978, 1981). As a result, dissolution is regulated by transport of these ions *via* advection or diffusion away from the mineral surface. Transport-controlled kinetics includes reactions whose rates are limited by diffusion through a 'leached' layer. The surfaces of minerals dissolving by transport control are smooth, rounded, and featureless (Berner, 1978, 1981; Velbel, 2004). In contrast, during pure interface-controlled dissolution, ion detachment from the mineral surface is so slow that the relatively rapid transport of solutes away from the mineral prevents an increase in ion concentration adjacent to the crystal surface (Berner, 1978, 1981; Schott and Petit, 1987). Under such circumstances, increased advection or diffusion away from the mineral surface has no effect on the dissolution rate (Berner, 1978, 1981). Interface-limited mechanisms result in etch pit formation on mineral surfaces, reflecting the site-selective nature of the interfacial reaction (Wilson, 1975; Berner and Holdren, 1977; 1979; Berner, 1978, 1981; Berner *et al.*, 1980; Berner and Schott, 1982; Brantley *et al.* 1986; Lasaga and Blum, 1986; Blum and Lasaga, 1987). Interface-limited kinetics are now widely accepted for most major rock-forming silicates, including feldspars, pyroxenes, amphiboles, and olivine (Velbel, 1993; Blum and Stillings, 1995; Brantley and Chen, 1995; Brantley, 2005, 2008; Lüttge and Arvidson, 2008).

Velbel (1984a, 1993) described almandine garnet replacement textures and the formation of PSLs developed during chemical weathering. Velbel (1993) determined that protective surface layers can only form if: (1) the immobile elements (*e.g.* Al and Fe) behave conservatively at the scale of the garnet-grain surface; and (2) the volume of product(s) formed during weathering are equal to or greater than the volume of the reacting garnet replaced. Velbel (1984a, 1993) suggested that an almandine with a PSL composed of goethite and gibbsite would experience diffusion-limited dissolution. That is, the rate-determining step during weathering reflects transported-controlled kinetics in the form of diffusion of ions through the PSL, with diffusion being the slowest form of transport (Berner, 1978, 1981). The almandine garnet grains that develop PSLs weather more slowly than the grains which do not (Embrechts and Stoops, 1982; Velbel, 1984a). Almandine garnet surfaces beneath the PSL are smooth and featureless, with rounding of grain corners, reflecting uniform attack on the surface (Berner, 1978, 1981). In contrast, if the surface layer is significantly permeable and unprotective (USL), then diffusion through the open pore network is not sufficiently slow to affect garnet dissolution. Under such circumstances, interface-controlled kinetics is favored with the rate-determining step being processes occurring at the mineral–solution interface, and etch pits form (Berner, 1978, 1981).

Velbel's (1984a, 1993) work on almandine garnet weathering reflects observations for the regolith of the Appalachian Southern Blue Ridge Physiographic Province, USA. In addition to goethite and gibbsite weathering products identified by Velbel (1984a, 1993), hematite has also been observed (Graham *et al.*, 1989a, 1989b, 1990a, 1990b). To date, hematite, goethite, and gibbsite are the only weathering products for almandine garnet reported for the Southern Blue Ridge (Graham *et al.*, 1989a, 1989b, 1990a, 1990b; Velbel 1984a, 1984b, 1993). Despite the release of Si and Al during almandine dissolution, no studies to date have identified kaolinite as a weathering product.

The formation of USLs on hornblende in the Southern Appalachian Blue Ridge Mountains of northeastern Georgia, USA, was investigated by Velbel *et al.* (2009). From hornblende-product molar volume calculations, these authors found that Al must be imported to the hornblende-surface layer system during early-stage weathering. Although Al is typically considered negligibly mobile during weathering, some previous work identified instances of substantial Al mobilization (*e.g.* Gardner, 1992). Velbel *et al.* (2009) suggested that the source of the imported Al in the weathering products of hornblende they studied is from garnet weathering known to occur in the same rock unit. For the textbook end-member almandine garnet composition, Velbel (1993) showed that a PSL may form while up to 15% of the Al and Fe produced during almandine garnet dissolution may be exported from the almandine garnet-PSL microenvironment.

### *Study area*

The study area is the U.S. Forest Service Coweeta Hydrologic Laboratory (CHL) located in the southeastern Blue Ridge Physiographic Province of western North Carolina (Figure 1). The Coweeta Basin is underlain by amphibolite-facies metamorphosed sediments of the Coweeta Group (mid-Ordovician; Miller *et al.*, 2000) and the Otto Formation (Upper Precambrian; Hatcher 1980, 1988). The Coweeta Group is subdivided into three lithostratigraphic units. The basal Persimmon Creek Gneiss is predominantly a massive quartz diorite orthogneiss with interlayers of metasandstone, quartz-feldspar gneiss, and pelitic schist (Hatcher, 1980). The overlying Coleman River Formation is characterized by metasandstone and quartz-feldspar gneiss with lesser pelitic schist and calc-silicate quartzite. The Coleman River Formation is overlain by the Ridgepole Mountain

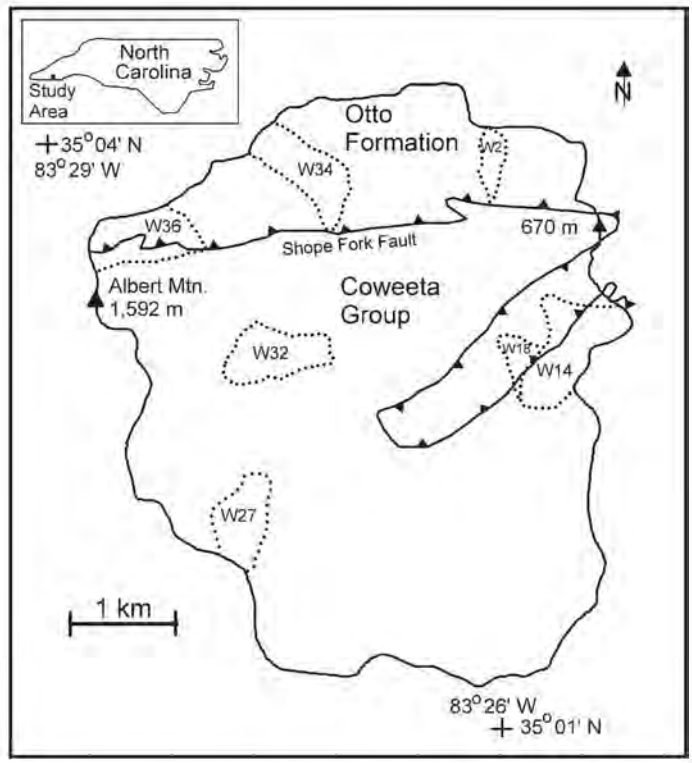


Figure 1. Map of Coweeta Hydrologic Laboratory showing the locations of control watersheds.

Formation; a mineralogically more mature coarse biotite-garnet schist, pelitic schist, metaorthoquartzite, garnetiferous metasandstone, and muscovite-chlorite quartzite (Hatcher, 1980). In contrast to the maturity of the Coweeta Group protolith sediments (*e.g.* arkoses and quartz arenites), the Otto Formation is derived from sedimentary protoliths of low compositional maturity (*e.g.* greywackes) and is feldspar- and biotite-rich (Hatcher, 1980, 1988).

The average weathering profile (saprolite and soil) at Coweeta is ~6 m thick (Berry, 1976; Yeakley *et al.*, 1998). The saprolite at Coweeta is not an ancient, relict, deep weathering profile, as shown by its great thickness (up to 18 m; Berry, 1976; Ciampone, 1995) despite residing on very steep slopes (average slope of ~45%/23°; Velbel, 1985). On such steep slopes, ancient weathering profiles would probably have succumbed to mass wasting and not have survived to the present. Coweeta soils are mostly Ultisols and Inceptisols (Velbel, 1988). Coweeta soils are typically limited in thickness to the uppermost 30 cm of the profile and differ from the underlying saprolite in that they are friable and the residual parent rock structure and fabric have been destroyed by soil forming processes, including transformation or neoformation of soil minerals, mass-wasting, slope creep, root throw, and bioturbation (Velbel, 1985). Soil textures range from fine/coarse loamy, micaceous to fine/coarse loamy, mixed (Browning and Thomas, 1985) and most Coweeta soils are well to extremely well drained. Umbric Dystrochrepts occur at high elevations on steep, rocky north- and south-facing slopes, Typic Dystrochrepts occur on south-facing slopes underlain by the Otto Formation, and Typic Haplumbrepts (Inceptisols) occur on colluvium in hollows and coves. Ultisols have formed in residuum of weathered schists and gneisses and include Typic Hapludults and Humic Hapludults. Typic Hapludults are the most prevalent soil type at Coweeta and are found on sloping ridges and side slopes. Humic Hapludults are found on cooler, steep, north-facing slopes (Swank and Crossley, 1988).

## METHODS

### *Application of the Pilling-Bedworth Rule*

The Pilling-Bedworth method was established by metallurgists to explain and predict oxidation products on metals (*e.g.* Kubaschewski and Hopkins, 1962; Hauffe, 1965). Velbel (1993) and Velbel *et al.* (2009) adapted the criterion for application to the chemical weathering of silicate minerals and their possible secondary products, including garnets. The Pilling-Bedworth rule may be important for reaction products in which diffusion of matter is from the outer surface of the product toward the metal–product interface (Kubaschewski and Hopkins, 1962; Fromhold, 1976).

This geometry is analogous to observed centripetal garnet replacement textures characterized by Velbel (1984a, 1993).

The Pilling-Bedworth criterion applied to the weathering of rock-forming minerals involves calculation of the ratio of the volume of the secondary weathering products ($V_p$) replacing a primary weathering mineral to the volume of primary mineral replaced ($V_r$). When $V_p/V_r \geq 1$, the surface layer of secondary minerals will occupy at least the same volume as the portion of the reactant mineral replaced. Such a surface layer is pore free and thus a PSL (Kubaschewski and Hopkins, 1962; Hauffe, 1965; Velbel, 1993). Diffusion through a PSL (by grain-boundary diffusion between product-mineral crystals or volume diffusion through the product-mineral crystal structures) is rate determining for the chemical weathering of the reactant mineral. With a PSL the kinetics of the weathering primary mineral are transport- (diffusion)-limited, the mineral grains exhibit sharp, smooth contact with the PSL, and primary grain edges and corners become rounded (Velbel, 1984a, 1993). When $V_p/V_r < 1$, the surface layer of secondary minerals is of insufficient volume to be continuous and uninterrupted, and is, therefore, an USL. An USL yields a primary mineral surface that is vulnerable to direct attack by reacting fluids. Also, with an USL the kinetics of the weathering primary mineral are interface limited, and the mineral grains exhibit etched surfaces (Velbel, 1984a, 1993).

Following the Pilling-Bedworth criterion, as presented by Velbel (1993), the total number of moles of a given element ($e$) in any arbitrary volume of reactant or product mineral is given by

$$m_{e,i} = \frac{n_{e,i} V_i}{V_i^o} \quad (1)$$

where,

$m_{e,i}$ = total number of moles of element $e$ in mineral $i$

$n_{e,i}$ = stoichiometric coefficient of element $e$ in mineral $i$

$V_i$ = volume of mineral $i$

$V_i^o$ = molar volume of mineral $i$

Writing equations for $i$ = reactant mineral, r, and for $i$ = product mineral, p, setting $m_{e,r} = m_{e,p}$ (that is, conserving element $e$ such that all of element $e$ present in the reactant mineral is incorporated into the product mineral), and combining the equations for reactant and product minerals, and rearranging, yields:

$$V_p/V_r = \frac{n_{e,r} V_p^o}{n_{e,p} V_r^o} \quad (2)$$

where,

$V_p/V_r$ = the volume of product mineral produced per unit volume of reactant mineral if element $e$ is conserved.

By analogy with the Pilling-Bedworth rule, for a primary rock-forming silicate mineral to form a PSL by replacement, conservation of the least mobile elements such as Fe, Al, and Mn must be assumed (Velbel, 1993).

Molar volumes for reactant garnets ($V_r^o$) were calculated by dividing the molar mass of a mineral by its specific gravity. In the absence of analytically determined primary-mineral chemistries, molar volumes are available from Smyth and Bish (1988). However, using calculated molar volumes determined from site-specific analyzed mineral chemistries yield more meaningful results for the system being investigated. Molar volumes for secondary products ($V_p^o$) included in this study (Table 1) are from Smyth and Bish (1988), reported by Velbel (1993, table 1). Secondary products investigated in this study are hematite, goethite, gibbsite, kaolinite, and pyrolusite. These minerals are ubiquitous in the CHL regolith (*e.g.* Velbel, 1984a, 1984b; Price, 2003; Price *et al.*, 2005), and some of these have been reported to be associated with garnet weathering in the southern Appalachian Blue Ridge Physiographic Province (*e.g.* Graham *et al.*, 1989a, 1989b, 1990a, 1990b; Velbel, 1984a, 1984b, 1993) and elsewhere (*e.g.* Embrechts and Stoops, 1982; Parisot *et al.*, 1983; Robertson and Butt, 1997).

### *Published data for natural almandine garnets*

Chemical data from Deer *et al.* (1997) were used to establish a conceptual framework for surface layer formation on natural almandine garnets. These data are ideally suited as Deer *et al.* (1997) not only provide analyses spanning a wide range of natural almandine

Table 1. Stoichiometric coefficients and molar volumes for secondary weathering products characteristic of well leached oxidizing conditions.

| Mineral | Formula | Element conserved ($e$) | $n_e$ | $V^o$ | $V^o/n_e$ |
|---|---|---|---|---|---|
| Hematite | $Fe_2O_3$ | Fe | 2 | 30.388 | 15.194 |
| Goethite | FeOOH | Fe | 1 | 20.693 | 20.693 |
| Gibbsite | $Al(OH)_3$ | Al | 1 | 32.222 | 32.222 |
| Kaolinite | $Al_2Si_2(OH)_5O_4$ | Al | 2 | 99.236 | 49.618 |
| Pyrolusite | $MnO_2$ | Mn | 1 | 16.708 | 16.708 |

Data from Smyth and Bish (1988) and reported by Velbel (1993; his table 1).

garnet compositions, but also include the garnets' specific gravities with many of their chemical analyses. A total of 18 garnet analyses and associated specific gravities (Table 2) were used in the present study.

All surface-layer calculations in this study assumed conservation of Fe in hematite or goethite, and conservation of Al in gibbsite and/or kaolinite (Velbel, 1993; Table 1). For a PSL composed solely of goethite and kaolinite when $V_p/V_r = 1$ the following equation applies:

$$V_r = V_p = Fe_{Grt}V^o_{Gt} + 0.5Al_{Kln}V^o_{Kln} \quad (3)$$

where,

$Fe_{Grt}$ = Fe stoichiometric coefficient of the garnet; assume that all Fe conserved in PSL goethite

$V^o_{Gt}$ = molar volume of goethite

$Al_{Kln}$ = moles of Al in kaolinite of PSL

$V^o_{Kln}$ = molar volume of kaolinite

All subscripts are the standard mineral symbols of Kretz (1983). Rearranging equation 3 yields

$$Al_{Kln} = (V_r - Fe_{Grt}V^o_{Gt})/0.5V^o_{Kln} \quad (4)$$

In order to determine the quantity of Al needed to form a PSL of goethite, gibbsite, and kaolinite when $V_p/V_r = 1$, a gibbsite term must be added to equation 3 as follows:

$$V_r = V_p = Fe_{Gt}V^o_{Gt} + 0.5Al_{Kln}V^o_{Kln} + Al_{Gbs}V^o_{Gbs} \quad (5)$$

where,

$Al_{Gbs}$ = moles of Al in gibbsite of PSL

Rearranging equation 5 yields

$$Al_{Kln} = (V_r - Fe_{Gt}V^o_{Gt} - Al_{Gbs}V^o_{Gbs})/0.5V^o_{Kln} \quad (6)$$

The excess Al available for export is the difference between the number of moles of Al needed to produce a PSL of goethite, gibbsite, and kaolinite when $V_p/V_r = 1$, and the Al stoichiometric coefficient of the parent garnet.

*Almandine garnets from Coweeta Hydrologic Laboratory*

Three different almandine garnet compositions have been collected from CHL (Figure 1) (Velbel, 1984a, 1984b; Price, 2003; Price *et al.*, 2005), all of which form PSLs during weathering (Velbel, 1984a, 1984b; Bryan, 1994; Price, 2003; Price *et al.*, 2005). Evaluation of these grains permits further exploration of the conceptual framework for surface-layer formation, direct observations of garnet-surface textures, and production of excess Al associated with almandine garnet weathering.

*Pilling-Bedworth criterion.* The specific gravity of CHL almandine garnets could not be measured so the average of those reported by Deer *et al.* (1997) of 4.05 was used. Calculations were also made using a specific gravity from Klein and Hurlbut (1999) of 4.32. However, the exact specific gravity value used does not appreciably influence the results, and has no influence on the conclusions of this study.

*Field sampling and petrography.* Almandine garnet samples examined were collected and described by Velbel (1984a, 1984b), Bryan (1994), Price (2003), and Price *et al.* (2005). Parent rock was collected from outcrops, and regolith samples were collected from roadcuts and hand-augered cores. Samples were collected from saprolite (>60 cm below surface grade (b.s.g.)),

Table 2. Almandine garnet analyses from Deer *et al.* (1997) utilized in the present study ($n = 18$).

| Sample | Si | Al | Al | $Fe^{3+}$ | Ti | Mg | $Fe^{2+}$ | Mn | Ca | O | Specific gravity | Molar mass | $V_r$ |
|---|---|---|---|---|---|---|---|---|---|---|---|---|---|
| 3 | 5.974 | 0.026 | 3.879 | 0.1 | 0.014 | 0.917 | 4.86 | 0.116 | 0.07 | 24 | 4.235 | 966 | 228 |
| 11 | 5.879 | 0.121 | 3.872 | 0.057 | 0.062 | 0.951 | 4.506 | 0.247 | 0.277 | 24 | 4.09 | 962 | 235 |
| 12 | 6.052 | 0 | 3.891 | 0.083 | 0.081 | 0.621 | 4.29 | 0.295 | 0.507 | 24 | 4.1 | 959 | 234 |
| 15 | 5.789 | 0.211 | 3.628 | 0.227 | 0.143 | 0.277 | 4.414 | 0.399 | 0.882 | 24 | 4.03 | 980 | 243 |
| 20 | 5.984 | 0.016 | 3.944 | 0.082 | 0.002 | 0.299 | 4.1 | 0.297 | 1.211 | 24 | 4.13 | 965 | 234 |
| 23 | 5.984 | 0.016 | 3.914 | 0.061 | 0.012 | 1.827 | 3.929 | 0.049 | 0.153 | 24 | 3.967 | 935 | 236 |
| 24 | 5.937 | 0.063 | 3.994 | 0.103 | 0 | 1.51 | 3.808 | 0.208 | 0.301 | 24 | 4.08 | 939 | 230 |
| 25 | 5.901 | 0.099 | 3.837 | 0.13 | 0.012 | 0.44 | 3.943 | 0.169 | 1.465 | 24 | 4.067 | 963 | 237 |
| 26 | 6 | 0 | 3.795 | 0.217 | 0.007 | 0.573 | 3.698 | 0.597 | 1.03 | 24 | 4.1 | 962 | 235 |
| 28 | 5.923 | 0.077 | 3.783 | 0.232 | 0.004 | 1.827 | 3.664 | 0.084 | 0.376 | 24 | 3.99 | 936 | 235 |
| 30 | 5.871 | 0.129 | 3.955 | 0.056 | 0.024 | 2.1 | 3.541 | 0.154 | 0.143 | 24 | 4.04 | 926 | 229 |
| 32 | 5.948 | 0.052 | 3.771 | 0.19 | 0.044 | 0.731 | 3.4 | 0.078 | 1.729 | 24 | 3.99 | 948 | 238 |
| 36 | 5.942 | 0.058 | 3.782 | 0.208 | 0.011 | 0.992 | 3.172 | 0.044 | 1.76 | 24 | 3.97 | 941 | 237 |
| 38 | 5.843 | 0.157 | 3.766 | 0.206 | 0.015 | 0.216 | 3.16 | 1.571 | 1.086 | 24 | 4.06 | 978 | 241 |
| 42 | 5.937 | 0.063 | 3.933 | 0.036 | 0 | 1.065 | 2.751 | 0.563 | 1.6 | 24 | 3.99 | 935 | 234 |
| 43 | 6.017 | 0 | 3.866 | 0.12 | 0.018 | 1.782 | 2.664 | 0.085 | 1.361 | 24 | 3.93 | 916 | 233 |
| 44 | 5.911 | 0.089 | 3.686 | 0.274 | 0.03 | 0.513 | 2.658 | 2.331 | 0.485 | 24 | 4.14 | 977 | 236 |
| 48 | 5.992 | 0.008 | 3.614 | 0.32 | 0.017 | 0.539 | 1.942 | 1.487 | 2.048 | 24 | 3.971 | 954 | 240 |

middle soil horizons (17–60 cm b.s.g.), and upper soil horizons (0–10 cm b.s.g.). Samples were thin sectioned and examined with polarized-light microscopy with weathering textures being photographed with a 35 mm film camera mounted on a petrographic microscope.

Weathered almandine garnets were hand-picked from the >1 mm fraction of the saprolite and soil samples. Samples were washed with deionized water through a 1 mm sieve and the >1 mm fraction dried at 60°C for 24 h. Almandine garnet grains from the >1 mm regolith fraction and from rock outcrops were hand picked under a binocular microscope.

*X-ray diffractometry (XRD).* Separation into the <2 mm size fraction was performed by gravity settling, with the <2 mm size fraction being separated with a pipette, and the aliquots being filtered onto a 0.45 μm Millipore® filter following rapid-suction mounting techniques (production of oriented mounts; also termed the Millipore® Filter Transfer Method of Drever (1973); this method was described thoroughly by Moore and Reynolds (1997)). Almandine garnet samples and clay minerals in the <2 μm size fraction were initially analyzed by XRD at Michigan State University utilizing a Philips APD (Automated Powder Diffraction) 3720 X-ray diffractometer equipped with an APD 3521 goniometer, a Philips goniometer with CuKα radiation (35 kV, 20 mA), a 1° divergence slit, a 0.2 mm receiving slit, a 1° anti-scatter slit, and a graphite monochromator on the diffracted beam. Almandine garnet samples were step-scanned for various intervals at 0.05°2θ steps using a counting time of 2 s per step.

Additional scans were completed at Franklin and Marshall College, Lancaster, Pennsylvania, using a fully computer-controlled PANalytical X'Pert Pro XRD. Radiation was CuKα (45 kV, 40 mA), with an automated preprogrammed divergence slit that allowed for a constant sample irradiation length of 10 mm, and a 2° anti-scatter slit. Six detectors operated throughout the scan and the sample was rotated continuously during measurement.

*Electron microscopy.* Hand-picked almandine garnet grains from one or two intermediate points in each profile were mounted to scanning electron microscopy (SEM) stubs with press-on adhesive tabs designed for SEM work. Whole and fractured (by gentle crushing) garnet grains were prepared in the same manner. Grains prepared in this manner were examined by scanning electron microscopy (SEM) in secondary electron imaging (SEI) mode. Polished thin sections of Coweeta bedrock and regolith were imaged using SEM in backscattered-electron imaging (BEI) mode, and energy-dispersive X-ray spectroscopy (EDS). The SEM stubs were gold-coated, and thin sections were either carbon- or gold-coated. Gold-coating of thin sections was often necessary because carbon-coating did not always provide adequate conductivity to prevent sample charging. Imaging and analyses were performed at Michigan State University's Center for Advanced Microscopy (CAM) using a JEOL JSM-35CF SEM. More than 200 micrographs were taken of garnet weathering textures, with the most informative images included herein. Additional photomicrographs may be found in Bryan (1994).

*Electron microprobe phase analyses (EMPA).* Electron microprobe analyses of Otto Formation, Coleman River Formation, and Ridgepole Mountain Formation garnets in thin section were completed at the University of Michigan's Electron Microbeam Analysis Laboratory (EMAL), using a wavelength dispersive Cameca SX 100 electron microprobe analyzer. The accelerating voltage and beam current were 15 keV and 10 nA, respectively, and a beam diameter of 2 μm was used. Calibration standards for Si, Al, Mg, Fe, Mn, Ti, and Ca were tanzanite (natural), andalusite (natural), enstatite (synthetic), ferrosilite (synthetic), rhodonite (natural Broken Hill), geikielite (natural), and tanzanite (natural), respectively. All garnet formulae reported in this study were reported on an anion basis of $O_{24}$.

## RESULTS

### *Application of Pilling-Bedworth rule to naturally occurring almandine garnet compositions*

None of the 18 almandine garnet samples reported by Deer *et al.* (1997) would produce a PSL of hematite and gibbsite (Table 3). Hematite has a relatively low molar volume per mole of Fe, with $V^o/n_e$ = 30.388/2 = 15.194 (Table 1). Because goethite has $V^o/n_e$ = 20.693, having goethite as the Fe host is more likely to yield a PSL than one in which hematite is the Fe host. Similarly, kaolinite has a greater $V^o/n_e$ value (49.618) than does gibbsite (32.222) (Table 1). Thus, a surface layer in which kaolinite is the Al host is more likely to be protective than one in which gibbsite is the Al host. The importance of the presence of kaolinite in a surface layer is reflected in the fact that 89% of the almandine garnets (Table 3) could form a PSL composed of hematite and kaolinite, despite hematite being the Fe host. To weather to a PSL of hematite and kaolinite, almandine garnet would have to possess minimum Fe and Al stoichiometric coefficients of ~2.8 a.p.f.u. and ~3.78 a.p.f.u., respectively (anion basis of $O_{24}$) (Figure 2a). Most of the almandine garnets investigated satisfied this criterion (Table 2). In contrast, only one of the 18 almandine garnet samples (6%) reported by Deer *et al.* (1997) (sample 3) had an appropriate chemistry to produce a PSL of solely goethite and gibbsite (Table 3; Figure 2b). Sample 3 producing a PSL of goethite and gibbsite did so because of the garnet's relatively high Fe stoichiometric coefficient (Table 2). This Fe stoichiometric coefficient is above an approximate minimum of ~4.7 (anion basis of $O_{24}$)

Table 3. Results of surface-layer calculations for garnet compositions and specific gravities, as reported by Deer *et al.* (1997).

| Sample | $V_p/V_r$ | | | | | | | | Moles of Al needed for $V_p/V_r = 1$ (PSL of goethite + kaolinite) | Excess Al when $V_p/V_r = 1$ (PSL of goethite + kaolinite) |
|---|---|---|---|---|---|---|---|---|---|---|
| | Hematite + Gibbsite | Hematite + Kaolinite | Goethite + Gibbsite | Goethite + Kaolinite | Hematite + Gibbsite + Pyrolusite | Hematite + Kaolinite + Pyrolusite | Goethite + Gibbsite + Pyrolusite | Goethite + Kaolinite + Pyrolusite | | |
| 3 | 0.88 | 1.18 | 1.00 | 1.30 | 0.89 | 1.19 | 1.01 | 1.31 | 2.53 | 1.38 |
| 11 | 0.84 | 1.14 | 0.95 | 1.24 | 0.86 | 1.15 | 0.97 | 1.26 | 2.87 | 1.12 |
| 12 | 0.82 | 1.11 | 0.92 | 1.21 | 0.84 | 1.13 | 0.94 | 1.23 | 2.92 | 0.97 |
| 15 | 0.80 | 1.07 | 0.90 | 1.18 | 0.83 | 1.10 | 0.93 | 1.21 | 3.00 | 0.84 |
| 20 | 0.82 | 1.11 | 0.92 | 1.21 | 0.84 | 1.13 | 0.94 | 1.23 | 2.99 | 0.97 |
| 23 | 0.79 | 1.08 | 0.89 | 1.18 | 0.80 | 1.09 | 0.89 | 1.18 | 3.11 | 0.82 |
| 24 | 0.83 | 1.13 | 0.92 | 1.23 | 0.84 | 1.15 | 0.93 | 1.24 | 3.03 | 1.02 |
| 25 | 0.80 | 1.09 | 0.89 | 1.18 | 0.81 | 1.10 | 0.90 | 1.19 | 3.10 | 0.84 |
| 26 | 0.77 | 1.06 | 0.87 | 1.15 | 0.82 | 1.10 | 0.91 | 1.19 | 3.12 | 0.67 |
| 28 | 0.78 | 1.07 | 0.87 | 1.16 | 0.79 | 1.07 | 0.88 | 1.17 | 3.13 | 0.73 |
| 30 | 0.81 | 1.12 | 0.90 | 1.21 | 0.82 | 1.13 | 0.91 | 1.22 | 3.15 | 0.94 |
| 32 | 0.75 | 1.03 | 0.83 | 1.11 | 0.75 | 1.03 | 0.84 | 1.12 | 3.32 | 0.51 |
| 36 | 0.74 | 1.02 | 0.82 | 1.10 | 0.74 | 1.02 | 0.82 | 1.10 | 3.39 | 0.45 |
| 38 | 0.74 | 1.02 | 0.81 | 1.10 | 0.85 | 1.13 | 0.92 | 1.21 | 3.47 | 0.45 |
| 42 | 0.73 | 1.03 | 0.80 | 1.09 | 0.77 | 1.07 | 0.84 | 1.13 | 3.58 | 0.42 |
| 43 | 0.72 | 1.00 | 0.78 | 1.07 | 0.72 | 1.01 | 0.79 | 1.08 | 3.56 | 0.31 |
| 44 | 0.70 | 0.98 | 0.77 | 1.05 | 0.87 | 1.15 | 0.94 | 1.22 | 3.55 | 0.22 |
| 48 | 0.63 | 0.89 | 0.68 | 0.94 | 0.73 | 0.99 | 0.78 | 1.05 | Not applicable | |
| % Forming PSL | 0 | 89 | 6 | 94 | 0 | 94 | 6 | 100 | | |

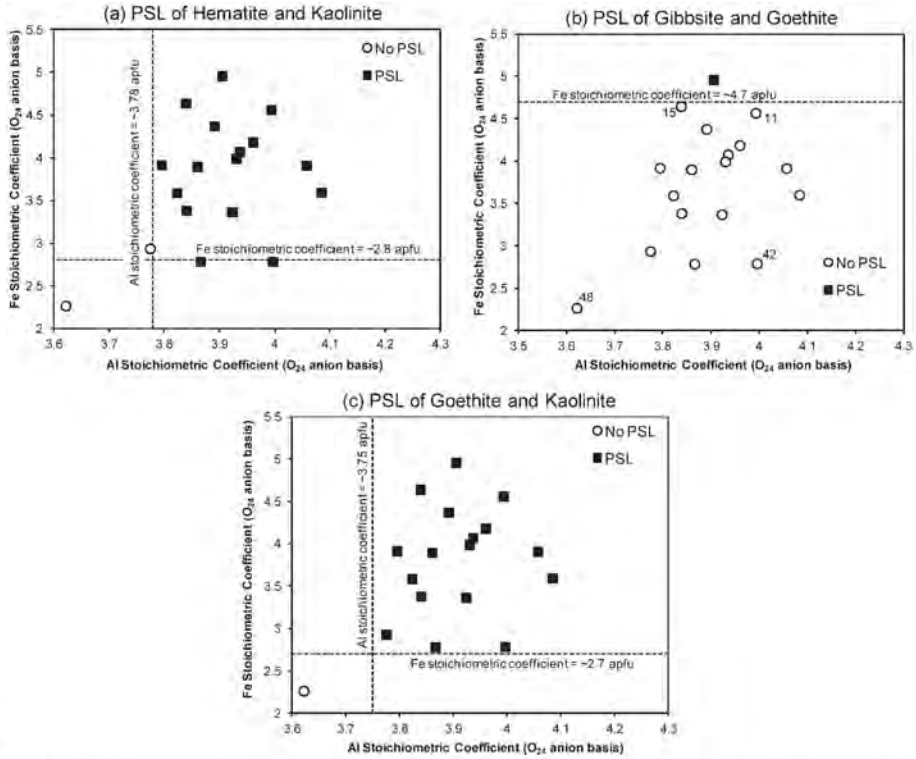


Figure 2. Results of almandine garnet surface-layer calculations for surface layers composed of (a) hematite and kaolinite, (b) goethite and gibbsite, and (c) goethite and kaolinite. 'PSL' indicates that the surface layer is protective, with $V_p/V_r \geqslant 1$. Minimum Fe and Al stoichiometric coefficients needed to produce a PSL are provided.

required for PSL formation (Figure 2b). This is consistent with the $V_p/V_r$ calculations of Velbel (1993) for end-member almandine garnet. Of the remaining samples, all but one (sample 48) would produce a PSL of goethite and kaolinite (Table 3; Figure 2c). This illustrates that formation of PSLs on most naturally occurring almandine garnets requires more complicated combinations of actual primary-mineral compositions and product assemblages than the end-member almandine garnet invoked by Velbel (1993). To form a PSL of goethite and kaolinite an almandine garnet would have to possess a minimum Fe stoichiometric coefficient of ~2.7 a.p.f.u. and a minimum Al stoichiometric coefficient of ~3.75 a.p.f.u. (anion basis of $O_{24}$) (Figure 2c). These stoichiometric coefficients are only slightly lower than those reported for a PSL composed of hematite and kaolinite (Figure 2a). Adding pyrolusite to the surface layer only increases $V_p/V_r$ to $\geqslant 1$ for one sample (44) when the other product minerals are hematite and kaolinite, and one additional sample (48) when the other product minerals are goethite and kaolinite (Table 3). Therefore, including the volume of pyrolusite formed if Mn behaves conservatively in a surface layer will only modify it from a USL to a PSL for a relatively small number of almandine garnets which host substantial quantities of Mn. However, the only product mineralogy that allows for formation of a PSL on all of the almandine garnets (Table 3) is goethite, kaolinite, and pyrolusite. The influence of the Mn stoichiometric coefficient on formation of PSL is probably far more significant for spessartine garnets which are not evaluated in this study.

All but two of the $V_p/V_r$ values for a surface layer of hematite and kaolinite are >1, and all but one of $V_p/V_r$ values for a surface layer of goethite and kaolinite are >1 (Table 3; Figure 2). $V_p/V_r$ values >1 imply that typically not all of the Fe and/or Al released during garnet weathering is required to be incorporated in the PSL. To address the production of excess Al during almandine garnet weathering (Velbel *et al.*, 2009) and PSL formation, focus was placed on surface layers in which all of the Fe was conserved in the PSL, and the Fe-host was goethite, as this combination had the largest $V_p/V_r$ values (Table 3). Sample 48 had $V_p/V_r < 1$ for a surface layer that included either gibbsite or kaolinite as the Al-host (Table 3) and, thus, has not been included in the evaluation that follows. Using equation 4 above, the minimum number of moles of Al needed to produce a PSL of goethite and kaolinite has been calculated (second to the last column on the right of Table 3). The difference between this value and the Al stoichiometric coefficient of the parent almandine garnet yields the number of moles of Al available for export away from the almandine garnet while the PSL is still preserved (far right column of Table 3). In all 17 samples investigated, the maximum number of moles

of Al in excess of that required for PSL formation with $V_p/V_r = 1$ was substantial, ranging from 0.22 to 1.38.

The moles of Al released by almandine garnet weathering in excess of that needed to form a PSL using equation 4 was based on a PSL consisting of goethite and kaolinite (Table 3). However, XRD analyses of almandine garnet PSLs reported by Velbel (1984a, 1993) from western North Carolina indicated that gibbsite was ubiquitous in the PSL. Equation 6 was used to explore the relative proportions of gibbsite and kaolinite in a PSL at $V_p/V_r = 1$ in which all of the Fe was conserved in goethite. This relationship was investigated using four Deer *et al.* (1997) samples which represented the following parent garnet scenarios: (1) high Al and high Fe stoichiometric coefficients; (2) low Al and high Fe stoichiometric coefficients; (3) low Fe and high Al stoichiometric coefficients; and (4) low Al and low Fe stoichiometric coefficients. The samples used were 11 (high Al and high Fe stoichiometric coefficients), 15 (low Al and high Fe stoichiometric coefficients), 42 (low Fe and high Al stoichiometric coefficients), and 48 (low Al and low Fe stoichiometric coefficients) (Figures 2b, 3). The almandine garnet Fe stoichiometric coefficient exerted a strong influence on the formation of PSLs (Figure 3, Tables 3, 4). A relatively high almandine garnet Fe stoichiometric coefficient is capable of counteracting a relatively low Al stoichiometric coefficient by creating a PSL relatively rich in goethite and/or hematite. Specifically, sample 15 had a relatively high $V_p/V_r$ value despite having a relatively low Al stoichiometric coefficient.

Using equation 6, the relative proportions of Al hosted by gibbsite and kaolinite were included in the PSL for samples 11, 42, and 15 (Table 4, Figure 4). Sample 48 was not included because it does not form a PSL even when kaolinite is substituted for gibbsite in the PSL (Table 3). As the proportion of gibbsite in a PSL increases relative to kaolinite, the quantity of excess Al available for export decreases (Table 4, Figure 4). For sample 11 with a PSL at $V_p/V_r = 1$, when ~0.70 moles of Al were consumed by kaolinite, and 3.30 moles of Al were consumed by gibbsite, the quantity of excess Al available for export was approximately zero (Table 4, Figure 4). Almandine garnets with relatively high Fe and low Al stoichiometric coefficients (*e.g.* sample 15) were capable of yielding more excess Al than an almandine garnet with relatively high Al and low Fe stoichiometric coefficients (*e.g.* sample 42) (Table 4, Figures 2 and 4).

| | High Al | Low Al |
|---|---|---|
| High Fe | **DHZ Sample: 11**<br>$V_p/V_r$: High<br>PSL: Goethite + kaolinite<br>Excess Al: High | **DHZ Sample: 15**<br>$V_p/V_r$: High<br>PSL: Goethite + kaolinite<br>Excess Al: High |
| Low Fe | **DHZ Sample: 42**<br>$V_p/V_r$: Intermediate<br>PSL: Goethite + kaolinite<br>Excess Al: Low to intermediate | **DHZ Sample: 48**<br>$V_p/V_r$: Low<br>PSL: None<br>Excess Al: None |

Figure 3. Matrix displaying the relationship of $V_p/V_r$, PSL formation, and excess Al available for export as a function of parent almandine garnet relative to Al and Fe stoichiometric coefficients.

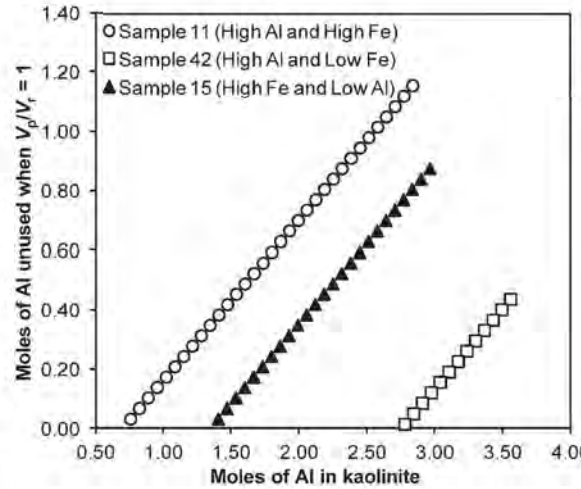


Figure 4. Relationship between Al stoichiometric coefficient of PSL kaolinite and the quantity of excess Al available for export from the almandine garnet-PSL microenvironment. Calculations (Table 4) based on almandine garnet data from Deer *et al.* (1997) (Table 2).

*Garnets from Coweeta Hydrologic Laboratory*

*Mineralogy.* Composition data on almandine garnets from the Upper Precambrian Otto Formation and the Mid-Ordovician Coleman River and Ridgepole Mountain Formations are provided in Table 5. X-ray diffractograms of weathered Coweeta almandine garnets displayed peaks indicative of quartz and gibbsite (all samples), hematite (in samples from the warmer, lower elevation Watershed 2), and goethite (in samples from Watersheds 18, 34, and 36) (Bryan, 1994). With the exception of hematite, these results compare favorably with those reported by Velbel (1984a, 1985, 1993). X-ray diffractograms generated as part of this study also yielded peaks for the aforementioned minerals, but also displayed peaks for kaolinite and pyrolusite (Figure 5). Consistent with Bryan (1994), hematite peaks for the Watershed 2 sample (Otto Formation) were taller, sharper, and generally more evident than those for the Watershed 27 sample (Coleman River Formation) (Figures 1 and 5). The same trend was observed for kaolinite.

*Pilling-Bedworth Calculations.* The methods and Pilling-Bedworth-based concepts outlined above may be applied to almandine garnets found at CHL (Table 5). The results for the CHL garnets are very comparable to

Table 4. Calculations of excess Al available for export for almandine garnet samples, taken from Deer *et al.* (1997).

| – 11 (High Al and high Fe) – | | | – 42 (High Al and low Fe) – | | | – 15 (High Fe and low Al) – | | |
|---|---|---|---|---|---|---|---|---|
| $Al_{Gbs}$ | $Al_{Kln}$ | Excess Al when $V_p/V_r = 1$ | $Al_{Gbs}$ | $Al_{Kln}$ | Excess Al when $V_p/V_r = 1$ | $Al_{Gbs}$ | $Al_{Kln}$ | Excess Al when $V_p/V_r = 1$ |
| 0.00 | 2.84 | 1.15 | 0.00 | 3.56 | 0.43 | 0.00 | 2.97 | 0.87 |
| 0.10 | 2.77 | 1.12 | 0.10 | 3.50 | 0.40 | 0.10 | 2.90 | 0.84 |
| 0.20 | 2.71 | 1.08 | 0.20 | 3.43 | 0.36 | 0.20 | 2.84 | 0.80 |
| 0.30 | 2.64 | 1.05 | 0.30 | 3.37 | 0.33 | 0.30 | 2.77 | 0.77 |
| 0.40 | 2.58 | 1.013 | 0.40 | 3.30 | 0.29 | 0.40 | 2.71 | 0.73 |
| 0.50 | 2.51 | 0.978 | 0.50 | 3.24 | 0.26 | 0.50 | 2.64 | 0.70 |
| 0.60 | 2.45 | 0.943 | 0.60 | 3.17 | 0.22 | 0.60 | 2.58 | 0.66 |
| 0.70 | 2.38 | 0.908 | 0.70 | 3.11 | 0.19 | 0.70 | 2.51 | 0.63 |
| 0.80 | 2.32 | 0.873 | 0.80 | 3.04 | 0.15 | 0.80 | 2.45 | 0.59 |
| 0.90 | 2.25 | 0.838 | 0.90 | 2.98 | 0.12 | 0.90 | 2.38 | 0.56 |
| 1.00 | 2.19 | 0.803 | 1.00 | 2.91 | 0.08 | 1.00 | 2.32 | 0.52 |
| 1.10 | 2.13 | 0.768 | 1.10 | 2.85 | 0.05 | 1.10 | 2.25 | 0.49 |
| 1.20 | 2.06 | 0.733 | 1.20 | 2.78 | 0.01 | 1.20 | 2.19 | 0.45 |
| 1.30 | 2.00 | 0.698 | 1.30 | 2.72 | −0.02 | 1.30 | 2.12 | 0.42 |
| 1.40 | 1.93 | 0.663 | | 1.40 | 2.06 | 0.38 | | |
| 1.50 | 1.87 | 0.628 | | 1.50 | 1.99 | 0.35 | | |
| 1.60 | 1.80 | 0.593 | | 1.60 | 1.93 | 0.31 | | |
| 1.70 | 1.74 | 0.558 | | 1.70 | 1.86 | 0.28 | | |
| 1.80 | 1.67 | 0.522 | | 1.80 | 1.80 | 0.24 | | |
| 1.90 | 1.61 | 0.487 | | 1.90 | 1.73 | 0.21 | | |
| 2.00 | 1.54 | 0.452 | | 2.00 | 1.67 | 0.17 | | |
| 2.10 | 1.48 | 0.417 | | 2.10 | 1.60 | 0.14 | | |
| 2.20 | 1.41 | 0.382 | | 2.20 | 1.54 | 0.10 | | |
| 2.30 | 1.35 | 0.347 | | 2.30 | 1.47 | 0.07 | | |
| 2.40 | 1.28 | 0.312 | | 2.40 | 1.41 | 0.03 | | |
| 2.50 | 1.22 | 0.277 | | 2.50 | 1.34 | 0.00 | | |
| 2.60 | 1.15 | 0.242 | | | | | | |
| 2.70 | 1.09 | 0.207 | | | | | | |
| 2.80 | 1.02 | 0.172 | | | | | | |
| 2.90 | 0.96 | 0.137 | | | | | | |
| 3.00 | 0.89 | 0.102 | | | | | | |
| 3.10 | 0.83 | 0.067 | | | | | | |
| 3.20 | 0.76 | 0.032 | | | | | | |
| 3.30 | 0.70 | −0.003 | | | | | | |

those of Deer *et al.* (1997) in that the formation of a PSL is very uncommon when the surface layer is composed solely of hematite and gibbsite, or solely of goethite and gibbsite (Table 6). However, a PSL did form in two of three garnets when composed of hematite and kaolinite, and all of the CHL garnets formed a PSL composed of goethite and kaolinite. When $V_p/V_r$ values were above unity, excess Al was available for export. With the exception of the Ridgepole Mountain Formation, adding pyrolusite to a surface layer composed of hematite and kaolinite was insufficient to increase product volume to render an otherwise unprotective layer protective (Table 6). Calculations may also be made when Fe is conserved in goethite and $V_p/V_r$ values are thereby highest, and Al is distributed between gibbsite and kaolinite in a PSL when $V_p/V_r = 1$. The results of these calculations demonstrate that the CHL garnets can possess a PSL of goethite, gibbsite, and kaolinite, and still have significant Al available for export (Table 7, Figure 6). For the Otto Formation garnet, no excess Al will be present when approximately equal molar quantities of Al (~2.0) are distributed between gibbsite and kaolinite (Table 7). Garnet of the Coleman River Formation would have more of the Al hosted by gibbsite than kaolinite when excess Al is zero. The Otto Formation and Coleman River Formation have identical Al stoichiometric coefficients, nearly identical molar masses, and the same specific gravity is used for garnets from both bedrock units. The higher excess Al for the Coleman River Formation reflects its higher Fe stoichiometric coefficients relative to that of the Otto Formation (Table 5). This again illustrates the strong influence of Fe stoichiometry on PSL formation and excess Al when all of the Fe is conserved in a weathering product. The Ridgepole Mountain Formation garnet has the lowest stoichiometric coefficients of both Al and Fe, and would require a PSL relatively rich in kaolinite to yield any excess Al (Table 7).

Table 5. Data on garnets collected from Coweeta Hydrologic Laboratory. Mineral chemistry for the Otto Formation and the Coleman River Formation from Price *et al.* (2005). Specific gravity reflects an average of 18 samples reported by Deer *et al.* (1997).

| Rock unit | Age | Si | Al | Fe | Mg | Mn | Ca | O | Specific gravity | Molar mass | $V_r$ |
|---|---|---|---|---|---|---|---|---|---|---|---|
| Otto Formation | Upper Precambrian | 6 | 4 | 3.52 | 0.72 | 1.0 | 0.82 | 24 | 4.05 | 962 | 238 |
| Coleman River Formation | Mid-Ordovician | 6 | 4 | 4.26 | 0.88 | 0.44 | 0.60 | 24 | 4.05 | 968 | 239 |
| Ridgepole Mountain Formation | Mid-Ordovician | 6 | 3.72 | 2.82 | 0.74 | 0.9 | 1.74 | 24 | 4.05 | 948 | 234 |

Table 6. Results of surface-layer calculations for Coweeta Hydrologic Laboratory almandine garnets.

| | $V_p/V_r$ | | | | | | | |
|---|---|---|---|---|---|---|---|---|
| Rock unit | Hematite + Gibbsite | Hematite + Kaolinite | Goethite + Gibbsite | Goethite + Kaolinite | Hematite + Gibbsite + Pyrolusite | Hematite + Kaolinite + Pyrolusite | Goethite + Gibbsite + Pyrolusite | Goethite + Kaolinite + Pyrolusite |
| Otto Formation | 0.77 | 1.06 | 0.85 | 1.14 | 0.84 | 1.13 | 0.92 | 1.21 |
| Coleman River Formation | 0.81 | 1.10 | 0.91 | 1.20 | 0.84 | 1.13 | 0.94 | 1.23 |
| Ridgepole Mountain Formation | 0.70 | 0.97 | 0.76 | 1.04 | 0.76 | 1.04 | 0.83 | 1.10 |

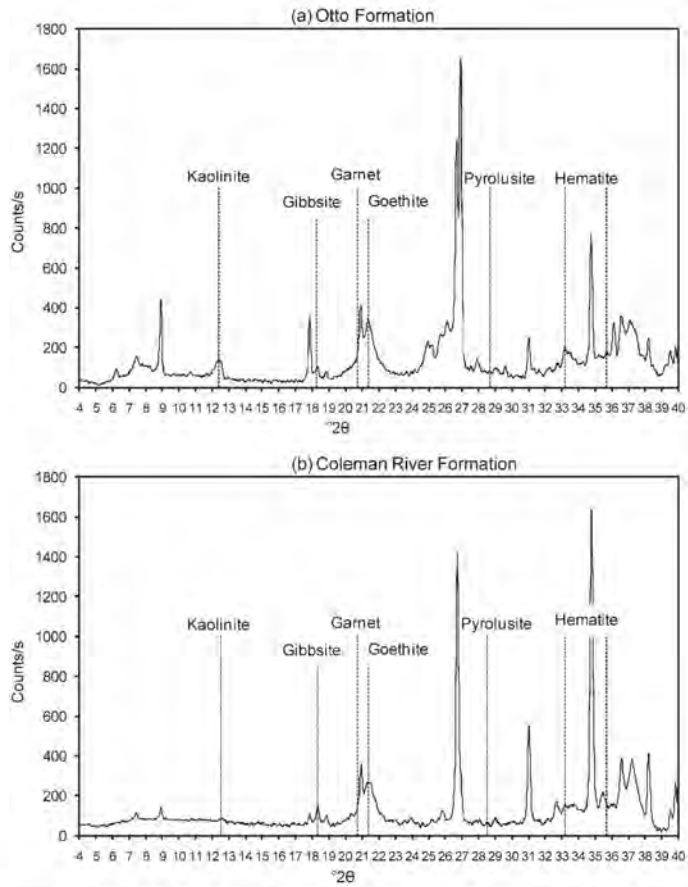


Figure 5. XRD patterns for hand-picked weathered garnet grains from Coweeta regolith. The unlabeled larger peaks include micas (10 Å) and their weathering products and quartz, all of which may be intergrown with garnet grains. Otto Formation samples W2-10, and Coleman River Formation sample W27-7.

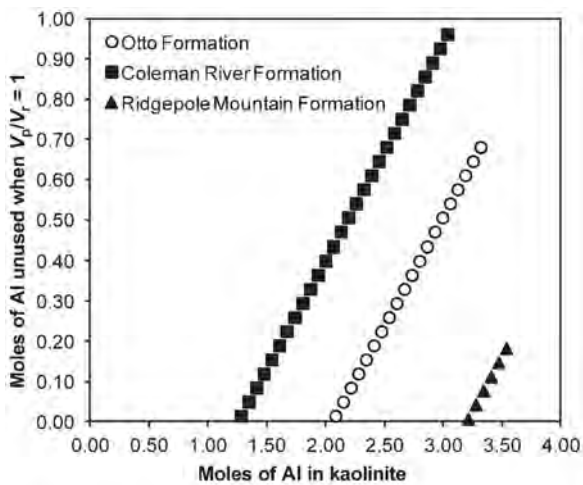


Figure 6. Relationship between Al stoichiometric coefficient of PSL kaolinite and the quantity of excess Al available for export from the almandine garnet-PSL microenvironment for almandine garnets at the Coweeta Hydrologic Laboratory (Table 7).

Energy-dispersive X-ray spectra for CHL almandine garnet from the Otto Formation (Figures 7 and 8) revealed that Si is present in all PSL EDS spectra, probably reflecting the presence of kaolinite identified by XRD (Figure 5). The relative abundance of Si varies depending on the sample and location of the analysis, but variation in brightness of the PSL in a backscattered-electron image indicated that the PSL was not mineralogically homogeneous (Figure 8).

The influence of pyrolusite (Figure 5) on the protectiveness of a surface layer was demonstrated for Coweeta garnets (Table 8). The presence of pyrolusite in the PSL reduces the percentage of Al needing to be hosted by kaolinite by up to 46% (for the Otto Formation; Table 8). Therefore, while pyrolusite in a surface layer may not greatly increase the likelihood of the layer being protective, the presence of pyrolusite does significantly decrease the quantity of kaolinite needed to make a surface layer protective.

*Micromorphology of garnets and their surface layers.* Garnet grains from CHL exhibited a variety of textures and shapes in thin section. Most garnet grains were

Table 7. Calculations of excess Al (a.p.f.u.) available for export for almandine garnet samples collected at Coweeta Hydrologic Laboratory.

| Otto Formation | | | Coleman River Formation | | | Ridgepole Mountain Formation | | |
|---|---|---|---|---|---|---|---|---|
| $Al_{Gbs}$ | $Al_{Kln}$ | Excess Al when $V_p/V_r = 1$ | $Al_{Gbs}$ | $Al_{Kln}$ | Excess Al when $V_p/V_r = 1$ | $Al_{Gbs}$ | $Al_{Kln}$ | Excess Al when $V_p/V_r = 1$ |
| 0.00 | 3.32 | 0.68 | 0.00 | 3.04 | 0.96 | 0.00 | 3.54 | 0.18 |
| 0.10 | 3.26 | 0.64 | 0.10 | 2.98 | 0.92 | 0.10 | 3.47 | 0.15 |
| 0.20 | 3.19 | 0.61 | 0.20 | 2.91 | 0.89 | 0.20 | 3.41 | 0.11 |
| 0.30 | 3.13 | 0.57 | 0.30 | 2.85 | 0.85 | 0.30 | 3.34 | 0.08 |
| 0.40 | 3.06 | 0.54 | 0.40 | 2.78 | 0.82 | 0.40 | 3.28 | 0.04 |
| 0.50 | 3.00 | 0.50 | 0.50 | 2.72 | 0.78 | 0.50 | 3.21 | 0.01 |
| 0.60 | 2.93 | 0.47 | 0.60 | 2.65 | 0.75 | 0.60 | 3.15 | −0.03 |
| 0.70 | 2.87 | 0.43 | 0.70 | 2.59 | 0.71 | | | |
| 0.80 | 2.80 | 0.40 | 0.80 | 2.52 | 0.68 | | | |
| 0.90 | 2.74 | 0.36 | 0.90 | 2.46 | 0.64 | | | |
| 1.00 | 2.67 | 0.33 | 1.00 | 2.39 | 0.61 | | | |
| 1.10 | 2.61 | 0.29 | 1.10 | 2.33 | 0.57 | | | |
| 1.20 | 2.54 | 0.26 | 1.20 | 2.26 | 0.54 | | | |
| 1.30 | 2.48 | 0.22 | 1.30 | 2.20 | 0.50 | | | |
| 1.40 | 2.41 | 0.19 | 1.40 | 2.13 | 0.47 | | | |
| 1.50 | 2.35 | 0.15 | 1.50 | 2.07 | 0.43 | | | |
| 1.60 | 2.28 | 0.12 | 1.60 | 2.00 | 0.40 | | | |
| 1.70 | 2.22 | 0.08 | 1.70 | 1.94 | 0.36 | | | |
| 1.80 | 2.15 | 0.05 | 1.80 | 1.87 | 0.33 | | | |
| 1.90 | 2.09 | 0.01 | 1.90 | 1.81 | 0.29 | | | |
| 2.00 | 2.02 | −0.02 | 2.00 | 1.74 | 0.26 | | | |
| | | | 2.10 | 1.68 | 0.22 | | | |
| | | | 2.20 | 1.61 | 0.19 | | | |
| | | | 2.30 | 1.55 | 0.15 | | | |
| | | | 2.40 | 1.48 | 0.12 | | | |
| | | | 2.50 | 1.42 | 0.08 | | | |
| | | | 2.60 | 1.35 | 0.05 | | | |
| | | | 2.70 | 1.29 | 0.01 | | | |
| | | | 2.80 | 1.22 | −0.02 | | | |

embayed or euhedral, and highly fractured. Large crystals were inclusion rich (poikiloblastic), containing (in order of decreasing abundance) quartz, magnetite, biotite, muscovite, chlorite, and epidote. Many internal fractures originated near inclusions (Embrechts and Stoops, 1982) and radial fractures (Wendt *et al.*, 1993) occurred near some quartz inclusions. Other fractures occurred across embayments in rocks with strong preferred orientation and compositional banding. The fractures were perpendicular to foliation and are parallel to each other.

Ferruginous surface layers formed on most weathered almandine garnet grains. Continuous surface layers were more prevalent on euhedral, inclusion-poor grains and on grains that were extremely weathered. Discontinuous surface layers were more prevalent on embayed, inclusion-rich grains and on grains which border iron-rich phyllosilicates (chlorite or biotite). In these instances, weathering products were "co-mingled" with those from the surrounding chlorite or biotite minerals. Orange, red, and yellow-brown ferruginous deposits formed surface layers and boxworks along internal

Table 8. Calculations illustrating the influence of pyrolusite on Al distribution in PSLs ($V_p/V_r = 1$) for almandine garnet samples collected at Coweeta Hydrologic Laboratory.

| Rock Unit | % Al in kaolinite for PSL of goethite + gibbsite + kaolinite | % Al in kaolinite for PSL of goethite + gibbsite + kaolinite + pyrolusite | % Difference |
|---|---|---|---|
| Otto Formation | 52 | 28 | 46 |
| Coleman River Formation | 32 | 21 | 34 |
| Ridgepole Mountain Formation | 86 | 63 | 27 |

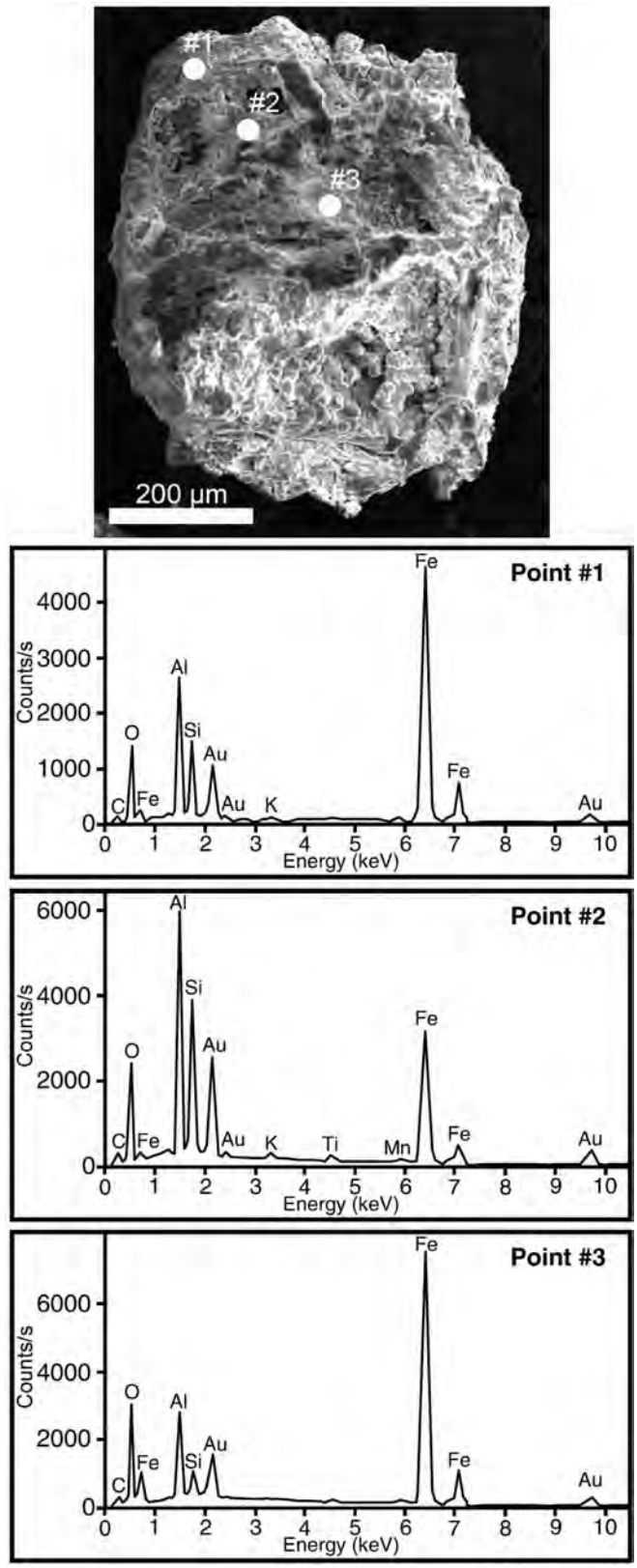


Figure 7. SEM-SEI image and EDS spectra of an Otto Formation garnet with surface layer hand picked from the regolith. Note the presence of Si in all spectra. Sample W34-6.

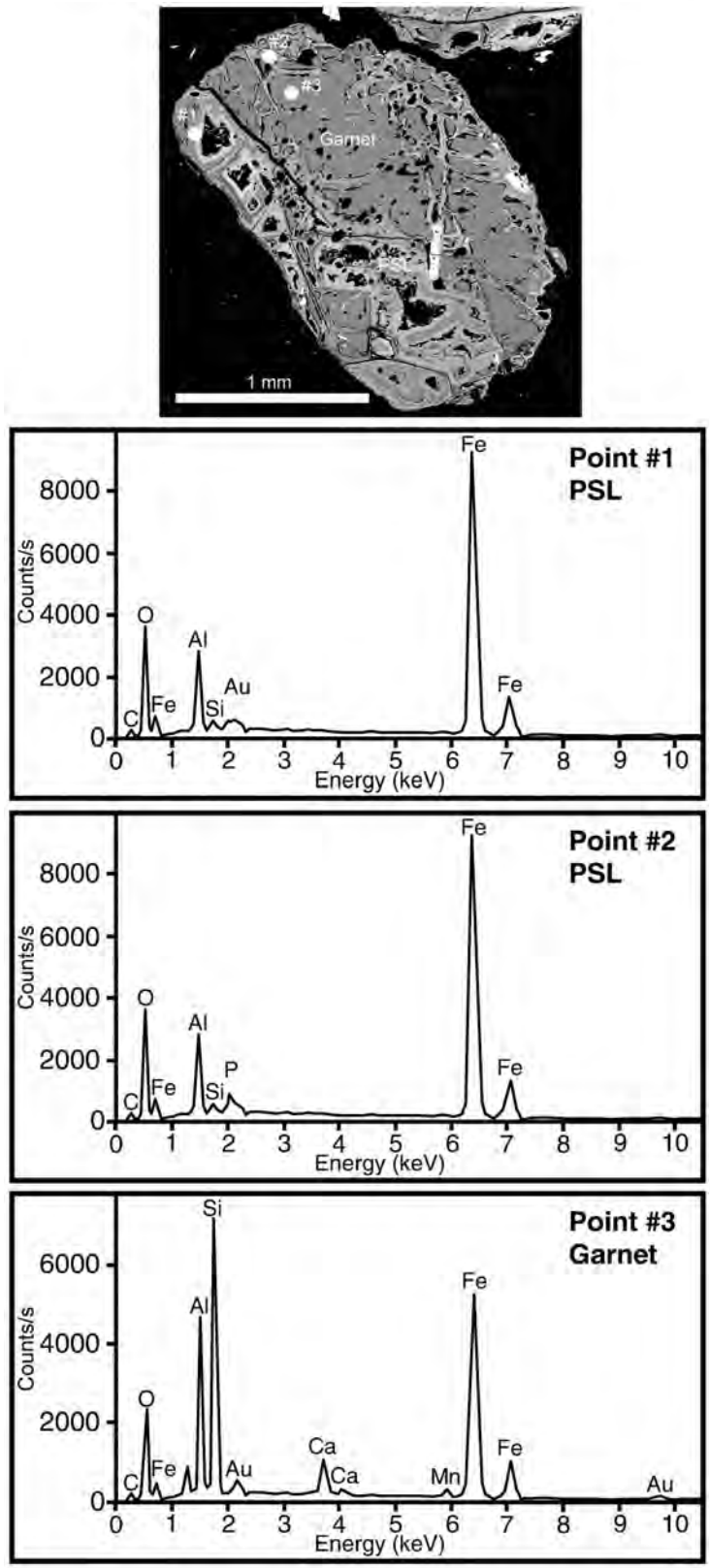


Figure 8. SEM-BEI image and EDS spectra of an Otto Formation garnet with surface layer. Points #1 and #2 are from the PSL and Point #3 is the unweathered garnet. Note the presence of Si in both PSL spectra. Sample W2-5.

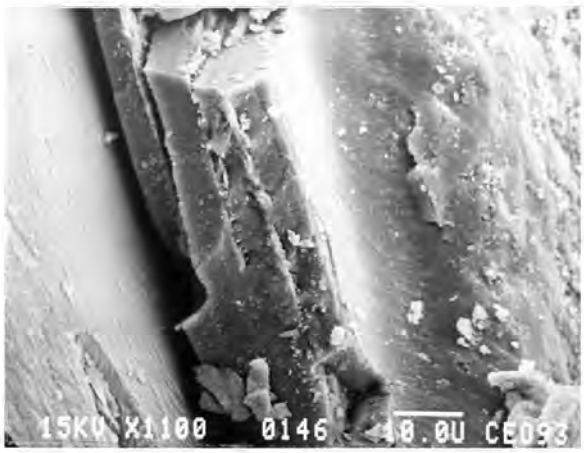


Figure 9. SEM-SEI image of 'onion skin-like' appearance of PSL on almandine garnet. Scale bar is 10 μm.

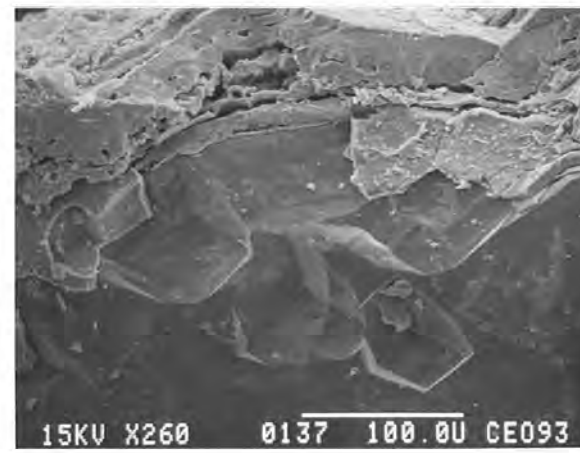


Figure 11. SEM-SEI image of dodecahedral etch pits on almandine garnet preserved in negative relief directly beneath a PSL. Scale bar is 100 μm.

fractures. In some thin sections, ferruginous deposits originating from a garnet occurred in rock fractures and stain surrounding unweathered minerals, suggesting that some garnet weathering products were being transported away from garnet grain boundaries.

Weathered almandine garnets from Coweeta exhibited both PSLs and USLs depending on sample locality and depth. Protective surface layers were the most common, exhibited minimal porosity, and were thickest in the saprolite and decreased in thickness higher in the soil profile. Protective surface layers were continuous over the entire grain surface and had no microporosity perpendicular to grain surfaces, no microporosity parallel to grain surfaces in outcrop samples, and minor (0.8–>5.0 mm in width) microporosity parallel to grain surfaces in profile samples. A PSL may become discontinuous and/or separated from the garnet's surface, probably due to dissolution and abrasion and have an 'onion skin-like' appearance in which successive layers are deposited in contact with previous layers (Figure 9).

Despite being protective as determined from $V_p/V_s$ ratios, some occurrences of surface layers were found covering euhedral (dodecahedral) etch pits on subjacent garnets. Some etch pits were directly observable (Figures 10 and 11), others were preserved as casts on the undersides of the product layers (Figure 12). Unprotective surface layers only occurred in the warmer, dryer Watershed 2 (Figure 1), were more porous, and may have contained relatively high concentrations of hematite (Figure 5). An USL was continuous over the entire grain surface and had microporosity perpendicular to grain surfaces (pores of 8.0–10.0 mm in diameter) and little or no microporosity parallel to the grain surface. Unprotective surface layers were thickest in the upper

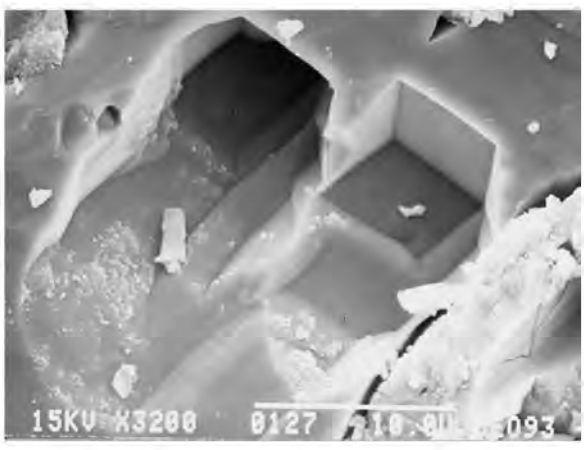


Figure 10. SEM-SEI image of dodecahedral etch pits on almandine garnet. Scale bar is 10 μm.

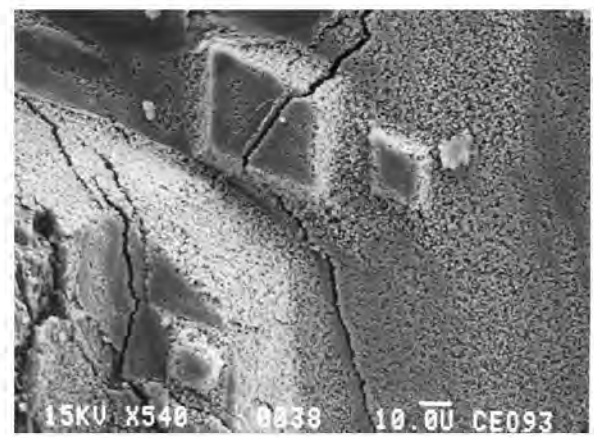


Figure 12. SEM-SEI image of casts of euhedral etch pits preserved in positive relief on the base of PSL separated from an almandine garnet–PSL interface by sample preparation. Scale bar is 10 μm.

horizons and decreased in thickness lower in the soil profile.

## DISCUSSION

### *Application of Pilling-Bedworth rule to natural almandine garnet compositions*

The results above indicate that very few natural almandine garnets have compositions sufficiently close to end-member almandine to allow the formation of PSL consisting of only goethite and gibbsite as suggested by Velbel (1984a, 1993). Based on the findings of the present study, in nearly all naturally occurring almandine garnets, some kaolinite likely must be present in a surface layer to make it protective. The addition of pyrolusite to the surface layer is capable of dramatically lowering the fraction of kaolinite required to make a PSL (Table 8). However, the addition of pyrolusite does not appear to be capable of completely eliminating the need for kaolinite within a PSL.

### *Micromorphology of CHL garnets and their surface layers*

Ferruginous weathering products on naturally weathered saprolite almandine garnets exhibiting rounded and featureless surfaces and having calculated $V_p/V_r \geqslant 1$ have been interpreted as being a PSL. In contrast, etch pits on naturally weathered soil almandines have been interpreted to indicate interface-limited reaction processes (Velbel, 1984a, 1993; Velbel *et al.*, 2007). Garnet etch pits (*e.g.* Figure 10) formed in the absence of PSLs occur in a variety of soil types, apparently where pedogenic complexing agents mobilize Al and/or Fe, and thereby prevent the formation of PSLs (Velbel, 1984a; Ghabru *et al.*, 1989; Velbel *et al.*, 2007). The occurrence of etch pits (Figure 11) and etch-pit casts (Figure 12) in association with surface layers reported here for the first time requires reexamination of the relationship between specific secondary minerals and the rate-determining processes associated with those minerals. Two possible explanations for the presence of PSL-associated etch pits and etch-pit casts are offered: (1) almandine garnet weathers first to a USL followed by mineralogical changes yielding a PSL (*e.g.* hematite hydrating to goethite; Schwertmann, 1971; Campbell and Schwertmann, 1984); or (2) almandine weathers to a surface layer in a mixed-kinetic regime. Each of these possible scenarios is explored below.

*Conversion of a USL to a PSL.* The presence of a PSL covering etch pits (Figures 11, 12) implies that the surface layer was not diffusion limiting at the time of etch-pit formation, but rather almandine garnet weathering was interface limited. These observations, combined with the Pilling-Bedworth calculations permit the hypothesis that secondary hematite formed at the onset of garnet weathering, forming a USL that allowed rapid solute transport. In the cooler, wetter localities found at the higher elevations of CHL, the early-formed hematite subsequently hydrated to form (tertiary) goethite in a PSL. In virtually all CHL sample sites, almandine garnet is weathering to predominantly goethite (*e.g.* Figure 5). Goethite has also been identified as a predominant weathering product of almandine garnet at other sites (Embrechts and Stoops, 1982; Parisot *et al.*, 1983; Velbel, 1984a; Graham *et al.* 1989a; Robertson and Butt, 1997). The molar volume per Fe is greater for goethite than for hematite (Table 1), and the hydration of Fe products caused a volume increase. This volume increase allowed the hydrated products to occupy formerly vacant space, reducing porosity and thereby filling etch pits and forming casts (Figure 12). The increase in product volume as the goethitic surface layer became protective caused by the hydration process would fill or cover pre-existing etch pits and would prevent additional etch pits from forming.

Based on the discussion above, drawing mechanistic inferences from product mineralogy alone (without information on textural relationships, *e.g.* centripetal replacement textures) is hazardous. For instance, hematite is believed to form from almandine garnet in at least some Southern Blue Ridge weathering profiles (Graham *et al.*, 1989a, 1989b, 1990a, 1990b), and has been identified in the Coweeta PSLs (Figure 5). If almandine garnet weathered directly to secondary hematite, Velbel's (1993) calculations and those as part of this study (Table 6) would suggest that the hematite-bearing product is far less likely to yield a PSL, especially in combination with gibbsite as the sole Al-bearing product. In the present study, etch-pit casts occur only with a PSL containing goethite as the dominant ferruginous product. While no direct evidence of a hematite precursor for these specific goethites was observed, such transformations between hydrous and anhydrous iron oxides are common in weathering environments (*e.g.* Schwertmann, 1971; Campbell and Schwertmann, 1984), and hematite has formed during the weathering history of CHL saprolites (*e.g.* Figure 5). Textural evidence such as etch-pit casts preserve remnant reactant garnet surface textures and suggest, in such instances, both the pathway of goethite formation and the change over time in the rate-determining role of the product. Thus, in the absence of information from replacement textures, the present mineralogy alone of a product assemblage with $V_p/V_r < 1$ is not a sufficient criterion for dismissing the protective surface layer hypothesis, or for confirming that the product itself was not rate determining.

Temporal changes in surface layer mineralogy and kinetic regime are not limited to the Fe-bearing phases hematite and goethite. The Pilling-Bedworth calculations indicate that a PSL is unlikely to form in the absence of kaolinite when gibbsite is the sole aluminous phase. Gibbsite has also been identified as a weathering

product of garnet by previous workers (Velbel, 1984a; Graham *et al.*, 1989a, 1989b, 1990b). However, to transition from interface-controlled to diffusion-controlled kinetics would require the silication of a 0:1 clay (*i.e.* gibbsite). Typically, with progressive weathering, kaolinite will desilicate to gibbsite. Following this premise, kaolinite would probably form at the beginning of garnet weathering, although some desilication could occur afterwards as long as adequate kaolinite remained to maintain the PSL. Excess Si associated with garnet weathering to a PSL (discussed in the next section) would be available for silication of gibbsite. However, conservation of Si in the almandine garnet-surface layer system would probably only occur with a PSL already present, *i.e.* when Si loss was inhibited by diffusion through the PSL. Based on this reasoning, a conversion from a USL to a PSL, and associated change from interface-controlled to transport-controlled kinetics, would be the more likely result of hematite hydrating to goethite with some kaolinite already present in the surface layer.

*Mixed-kinetic control.* Weathering regimes which form both etch pits and protective surface layers might be intermediate between transport- and interface-limited kinetic regimes (the mixed-kinetics regime of Berner, 1978, 1981). Where a PSL is slightly discontinuous (Figure 9), interface-limited weathering reactions operate and etch pits form (Figure 11).

Unprotective surface layers increase in thickness higher in the weathering profile. This observation indicates that garnets with USLs weather by centripetal replacement. Almandine garnet grains with USLs appear to have no dissolution features (*e.g.* etch pits) on their surfaces, although the etch pits may be covered by the oxides which form a USL. As reported by Velbel (1984a) and Embrechts and Stoops (1982), regardless of type of surface layer that may form by weathering in the saprolite prior to pedogenesis, almandine garnet weathering in soil horizons proceeds with the formation of a USL which is commonly removed completely with continued pedogenesis in soil horizons (Velbel, 1984a; Ghabru *et al.*, 1989; Velbel *et al.*, 2007).

The two aforementioned explanations of the occurrence of etch pits under a PSL offer plausible explanations for the previously unreported and unexpected weathering texture of etch pits covered by a subsequent layer of secondary (or tertiary) products (Figure 11). The almandine garnet grain was removed directly from rock outcrop. The almandine garnet surface layer is discontinuous and may be so because of mechanical separation from the surrounding matrix or because the surface layer is still forming. The surface layer did form well below the rooting zone and is not discontinuous due to biochemical dissolution. Also, because the almandine garnet was removed from outcrop, the etch pits were not covered by products as a result of direct introduction into the rooting zone followed by reburial. The most probable explanations are that the etch pits formed during preliminary dissolution of the almandine garnet surface and were later filled by the products of the replacement process, or formed while the almandine garnet surface was covered by a porous, hematitic surface layer and were later filled by goethite as the hematite hydrated. The morphological consequences of the last part of this proposed sequence of phenomena may be expressed and preserved at the inner margin of a PSL where it is in direct contact with, and forms a cast of, the etched almandine surface (Figure 12).

*Elemental imports and exports for the CHL almandine garnet-PSL system*

A surface layer composed of goethite, gibbsite, and kaolinite would probably be protective. Furthermore, an excess of Al is feasible and thus available for export. Velbel (1993) determined that up to 15% of the Al and Fe produced during almandine garnet weathering could be exported from the garnet-PSL microenvironment. For the almandine garnet compositions from Deer *et al.* (1997) used in the present study, up to 35% of the Al produced during almandine garnet weathering may be exported. Such a large value is only possible if all of the Fe is conserved and substantial quantities of kaolinite are present in the PSL. However, petrographic observations reveal that occasionally ferruginous material will extend from a garnet grain into fractures and around adjacent minerals. Migration of Fe from a garnet grain indicates that the assumption of conservation of all almandine garnet-derived Fe in the surface layer may not be valid for some grains. If the quantity of Fe available for surface layer is reduced, then the proportion of kaolinite in a PSL would have to increase relative to gibbsite. This relative increase in PSL kaolinite would also reduce the quantity of Al available for export from the almandine garnet-surface layer microenvironment.

Velbel *et al.* (2009) investigated the formation of USL on hornblende sampled from regolith of the southern Appalachian Blue Ridge of northeastern Georgia, USA. Using similar molar volume calculations as this study, these authors determined that Al must be imported into early-stage weathering products of the hornblende. During the early stages for weathering, considerable mobilization of Al occurred while Si was immobile, despite Al typically being considered minimally mobile during weathering. Velbel *et al.* (2009) suggested that Al is mobilized from shallow depths to greater depths in the weathering profile where incipient weathering is occurring. Further, Velbel *et al.* (2009) proposed that the source of the imported Al is from almandine garnet weathering known to occur in their rock unit of study, although no unweathered almandine garnet was observed in their specific sample. Velbel *et al.* (2009) showed how the proposed Al mobility is consistent with the results of Gardner (1992), White *et*

*al.* (1998), and Schroeder *et al.* (2000) based on bulk-sample-scale and profile-scale mineralogical data, solid-phase bulk-chemical analyses of saprolitic weathering profiles, and solute-phase chemical data from soil solutions, groundwater, and modern surface water associated with deeply weathered landscapes.

The possibility of import of element(s) into the almandine garnet-PSL system also warrants investigation. For Coweeta almandine garnets, the balanced weathering reactions for a PSL of goethite and kaolinite, thereby reflecting the maximum production of excess Al (Tables 3 and 7), are as follows:

*Otto Formation.*

$$Ca_{0.82}Mg_{0.72}Mn_{1.0}Fe_{3.52}Al_4Si_6O_{24} + 7.88\ H_2O + 5.12\ H^+ + 1.41\ O_2 \rightarrow 3.52\ FeOOH + 1.66\ Al_2Si_2O_5(OH)_4 + 2.68\ H_4SiO_4 + 1.0\ MnO_2 + 0.82\ Ca^{2+} + 0.72\ Mg^{2+} + 0.68\ Al^{3+} \quad (7)$$

*Coleman River Formation.*

$$Ca_{0.60}Mg_{0.88}Mn_{0.44}Fe_{4.26}Al_4Si_6O_{24} + 8.17\ H_2O + 5.84\ H^+ + 1.38\ O_2 \rightarrow 4.26\ FeOOH + 1.52\ Al_2Si_2O_5(OH)_4 + 2.96\ H_4SiO_4 + 0.44\ MnO_2 + 0.60\ Ca^{2+} + 0.88\ Mg^{2+} + 0.96\ Al^{3+} \quad (8)$$

*Ridgepole Mountain Formation.*

$$Ca_{1.74}Mg_{0.74}Mn_{0.90}Fe_{2.82}Al_{3.72}Si_6O_{24} + 7.12\ H_2O + 5.50\ H^+ + 1.05\ O_2 \rightarrow 2.82\ FeOOH + 1.77\ Al_2Si_2O_5(OH)_4 + 2.46\ H_4SiO_4 + 0.90\ MnO_2 + 1.74\ Ca^{2+} + 0.74\ Mg^{2+} + 0.18\ Al^{3+} \quad (9)$$

These balanced reactions for the formation of a goethite and kaolinite PSL demonstrate that no other major elements need be imported into the PSL-garnet system at Coweeta. However, significantly more Si than Al is released, providing the elements needed to form kaolinite. For the Al to be exported rather than consumed as either kaolinite and/or gibbsite precipitate, the pore solutions must be undersaturated with respect to these phases.

*Evaluation of the hypothesis and unresolved issues*

The hypothesis for this study was that the role of the kinetics of almandine garnet's weathering products varies with the composition of the specific almandine experiencing weathering. The results of the Pilling-Bedworth calculations and microtextural observations of naturally weathered garnet surfaces from all levels in the CHL weathering profile are consistent with this hypothesis.

The findings of this study yield numerous additional unresolved issues regarding the formation of surface layers on garnets during chemical weathering. The temporal changes in surface-layer mineralogy that may result in etch pits occurring beneath PSLs requires additional investigation. This includes the hypothesized conversion of early-formed hematite to goethite, and the potential role of Si in conversions between gibbsite and kaolinite. Such mineralogical changes should be related directly to the surface microtextures of the dissolving garnet and Pilling-Bedworth calculations. The generation and mobility of Al during incipient garnet weathering, and the potential uptake of that Al by the weathering products of other primary minerals, also warrant further investigation. All of the methods and unresolved questions outlined in this study for almandine garnets may also be applied to garnets representing a wider range of compositions (*e.g.* other garnet solid-solution series) and environmental settings.

## SUMMARY AND CONCLUSIONS

The mineralogy of surface layers exerts a major influence on the chemical weathering kinetics of almandine garnet; different product minerals occupy different proportions of the replacement volume and thereby influence the solute-transport properties of the product. During chemical weathering, almandine garnet grains can develop either protective or unprotective surface layers depending on the almandine garnet's Al and Fe stoichiometric coefficients, molar mass, specific gravity, mineralogy of secondary products, and environmental conditions. The results of this study are consistent with the hypothesis that the role of the kinetics of almandine garnet's weathering products varies with the composition of the specific almandine garnet experiencing weathering. Most natural almandine garnets lack adequate Fe and Al to form PSLs composed only of goethite and gibbsite. Having kaolinite in a surface layer dramatically increases the probability of a surface layer being protective. At CHL for almandine garnets from the three units studied, in order to form a PSL, kaolinite must be a weathering product. The lack of kaolinite being reported in the literature may be due to inadequacy of XRD. Energy-dispersive X-ray spectra and XRD analyses as part of this study support the presence of kaolinite in Coweeta almandine garnet PSLs. The greatest likelihood that a surface layer will be protective is when it contains goethite, kaolinite, and pyrolusite. With adequate Mn in the parent garnet and if pyrolusite precipitates in the PSL, the $V_p/V_r$ value will increase. However, pyrolusite in a surface layer may not increase greatly the likelihood of the layer being protective; the presence of pyrolusite does significantly decrease the quantity of kaolinite needed to make a surface layer protective.

Based on an almandine garnet anion basis of $O_{24}$, to form a PSL composed of hematite and kaolinite, an almandine garnet must have a minimum Al stoichiometric coefficient of ~3.78 a.p.f.u. and a minimum Fe stoichiometric coefficient of ~2.8 a.p.f.u. To form a PSL of goethite and kaolinite, an almandine garnet must have a minimum Al stoichiometric coefficient of

~3.75 a.p.f.u. and a minimum Fe stoichiometric coefficient of ~2.7 a.p.f.u. A relatively large parent garnet Fe stoichiometric coefficient is more important in PSL formation and determination of excess Al than is the parent almandine garnet Al stoichiometric coefficient.

Almandine garnet and ferruginous product(s) in thin section form three distinct textures: (1) grains in which ferruginous product is in contact with the garnet remnant; (2) grains in which ferruginous product is not in contact with the almandine garnet remnant (formation of a peripheral void around remnant); and (3) grains in which ferruginous product has formed a porous pseudomorph after garnet. Almandine garnet grains in environments dominated by biochemical processes and advective flow undergo interface-limited reactions. Almandine garnet grains in environments not dominated by these processes experience supersaturation with respect to iron and aluminum products near the grain surface. When the requirements for nucleation are met, the products reprecipitate to form a PSL.

Etch pits occur on almandine garnet grains beneath some PSLs. This association of etch pits (which indicate interface-limited kinetics) and PSLs (which should inhibit transport of mobile species to and/or from the almandine's surface, result in reaction kinetics limited by transport through the product, and thereby prevent the formation of etch pits) is unexpected based on the original formulation of the hypothesis. The Pilling-Bedworth calculations of this study suggest a modification of the hypothesis. Several combinations of changes of secondary minerals into tertiary minerals could result in the newly reported association between etch pits (formed in the kinetic regime influenced by the secondary minerals) and PSLs (consisting of tertiary minerals modified from the secondary minerals after the etch pits formed). Early-formed (secondary) product minerals formed USLs and allowed interface-limited attack upon, and etching of, the underlying almandine garnet's surface. This was followed by modification of the secondary product minerals to tertiary product minerals with increased volume that rendered the surface layers protective of the underlying surface after the etch pits had formed.

Several secondary-tertiary product-mineral paragenetic sequences are consistent with this time-variant extension of the original hypothesis. Filled etch pits under PSLs may be the result of hematitic surface layers hydrating to goethitic surface layers or the result of dissolution-reprecipiation processes. The initial formation of hematite in an USL, followed by hydration of hematite to form goethite, reduces porosity. Consequently, the product's transport properties are reduced such that the previously USL of product becomes a PSL only after the etch pits had formed. Similarly, the silication of gibbsite to kaolinite after initial formation of an USL in which Al was hosted by gibbsite would increase product volume, reduce porosity, and change the rate-determining process only after the etch pits had formed. Alternatively, almandine garnet dissolution processes which form PSLs and etch pits may be intermediate between transport- and interface-limited kinetic regimes (Berner, 1978; 1981). Discontinuous surface layers permit the formation of etch pits.

With a PSL of goethite, gibbsite, and kaolinite, excess Al may reasonably be assumed to be available for export. A reduction in the quantity of kaolinite in a PSL resulting from the presence of pyrolusite increases the quantity of Al available for export from the garnet-PSL system. For CHL garnets with PSL and excess Al, no other element need be imported into the garnet-PSL system to produce the observed weathering-product mineral assemblages.

## ACKNOWLEDGMENTS

The authors thank S. Anderson, R. Schaetzl, D. Schulze, E. Danielewicz, S. Flegler, D. Mokma, C. Basso, W. Swank, and the staff at the Coweeta Hydrologic Laboratory. Appreciation is also expressed to S. Sylvester at Franklin & Marshall College for assistance with XRD. The present study was funded in part by a grant from The Clay Minerals Society to D. Bryan. Thanks, too, to Editor-in-Chief J.W. Stucki and Associate Editor W.D. Huff for editorial handling, as well as two anonymous reviewers whose constructive reviews greatly strengthened this manuscript.

## REFERENCES

Berner, R. (1978) Rate control of mineral dissolution under earth surface conditions. *American Journal of Science*, **278**, 1235–1252.

Berner, R. (1981) Kinetics of weathering and diagenesis. Pp. 111–134 in: *Kinetics of geochemical processes* (A. Lasaga and R. Kirkpatrick, editors). Reviews in Mineralogy, **8**. Mineralogical Society of America, Washington, D.C.

Berner, R.A. and Holdren, G.R. (1977) Mechanism of feldspar weathering: Some observational evidence. *Geology*, **5**, 369–372.

Berner, R.A. and Holdren, G.R. (1979) Mechanism of feldspar weathering II: Observations of feldspar from soils. *Geochimica et Cosmochimica Acta*, **43**, 1173–7786.

Berner, R. and Schott, J. (1982) Mechanism of pyroxene and amphibole weathering II. Observations of soil grains. *American Journal of Science*, **282**, 1214–1231.

Berner, R., Sjoberg, E., Velbel, M., and Krom, M. (1980) Dissolution of pyroxenes and amphiboles during weathering. *Science*, **207**, 1205–1206.

Berry, J.L. (1976) Study of chemical weathering in the Coweeta Hydrologic Laboratory, Macon County, North Carolina, 62 pp. Unpublished report.

Blum, A.E. and Lasaga, A.C. (1987) Monte Carlo simulations of surface reaction rate laws. Pp. 255–292 in: *Aquatic Surface Chemistry* (W. Stumm, editor). John Wiley & Sons, New York.

Blum, A.E. and Stillings, L.L. (1995) Feldspar dissolution kinetics. Pp. 291–342 in: *Chemical Weathering Rates of Silicate Minerals* (A.F. White and S.L. Brantley, editors). Reviews in Mineralogy **31**, Mineralogical Society of America, Washington, D.C.

Brantley, S.L. (2005) Reaction kinetics of primary rock-forming minerals under ambient conditions. Pp. 73–117

in: *Surface and Ground Water, Weathering, and Soils* (J.I. Drever, editor), Treatise on Geochemistry **5**, Elsevier-Pergamon, Oxford, UK.

Brantley, S.L. (2008) Kinetics of mineral dissolution. Pp. 151–210 in: *Kinetics of Water–Rock Interaction* (S.L. Brantley, J.D. Kubicki, and A.F. White, editors). Springer, New York.

Brantley, S.L. and Chen, Y. (1995) Chemical weathering rates of pyroxenes and amphiboles. Pp. 119–172 in: *Chemical Weathering Rates of Silicate Minerals* (A.F. White and S.L. Brantley, editors). Reviews in Mineralogy, **31**, Mineralogical Society of America, Washington, D.C.

Brantley, S.L., Crane, S.R., Crerar, D.A., Hellmann, R., and Stallard, R. (1986) Dissolution at dislocation etch pits in quartz. *Geochimica et Cosmochimica Acta*, **50**, 2349–2361.

Browning, S. and Thomas, D. (1985) Soil map of Coweeta Hydrologic Laboratory. U.S. Department of Agriculture, Forest Service, Southeastern Forest Experiment Station.

Bryan, D.S. (1994) Factors controlling the occurrence and distribution of hematite and goethite in soils and saprolites derived from schists and gneisses in western North Carolina. M.S. thesis, Michigan State University, East Lansing, Michigan, USA, 125 pp.

Campbell, A. and Schwertmann, U. (1984) Iron oxide mineralogy of placic horizons. *Journal of Soil Science*, **35**, 569–582.

Ciampone, M.A. (1995) Non-systematic weathering profile on metamorphic rock in the southern Blue Ridge Mountains, North Carolina: Petrography, bulk chemistry, and mineral chemistry of biotite. M.S. thesis, University of Cincinnati, Cincinnati, Ohio, USA, 86 pp.

Deer, W.A., Howie, R.A., and Zussman, J. (1997) *Rock-Forming Minerals – Orthosilicates*, **1A**, second edition. The Geological Society, London.

Drever, J.I. (1973) The preparation of oriented clay mineral specimens for X-ray diffraction analysis by a filter-membrane peel technique. *American Mineralogist*, **58**, 553–554.

Embrechts, J. and Stoops, G. (1982) Microscopical aspects of garnet weathering in a humid tropical environment. *Journal of Soil Science*, **33**, 535–545.

Fromhold, A.T., Jr. (1976) *Theory of Metal Oxidation. I. Fundamentals*. Defects in Crystalline Solids Series, **9**. North-Holland, Amsterdam.

Gardner, L.R. (1992) Long-term isovolumetric leaching of aluminum from rocks during weathering: Implications for the genesis of saprolite. *Catena*, **19**, 521–537.

Ghabru, S., Mermut, A., and St. Arnaud, R. (1989) Characterization of garnets in a typic Cryoboralf (Gray luvisol) from Saskatchewan, Canada. *Soil Science of America Journal*, **53**, 575–582.

Graham, R., Weed, S., Bowen, L., and Buol, S. (1989a) Weathering of iron-bearing minerals in soils and saprolite on the North Carolina Blue Ridge Front: I. Sand-size primary minerals. *Clays and Clay Minerals*, **37**, 19–28.

Graham, R., Weed, S., Bowen, L., and Buol, S. (1989b) Weathering of iron-bearing minerals in soils and saprolite of the North Carolina Blue Ridge Front: II. Clay Mineralogy. *Clays and Clay Minerals*, **37**, 29–40.

Graham, R., Daniels, R., and Buol, S. (1990a) Soil geomorphic relations on the Blue Ridge Front: I. Regolith types and slope processes. *Soil Science Society of America Journal*, **54**, 1362–1367.

Graham, R., Daniels, R., and Buol, S. (1990b) Soil geomorphic relations on the Blue Ridge Front: II. Soil Characteristics and Pedogenesis. *Soils Science Society of America Journal*, **54**, 1367–1377.

Hansley, P.L. (1987) Petrologic and experimental evidence for the etching of garnets by organic acids in the Upper Jurassic Morrison Formation, northwestern New Mexico. *Journal of Sedimentary Petrology*, **57**, 666–681.

Hatcher, R.D. (1980) Geologic map of Coweeta Hydrologic Laboratory, Prentiss Quadrangle, North Carolina: State of North Carolina, Department of Natural Resources and Community Development, in Cooperation with the Tennessee Valley Authority, scale 1:14,400, 1 sheet.

Hatcher, R.D. (1988) Bedrock geology and regional geologic setting of Coweeta Hydrologic Laboratory in the Eastern Blue Ridge. Pp. 81–92 in: *Forest Hydrology and Ecology at Coweeta* (W.T. Swank and D.A. Crossley, Jr., editors). Springer-Verlag, New York.

Hauffe, K. (1965) *Oxidation of Metals*. Plenum, New York.

Kretz, R. (1983) Symbols for rock-forming minerals. *American Mineralogist*, **68**, 277–279.

Klein, C. and Hurlbut, C.S. (1999) *Manual of Mineralogy*. John Wiley & Sons, Inc., New York.

Kubaschewski, O. and Hopkins, B.E. (1962) *Oxidation of Metals and Alloys* (2nd edition). Butterworths, London.

Lasaga, A. and Blum, A. (1986) Surface chemistry, etch pits and mineral water reactions. *Geochimica et Cosmochimica Acta*, **50**, 2363–2379.

Lüttge, A. and Arvidson, R.S. (2008) The mineral–water interface. Pp. 73–107 in: *Kinetics of Water–Rock Interaction* (S.L. Brantley, J.D. Kubicki, and A.F. White, editors). Springer, New York.

Miller, C.F., Hatcher, R.D., Jr., Ayers, J.C., Coath, C.D., and Harrison, T.M. (2000) Age and zircon inheritance of eastern Blue Ridge plutons, southwestern North Carolina and northeastern Georgia, with implications for magma history and evolution of the southern Appalachian orogen. *American Journal of Science*, **300**, 142–172.

Moore, D.M. and Reynolds, Jr., R.C. (1997) *X-ray Diffraction and the Identification and Analysis of Clay Minerals*. Oxford University Press, New York.

Parisot, J.C., Delvigne, J., and Groke, M.T.C. (1983) Petrographical aspects of the supergene weathering of garnet in the Serra dos Carajas (Para, Brazil). P. 47 in: *International Colloquium CNRS on the Petrology of Weathering and Soils, Abstracts* (D. Nahon and Y. Noack, editors). Centre National de la Recherche Scientifique, Paris.

Price, J.R. (2003) Allanite weathering and rare earth elements in mass balance calculations of clay genesis rates at the Coweeta Hydrologic Laboratory, western North Carolina, USA: The response times of changes in clay mineral assemblages to fluctuations in climate. Ph.D. thesis, Michigan State University, East Lansing , Michigan, USA, 237 pp.

Price, J.R., Velbel, M.A., and Patino, L.C. (2005) Rates and timescales of clay-mineral formation in the southern Appalachian Mountains from geochemical mass balance, *Geological Society of America Bulletin*, 117, 783–794.

Robertson, I.D.M. and Butt, C.R.M. (1997) *Atlas of Weathered Rocks*. CRC LEME Open File Report **390**, 1st Revision. Cooperative Research Centre for Landscape Evolution and Mineral Exploration, Wembley, Western Australia.

Salvino, J.F. and Velbel, M.A. (1989) Faceted garnets from sandstones of the Munising Formation (Cambrian), northern Michigan: petrographic evidence for origin by intrastratal dissolution. *Sedimentology*, **36**, 371–379.

Schott, J. and Petit, J.-C. (1987) New evidence for the mechanisms of dissolution of silicate minerals. Pp. 255–292 in: *Aquatic Surface Chemistry* (W. Stumm, editor). John Wiley & Sons, New York.

Schroeder, P.A., Melear, N.D., West, L.T., and Hamilton, D.A. (2000) Meta-gabbro weathering in the Georgia Piedmont, USA: implications for global silicate weathering rates. *Chemical Geology*, **163**, 235–245.

Schwertmann, U. (1971) Transformations of hematite to goethite in soils. *Nature*, **232**, 624–625.

Smyth, J.R. and Bish, D.L. (1988) *Crystal Structures and Cation Sites of the Rock-Forming Minerals*. Allen & Unwin, Boston, Massachusetts, USA.

Swank, W. and Crossley, I. (1988) Introduction and site description. Pp. 3–15 in: *Forest Hydrology and Ecology at Coweeta* (W.T. Swank and D.A. Crossley, Jr., editors). Springer-Verlag, New York.

Velbel, M. (1984a) Natural weathering mechanisms of almandine garnet. *Geology*, **12**, 631–634.

Velbel, M. (1984b) Mineral transformations during rock weathering, and geochemical mass-balances in forested watersheds of the Southern Appalachians. Ph.D. thesis, Yale University, New Haven, Connecticut, USA, 175 pp.

Velbel, M. (1985) Geochemical mass balances and weathering rates in forested watersheds of the southern Blue Ridge. *American Journal of Science*, **285**, 904–930.

Velbel, M.A. (1988) Weathering and soil-forming processes. Pp. 93–102 in: *Forest Hydrology and Ecology at Coweeta* (W.T. Swank and D.A. Crossley, Jr., editors). Springer-Verlag, New York.

Velbel, M.A. (1989) Weathering of hornblende to ferruginous products by a dissolution-reprecipitation mechanism: petrography and stoichiometry. *Clays and Clay Minerals*, **37**, 515–524.

Velbel, M.A. (1990) Mechanisms of saprolitization, isovolumetric weathering, and pseudomorphous replacement during rock weathering – a review. *Chemical Geology*, **84**, 17–18.

Velbel, M.A. (1993) Formation of protective surface layers during silicate-mineral weathering under well-leached, oxidizing conditions. *American Mineralogist*, **78**, 408–417.

Velbel, M.A. (2004) Laboratory and homework exercises in the geochemical kinetics of mineral–water reaction: rate law, Arrhenius activation energy, and the rate-determining step in the dissolution of halite. *Journal of Geoscience Education*, **52**, 52–59.

Velbel, M.A. (2007) Surface textures and dissolution processes of heavy minerals in the sedimentary cycle: examples from pyroxenes and amphiboles. Pp. 113–150 in: *Heavy Minerals in Use* (M.A. Mange and D.T. Wright, editors). Developments in Sedimentology, **58**, Elsevier, New York.

Velbel, M.A. and Barker, W.W. (2008) Pyroxene weathering to smectite: Conventional and low-voltage cryo-field emission scanning electron microscopy, Koua Bocca ultramafic complex, Ivory Coast. *Clays and Clay Minerals*, **56**, 111–126.

Velbel, M.A., McGuire, J.T., and Madden, A.S. (2007) Scanning electron microscopy of garnet from southern Michigan soils: Etching rates and inheritance of pre-glacial and pre-pedogenic grain-surface textures. Pp. 413–432 in: *Heavy Minerals in Use* (M.A. Mange and D.T. Wright, editors). Developments in Sedimentology, **58**, Elsevier, New York.

Velbel, M.A., Donatelle, A.R., and Formolo, M.J. (2009) Reactant-product textures, volume relations, and implication for major-element mobility during natural weathering of hornblende, Tallulah Falls Formation, Georgia Blue Ridge, U.S.A. *American Journal of Science*, **309**, 661–688.

Wendt, A., D'Arco, P., Goffé, B., and Oberhänsli, R. (1993) Radial cracks around α-quartz inclusions in almandine: Constraints on the metamorphic history of the Oman Mountains. *Earth and Planetary Science Letters*, **114**, 449–461.

White, A.F., Blum, A.E., Schulz, M.S., Vivit, D.V., Stonestrom, D.A., Larsen, M., Murphy, S.F., and Eberl, D. (1998) Chemical weathering in a tropical watershed, Luquillo Mountains, Puerto Rico: I. Long-term versus short-term weathering fluxes. *Geochimica et Cosmochimica Acta*, **62**, 209–226.

Wilson, M.J. (1975) Chemical weathering of some primary rock-forming minerals. *Soil Science*, **119**, 349–355.

Yeakley, J.A., Swank, W.T., Swift, L.W., Hornberger, G.M., and Shugart, H.H. (1998) Soil moisture gradients and controls on a southern Appalachian hillslope from drought through recharge. *Hydrology and Earth System Sciences*, **2**, 41–49.

*(Received 27 August 2012; revised 18 February 2013; Ms. 706; AE: W.D. Huff)*

*Clays and Clay Minerals*, Vol. 61, No. 1, 57–74, 2013.

# SPECTRAL AND HYDRATION PROPERTIES OF ALLOPHANE AND IMOGOLITE

JANICE L. BISHOP[1,*], ELIZABETH B. RAMPE[2], DAVID L. BISH[3], ZAENAL ABIDIN[4,5], LESLIE L. BAKER[6], NAOTO MATSUE[4], AND TERUO HENMI[4]

[1] Carl Sagan Center, SETI Institute and NASA-ARC, 189 Bernardo Avenue, Mountain View, CA 94043, USA
[2] NASA-JSC, Mail Code KA, Houston, TX 77058, USA
[3] Department of Geological Sciences, Indiana University, 1001 E. 10th St., Bloomington, IN 47405, USA
[4] Faculty of Agriculture, Ehime University, Tarumi 3-5-7, Matsuyama 790-8566, Japan
[5] Inorganic Chemistry Laboratory, Department of Chemistry, Faculty of Mathematics and Natural Science, Bogor Agricultural University, Jl. Agatis Kampus IPB Darmaga, Bogor, West of Java, 16680, Indonesia
[6] Department of Plant, Soil and Entomological Sciences, University of Idaho, 875 Perimeter Drive MS 2339, Moscow, ID 83844, USA

**Abstract**—Allophane and imogolite are common alteration products of volcanic materials. Natural and synthetic allophanes and imogolites were characterized in the present study in order to clarify the short-range order of these materials and to gain an understanding of their spectral properties. Spectral analyses included visible/near-infrared (VNIR), and infrared (IR) reflectance of particulate samples and thermal-infrared (TIR) emissivity spectra of particulate and pressed pellets. Spectral features were similar but not identical for allophane and imogolite. In the near-infrared (NIR) region, allophane spectra exhibited a doublet near 7265 and 7120 $cm^{-1}$ (1.38 and 1.40 μm) due to $OH_{2\nu}$, a broad band near 5220 $cm^{-1}$ (1.92 μm) due to $H_2O_{\nu+\delta}$, and a band near 4560 $cm^{-1}$ (2.19 μm) due to $OH_{\nu+\delta}$. Reflectance spectra of imogolite in this region included a doublet near 7295 and 7190 $cm^{-1}$ (1.37 and 1.39 μm) due to $OH_{2\nu}$, a broad band near 5200 $cm^{-1}$ (1.92 μm) due to $H_2O_{\nu+\delta}$, and a band near 4565 $cm^{-1}$ (2.19 μm) due to $OH_{\nu+\delta}$. A strong broad band was also observed near 3200–3700 $cm^{-1}$ (~2.8–3.1 μm) which is a composite of $OH_\nu$, $H_2O_\nu$, and $H_2O_{2\delta}$ vibrations. Visible/near-infrared spectra were also collected under two relative humidity (RH) conditions. High-RH conditions resulted in increasing band strength for the $H_2O$ combination modes near 6900–6930 $cm^{-1}$ (1.45 μm) and 5170–5180 $cm^{-1}$ (1.93 μm) in the allophane and imogolite spectra due to increased abundances of adsorbed $H_2O$ molecules. Variation in adsorbed $H_2O$ content caused an apparent shift in the bands near 1.4 and 1.9 μm. A doublet $H_2O_\delta$ vibration was observed at 1600–1670 $cm^{-1}$ (~6.0–6.2 μm) and a band due to OH bending for $O_3SiOH$ was observed at ~1350–1485 $cm^{-1}$ (~6.7–7.4 μm). The Si–O–Al stretching vibrations occurred near 1030 and 940 $cm^{-1}$ (~9.7 and 10.6 μm) for allophane and near 1010 and 930 $cm^{-1}$ (~9.9 and 10.7 μm) for imogolite. OH out-of-plane bending modes occurred near 610 $cm^{-1}$ (16.4 μm) for allophane and at 595 $cm^{-1}$ (16.8 μm) for imogolite. Features due to Si–O–Al bending vibrations were observed at 545, 420, and 335 $cm^{-1}$ (~18, 24, and 30 μm) for allophane and at 495, 415, and 335 $cm^{-1}$ (~20, 24, and 30 μm) for imogolite. The emissivity spectra were obtained from pressed pellets of the samples, which greatly enhanced the spectral contrast of the TIR absorptions. Predicted NIR bands were calculated from the mid-IR fundamental stretching and bending vibrations and compared with the measured NIR values. Controlled-RH X-ray diffraction (XRD) experiments were also performed in order to investigate changes in the mineral structure with changing RH conditions. Both allophane and imogolite exhibited decreasing low-angle XRD intensity with increasing RH, which was probably a result of interactions between $H_2O$ molecules and the curved allophane and imogolite structures.

**Key Words**—Allophane, Emission Spectroscopy, Imogolite, Reflectance Spectroscopy, XRD.

## INTRODUCTION

Allophane and imogolite frequently occur together as clay-sized soil components derived from volcanic ash and pumice or as alteration products of basaltic saprolite (*e.g.* Henmi and Wada, 1976; Wada, 1987; Parfitt, 2009). These two aluminosilicates form under related geochemical conditions, but they have different structures. They are listed as minerals by the International Mineralogical Association (http://www.ima-mineralogy.org/), but are considered non-mineral phases by The Clay Minerals Society (http://www.clays.org/GLOSSARY/GlossIntro.html) due to their lack of sufficiently well defined structures. The ideal chemical formula for imogolite is $(OH)_3{\cdot}Al_2O_3{\cdot}SiOH$ (Parfitt, 2009). The chemical formula of allophane is variable and has been given as $1.0–2.0SiO_2{\cdot}Al_2O_3{\cdot}2.5–3.0H_2O$ (Wada, 1987). Both minerals readily adsorb $H_2O$ and hold significantly more $H_2O$ per formula unit under moist conditions than under dry conditions. Previous studies have examined in detail the mineral structure, chemistry, and infrared transmission spectra (*e.g.* Henmi and Wada, 1976; Farmer *et al.*, 1977; Parfitt *et al.*, 1980).

* E-mail address of corresponding author:
jbishop@seti.org
DOI: 10.1346/CCMN.2013.0610105

The present study builds on this previous work to measure and analyze the spectral properties of allophane and imogolite by using reflectance spectra in the VNIR and mid-IR regions and emissivity spectra in the TIR region. These reflectance and emissivity spectra are necessary for remote mineral identification, and this study will enable inclusion of allophane and imogolite in spectral libraries. This will further allow for their consideration in remote sensing investigations on Earth and other planets. Both natural samples from Japan (Figure 1) and synthetic samples are characterized in the present study. In order to examine the effects of humidity and changing hydration state of the samples on the spectral features, XRD data have been acquired over a range of relative humidity (RH) conditions and VNIR reflectance spectra were obtained under two RH conditions. The influence of hydration level on the IR and XRD signatures are especially important for remote sensing studies of allophane and imogolite on Earth and the identification of these components on Mars and other planetary bodies that have a much drier environment.

## BACKGROUND

Allophane and imogolite form primarily through alteration of volcanic ash and most commonly occur where ash is an important soil component (*e.g.* Fieldes, 1955; Yoshinaga and Aomine, 1962; Wada, 1967; Wada *et al.*, 1972; Henmi and Wada, 1976; Nagasawa, 1978; Theng *et al.*, 1982; Parfitt, 2009). X-ray diffraction (*e.g.* van der Gaast *et al.*, 1985; Parfitt, 1990), IR spectroscopy (Russell *et al.*, 1969; Cradwick *et al.*, 1972; Henmi and Wada, 1976; Farmer *et al.*, 1979; Parfitt *et al.*, 1980), electron microscopy (Henmi and Wada, 1976), NMR (Shimizu *et al.*, 1988), and chemical (Henmi and Wada, 1976) and thermal (Henmi, 1980;

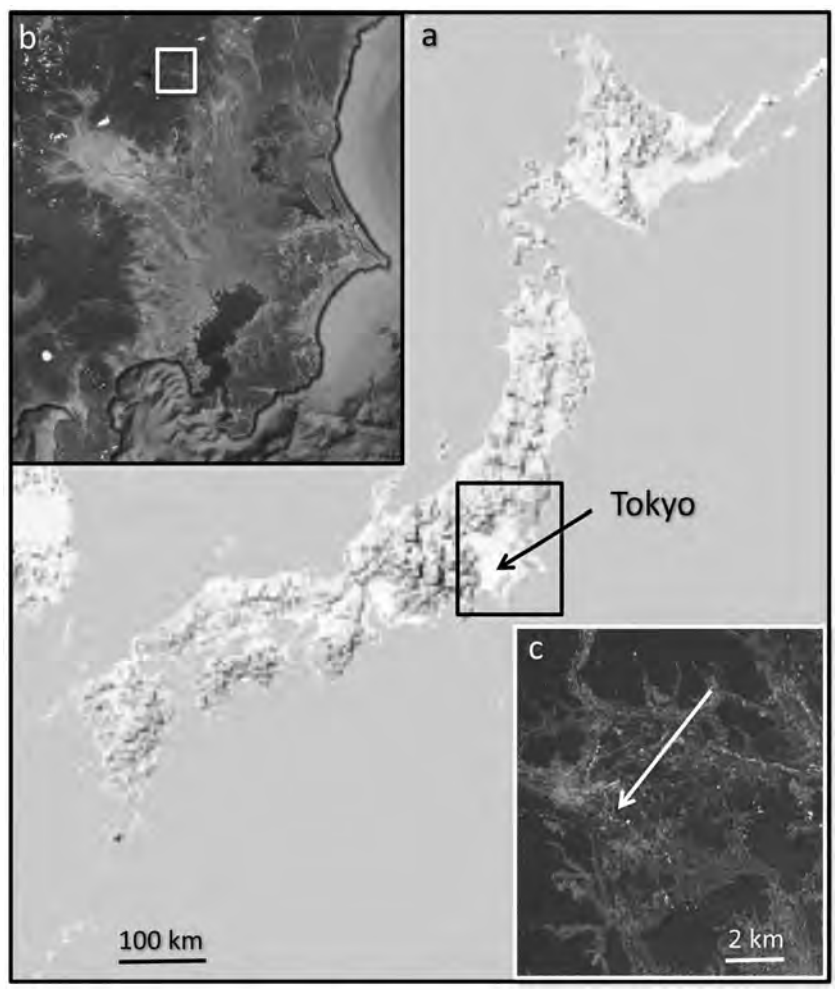


Figure 1. Map of sample location at Imaichi, Nikko, near Tokyo (36°43′16.276″N, 139°42′14.688″E), where natural samples were collected: (a) map of Japan; (b) region NW of Tokyo; and (c) sample location. Image credit: 2012 CNES/SPOT, Google Earth, Feb. 10, 2012.

MacKenzie *et al.*, 1989) studies of these minerals have led to a general understanding of their character. These studies have shown that allophane is nearly X-ray amorphous and has a hollow-sphere structure with a diameter of 3.5–5 nm, whereas imogolite has a discrete XRD pattern and a tubular structure. Thus, allophane has only short-range ordering, but imogolite has long-range ordering in one dimension. Although these materials are poorly and para-crystalline, they have distinct and recognizable XRD patterns (*e.g.* van der Gaast *et al.*, 1985). Allophane has a molar Si/Al ratio between 0.5 and 1; imogolite, near 0.5. Henmi and Wada (1976) found a change in the Al configuration as volcanic glass altered: Al is largely 4-coordinated in volcanic glass, 4- and/or 6-coordinated in allophane, and mostly 6-coordinated in imogolite. Allophane and imogolite can be identified in soils by their dissolution in 0.2 M oxalate-oxalic acid at pH 3 (Wada, 1987).

Synthesis of allophane and imogolite can be achieved by heating solutions of orthosilicic acid and hydroxy-Al cations at 95–100°C (Farmer *et al.*, 1977; Wada *et al.*, 1979; Farmer *et al.*, 1983). Both mineraloids form together in about 1 week, although imogolite is favored at lower Si/Al ratios and a pH near 5, whereas allophane is favored at pH values of 6–8. However, imogolite-like products were also found up to pH 8 for Si/Al ratios $\leqslant$0.25 (Farmer *et al.*, 1979). Combined synthesis experiments and molecular orbital calculations showed that Ca and Na cations in solution greatly facilitate the formation of allophane and suppress the formation of imogolite (Abidin *et al.*, 2007a). The alkali metal cations in solution inhibit imogolite formation for Ca/Al >10 and Na/Al > 50 as shown by IR and XRD analyses.

Transmittance spectra indicate a shift in the Si–O stretching vibration from ~1000 $cm^{-1}$ for silica gel to near 940 $cm^{-1}$ for allophane and imogolite (Farmer *et al.*, 1979). These spectra exhibit a shoulder near 1000 $cm^{-1}$ for imogolite that is close to the band for most forms of opal and silica gel. Farmer *et al.* (1979) further observed that the Si–O stretching vibration is generally narrower in natural samples and broader in spectra of synthetic ones. Those authors suggested that this is due to a limited range of Si–O bond environments in natural samples. Cradwick *et al.* (1972) interpreted the IR spectra to indicate a structure composed of isolated orthosilicate groups with their Si to apical O bonds perpendicular to the axis of the fiber.

The structure of imogolite is based on a gibbsite-like sheet made up of Si–O–Al and Al–O–Al bonds that is curled in one direction (Figures 2a, 3a,c); Si–O–Si bonds normally are not observed (Wada, 1987). Imogolite forms elongated fibers up to 1 μm long with diameters of <2 nm (Wada, 1989). In contrast, allophane is composed of similar sheets that curl on three edges (Figures 2b, 3b,d), have diameters of ~3.5–5 nm, and tend to form globular aggregates (Wada and Wada, 1977). The structures of imogolite and allophane were examined in more detail recently using molecular orbital calculations (Abidin *et al.*, 2007a; Creton *et al.*, 2008a, 2008b; Konduri *et al.*, 2006; Tamura and Kawamura, 2002) and density functional theory modeling (Alvarez-Ramirez, 2007; Demichelis *et al.*, 2010; Guimarães *et al.*, 2007). Al–O and Si–O bond distances, Al...Al and Si...Si distances, several bond angles, and calculated XRD and IR parameters for model structures were determined for these structures and compared with experimental values for gibbsite (Saalfeld and Wedde, 1974) and imogolite (Cradwick *et al.*, 1972). This work confirmed that imogolite and protoimogolite allophane consist of an interior layer of tetrahedral Si bonded to an outer layer of octahedral Al with OH groups pointing outside and inside the tube (Figure 2a,b). The allophane structure is more complex with clusters of tetrahedral Si and octahedral Al, as well as OH groups pointing outside and inside the sphere (Figure 2b). Imogolite and allophane were found to have similar ideal structures on a unit-cell level based on a gibbsite sheet with orthosilicate clusters ($SiO_4$) inserted at the vacant octahedral sites such that the O...O distance is shortened in one gibbsite layer and lengthened in the neighboring layer. This causes curling of the structure to produce a tubular structure for imogolite and a nanoball structure for allophane (Abidin *et al.*, 2007a). Reactions performed on allophane surfaces suggest that variations in the Si/Al ratio affect the surface chemistry of the hollow spheres, the development of silanol groups, and the degree of enlargement of pores in the sphere walls (Abidin *et al.*, 2007b).

Relative humidity-controlled XRD studies have been applied to a variety of mineral systems to understand the nature of the interaction of mineral/solid surfaces with $H_2O$ molecules (*e.g.* Bish *et al.*, 1999; Chipera *et al.*, 1997). These measurements, generally performed from 0 to ~95% RH, are particularly sensitive to small changes in surface properties, as exemplified in comparisons of untreated and steam-treated smectites (Bish *et al.*, 1999).

Imogolite and allophane are important soil constituents. They control the physical and chemical character of soils due to their large surface area, unique structures, and high reactivity which enable adsorption of organic molecules and anions such as sulfate and phosphate (*e.g.* Abidin *et al.*, 2007a; Parfitt, 2009). Imogolite and allophane frequently occur together as clay components of soils derived from volcanic ash and pumice, largely by alteration of volcanic glass. Favorable environments for the formation of these minerals generally include a moderate water/rock ratio, mildly acidic conditions, and good drainage, where Si and bases are leached from parent material. Imogolite and allophane often form in the subsurface, whereas opaline silica forms at the surface (*e.g.* Wada, 1987). Imogolite was found in the youngest soils, allophane in intermediate soils, and halloysite in the oldest soils in several alteration studies of volcanic tephra (*e.g.* Wada, 1987). Allophane and

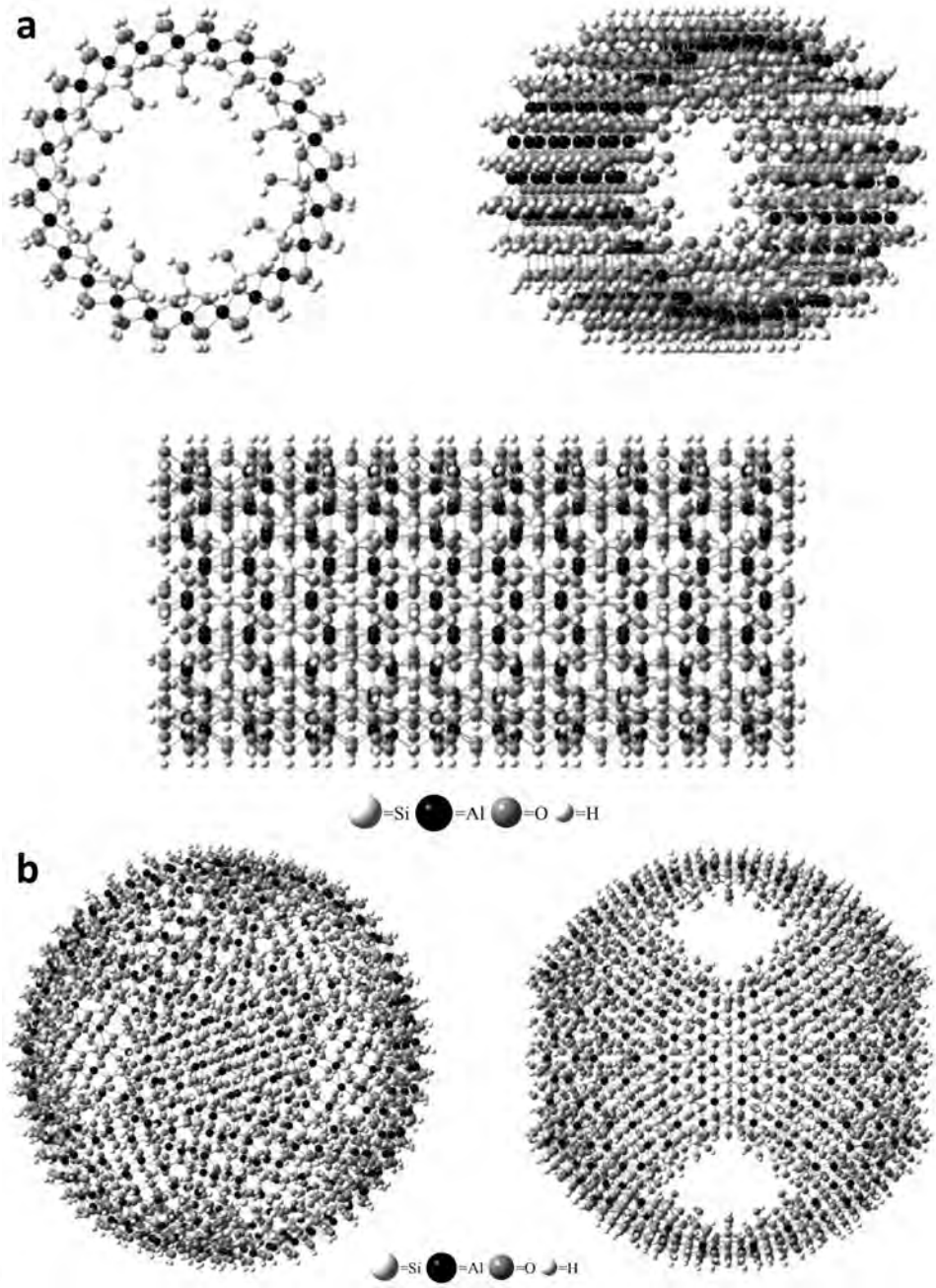


Figure 2. Mineral structures (after Abidin *et al.*, 2007a): (a) nano-tube structure of imogolite; (b) nano-ball structure of allophane.

halloysite were found to be more abundant in Hawaiian soils formed from volcanic tephra under less humid conditions, while ferrihydrite and gibbsite were more prevalent in soils formed under tropical conditions (Parfitt *et al.*, 1988). A study of Ecuadorian Andosols found allophane-rich facies in the upper few meters, halloysite-rich facies at 11–15 m depth, and gibbsite at the transition zone (Kaufhold *et al.*, 2009, 2010). A study of Andosols from Guadeloupe found that gibbsite and kaolinite were present with allophane in areas that experienced intense leaching of silica (Ndayiragije and Delvaux, 2003). Poorly crystalline minerals such as allophane and imogolite were observed as the favored alteration products in young soils derived from a variety of volcanic ash deposits (Shoji *et al.*, 1993). Therefore, allophane and/or imogolite are indicators of immature soils formed *via* alteration of volcanic material.

Allophane and imogolite also form in the B horizon of Spodosol-like soils derived from Si-rich parent rocks following leaching of the upper E soil horizon and

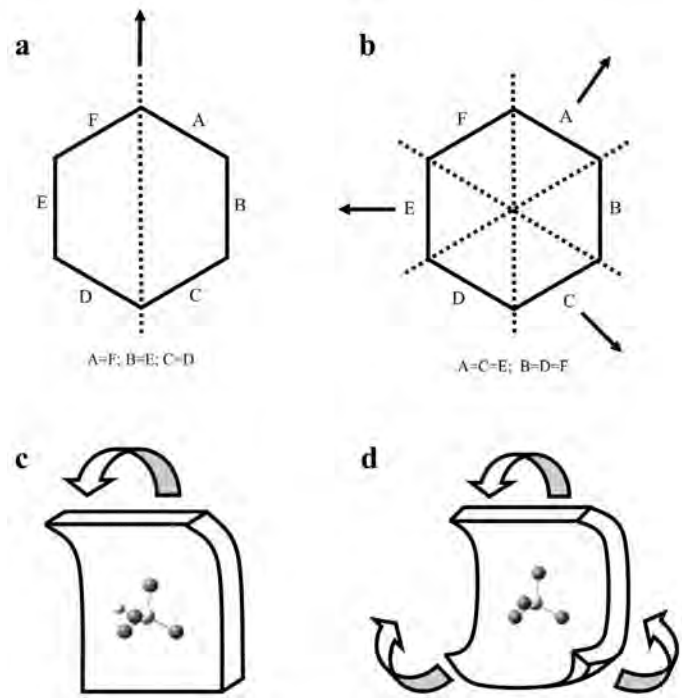


Figure 3. Models of imogolite and allophane symmetry and particle growth patterns: (a) symmetry of imogolite; (b) symmetry of allophane; (c) formation pattern of imogolite; and (d) formation pattern of allophane.

degradation of organometallic complexes in the soil (Buurman and Van Reeuwijk, 1984). Acidic conditions in Sweden were found to favor complexation of Al by organic matter, which inhibits formation of allophane and imogolite (Gustafsson *et al.*, 1998). Al and Fe leached out of the E horizon are bound by organic acids and transferred to the lower B horizon (Lundström *et al.*, 2000). Once microbial activity sufficiently degrades the organometallic complexes, Al becomes free to form gibbsite, imogolite, and allophane (Buurman and Van Reeuwijk, 1984; Gustafsson *et al.*, 1998). Another study of Canadian soils found greater abundances of opaline silica in the surface A horizon and elevated allophane and ferrihydrite in the subsurface B horizon (Kodama and Wang, 1989), similar to studies of volcanic soils. Thus, allophane and imogolite are not entirely unique to volcanic settings because, although uncommon, they can form in soils derived from other parent materials.

## METHODS

### *Samples*

The natural imogolite and allophane samples were prepared from pumice that was collected ~30 y ago at Imaichi, Nikko, near Tokyo (Figure 1). This site is located at 36°43′16.276″N, 139°42′14.688″E and the materials here formed by alteration of volcanic material. The imogolite sample was scraped off the outer portion of the pumice. The allophane sample was taken from the remaining inner part of the pumice and had a molar Si/Al ratio of 0.82. Post-collection modification of the samples during storage in the laboratory was assumed to have been minor, no evidence of formation of phyllosilicates was seen in the XRD or IR data. Iron (oxyhydr)oxide phases were removed from the samples using the standard dithionite-citrate-bicarbonate (DCB) treatment described by Mehra and Jackson (1960).

The synthetic imogolite sample was prepared by mixing orthosilicic acid, $H_4SiO_4$, with aluminum nitrate hexahydrate, $Al(NO_3)_3{\cdot}6H_2O$, to yield an Si/Al ratio of 0.5 for a previous study (Henmi and Huang, 1987). The solution mixtures were titrated with NaOH until an OH/Al molar ratio of 2 was achieved. The Si concentration of the resulting solution was 1.6 mM and the pH was 4.1. The mixture solution was heated at 100°C for 48 h in an autoclave, then allowed to cool, at which point the pH was 3.0. The product was flocculated by adding saturated sodium chloride solution to the cooled mixture solution. The gelatinous product was centrifuged, dialyzed to remove excess sodium chloride, and freeze-dried to create a powder. Analysis using XRD, scanning electron microscopy (SEM), and differential thermal analysis (DTA) showed the product to be imogolite (Abidin *et al.*, 2008, 2009).

The synthetic allophane sample was prepared using the method described by Montarges-Pelletier *et al.* (2005), with 0.1 M $AlCl_3$ and tetraethyl orthosilicate (TEOS) (5 mL TEOS to 225 mL 0.1 M $AlCl_3$) to produce an Al:Si ratio of 1:1 (Baker and Strawn, 2012). The method was modified to produce an Fe-substituted

allophane by adding 11.25 mL of 0.1 M $FeCl_3$ to the starting materials to produce a final Fe:Al ratio of 1:20. The gel produced by this synthesis was dialyzed against flowing deionized water and then freeze-dried for analysis.

*Reflectance measurements*

Reflectance spectra were measured for particulate samples in a horizontal sample dish using a bi-directional VNIR spectrometer and a Nicolet FTIR spectrometer at Brown University's RELAB as in previous studies (*e.g.* Bishop *et al.*, 2008). Spectra were measured relative to Halon from 0.3 to 2.5 μm under ambient conditions with 5 nm spectral sampling. Infrared reflectance spectra were measured relative to a rough gold surface in a biconical configuration with 2 $cm^{-1}$ spectral sampling from 1–50 μm in an environment purged of $H_2O$ and $CO_2$ for 10–12 h. Composite, absolute reflectance spectra were prepared by scaling the FTIR data to the bidirectional data near 1.2 μm.

*Emissivity measurements*

TIR emissivity spectra of particulate and pellet samples were collected at the Mars Space Flight Facility at Arizona State University using a Nicolet Nexus 670 spectrometer configured to measure emitted energy (Christensen and Harrison, 1993; Ruff *et al.*, 1997). Samples were placed in copper sample cups painted black so that they behaved as a spectral blackbody, and were heated to 80°C before and during the experiments to increase the signal-to-noise ratio. Spectra were scanned 240 times over the course of ~4 min, from 200 to 2000 $cm^{-1}$ with 2 $cm^{-1}$ spectral resolution. Blackbodies at 70 and 100°C were measured to calibrate raw data to radiance (Christensen and Harrison, 1993). Radiance spectra were transformed to emissivity spectra by normalizing to the Planck curve corresponding to the sample temperature (Ruff *et al.*, 1997). Pellets were created by compressing ~0.2 g of particulate material to ~70 MPa (uncorrected for friction) in a hydraulic press for 3 min (Michalski *et al.*, 2005). Pellets were 1 cm in diameter and a few mm thick.

*XRD-RH experiments*

Powders for controlled-humidity powder XRD measurements were mounted as thin slurries on 'zero-background' quartz plates, which were mounted in an environmental chamber on a Bruker D8 powder diffractometer using CuKα radiation and an energy-dispersive Sol-X detector (Bruker, Karlsruhe, Germany). The use of thin slurry sample mounts allowed the powders to equilibrate quickly with the controlled-RH atmosphere. Relative humidity was controlled by an InstruQuest Inc. (Florida, USA) VGen RH generator. Diffraction measurements were made at 0 to 95% RH and back to 0% RH, in 10% RH steps to 90%, 5% steps from 90–95–90%, and 10% RH steps back to 0% RH. An initial equilibration time of 2 h was used at 0% RH, and a 1 h equilibration time was used before all other XRD measurements at each RH level. The XRD data were measured for allophane from 2 to 36°2θ and for imogolite from 2 to 18°2θ, counting for 2 s/0.02° step.

## RESULTS

*VNIR reflectance spectra*

The VNIR reflectance spectra of allophane included bands near 1.4, 1.9, and 2.2 μm, plus a strong band that was nearly saturated from 2.7–3.5 μm (Figure 4a). For the spectra measured under ambient conditions where substantial adsorbed $H_2O$ was present, the bands near 1.4 and 1.9 μm were much stronger and shifted toward longer wavelengths, as expected (*e.g.* Bishop *et al.*, 1994). The VNIR spectral properties of synthetic allophane and purified natural allophane were similar. The allophane-rich soil spectrum (Figure 4a) contained a weak broad band near 0.9–1 μm and an increasing slope from 0.4 to 0.6 μm compared to the pure allophane spectra. These additional features in the spectra of the untreated samples are consistent with the presence of iron and are typical of iron (oxyhydr)oxides (*e.g.* Morris *et al.*, 1985; Bishop and Murad, 1996). These features are also consistent with Fe(III)-bearing phyllosilicates (*e.g.* Bishop *et al.*, 1999, 2008), but no $Fe_3OH$ bands were observed near 2.3 μm as are present in Fe(III)-bearing phyllosilicates and no evidence of phyllosilicates in the XRD patterns was noted. The synthetic Fe-bearing allophane contained similar features near 0.4–0.6 and 0.9–1 μm which are attributed to the Fe(III) shown to be present in isomorphic substitution for Al in the allophane structure through EXAFS experiments (Baker and Strawn, 2012). Note that in addition to the weak, broad Fe(III) band near 0.9–1.0 μm, an $H_2O$ overtone centered at 0.97 μm was observed, which increased in intensity toward 1.0 μm in the spectra measured under hydrated conditions (dotted lines in Figure 4). This $H_2O$ band was stronger in spectra of the synthetic samples than in spectra of the natural samples. The bands near 1.4, 1.9, and 2.2 μm were due to overtones and combinations of $H_2O$ and OH in the structure and are described in more detail in a later section.

The VNIR reflectance spectra of imogolite also included bands near 1.4, 1.9, 2.2, and 2.7–3.5 μm (Figure 4b), and the 1.4 and 1.9 μm bands were again greatly intensified for spectra measured under ambient conditions where adsorbed $H_2O$ contributes to the spectral features.

*Mid-IR reflectance and emissivity spectra of fundamental vibrations*

Reflectance ($R$) and emittance ($E$) both depend on the real ($n$) and imaginary ($k$) components of the index of

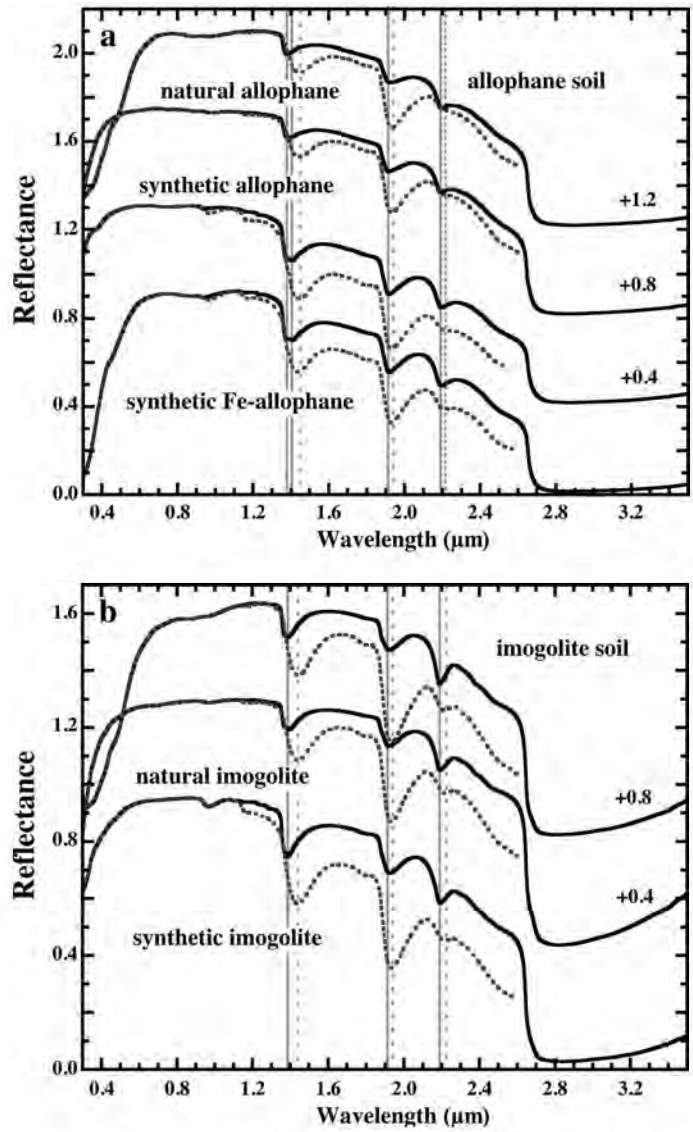


Figure 4. VNIR reflectance spectra of (a) allophane and (b) imogolite. Spectra are offset for clarity. Dashed lines refer to spectra measured under ambient RH conditions (0.3–2.5 μm). Solid lines refer to spectra measured under low-RH conditions (1–3.3 μm).

refraction and are, thus, influenced by surface scattering and particle size. They are related by Kirchhof's Law, where $R = 1-E$, which generally holds for Lambertian surfaces and larger grain sizes, although discrepancies are often noted for small particle sizes (Salisbury, 1993). Reflectance and emittance are both distinct from transmittance spectra, which only depend on $k$. $H_2O$ bending vibrations were observed near 1650 $cm^{-1}$ (~6.1 μm) for allophane (Figure 5a,b) and imogolite (Figure 5c,d). A strong single upward band (in inverse reflectance – note that this would be a downward band in reflectance) was observed for the synthetic allophane (Figure 5b) and synthetic imogolite (Figure 5d) spectra, whereas a weaker doublet feature was observed in the reflectance spectra of the natural samples (Figure 5a,c). These features indicated that additional hydrated phases were present in the natural samples and were not removed by the purification process. The spectral features at longer wavelengths were largely similar for the inverse reflectance spectra of loose powders and the emissivity spectra of pressed powders; however, the spectral bands were stronger for the spectra of the pressed powders, as expected (*e.g.* Michalski *et al.*, 2006).

*Si–O stretching region*

The Si–O–Al stretching vibrations occurred near 1010 $cm^{-1}$ (9.9 μm) and 930 $cm^{-1}$ (10.8 μm) in reflectance spectra of imogolite and near 1030 $cm^{-1}$ (9.7 μm) and 940 $cm^{-1}$ (10.6 μm) in reflectance spectra

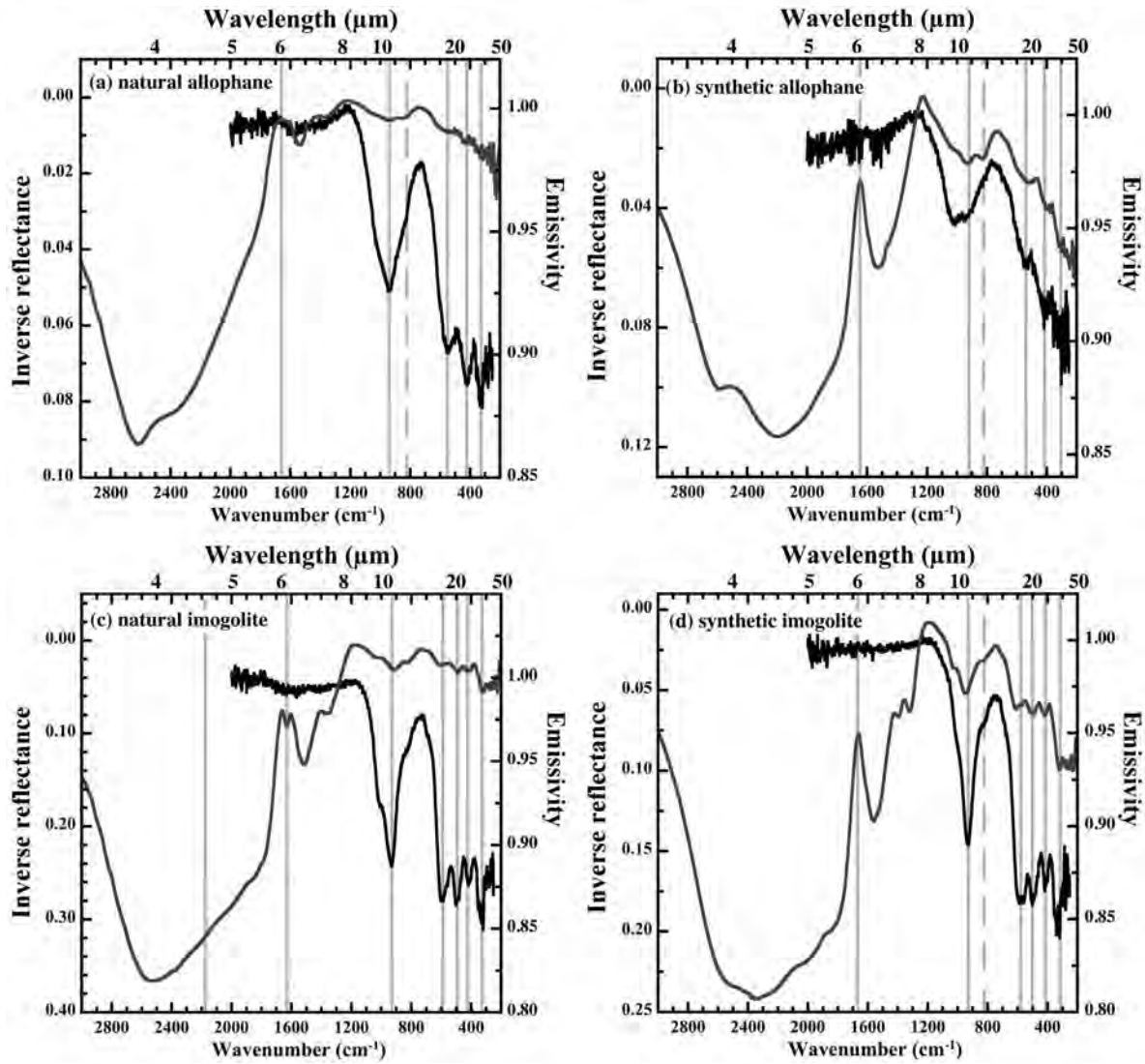


Figure 5. Mid-infrared reflectance and emissivity spectra from 200 to 3000 $cm^{-1}$ (~3–50 μm) of (a) natural allophane, (b) synthetic allophane, (c) natural imogolite, and (d) synthetic imogolite.

of allophane (Figure 6). These are similar to the emissivity bands for Si–O stretching in high-silica aluminosilicate gel observed near 1070 $cm^{-1}$ (9.3 μm) (*e.g.* Rampe *et al.*, 2012), near 1270 $cm^{-1}$ (7.9 μm) and 1120 $cm^{-1}$ (8.9 μm) for opal, and near 1130 $cm^{-1}$ (8.8 μm) and 1045 $cm^{-1}$ (9.6 μm) for Si–O–Al stretching in phyllosilicates (Michalski *et al.*, 2005; Bishop *et al.*, 2008). Rampe *et al.* (2012) observed a single band centered near 940 $cm^{-1}$ in emissivity spectra of allophanes with low Si/Al ratios and a broad doublet feature near 1030 $cm^{-1}$ and 940 $cm^{-1}$ for allophanes with an Si/Al ratio of 0.92, similar to that observed for the natural allophane in the present study (Figure 6) which has an Si/Al ratio of 0.82. This doublet was shifted toward the 1030 $cm^{-1}$ band in the synthetic sample (Figure 6), indicating that more Si–O–Si bonds were present. The Si–O–Al stretching band occurred near 985–995 $cm^{-1}$ in transmittance spectra of allophane with high Si/Al ratios and near 962–970 $cm^{-1}$ in transmittance spectra of allophane with low Si/Al ratios (Parfitt and Henmi, 1980; Henmi *et al.*, 1981). This band occurred as a doublet near 950–1000 $cm^{-1}$ in transmittance spectra of imogolite and near 1000–1050 $cm^{-1}$ in transmittance spectra of silica gel (Farmer *et al.*, 1979).

*OH-bending region*

OH-bending vibrations are generally observed from 590 $cm^{-1}$ (16.9 μm) to 940 $cm^{-1}$ (10.6 μm) in phyllosilicates (*e.g.* Farmer, 1974). A shoulder feature near 825 $cm^{-1}$ (12.1 μm) was observed in reflectance

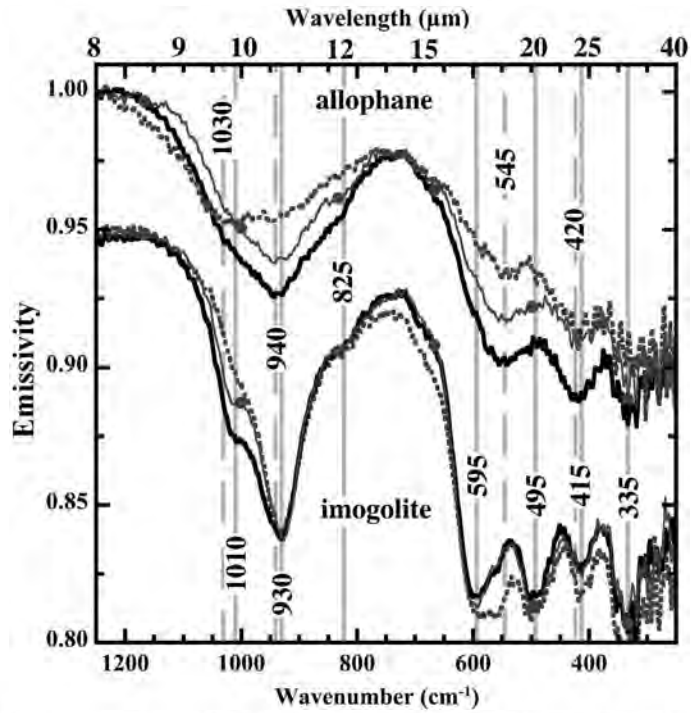


Figure 6. Emittance spectra from 1250–250 $cm^{-1}$ (8–40 μm) showing the Si–O–Al stretching and bending vibrations. Spectra of the natural allophane and imogolite samples are shown in solid lines, spectra of the natural allophane and imogolite soils are shown with symbols, and spectra of the synthetic allophane and imogolite are shown in dashed lines. The imogolite spectra are offset by 0.05 on the vertical scale for clarity.

spectra of both allophane and imogolite and is attributed to in-plane Al–OH bending vibrations, based on this feature in phyllosilicates (*e.g.* Bishop *et al.*, 2002b). An additional band was observed at 595 $cm^{-1}$ (16.8 μm) in imogolite spectra and a shoulder was present near 620 $cm^{-1}$ (16.1 μm) in allophane spectra. These are more consistent with out-of-plane bending vibrations (*e.g.* Farmer, 1974) and are generally only observed in phyllosilicates when the structure is disrupted (*e.g.* Bishop *et al.*, 2002b). The features near 595 and 620 $cm^{-1}$ could also be due to Al–O vibrations (Farmer, 1974). Bending vibrations for Si–OH in silica occur near 795 $cm^{-1}$ (12.6 μm) and were observed only as a weak shoulder if at all in the allophane and imogolite spectra. This is consistent with the structural models (Figure 2) for allophane and imogolite that indicate a much greater abundance of OH bound to Al than to Si. Transmittance spectra of allophane and imogolite included a band near 690 $cm^{-1}$ (Parfitt *et al.*, 1980; Parfitt and Henmi, 1980) that is probably related to the 595–620 $cm^{-1}$ reflectance feature.

*Si–O bending region*

The bands near 545 $cm^{-1}$ (18.3 μm) in the allophane spectra and near 495 $cm^{-1}$ (20.2 μm) in the imogolite spectra (Figure 6) are attributed to Si–O–Al deformation, and the bands near 420 $cm^{-1}$ (23.8 μm) in the allophane spectra and near 415 $cm^{-1}$ (24.1 μm) in the imogolite spectra (Figure 6) are attributed to Si–O bending based on studies of phyllosilicate spectra (*e.g.* Farmer, 1974; Bishop *et al.*, 2002a; Michalski *et al.*, 2005). Related spectral bands are observed for Si–O bending vibrations for silica gel (near 440 $cm^{-1}$, 22.7 μm, Rampe *et al.*, 2012) and for opal (481 $cm^{-1}$, 20.8 μm, Bishop *et al.*, 2011). Shifts were not observed in the 545 and 420 $cm^{-1}$ allophane bands with changing Si/Al ratio (Rampe *et al.*, 2012). Differences in these features for allophane and imogolite are attributed to the curvature of the structures as Si–O bending vibrations are probably sensitive to the position of neighboring atoms. An additional band was observed near 325–335 $cm^{-1}$ (~30 μm) in emissivity and reflectance spectra of all allophane and imogolite samples. This also falls in the spectral region due to Si–O bending (Farmer, 1974) and was observed at 348 $cm^{-1}$ in transmittance spectra of imogolite and allophane (Farmer *et al.*, 1977).

*$H_2O$ bending region*

Single bands were observed in the $H_2O$ bending region at 1645 $cm^{-1}$ (6.08 μm) for reflectance spectra of synthetic allophane (Figure 7a) and 1662 $cm^{-1}$ (6.02 μm) for synthetic imogolite (Figure 7b). Reflectance spectra of the natural samples exhibited doublets in this region: 1667 and 1606 $cm^{-1}$ for allophane and 1662 and 1604 $cm^{-1}$ for imogolite (Figure 7). A related band with variable width was

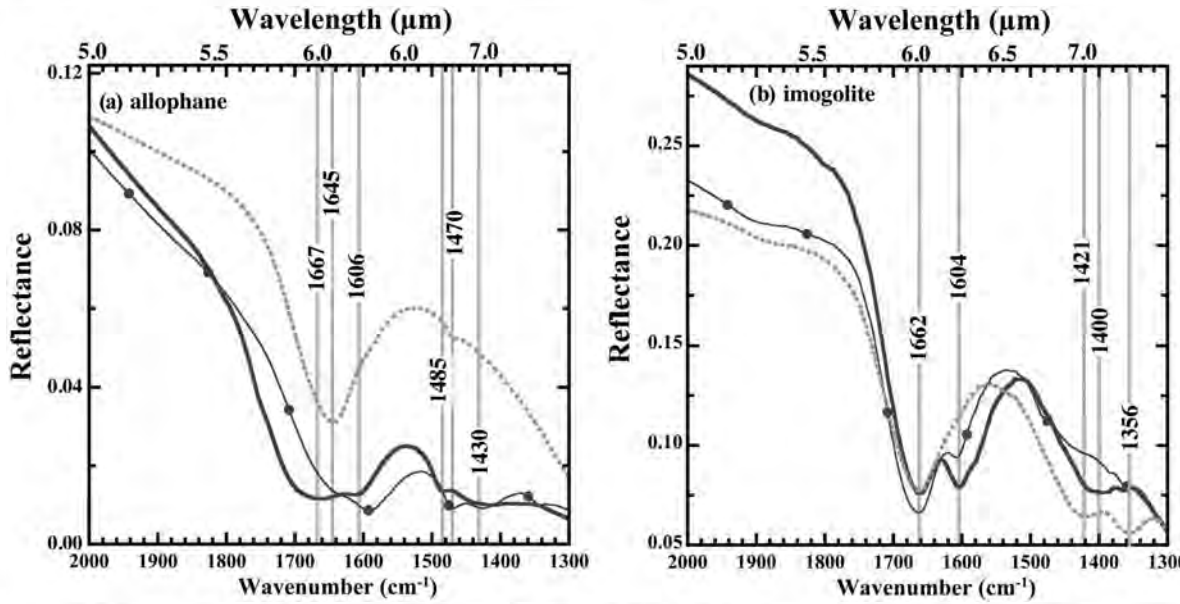


Figure 7. Reflectance spectra from 1300 to 2000 $cm^{-1}$ (5–7.5 μm) of the $H_2O$ bending region for (a) allophane and (b) imogolite. Spectra of the natural allophane and imogolite samples are shown in solid lines, spectra of the natural allophane and imogolite soils are shown with symbols, and spectra of the synthetic allophane and imogolite are shown in dashed lines. The natural allophane spectra were increased by a factor of two on the vertical scale for comparison with the synthetic spectrum.

observed in transmittance spectra of allophane and imogolite (Parfitt and Henmi, 1980). An additional feature was observed near 1400 $cm^{-1}$ in reflectance spectra (Figure 7) and transmittance spectra (Parfitt and Henmi, 1980) of allophane and imogolite. A doublet was observed for the natural allophane (1485, 1430 $cm^{-1}$) and a single weak band was observed for the synthetic allophane (1470 $cm^{-1}$), whereas a doublet was observed for the synthetic imogolite (1421, 1356 $cm^{-1}$) and a single band was observed for the natural imogolite (1400 $cm^{-1}$). This band is attributed to OH bending vibrations of acid salts such as $O_3SiOH$ groups that can be split into a doublet by resonance interactions (Ryskin, 1974). Alternatively, nitrates could be causing this feature near 1400 $cm^{-1}$ (*e.g.* Pavia *et al.*, 1979). However, as a related feature has been observed in reflectance and transmittance spectra of some ferrihydrite samples, particularly natural samples containing Si (Bishop and Murad, 2002), the $O_3SiOH$ interpretation may be more likely for these samples. Organic residues from the soil and/or Fe removal treatment could also be contributing to spectral features in this region. The band at 1356 $cm^{-1}$ was probably due to organic admixtures. A sharper band was observed near 1380 $cm^{-1}$ in transmittance spectra of the natural samples (not shown).

*$H_2O$ stretching region*

A broad reflectance band was observed for both allophane and imogolite in the $H_2O$ stretching region (Figure 8). This feature extended from ~3000–3700 $cm^{-1}$ and is a composite of symmetric

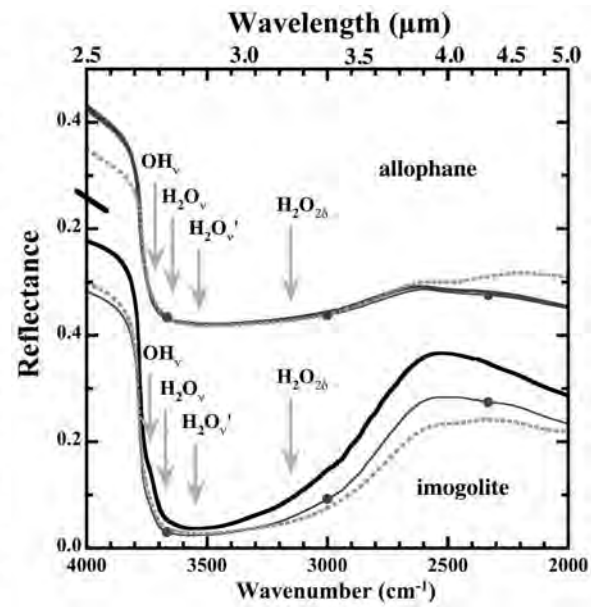


Figure 8. Reflectance spectra from 2000 to 4000 $cm^{-1}$ (2.5–5 μm) of the OH and $H_2O$ stretching region for allophane and imogolite. Spectra of the natural allophane and imogolite samples are shown in solid lines, the natural allophane and imogolite soils are shown with symbols, and the synthetic allophane and imogolite are shown in dashed lines. The positions of the features contributing to the broad band are marked as $OH_v$ for OH stretching, $H_2O_v$ for $H_2O$ stretching, $H_2O_v'$ for $H_2O$ stretching at hydrated sites, and $H_2O_{2\delta}$ for bending overtones as described by Bishop *et al.* (1994).

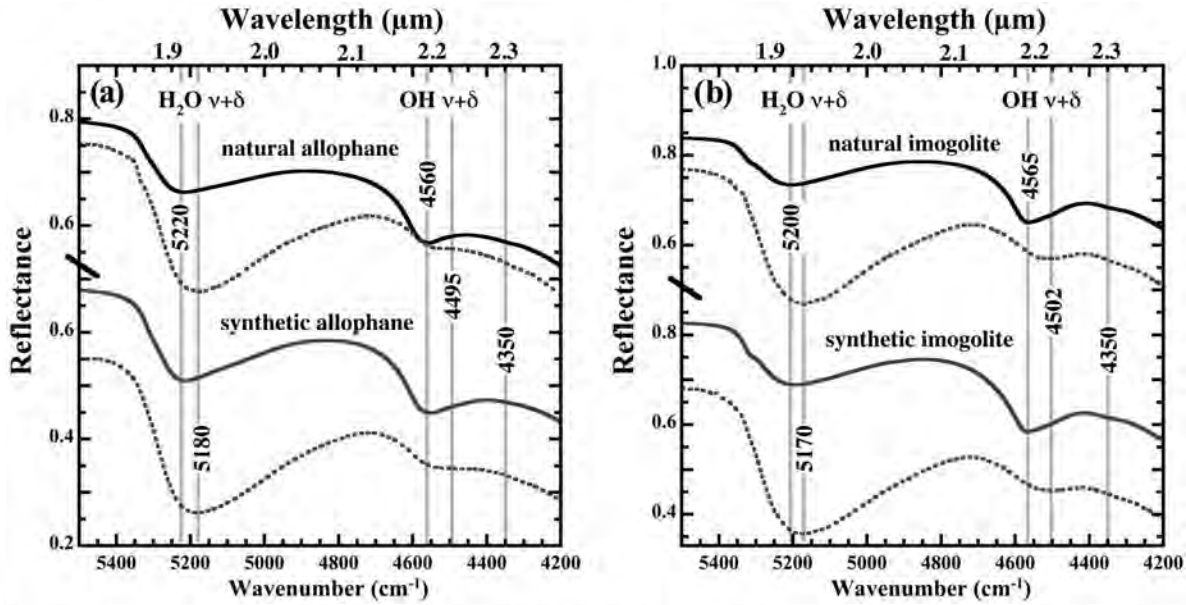


Figure 9. Reflectance spectra from 4200 to 5500 $cm^{-1}$ (~1.8–2.4 μm) of the OH and $H_2O$ combination band region for (a) allophane and (b) imogolite. Dashed lines refer to spectra measured under ambient RH conditions, whereas solid lines refer to spectra measured under low-RH conditions. ν+δ indicate the combination bending plus stretching vibration.

and asymmetric $H_2O$ stretching vibrations, OH-stretching vibrations, and an overtone of the $H_2O$ bending vibration as summarized for phyllosilicates (*e.g.* Bishop *et al.*, 1994). A broad, composite band was also observed in this region in transmittance spectra of allophane and imogolite (Parfitt and Henmi, 1980).

*NIR reflectance spectra of combinations and overtones*

*OH combination band.* An OH combination stretching plus bending band was observed at 4560 $cm^{-1}$ (2.193 μm) for allophane (Figure 9a) and at 4565 $cm^{-1}$ (2.191 μm) for imogolite (Figure 9b) measured under controlled, low-humidity conditions in reflectance spectra. These OH combination bands ($OH_{\nu+\delta}$) were broadened and shifted toward longer wavelengths, particularly in the case of imogolite for spectra measured under ambient (elevated RH) conditions (Figure 9). In reflectance spectra of phyllosilicates, these OH combination bands were not affected by humidity level and adsorbed $H_2O$ molecules (*e.g.* Bishop *et al.*, 1994); however, this OH band in opal-A, opal-CT, and hydrated silica is dependent on adsorbed $H_2O$ and H-bonding of the OH species (Anderson and Wickersheim, 1964). Thus, the OH bonds in allophane and imogolite are more similar in character to hydrated amorphous materials than to phyllosilicates.

*$H_2O$ combination band.* The $H_2O$ combination stretching plus bending band was observed at 5220 $cm^{-1}$ (1.916 μm) for allophane (Figure 9a) and at 5200 $cm^{-1}$ (1.923 μm) for imogolite (Figure 9b). Both of these bands were broad and asymmetric, similar to the $H_2O$ stretching band shape. The magnitude of the $H_2O$ combination band ($H_2O_{\nu+\delta}$) was greatly increased for spectra measured under ambient (elevated humidity) conditions, as expected. The band center was also shifted toward lower wavenumbers (longer wavelengths) due to the additional H-bonding as in the case of adsorbed $H_2O$ in phyllosilicate spectra (Bishop *et al.*, 1994).

*OH and $H_2O$ overtones.* Overtone bands of the fundamental stretching vibration were present for both OH and $H_2O$ in allophane and imogolite spectra (Figure 10). A doublet occurred here due to the proximity of the OH overtone ($OH_{2\nu}$) and $H_2O$ overtone ($H_2O_{2\nu}$). The $OH_{2\nu}$ occurred near 7263 $cm^{-1}$ (1.377 μm) for allophane and near 7285–7305 $cm^{-1}$ (1.369–1.373 μm) for imogolite, and the $H_2O_{2\nu}$ occurred near 7104–7139 $cm^{-1}$ (1.401–1.407 μm) for allophane and near 7170–7205 $cm^{-1}$ (1.388–1.395 μm) for imogolite. The exact positions of these overtone band centers varied among the natural and synthetic samples in the present study and probably depended on the Si/Al ratio and curvature of the structure. The $OH_{2\nu}$ band in phyllosilicates depends on the cation to which it relates. It shifts from near ~7000 $cm^{-1}$ (1.42–1.43 μm) for Fe-smectite to ~7100 $cm^{-1}$ (1.40–1.41 μm) for Al-smectite and to ~7200 $cm^{-1}$ (1.38–1.39 μm) for Mg-smectite and also hydrated silica (*e.g.* Anderson and Wickersheim, 1964; Bishop *et al.*, 2002b, 2008). A broad $H_2O$ stretching overtone band was also observed for adsorbed or outer-sphere $H_2O$ in the allophane spectra near 6900 $cm^{-1}$ (1.45 μm) (Figure 10a) and in the imogolite spectra near

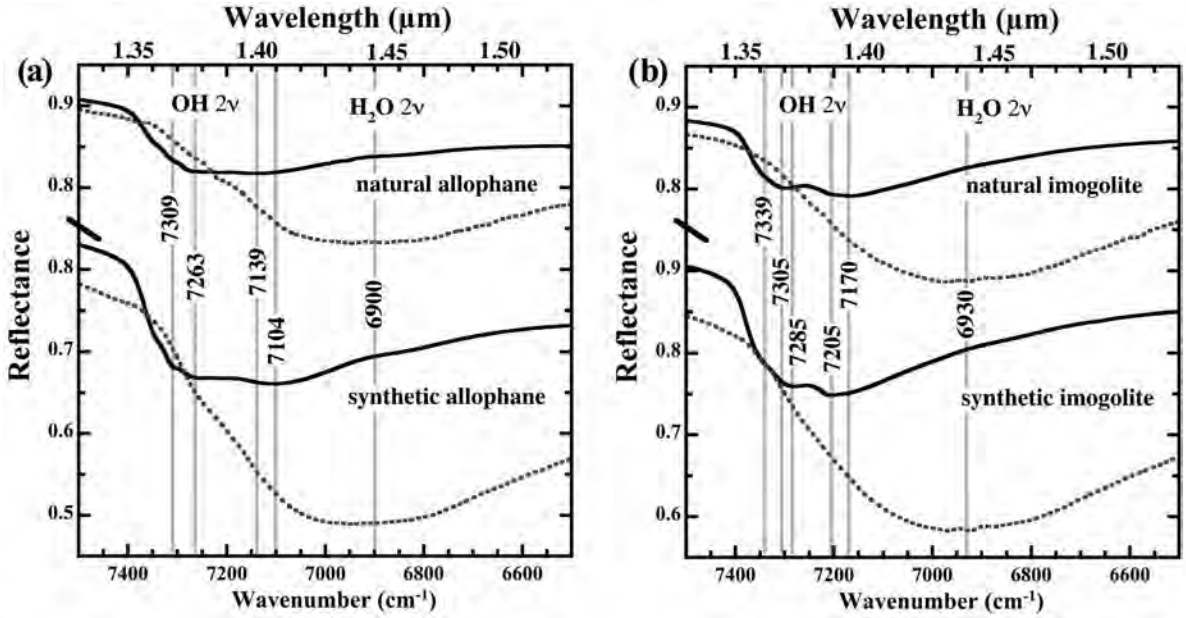


Figure 10. Reflectance spectra from 6500 to 7500 $cm^{-1}$ (~1.3–1.55 μm) of the OH and $H_2O$ stretching overtone (2ν) region for (a) allophane and (b) imogolite. Dashed lines refer to spectra measured under ambient RH conditions, whereas solid lines refer to spectra measured under low-RH conditions.

6930 $cm^{-1}$ (1.44 μm) (Figure 10b). This band occurred for the samples measured under ambient (elevated humidity) conditions but was not observed for the samples measured under hydrated conditions.

*XRD-RH experiments*

The XRD data for imogolite (Figure 11) showed the expected strong, broad peak at 2–3°2θ, the broad maximum at ~5–7°2θ, and the weaker peak near 12°2θ consistent with the partially ordered structure (*e.g.* van der Gaast *et al.*, 1985). However, these data measured as a function of relative humidity (RH) revealed unexpected changes as a function of RH, with large decreases in low-angle scattering intensity with increasing RH. The low-angle scattering behavior of imogolite at 0 and 100% RH and at elevated temperatures was measured by van der Gaast *et al.* (1985), and their data (Figure 6 in van der Gaast *et al.*, 1985) showed a significant decrease in the intensity of low-angle scattering with increasing temperature, but they do not show the significant decrease in intensity of low-angle scattering observed under elevated RH conditions. In a study comparing XRD patterns of natural and synthetic imogolite, Farmer and Fraser (1979) noted shifts to larger *d* spacings or smaller 2θ values and attributed the sharp, low-angle peak to a hexagonal, close-packing array of the imogolite tubes. Although the positions of the broad maxima were unchanged in the present study, the intensity of the broad maximum from ~4 to 9°2θ decreased systematically from 0 to 95% RH and then

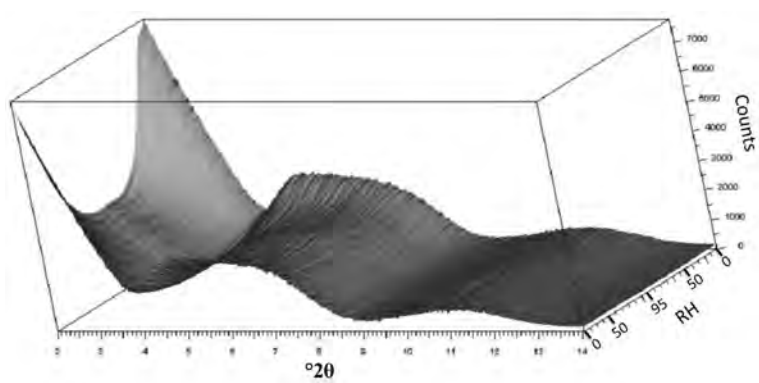


Figure 11. 3D representation of XRD data for the natural imogolite sample as the RH was increased from 0% to 95% and back to 0% (*z* axis). The low-angle (<9°2θ) intensity decreased at elevated RH levels. The XRD pattern is characteristic of imogolite.

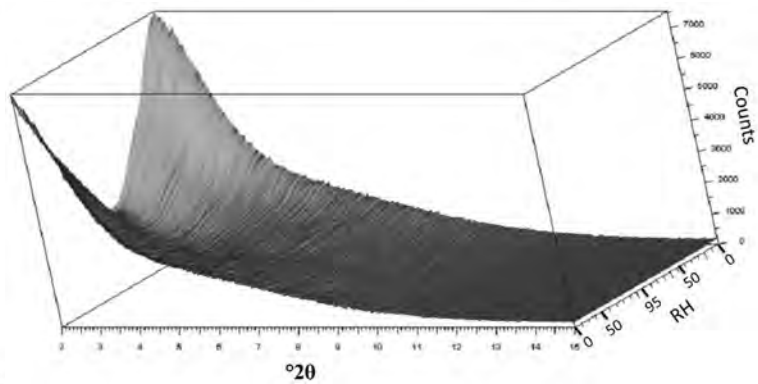


Figure 12. 3D representation of XRD data for the natural allophane sample as the RH was increased from 0% to 95% and back to 0% (z axis). The low-angle (<9°2θ) intensity decreased at elevated RH levels. This allophane exhibits no diffraction maxima, as expected.

increased again with a reduction in RH toward 0%. The low-angle scattered intensity changed in a similar manner. The broad maximum from ~9 to 14°2θ showed no significant change in intensity with RH. Such intensity changes are not common with well ordered, macrocrystalline materials, but they are similar to those observed with other poorly ordered materials such as opal-A and are probably related to adsorption of $H_2O$ molecules onto the imogolite surface, as suggested by van der Gaast *et al.* (1985) for allophane.

The XRD data for allophane (Figure 12) showed a characteristic broad maximum near 3°2θ and a largely featureless diffraction pattern. Data measured as a function of RH showed large decreases in low-angle scattering intensity with increasing RH similar to those observed for imogolite (Figure 11). In the experiment with allophane, the present results were similar to a previous study (figure 1 in van der Gaast *et al.*, 1985) where the strong ~3°2θ peak observed under low-RH conditions disappeared under 100% RH. However, these results are different from those of Kaufhold *et al.* (2010) who measured the XRD pattern of an allophane-rich soil under variable RH conditions and observed little change in the scattering intensity. In that study, however, the XRD pattern appears to reflect the minor feldspar and quartz minerals rather than the allophane. In the present study, the low-angle peak at ~3°2θ decreased systematically from 0 to 95% RH and then increased again with a reduction in RH towards 0%. The character of the low-angle scattering changed significantly, with the greatest intensity increase at the lowest angles. As noted above, these intensity changes are not typically observed with well ordered materials, and are probably related to adsorption of $H_2O$ molecules onto the allophane surface, as suggested by van der Gaast *et al.* (1985). Those authors postulated that the adsorption of $H_2O$ molecules onto the allophane surfaces disrupted the regular packing of allophane pseudo-spherical particles. The present results for imogolite suggest the existence of a similar process in this tubular material.

## DISCUSSION

Band assignments were made for allophane and imogolite based on the results of the present study of reflectance and emissivity spectra and previous studies of transmittance spectra (*e.g.* Farmer *et al.*, 1977, 1979, 1983; Parfitt and Henmi, 1980; Parfitt *et al.*, 1980; Henmi *et al.*, 1981). These are expressed in both frequency (wavenumber) and wavelength units ($cm^{-1}$ and μm, respectively) for allophane (Table 1) and imogolite (Table 2) in order to facilitate usage in both the fields of chemistry and geology. The band centers for the OH and $H_2O$ bands were used to compare calculated

Table 1. Band assignments for spectral features observed for allophane.

| Wavenumber ($cm^{-1}$) | Wavelength (μm) | Feature |
|---|---|---|
| 7263 | 1.377 | $OH_{2\nu}$ |
| 7104–7139 | 1.401–1.407 | $OH_{2\nu}$ |
| 6900 | 1.45 | $H_2O_{2\nu}$ |
| 5220 | 1.916 | $H_2O_{\nu+\delta}$ |
| 4560 | 2.193 | $OH_{\nu+\delta}$ |
| 4495 | 2.225 | $OH_{\nu+\delta}$ |
| ~3640–3740 | ~2.67–2.74 | $OH_{\nu}$ |
| ~3500–3600 | ~2.78–2.86 | $H_2O_{\nu}$ |
| ~3120–3165 | ~3.2 | $H_2O_{2\delta}$ |
| 1606–1667 | 6.00–6.23 | $H_2O_{\delta}$ |
| 1430–1485 | 6.73–6.99 | $OH_{\delta}$ for $O_3SiOH$ |
| 1030 | 9.7 | $Si–O–Al_{\nu}$ |
| 940 | 10.6 | $Si–O–Al_{\nu}$ |
| 825 | 12.1 | $OH_{\delta}$ |
| 610 | 16.4 | out-of-plane $OH_{\delta}$ |
| 545 | 18.3 | $Si\text{-}O\text{-}Al_{\delta}$ |
| 420 | 23.8 | $Si–O_{\delta}$ |
| 335 | 29.9 | $Si–O_{\delta}$ |

ν indicates stretching vibration; δ indicates bending vibration; band assignments are based on the present study and on previous transmission IR studies (*e.g.* Farmer *et al.*, 1977; Parfitt *et al.*, 1980; Henmi *et al.*, 1981).

Table 2. Band assignments for spectral features observed for imogolite.

| Wavenumber ($cm^{-1}$) | Wavelength (μm) | Feature |
|---|---|---|
| 7285–7305 | 1.369–1.373 | $OH_{2\nu}$ |
| 7170–7205 | 1.388–1.394 | $OH_{2\nu}$ |
| 6930 | 1.44 | $H_2O_{2\nu}$ |
| 5200 | 1.923 | $H_2O_{\nu+\delta}$ |
| 4565 | 2.191 | $OH_{\nu+\delta}$ |
| 4502 | 2.221 | $OH_{\nu+\delta}$ |
| 3700 | | $OH_\nu$ |
| ~3670–3755 | ~2.66–2.72 | $OH_\nu$ |
| ~3500–3600 | ~2.78–2.86 | $H_2O_\nu$ |
| ~3150 | ~3.2 | $H_2O_{2\delta}$ |
| 1604–1662 | 6.02–6.23 | $H_2O_\delta$ |
| ~1400–1421 | 7.14–7.37 | OH bend for $O_3SiOH$ |
| 1010 | 9.9 | $Si-O-Al_\nu$ |
| 930 | 10.8 | $Si-O-Al_\nu$ |
| 825 | 12.1 | $OH_\delta$ |
| 595 | 16.8 | out-of-plane $OH_\delta$ |
| 495 | 20.2 | $Si-O-Al_\delta$ |
| 415 | 24.1 | $Si-O_\delta$ |
| 335 | 29.9 | $Si-O_\delta$ |

ν indicates stretching vibration; δ indicates bending vibration; band assignments are based on the present study and on previous transmission IR studies (*e.g.* Farmer *et al.*, 1977; Parfitt *et al.*, 1980; Henmi *et al.*, 1981).

and measured frequencies of the combination bands and overtones in relation to the fundamental vibrations (Tables 3 and 4) as in previous studies (Bishop *et al.*, 2002a; Petit *et al.*, 2004).

The frequency of the $OH_{\nu+\delta}$ combination band should equal the sum of the frequencies of the $OH_\nu$ and $OH_\delta$ bands. The $OH_\nu$ band is difficult to resolve in reflectance spectra because of the multiple, overlapping vibrations near 3300–3760 $cm^{-1}$ (~2.7–3.0 μm) due to a distribution of $H_2O_\nu$ and $H_2O_{2\delta}$ bands. The frequencies of the $OH_\nu$ vibration for allophane and imogolite were estimated by subtracting the $OH_\delta$ frequency from the $OH_{\nu+\delta}$ frequency as in Bishop *et al.* (2002a) for phyllosilicates. The $OH_\nu$ frequency was also estimated from the $OH_{2\nu}$ frequency using the equation $F_{2\nu} = 2\ (F_\nu) - 171.27$, where $F$ is frequency ($cm^{-1}$), as in Petit *et al.* (2004) for phyllosilicates. Good agreement was found using these two methods, lending support to the band assignments. Two sets of $OH_\nu$ vibrations were found for allophane and imogolite (Table 3b). The $OH_\nu$ vibrations were estimated at 3638–3670 $cm^{-1}$ (2.72–2.75 μm) and 3717–3740 $cm^{-1}$ (2.67–2.69 μm) for allophane and at 3671–3688 $cm^{-1}$ (2.71–2.72 μm) and 3728–3755 $cm^{-1}$ (2.66–2.68 μm) for imogolite. For both allophane and imogolite, a doublet was present for the $OH_{2\nu}$. The lower-frequency vibration was shown to be due to $OH_{2\nu}$ rather than $H_2O_{2\nu}$ as the derived $OH_\nu$ frequency is comparable to the $OH_\nu$ frequency derived from a shoulder on the $OH_{\nu+\delta}$ band and the $OH_\delta$ band. A very weak band was observed near 4350 $cm^{-1}$ (2.30 μm) for both allophane and imogolite ($OH_{\nu+\delta}$ (2), Table 3a). This band assignment was tested by calculating $OH_\nu$ from this and the potential $OH_\delta$ (2) band at 595–610 $cm^{-1}$ (Table 3b). The agreement of this $OH_\nu$ with that determined from the overtone is within 25 $cm^{-1}$, which suggests that the 610 $cm^{-1}$ band in allophane spectra and the 595 $cm^{-1}$ band in imogolite spectra are indeed due to OH-bending vibrations and not to Al–O vibrations.

The frequency of the $H_2O_\nu$ vibration was estimated in a similar manner to that of the $OH_\nu$, using the measured

Table 3a. Measured band centers for OH vibrations.

| | $OH_{2\nu}$ | $OH_{2\nu}$* | $OH_{\nu+\delta}$ (1) | $OH_{\nu+\delta}$ (1)* | $OH_{\nu+\delta}$ (2) | $OH_\delta$ (1) | $OH_\delta$ (2) |
|---|---|---|---|---|---|---|---|
| Allophane natural | 7263 | 7139 | 4560 | 4495 | 4350 | 825 | 610 |
| Allophane synthetic | 7263 | 7104 | 4560 | 4495 | 4350 | 825 | 610 |
| Imogolite natural | 7305 | 7170 | 4565 | 4502 | 4350 | 825 | 595 |
| Imogolite synthetic | 7285 | 7205 | 4565 | 4502 | 4350 | 825 | 595 |

ν indicates stretching vibration; δ indicates bending vibration; * indicates estimated band based on shoulder.

Table 3b. Calculated band centers for OH vibrations.

| | $OH_\nu$ calc. from $OH_{2\nu}$ | $OH_\nu$ * calc. from $OH_{2\nu}$ | $OH_\nu$ (1) calc. from $OH_{\nu+\delta}$ (1) | $OH_\nu$ (1)* calc. from $OH_{\nu+\delta}$ (1)* | $OH_\nu$ (2) calc. from $OH_{\nu+\delta}$ (2) |
|---|---|---|---|---|---|
| Allophane natural | 3717 | 3655 | 3735 | 3670 | 3740 |
| Allophane synthetic | 3717 | 3638 | 3735 | 3670 | 3740 |
| Imogolite natural | 3738 | 3671 | 3740 | 3677 | 3755 |
| Imogolite synthetic | 3728 | 3688 | 3740 | 3677 | 3755 |

ν indicates stretching vibration; δ indicates bending vibration; * indicates estimated band based on shoulder.

Table 4. Measured and calculated band centers for $H_2O$ vibrations.

| | $H_2O_\nu$ calc. from $H_2O_{2\nu}$ | $H_2O_\nu$ calc. from $H_2O_{\nu+\delta}$ | $H_2O_{2\delta}(1)$ calc. from $H_2O_\delta(1)$ | $H_2O_{2\delta}(2)$ calc. from $H_2O_\delta$ (2) | $H_2O_{2\nu}'$ meas. | $H_2O_{\nu+\delta}$ meas. | $H_2O_\delta(1)$ meas. | $H_2O_\delta$ (2) meas. |
|---|---|---|---|---|---|---|---|---|
| Allophane natural | 3536 | 3553 | 3163 | 3041 | 6900 | 5220 | 1667 | 1606 |
| Allophane synthetic | 3536 | 3575 | 3119 | | 6900 | 5220 | 1645 | |
| Imogolite natural | 3551 | 3538 | 3153 | 3037 | 6930 | 5200 | 1662 | 1604 |
| Imogolite synthetic | 3551 | 3538 | 3153 | | 6930 | 5200 | 1662 | |

Calc. is calculated band centers; meas. is measured band centers; ν indicates stretching vibration; δ indicates bending vibration; ′ indicates band that appeared under ambient (hydrated) conditions.

combination and overtone frequencies (Table 4). The $H_2O_{2\nu}$ vibration was greatly enhanced in the ambient spectra that were measured under higher humidity conditions, but was very weak in the low-RH spectra. The $H_2O_\nu$ frequencies calculated from this overtone were close to the $H_2O_\nu$ values determined from the measured frequencies of the clearly observed $H_2O_{\nu+\delta}$ and $H_2O_\delta$ bands (Tables 1 and 2). This supports the assignment of the $H_2O_{2\nu}$ frequency near 6900–6930 $cm^{-1}$ (1.44–1.45 μm) for allophane and imogolite, rather than at higher wavenumbers where the $OH_{2\nu}$ vibration is located.

The significant differences observed for the $H_2O$ bands in spectra measured under different RH conditions and the marked changes in XRD intensity with changing RH conditions indicate that both allophane and imogolite readily adsorb $H_2O$ molecules onto their surfaces and that this additional $H_2O$ affects their structures. The XRD intensity near 4–9°2θ for smectites increased with increasing RH, the opposite of what was observed for allophane and imogolite (Figures 11–12). The adsorption of $H_2O$ molecules at high relative humidity was suggested by van der Gaast *et al.* (1985) to disrupt the regular packing of allophane spheres, thereby disrupting the semi-regular arrangement and decreasing the low-angle scattering. Although van der Gaast *et al.* (1985) did not see a significant decrease in low-angle scattering intensity with humidity for imogolite, the present results suggest that a process similar to that of allophane also operates for imogolite. Additional low-angle scattering studies are needed to fully understand the XRD results.

The spectral signatures for the allophane-rich soil and purified allophane sample, as well as the imogolite-rich soil and the purified imogolite sample, were, in general, quite similar. This bodes well for remote detection of allophane and imogolite. The presence of ferric oxide-bearing phases contributes an increased slope to the spectra from 0.4–0.6 μm and adds a weak band near 0.9 μm (Figure 4). Ferric oxide-bearing phases have been observed in other studies of natural allophane-rich soils (*e.g.* Kaufhold *et al.*, 2010) and may be commonly present in these materials. Further, the Kaufhold *et al.* (2010) study suggested that some of the Fe is present in the allophane structure, supporting the need for additional analysis of synthetic Fe-bearing allophanes (*e.g.* Baker and Strawn, 2012) to better understand this phase. The spectral signatures in the TIR region (Figure 6) are also largely unchanged for the soils and purified samples. The spectral region that is affected the most is from 1300–1800 $cm^{-1}$ (5.6–7.7 μm) and may include contributions from organic admixtures. Changes were observed in the $H_2O$ bending doublet near 1604–1667 $cm^{-1}$ (6.0–6.2 μm) and in the OH-bending doublet attributed to $O_3SiOH$ near 1400–1485 $cm^{-1}$ (~7.1–7.4 μm). The doublets for both of these features tended to be shifted or less well resolved for spectra of the soils compared to spectra of the purified samples. Differences were also noted for these features in spectra of the natural and synthetic allophanes and imogolites, which suggest that these bands are less well defined for these samples than the spectral features in the VNIR and TIR regions more commonly used in remote-sensing studies.

## SUMMARY AND CONCLUSIONS

This study of the spectral and hydration properties of allophane and imogolite builds on the results of many earlier studies to produce reflectance and emissivity spectra needed for remote-sensing detection of these minerals. As imogolite and allophane are generally indicators of geochemical conditions different from phyllosilicates such as smectite and halloysite, identification of imogolite and allophane should enable a more complete view of the geochemical environment during formation. Both natural and synthetic samples were studied here in order to observe which spectral features are constant and which are variable, depending on minor differences in Si/Al ratio, hydration state, and other mineral parameters. The spectra of allophane-rich soil and imogolite-rich soil were also compared with the spectra of the purified samples in order to evaluate which spectral features could be changed or masked in natural environments. The diagnostic VNIR and TIR features for allophane and imogolite are mostly unchanged in the spectra of the soil and the natural

and synthetic samples. However, the spectral features in the range 1300–1800 $cm^{-1}$ (5.6–7.7 μm) exhibited variations among the soil and the natural and synthetic samples that make the features due to $H_2O_\delta$ and $OH_\delta$ in $O_3SiOH$ less useful for remote-sensing studies of allophane and imogolite.

Allophane and imogolite spectral properties are sufficiently different from each other and related clay minerals and hydrated silica components to allow for their identification using remote sensing. However, a wide distribution in structure and composition exists among allophane and imogolite types, and samples at the borders of these groups will, therefore, be more difficult to discriminate. Allophane can be identified in the NIR region using the OH overtone doublet at 1.38 and 1.40 μm, the $H_2O$ combination band at 1.92 μm, and the OH combination band at 2.19 μm. The doublet occurs at 1.37 and 1.39 μm for imogolite. The OH overtone doublet and combination band in spectra of allophane and imogolite occur at shorter wavelengths compared to these features in spectra of other aluminosilicates and opaline silica. The $H_2O$ combination band occurs at longer wavelengths for allophane and imogolite spectra. The OH combination band for allophane and imogolite is broader than that observed for smectites but narrower than that observed for opaline silica. The combination of these spectral parameters should enable identification and discrimination of allophane and imogolite from other aluminosilicates in reflectance spectroscopy investigations. As bands are observed near 1.4, 1.9, and 2.2 μm for many AlOH- and SiOH-bearing minerals, remote-sensing studies involving two or more of these features will be able to more accurately identify and distinguish allophane and imogolite from other aluminosilicates. The TIR region spectra of allophane and imogolite exhibit striking differences in the Si–O–Al stretching and bending vibrations compared with those in other aluminosilicates and opaline silica. The Si–O–Al stretching bands near 1030 and 940 $cm^{-1}$ (~9.7 and 10.6 μm) and the Si–O–Al bending bands near 545 and 420 $cm^{-1}$ (~18 and 24 μm) in spectra of allophane are shifted sufficiently from the Si–O–Al stretching bands near 1010 and 930 $cm^{-1}$ (~9.9 and 10.7 μm) and the Si–O–Al bending bands near 495 and 415 $cm^{-1}$ (~20 and 24 μm) in spectra of imogolite to distinguish these samples in emissivity spectra. The Si–O–Al stretching and bending bands for allophane and imogolite are shifted greatly from those of other aluminosilicates and opaline silica and should enable unique detections of these phases in emission spectroscopy studies.

## ACKNOWLEDGMENTS

Thanks are extended to C. Pieters, T. Hiroi, and NASA's PGG program and the NISLI for the reflectance spectra collected at Brown University's RELAB facility and to P. Christensen and the Mars Space Flight Facility at Arizona State University for the use of the thermal emission spectrometer facility. The authors are grateful to S. Petit, J. Stucki, and two anonymous reviewers for helpful comments that improved the manuscript. This work was supported by NASA's Mars Fundamental Research program and the NASA Postdoctoral Program.

## REFERENCES

Abidin, A., Matsue, N., and Henmi, T. (2007a) Differential formation of allophane and imogolite: Experimental and molecular orbital study. *Journal of Computer-Aided Materials Design*, **14**, 5–18.

Abidin, Z., Matsue, N., and Henmi, T. (2007b) Nanometer-scaled chemical modification of nano-ball allophane. *Clays and Clay Mineral*, **55**, 443–449.

Abidin, Z., Matsue, N., and Henmi, T. (2008) A new method for nano-tube imogolite synthesis. *Japanese Journal of Applied Physics*, **47**, 5079–5082.

Abidin, Z., Matsue, N., and Henmi, T. (2009) Validity of the new method for imogolite synthesis and its genetic implication. Pp. 331–341 in: *Interdisciplinary Studies on Environmental Chemistry – Environmental Research in Asia* (Y. Obayashi, T. Isobe, A. Subramanian, S. Suzuki, and S. Tanabe, editors). TERRAPUB.

Alvarez-Ramirez, F. (2007) Ab initio simulation of the structural and electronic properties of aluminosilicate and aluminogermanate natotubes with imogolite-like structure. *Physical Review B*, **76**, 125421.

Anderson, J.H. and Wickersheim, K.A. (1964) Near infrared characterization of water and hydroxyl groups on silica surfaces. *Surface Science*, **2**, 252–260.

Baker, L. and Strawn, D. (2012) Fe K-edge XAFS spectra of phyllosilicates of varying crystallinity. *Physics and Chemistry of Minerals*, **39**, 675–684.

Bish, D.L., Wu, W., Carey, J.W., Costanzo, P., Giese, R.F., Earl, W., and van Oss, C.J. (1999) Effects of steam on the surface properties of Na-smectite. Pp. 569–575 in: *Clays for Our Future* (H. Kodama, A.R. Mermut, and J.K. Torrance, editors). Proceedings of the 11th Annual International Clay Conference, Ottawa, Canada, 1997. ICC97 Organizing Committee.

Bishop, J.L. and Murad, E. (1996) Schwertmannite on Mars? Spectroscopic analyses of schwertmannite, its relationship to other ferric minerals, and its possible presence in the surface material on Mars. Pp. 337–358: *Mineral Spectroscopy: A tribute to Roger G. Burns*. (M.D. Dyar, C. McCammon, and M.W. Schaefer, editors). The Geochemical Society, St. Louis, Missouri, USA.

Bishop, J.L. and Murad, E. (2002) Spectroscopic and geochemical analyses of ferrihydrite from hydrothermal springs in Iceland and applications to Mars. Pp. 357–370 in: *Volcano–Ice Interactions on Earth and Mars* (J.L. Smellie and M.G. Chapman, editors). Special Publication No. **202**, Geological Society, London.

Bishop, J.L., Pieters, C.M., and Edwards, J.O. (1994) Infrared spectroscopic analyses on the nature of water in montmorillonite. *Clays and Clay Minerals*, **42**, 701–715.

Bishop, J.L., Murad, E., Madejová, J., Komadel, P., Wagner, U., and Scheinost, A. (1999) Visible, Mössbauer and infrared spectroscopy of dioctahedral smectites: Structural analyses of the Fe-bearing smectites Sampor, SWy-1 and SWa-1. Pp. 413–419 in: *11th International Clay Conference, June, 1997* (H. Kodama, A.R. Mermut, and J.K. Torrance, editors).

Bishop, J.L., Madeová, J., Komadel, P., and Fröschl, H. (2002a) The influence of structural Fe, Al and Mg on the infrared OH bands in spectra of dioctahedral smectites. *Clay Minerals*, **37**, 607–616.

Bishop, J.L., Murad, E., and Dyar, M.D. (2002b) The influence

of octahedral and tetrahedral cation substitution on the structure of smectites and serpentines as observed through infrared spectroscopy. *Clay Minerals*, **37**, 617–628.

Bishop, J.L., Lane, M.D., Dyar, M.D., and Brown, A.J. (2008) Reflectance and emission spectroscopy study of four groups of phyllosilicates: Smectites, kaolinite-serpentines, chlorites and micas. *Clay Minerals*, **43**, 35–54.

Bishop, J.L., Gates, W.P., Makarewicz, H.D., McKeown, N.K., and Hiroi, T. (2011) Reflectance spectroscopy of beidellites and their importance for Mars. *Clays and Clay Minerals*, **59**, 376–397.

Buurman, P. and van Reeuwijk, L.P. (1984) Proto-imogolite and the process of podzol formation: a critical note. *Journal of Soil Science*, **35**, 447–452.

Chipera, S.J., Carey, J.W., and Bish, D.L. (1997) Controlled-humidity XRD analyses: Application to the study of smectite expansion/contraction. Pp. 713–722 in: *Advances in X-ray Analysis* (J.V. Gilfrich, I.C. Noyan, R. Jenkins, T.C. Huang, R.L. Snyder, D.K. Smith, M.A. Zaitz, and P.K. Predecki, editors). Plenum Press, New York.

Christensen, P.R. and Harrison, S.T. (1993) Thermal infrared emission spectroscopy of natural surfaces: Application to desert varnish coatings on rocks. *Journal of Geophysical Research*, **98**, 19,819–19,834.

Cradwick, P.D.G., Farmer, V.C., Russell, J.D., Masson, C.R., Wada, K., and Yoshinaga, N. (1972) Imogolite, a hydrated aluminium silicate of tubular structure. *Nature Physical Science*, **240**, 187–189.

Creton, B., Bougeard, D., Smirnov, K.S., Guilment, J., and Poncelet, O. (2008a) Structural model and computer modeling study of allophane. *The Journal of Physical Chemistry C*, **112**, 358–364.

Creton, B., Bougeard, D., Smirnov, K.S., Guilment, J., and Poncelet, O. (2008b) Molecular dynamics study of hydrated imogolite. 1. Vibrational dynamics of the nanotube. *The Journal of Physical Chemistry C*, **112**, 10013–10020.

Demichelis, R., Noel, Y., D'Arco, P., Maschio, L., Orlando, R., and Dovesi, R. (2010) Structure and energetics of imogolite: a quantum mechanical ab initio study with B3LYP hybrid functional. *Journal of Materials Chemistry*, **20**, 10417–10425.

Farmer, V.C. (1974) The layer silicates. Pp. 331–363 in: *The Infrared Spectra of Minerals* (V.C. Farmer, editor). Monograph **4**, The Mineralogical Society, London.

Farmer, V.C. and Fraser, A.R. (1979) Synthetic Imogolite, a Tubular Hydroxyaluminium Silicate. Pp. 547–553 in: *Proceedings of the VI International Clay Conference, Oxford, UK* (M.M. Mortland and V.C. Farmer, editors). Developments in Sedimentology, **27**. Elsevier, Amsterdam.

Farmer, V.C., Fraser, A.R., and Tait, J.M. (1977) Synthesis of imogolite: a tubular aluminum silicate polymer. *Journal of the Chemical Society, Clinical Communications*, **12**, 462–463.

Farmer, V.C., Fraser, A.R., and Tait, J.M. (1979) Characterization of the chemical structures of natural and synthetic aluminosilicate gels and sols by infrared spectroscopy. *Geochimica et Cosmochimica Acta*, **43**, 1417–1420.

Farmer, V.C., Adams, M.J., Fraser, A.R., and Palmieri, F. (1983) Synthetic imogolite: properties, synthesis, and possible applications. *Clay Minerals*, **18**, 459–472.

Fieldes, M. (1955) Clay mineralogy of New Zealand soils, Part II: Allophane and related mineral colloids. *New Zealand Journal of Science and Technology*, **B37**, 336–350.

Guimarães, L., Enyashin, A.N., Frenzel, J., Heine, T., Duarte, H.A., and Seifert, G. (2007) Imogolite nanotubes: stability, electronic, and mechanical properties. *ACS Nano*, **1**, 362–368.

Gustafsson, J.P., Karltun, E., and Bhattacharya, P. (1998) *Allophane and imogolite in Swedish Soils*. Division of Land and Water Resources, Department of Civil and Environmental Engineering, Sweden, 33 pp.

Henmi, T. (1980) Effect of $SiO_2/Al_2O_3$ ratio on the thermal reactions of allophane. *Clays and Clay Minerals*, **28**, 92–96.

Henmi, T. and Huang, P.M. (1987) Effect of phosphate on the formation of imogolite. *Proceedings of the International Clay Conference 1985, Denver* (L.G. Schultz, H. van Olphen, and F.A. Mumpton, editors). The Clay Minerals Society, pp. 231–236.

Henmi, T. and Wada, K. (1976) Morphology and composition of allophane. *American Mineralogist*, **61**, 379–390.

Henmi, T., Tange, K., Minagawa, T., and Yoshinaga, N. (1981) Effect of $SiO_2/Al_2O_3$ ratio on the thermal reactions of allophane. II. Infrared and X-ray powder diffraction data. *Clays and Clay Minerals*, **29**, 124–128.

Kaufhold, S., Kaufhold, A., Jahn, R., Brito, S., Dohrmann, R., Hoffmann, R., Gliemann, H., Weidler, P., and Frechen, M. (2009) A new massive deposit of allophane raw material in Ecuador. *Clays and Clay Minerals*, **57**, 72–81.

Kaufhold, S., Ufer, K., Kaufhold, A., Stucki, J.W., Anastácio, A.S., Jahn, R., and Dohrmann, R. (2010) Quantification of allophane from Ecuador. *Clays and Clay Minerals*, **58**, 707–716.

Kodama, H. and Wang, C. (1989) Distribution and characterization of noncrystalline inorganic components in Spodosols and Spodosol-like soils. *Soil Science Society of America Journal*, **53**, 526–534.

Konduri, S., Mukherjee, S. and Nair, S. (2006) Strain energy minimum and vibrational properties of single-walled aluminosilicate nanotubes. *Physical Review B*, **74**, 033401.

Lundström, U.S., Van Breemen, N., and Bain, D.C. (2000) The podzolization process. A review. *Geoderma*, **94**, 91–107.

MacKenzie, K.J.D., Bowden, M.E., Brown, W.M., and Meinhold, R.H. (1989) Structure and thermal transformations of imogolite studied by $^{29}Si$ and $^{27}Al$ high-resolution solid-state nuclear magnetic resonance. *Clays and Clay Minerals*, **37**, 317–324.

Mehra, O.P. and Jackson, M.L. (1960) Iron oxide removal from soils and clays by a dithionite-citrate system buffered with sodium bicarbonate. *Clays and Clay Minerals*, **7**, 317–327.

Michalski, J.R., Kraft, M.D., Sharp, T.G., Williams, L.B., and Christensen, P.R. (2005) Mineralogical constraints on the high-silica Martian surface component observed by TES. *Icarus*, **174**, 161–177.

Michalski, J.R., Kraft, M.D., Sharp, T.G., Williams, L.B., and Christensen, P.R. (2006) Emission spectroscopy of clay minerals and evidence for poorly crystalline aluminosilicates on Mars from Thermal Emission Spectrometer data. *Journal of Geophysical Research*, **111**, E03004, doi:10.1029/2005JE002438.

Montarges-Pelletier, E., Bogenez, S., Pelletier, M., Razafitianamaharavo, A., Ghanbaja, J., Lartiges, B., and Michot, L. (2005) Synthetic allophane-like particles: textural properties. *Colloids and Surfaces A: Physicochemical and Engineering Aspects*, **255**, 1–10.

Morris, R.V., Lauer Jr., H.V., Lawson, C.A., Gibson Jr., E.K., Nace, G.A., and Stewart, C. (1985) Spectral and other physicochemical properties of submicron powders of hematite ($\alpha$-$Fe_2O_3$), maghemite ($\gamma$-$Fe_2O_3$), magnetite ($Fe_3O_4$), goethite ($\alpha$-FeOOH), and lepidocrocite ($\gamma$-FeOOH). *Journal of Geophysical Research*, **90**, 3126–3144.

Nagasawa, K. (1978) Weathering of volcanic ash and pyroclastic materials. Pp. 105–125 in: *Clays and Clay Minerals of Japan* (T. Sudo and S. Shimoda, editors). Developments in Sedimentology. Kodansha, Japan and Elsevier, Amsterdam.

Ndayiragije, S. and Delvaux, B. (2003) Coexistence of allophane, gibbsite, kaolinite and hydroxy-Al-interlayered

2:1 clay minerals in a perudic Andosol. *Geoderma*, **117**, 203–214.

Parfitt, R. (1990) Allophane in New Zealand – a review. *Soil Research*, **28**, 343–360.

Parfitt, R.L. (2009) Allophane and imogolite: role in soil biogeochemical processes. *Clay Minerals*, **44**, 135–155.

Parfitt, R.L. and Henmi, T. (1980) Structure of some allophanes from New Zealand. *Clays and Clay Minerals*, **28**, 285–294.

Parfitt, R.L., Furkert, R.J., and Henmi, T. (1980) Identification and structure of two types of allophane from volcanic ash soils and tephra. *Clays and Clay Minerals*, **28**, 328–334.

Parfitt, R.L., Childs, C.W., and Eden, D.N. (1988) Ferrihydrite and allophane in four andepts from Hawaii and implications for their classification. *Geoderma*, **41**, 223–241.

Pavia, D.L., Lampman, G.M., and Kriz, G.S. (1979) *Introduction to Spectroscopy: A Guide for Students of Organic Chemistry*. Saunders College, Philadelphia, USA.

Petit, S., Decarreau, A., Martin, F., and Buchet, R. (2004) Refined relationship between the position of the fundamental OH stretching and the first overtones for clays. *Physics and Chemistry of Minerals*, **31**, 585–592.

Rampe, E.B., Kraft, M.D., Sharp, T.G., Golden, D.C., Ming, D.W., and Christensen, P.R. (2012) Allophane detection on Mars with Thermal Emission Spectrometer data and implications for regional-scale chemical weathering processes. *Geology*, **40**, 995–998.

Ruff, S.W., Christensen, P.R., Barbera, P.W., and Anderson, D.L. (1997) Quantitative thermal emission spectroscopy of minerals: A technique for measurement and calibration. *Journal of Geophysical Research*, **102**, 14,899–14,913.

Russell, J.D., McHardy, W.J., and Fraser, A.R. (1969) Imogolite: A unique aluminosilicate. *Clay Minerals*, **8**, 87–99.

Ryskin, Y.I. (1974) The vibrations of protons in minerals: Hydroxyl, water and ammonium. Pp. 137–181 in: *The Infrared Spectra of Minerals* (V.C. Farmer, editor). Monograph **4**, The Mineralogical Society, London.

Saalfeld, H. and Wedde, M. (1974) Refinement of the crystal structure of gibbsite, $Al(OH)_3$. *Zeitschrift für Kristallographie*, **139**, 129–135.

Salisbury, J.W. (1993) Mid-infrared spectroscopy: Laboratory data. Pp. 79–98 in: *Remote Geochemical Analysis: Elemental and Mineralogical Composition* (C.M. Pieters and P.A.J. Englert, editors). Cambridge University Press, Cambridge, UK.

Shimizu, H., Watanabe, T., Henmi, T., Masuda, A., and Saito, H. (1988) Studies on allophane and imogolite by high resolution solid-state $^{29}Si$- and $^{17}Al$-NMR and ESR. *Geochemical Journal*, **22**, 23–31.

Shoji, S., Dahlgren, R., and Nanzyo, M. (1993) Genesis of volcanic ash soils. Pp. 37–71 in: *Volcanic Ash Soils. Genesis, Properties and Utilization* (S. Shoji, M. Nanzyo, and R. Dahlgren, editors). Elsevier, Amsterdam.

Tamura, K. and Kawamura, K. (2001) Molecular dynamics modeling of tubular aluminum silicate: imogolite. *The Journal of Physical Chemistry B*, **106**, 271–278.

Theng, B.K.G., Russell, M., Churchman, G.J., and Parfitt, R.L. (1982) Surface properties of allophane, halloysite, and imogolite. *Clays and Clay Minerals*, **30**, 143–149.

van der Gaast, S.J., Wada, K., Wada, S.-I., and Kakuto, Y. (1985) Small-angle X-ray powder diffraction, morphology, and structure of allophane and imogolite. *Clays and Clay Minerals*, **33**, 237–243.

Wada, K. (1967) A structural scheme of soil allophane. *American Mineralogist*, **52**, 690–708.

Wada, K. (1987) Minerals formed and mineral formation from volcanic ash by weathering. *Chemical Geology*, **60**, 17–28.

Wada, K. (1989) Allophane and imogolite. Pp. 1051–1087 in: *Minerals in Soil Environments* (J.B. Dixon and S.B. Weed, editors). Soil Science Society of America, Madison, Wisconsin, USA.

Wada, S.-I. and Wada, K. (1977) Density and structure of allophane. *Clay Minerals*, **12**, 289–298.

Wada, K., Henmi, T., Yoshinaga, N., and Patterson, S. H. (1972) Imogolite and allophane formed in saprolite of basalt on Maui, Hawaii. *Clays and Clay Minerals*, **20**, 375–380.

Wada, S.I., Eto, A., and Wada, K. (1979) Synthetic allophane and imogolite. *Journal of Soil Science*, **30**, 347–355.

Yoshinaga, N. and Aomine, S. (1962) Imogolite in some Ando soils. *Soil Science Plant Nutrition*, **8**, 22–29.

(*Received 28 March 2012; revised 11 February 2013; Ms. 664; AE: S. Petit*)

*Clays and Clay Minerals*, Vol. 61, No. 1, 75–82, 2013.

# HIGH-TEMPERATURE TRANSFORMATION OF ASBESTOS TAILINGS BY CARBOTHERMAL REDUCTION

ZHAO-HUI HUANG, WEN-JUAN LI, ZI-HE PAN, YAN-GAI LIU, AND MING-HAO FANG*

School of Materials Science and Technology, China University of Geosciences (Beijing), Beijing 100083, P.R. China

**Abstract**—The production and industrial use of asbestos cement and other asbestos-containing materials have been restricted in most countries because of the potential detrimental effects on human health and the environment. Chrysotile is the most common form of asbestos and investigations into how to recycle this serpentine phyllosilicate mineral have attracted extensive attention. Chrysotile asbestos tailings can be transformed thermally, at high temperature, by *in situ* carbothermal reduction (CR). The CR method aims to maximize use of the chrysotile available and uses high temperatures and carbon to change the mineral form and structure of the chrysotile asbestos tailings. When chrysotile asbestos is employed as the raw material and coke (carbon) powder is used as the reducing agent for CR transformation, stable, high-temperature composites consisting of forsterite, stishovite, and silicon carbide are formed. Forsterite ($Mg_2SiO_4$) was the most abundant crystalline phase formed in samples heat treated below 1500°C. At 1600°C, forsterite was exhausted through decomposition and β-SiC formed by reduction of stishovite. A larger proportion of β-SiC was generated as the carbon content was increased. This research revealed that both temperature and carbon addition play key roles in the transformation of chrysotile asbestos tailings.

**Key Words**—Asbestos Tailings, Carbothermal Reduction, Chrysotile, Forsterite, Thermal Transformation, Silicon Carbide.

## INTRODUCTION

Chrysotile, $Mg_3[Si_2O_5](OH)_4$, is considered to be a serpentine (curly) form of asbestos and is classified in the kaolin/serpentine clay mineral group with a 1:1 layer structure. The theoretical composition of chrysotile is MgO 43.0 wt.%, $SiO_2$ 44.1 wt.%, and $H_2O$ 12.9 wt.%. Chrysotile asbestos is a monoclinic serpentine-group mineral with a fibrous layer structure. It is a hydrated magnesium silicate consisting of sheets of silica tetrahedra linked to trioctahedral sheets of magnesia. Furthermore, trioctahedral-site occupancy causes the bilayers to curl into cylindrical rolls (Brindley and Brown, 1984; Auzende *et al.*, 2004).

Chrysotile has been used widely in industry in the production of asbestos cement and other asbestos-containing materials (*e.g.* insulation, fire-retardants, floor tiles, and roofing products) (Porcu *et al.*, 2005; Colangelo *et al.*, 2011). In light of the potential detrimental effects on human health caused by chrysotile asbestos, the World Health Organization (WHO) has classified all types of asbestos as carcinogenic to humans and restricts use of asbestos in structural materials (Nishikawa *et al.*, 2008). In addition, chrysotile asbestos tailings are also considered to be an environmentally destructive mineral waste. Because chrysotile is associated with coexisting gangue minerals and impurities, much of the available chrysotile material has a variable mineral composition which limits potential uses (Li *et al.*, 2012). A large amount of discarded chrysotile asbestos tailings exists, therefore, and has caused considerable environmental problems and may also have jeopardized human health. Appropriate chrysotile treatment prior to disposal in landfill sites is clearly of great importance (Gidarakos *et al.*, 2008).

Research concerning the modification (Papirer *et al.*, 1976; Valentine *et al.*, 1983; Mendelovici *et al.*, 2001; Zaremba and Peszko, 2008) and reutilization (Porcu *et al.*, 2005; Colangelo *et al.*, 2011) of asbestos has attracted a great deal of attention over the last few decades. The mineralogical and morphological transformation of chrysotile asbestos (Murphy and Rose, 1977; Gualtieri *et al.*, 2008a, 2008b, 2012; Zaremba *et al.*, 2010) is a promising and widely developed research solution for the 'asbestos problem'. Investigation of the recycling of chrysotile asbestos in various fields has made it a very important topic of research. For instance, studies have shown that high-grade chrysotile asbestos can be used to produce pure magnesium compounds or hydrated silica (Kim and Chung, 2003; Wypych *et al.*, 2005; Cheng and Hsu, 2006; Wang *et al.*, 2006). Other researchers have tried to use asbestos as a fused magnesium phosphate (fertilizer) additive (Huang, 1953), for stearic acid adsorption (Berkheiser, 1982), for carbon dioxide sequestration (Schulze *et al.*, 2004; Lin *et al.*, 2008; Pronost *et al.*, 2012), and even as a lubrication additive (Foresti *et al.*, 2003; Lyubimov *et al.*, 2011; Qi *et al.*, 2012).

In the present study, research was undertaken to better understand the mineralogical transformation of chrysotile asbestos tailings at high temperature. The

* E-mail address of corresponding author:
fmh@cugb.edu.cn
DOI: 10.1346/CCMN.2013.0610106

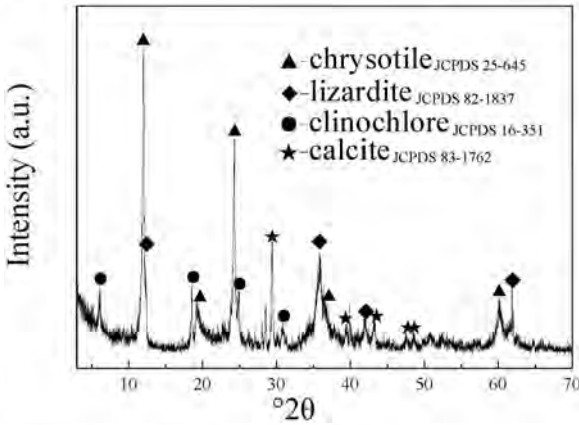


Figure 1. XRD pattern of untreated chrysotile asbestos tailings showing mineral phases.

effects of both temperature and the addition of a reductant on the mineral phases in chrysotile asbestos tailings were examined using the *in situ* CR method. By CR, the mineralogy and morphology of natural asbestos were changed to a high-temperature, stable, and harmless silicon carbide (β-SiC). The simple CR method used here may also produce forsterite/SiC/$SiO_2$ raw powders for use in refractories. The present study provides a theoretical basis for production of a forsterite/SiC-based refractory, and also provides a new perspective on high-efficiency chrysotile tailings use in the high-temperature industry.

## MATERIALS AND METHODS

Chrysotile asbestos tailings were collected from an open-pit serpentine mine in Jiangsu Province, China. The chemical composition measured was: 45.79% $SiO_2$, 39.08% MgO, 7.42% $Fe_2O_3$, 5.74% CaO, 1.02% $Al_2O_3$, 0.36% $Cr_2O_3$. X-ray powder diffraction (XRD) (Figure 1) indicated that chrysotile, lizardite, some clinochlore, and minor calcite were the mineral phases present.

The starting powder was passed through a sieve (mesh number 180) for the <0.088 mm chrysotile and through another sieve (mesh number 200) for the <0.074 mm carbon powder. The powders were mixed in a planetary ball mill (QM-WX4, NanDa Instrument Plant, Nanjing, China) for 2 h at a rotation speed of 200 rpm/min in order to achieve an homogenous mixture of the powders. The quantities used were dictated by the theoretical stoichiometry and other experiments were performed using 10, 50, and 100 wt.% excess of the theoretically established amount of coke required. Theoretical stoichiometry is defined by the proportions of chrysotile and carbon coke, with the $SiO_2$ component taken into consideration in the calculation (equation 1). The theoretical carbon value refers to the carbon content required by assuming that the $SiO_2$ component is completely reduced to silicon carbide based on the reaction

$$SiO_2 + 3C = SiC + 2CO \quad (1)$$

Based on these parameters, the proportions of chrysotile and carbon coke used in the experiments were calculated according to the theoretical stoichiometry of $SiO_2$:C = 1:3 (molar) as in Table 1. For excess carbon conditions, 10–100% more carbon than that required by the theoretical stoichiometry was added. The mixed powders were dried and pressed uniaxially into cylindrical pellets of Φ20 mm × 10 mm under a pressure of 30 MPa. The samples were then buried in carbon coke particles (0.1–1 mm) to provide a reducing atmosphere in a multi-function furnace for 4 h at a temperature range of 1300–1600°C.

The mineral phases in synthesized samples were characterized by XRD (XD-3, Cu$K\alpha_1$ radiation, λ = 0.15406 nm, Purkinje General Instrument Co., Ltd., Beijing, China). The microstructure of the samples synthesized was examined by means of scanning electron microscopy (SEM, JEM-6460LV, Japan Electron Optics Laboratory Co., Ltd., Tokyo, Japan). The SEM instrument was equipped with an energy dispersive spectroscopy detector (EDS, OXFORD INCA X-sight, UK).

## RESULTS

### *Synthesis-temperature effects on CR-product mineralogical transformations*

In order to investigate temperature effects on the mineralogical transformations in the final products, samples with 50 wt.% excess carbon were prepared *via* the CR method by heating at 1300, 1400, 1500, 1550, and 1600°C for 4 h (see Figure 2). The main crystalline phase in the processed samples was forsterite ($Mg_2SiO_4$) at temperatures below 1500°C. At 1550°C, the diffraction intensity of stishovite was enhanced, while that of

Table 1. Starting compositions of samples with different carbon contents.

| Samples | Theoretical addition | Excess carbon (10%) | Excess carbon (50%) | Excess carbon (100%) |
|---|---|---|---|---|
| Asbestos tailings (wt.%) | 78.45 | 76.79 | 70.82 | 65.54 |
| Carbon coke (wt.%) | 21.55 | 23.21 | 29.18 | 35.46 |

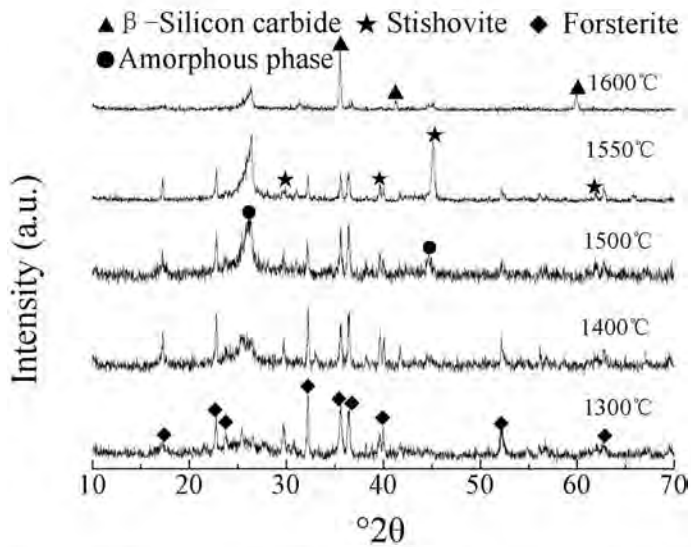


Figure 2. XRD patterns of chrysotile asbestos tailings samples mixed with 50% excess carbon and heated from 1300 to 1600°C.

forsterite diminished. At the higher temperature of 1600°C, stishovite and β-SiC phases both coexisted, whereas the diffraction intensity of forsterite could hardly be discerned. Remarkably, no MgO or Mg was detected in the samples.

*Effects of adding carbon coke on CR-product mineralogical transformations*

The XRD patterns (Figure 3) of samples produced after 4 h at 1600°C in CR reactions using different amounts of carbon revealed that both $Mg_2SiO_4$ and β-SiC were formed. With increased carbon content, the β-SiC diffraction peaks became stronger while the intensity of the $Mg_2SiO_4$ peaks decreased significantly. The results suggested that $Mg_2SiO_4$ decomposes into $SiO_2$ to a greater extent and more $SiO_2$ is subsequently reduced to β-SiC. According to the XRD pattern (Figure 3) of a sample that was heated to 1600°C with a 100% excess (*i.e.* twice the stoichimetric quantity) of carbon, the major mineral phase was β-SiC, even though a small amount of stishovite could still be detected as a remaining phase.

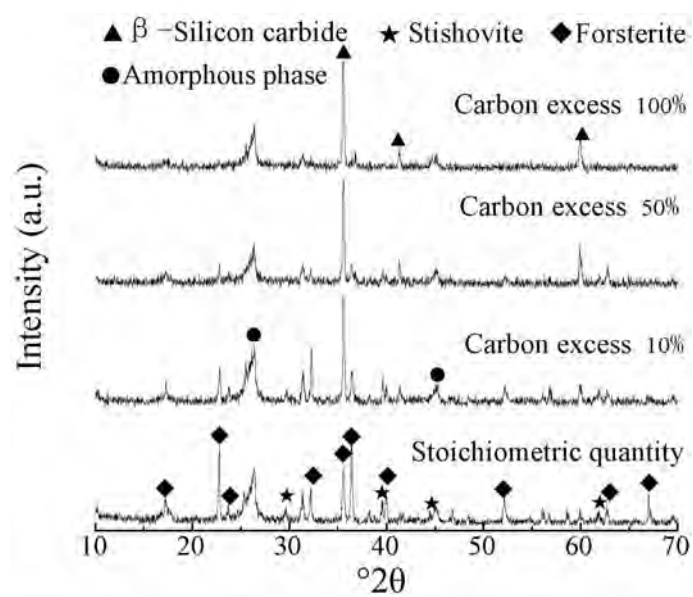


Figure 3. XRD patterns of chysotile asbestos tailings samples mixed with 0 to 100% excess carbon and heated to 1600°C.

## DISCUSSION

### *Thermodynamic analysis of the CR process*

*Idealized thermodynamic analysis in the MgO–$SiO_2$ system.* Thermodynamic analysis was also undertaken to further verify the results above. According to the redrawn binary MgO–$SiO_2$ stability phase diagram (Figure 4) of Bowen and Anderson (1914), forsterite ($2MgO.SiO_2$) and periclase (MgO) are formed at temperatures of <1850°C with <42% $SiO_2$. For $SiO_2$ contents of 42–59%, forsterite and clinoenstatite ($MgO{\cdot}SiO_2$) form at 1500°C and clinoenstatite melts at ~1557°C. At temperatures <1543°C with >59% $SiO_2$, cristobalite ($SiO_2$) and clinoenstatite coexist, but at >1543°C clinoenstatite melts. The chrysotile asbestos tailings used in the experiment contained a greater amount of $SiO_2$, which accounted for 54% of the total magnesia and silica, calculated according to the chemical composition of the chrysotile asbestos. Based on the analyses above, forsterite and clinoenstatite will initially be expected as the main phases using the CR route. In the experiment, no sign of clinoenstatite was observed in the XRD patterns. The major mineral phases in samples heated at 1300–1550°C were forsterite, stishovite, and an amorphous phase (Figure 2). One could assume that clinoenstatite would be unstable and formation would be limited in a complex reducing environment.

The standard Gibbs free energy of formation, $\Delta G_f^0$, at 25°C, and the corresponding values at 1300 and 1600°C, are given in Table 2. At temperatures between 1300 and 1600°C, the standard Gibbs free energies of the solid and liquid states of $2MgO{\cdot}SiO_2$ and $MgO{\cdot}SiO_2$ were calculated. As can be seen from the data (Table 2), (forsterite) $2MgO{\cdot}SiO_2$ (s) formation was more likely than (clinoenstatite) $MgO{\cdot}SiO_2$ (s) formation under the same conditions. The following reaction for the thermal transformation of serpentine minerals to forsterite was suggested by Brindley and Zussman (1957):

$$2Mg_3Si_2O_5(OH)_4 = 3Mg_2SiO_4 + SiO_2 + 4H_2O \qquad (2)$$

From the discussion above, the CR of asbestos tailings passes through two decomposition reactions in the first stage at temperatures below 1550°C. Over the temperature range from 1300 to 1550°C, the reaction process in the system was controlled by the decomposition of chrysotile. The decomposed products under a reducing atmosphere were mainly forsterite, an amorphous phase, and a small amount of stishovite ($SiO_2$). As temperature was increased, the forsterite generated began to decompose to stishovite and MgO. Forsterite decomposition was greatest at 1550°C, which explained the dramatically strengthened diffraction intensity of stishovite at 1550°C. At 1600°C, with forsterite decomposition almost complete, the CR of $SiO_2$ took control of the second stage of the reaction, and more stishovite was reduced to SiC. At the same time, no Mg phases were detected in the XRD patterns, indicating that increased foresterite decomposition was accompanied by the loss

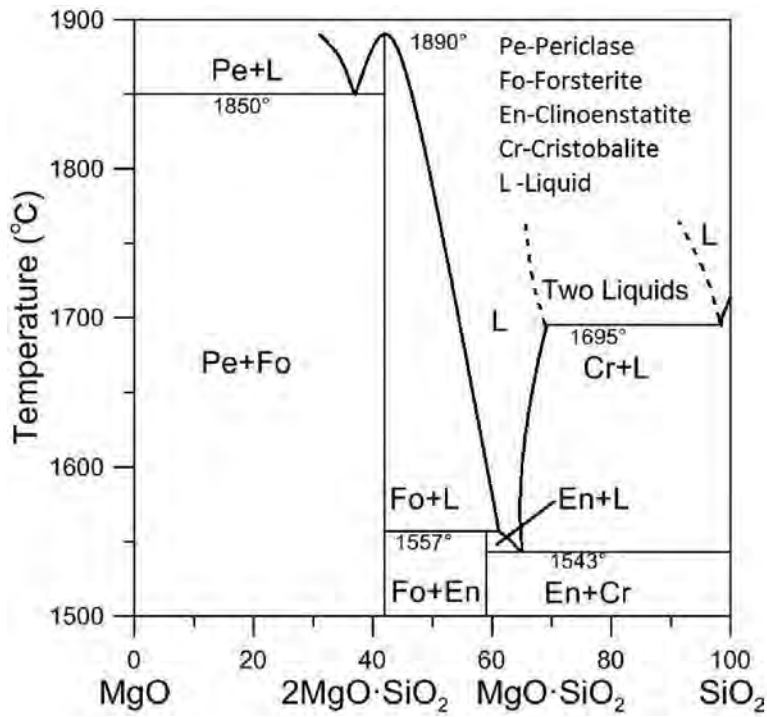


Figure 4. Stability phase diagram of the MgO–$SiO_2$ system.

Table 2. Standard Gibbs free energy ($\Delta G_f^0$) of formations at 25°C, as well as the corresponding values at 1300 and 1600°C.

| Chemical reactions | $\Delta G_f^0$ (J/mol) | $\Delta G_f^0$/1300°C (J/mol) | $\Delta G_f^0$/1600°C (J/mol) |
|---|---|---|---|
| $2MgO(s) + SiO_2(s) = 2MgO{\cdot}SiO_2(s)$ | $-67200 + 4.31T$ | −60420.4 | −59127.4 |
| $2MgO{\cdot}SiO_2(s) = 2MgO{\cdot}SiO_2(l)$ | $71100 - 32.60T$ | 19820.2 | 10040.2 |
| $MgO(s) + SiO_2(s) = MgO{\cdot}SiO_2(s)$ | $-41100 + 6.10T$ | −31504.7 | −29674.7 |
| $MgO{\cdot}SiO_2(s) = MgO{\cdot}SiO_2(l)$ | $75300 - 40.60T$ | 11436.2 | −743.8 |

of magnesium as a vapor phase. If carbon was used as a reductant under vacuum conditions, a temperature >1352°C was required to reduce and transform pure MgO into Mg vapor (Li *et al.*, 2005). Similar results were found in other studies. For example, nitridation on SiC and talc (37% MgO) was performed by Mazzoni and Aglietti (1998) and Mg volatilization occurred at high temperatures. Furthermore, vaporization was enhanced in a reducing atmosphere with high $N_2$ flow rates. Similarly, in the research of Lou *et al.* (1985), gaseous Mg loss at high temperatures (1630°C) was also enhanced quantitatively by MgO volatilization with the reducing gases.

*Idealized thermodynamic analysis of chemical reactions in a Si–C–O complex system.* At 1600°C, a Si–C–O system was involved in the second stage of the CR process. In a closed system with sufficient carbon, gas-phase CO accounted for almost 100% of the gas composition. The potential phases involved in the Si–C–O system are SiO, CO, Si, $SiO_2$, and SiC.

Based on the standard Gibbs free energies of formation of the main system components (Table 3), the possible reactions, the reaction standard Gibbs free energies, and the logarithms of the SiO partial pressures (for $p_{CO} = p^0 = 1.0 \times 10^5$Pa) are as follows:

$$SiO_2(s) + 3C(s) = SiC(s) + 2CO(g) \quad (3)$$
$$\Delta G_3^0 = 603150 - 331.98T,\ T \equiv = 1817(K)$$

$$SiO_2(s) + C(s) = SiO(s) + CO(g) \quad (4)$$
$$\Delta G_4^0 = 676720 - 330.69T,\ \ln(p_{SiO_2}/p^0) = -35349/T\ (K) + 17.274$$

$$SiO(g) + 2C(s) = SiC(s) + CO(g) \quad (5)$$
$$\Delta G_5^0 = -73570 - 1.29T,\ \ln(p_{SiO}/p^0) = -3843/T\ (K) - 0.067$$

$$SiO(g) + SiC(s) = Si(l) + CO(g) \quad (6)$$
$$\Delta G_6^0 = 155239 - 75.69T,\ \ln(p_{SiO}/p^0) = 8109/T\ (K) - 3.954$$

$$SiO_2(s) + SiO(g) + 3C(s) = 2Si(l) + 3CO(g) \quad (7)$$
$$\Delta G_7^0 = 758380 - 407.67T,\ \ln(p_{SiO}/p^0) = 39615/T\ (K) - 21.295$$

and

$$SiO_2(s) + Si(l) = 2SiO(g) \quad (8)$$
$$\Delta G_8^0 = 635890 - 292.2T,\ \ln(p_{SiO}/p^0) = -16605/T\ (K) + 7.63$$

Using the thermodynamic data above, first let $\Delta G_3^0 = 0$, so that the starting reaction temperature from equation 3 can be obtained in the standard state: $T = 603150/331.98 = 1817$ K (1544°C) (when $T \geqslant 1817$ K, with $p_{CO} = p^0 = 1.0 \times 10^5$ Pa), $SiO_2$(s) reacts with C(s) to generate SiC(s). In fact, the CR process involves a series of step-by-step reactions [equations 4 and 5], and is promoted by the reactive vapor intermediates, CO and SiO. Thus, the equilibrium partial pressure of SiO cannot be ignored. The values of $\ln(p_{SiO}/p^0)$ at different temperatures were obtained using the formula $\Delta G_f^0 = -RT\ln K^0$. According to the equilibrium relationships obtained by plotting $\ln(p_{SiO}/p^0)$ *vs.* $1/T$ (Figure 5), SiC can be synthesized at any particular temperature when CO and SiO partial pressures are sufficient. This result is in agreement with the above phase equilibrium analysis, whereupon SiC could be formed at at least 1817 K (1544°C) under standard pressure.

Thus, in the second stage of CR at the higher temperature range (1550–1600°C), the reduction of $SiO_2$ to β-SiC would be the dominant factor that affects the mineralogical transformation of asbestos tailings. With increased carbon contents, more of the $Mg_2SiO_4$ that is formed decomposes into $SiO_2$ and is subsequently reduced to β-SiC. Greater amounts of β-SiC can be produced by heating samples at 1600°C for 4 h using a

Table 3. Gibbs free energies of the main components in the Si–C–O system.

| Chemical reactions | $\Delta G_f^0$ (J/mol) |
|---|---|
| $C(s) + 1/2O_2(g) = CO(g)$ | $\Delta fG_{CO}^0 = -114400 - 85.77T$ |
| $Si(l) + 1/2O_2(g) = SiO(g)$ | $\Delta fG_{SiO}^0 = -155230 - 47.28T$ |
| $Si(l) + O_2(g) = SiO_2(s)$ | $\Delta fG_{SiO_2}^0 = -946350 + 197.64T$ |
| $Si(l) + C(s) = SiC(s)$ | $\Delta fG_{SiC}^0 = -114400 + 37.20T$ |
| $Si(l) + O_2(g) = SiO_2(l)$ | $\Delta fG_{SiO_2}^0 = -921740 + 185.91T$ |

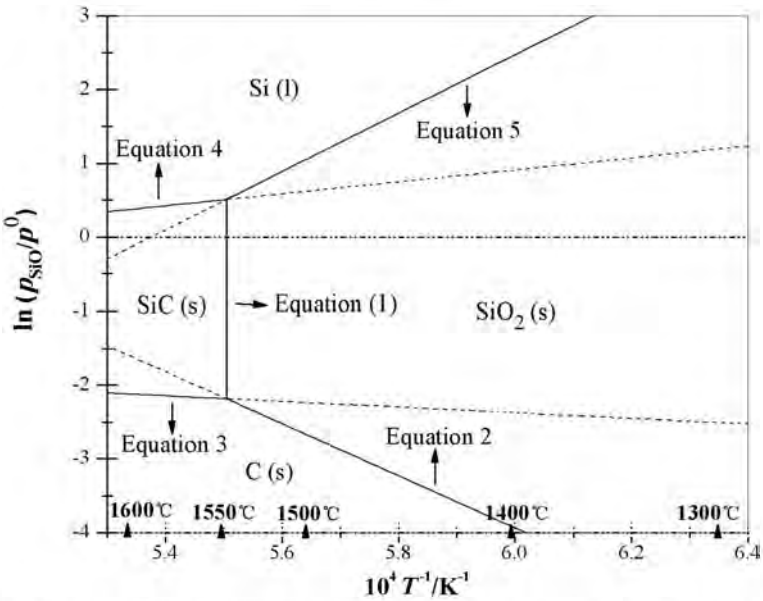


Figure 5. Stable regions of the condensed phases in Si–C–O system assuming that $p_{CO} = p^0 = 1.0 \times 10^5$ Pa.

100% excess of carbon powder (*i.e.* twice the stoichiometric quantity) as the reducing agent.

*Morphology of CR-product mineralogy by SEM*

Scanning electron microscopy (SEM) of the samples (Figure 6) revealed asbestos-like structures in a natural chrysotile (Figure 6a) that are destroyed completely (Figure 6b) after a 4 h CR treatment at 1600°C with twice the stoichiometric quantity of carbon added to the raw samples. This may have been a consequence of both chemical and melting transformations (Porcu *et al.*, 2005), which completely altered the natural chrysotile structure. The SEM observations were consistent with the XRD patterns (Figure 3) and confirmed that the initial mixture was completely converted to β-SiC, forsterite, and stishovite. The final products had morphologies that (Figure 6b) were consistent with well formed β-SiC and an undefined form of unreacted forsterite.

## CONCLUSIONS

When chrysotile asbestos tailings were used as a raw material mixed with carbon coke powder as a reducing agent, both the temperature and the addition of carbon affected significantly the mineralogical transformation of chrysotile by CR. The CR process occurred in two stages. In the first, <1550°C decomposition stage, natural chrysotile asbestos decomposed and generated forsterite as the major mineral phase at 1500°C or below, while at

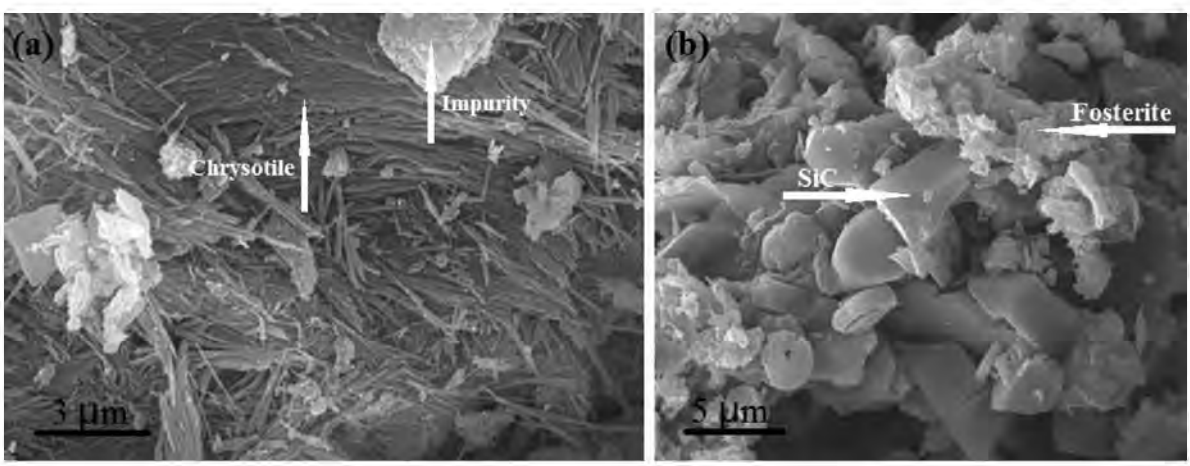


Figure 6. SEM images of (a) natural chrysotile asbestos tailings and (b) final products after heat treatment at 1600°C for 4 h.

the higher temperature (1550°C) the system reaction was controlled by decomposition of forsterite to stishovite with Mg lost as a vapor phase. In the higher temperature (1600°C) reduction stage, thermal reduction of stishovite to β-SiC was the dominant process and a greater proportion of stishovite was reduced to β-SiC as the carbon content was increased. After a high-temperature CR treatment, natural chrysotile structures were replaced by more stable β-SiC and forsterite. The optimal parameters for obtaining greater amounts of β-SiC were: (1) twice the theoretically required amount of carbon powder as a reducing agent, and (2) CR heat treatment at 1600°C for 4 h.

## ACKNOWLEDGMENTS

M.H. Fang conceived and supervised this project. Z.H. Huang and W.J. Li designed and implemented the experiments and wrote the manuscript with assistance from Z.H. Pan for preliminary analysis. Y.G. Liu assisted with discussions and recommendations. The authors gratefully acknowledge the financial support from the National Natural Science Foundation of China (Grant Nos. 50972134, and 51032007) and the New Star Technology Plan of Beijing (Grant No. 2007A080). W.J. Li acknowledges the China Scholarship Council (CSC) for providing a Doctoral Scholarship.

## REFERENCES

Auzende, A.L., Daniel, I., Reynard, B., Lemaire, C., and Guyot, F. (2004) High-pressure behavior of serpentine minerals: a Raman spectroscopic study. *Physics and Chemistry of Minerals*, **31**, 269–277.

Berkheiser, V.E. (1982) Adsorption of stearic acid by chrysotile. *Clays and Clay Minerals*, **30**, 91–96.

Brindley, G.W. and Brown, G. (1984) *Crystal Structure of Clay Minerals and their X-ray Identification*. Monograph **5**, Mineralogical Society, London.

Brindley, G.W. and Zussman, J. (1957) A structure study of the thermal transformation of serpentine minerals to forsterite. *American Mineralogist*, **42**, 461–474.

Bowen, N.L. and Anderson, O. (1914) The binary system MgO-$SiO_2$ phase diagram. *American Journal of Science*, **37**, 487–500.

Cheng, T.-W. and Hsu, C.-W. (2006) A study of silicon carbide synthesis from waste serpentine. *Chemosphere*, **64**, 510–514.

Colangelo, F., Cioffi, R., Lavorgna, M., Verdolotti, L., and De Stefano, L. (2011) Treatment and recycling of asbestos-cement containing waste. *Journal of Hazardous Materials*, **195**, 391–397.

Foresti, E., Gazzano, M., Gualtieri, A.F., Lesci, I.G., Lunelli, B., Pecchini, G., Renna, E., and Roveri, N. (2003) Determination of low levels of free fibres of chrysotile in contaminated soils by X-ray diffraction and FTIR spectroscopy. *Analytical and Bioanalytical Chemistry*, **376**, 653–658.

Gidarakos, E., Anastasiadou, K., Koumantakis, E., and Nikolaos, S. (2008) Investigative studies for the use of an inactive asbestos mine as a disposal site for asbestos wastes. *Journal of Hazardous Materials*, **153**, 955–965.

Gualtieri, A.F., Cavenati, C., Zanatto, I., Meloni, M., Elmi, G., and Gualtieri, M.L. (2008a) The transformation sequence of cement-asbestos slates up to 1200 degrees C and safe recycling of the reaction product in stoneware tile mixtures. *Journal of Hazardous Materials*, **152**, 563–570.

Gualtieri, A.F., Gualtieri, M.L., and Tonelli, M. (2008b) In situ ESEM study of the thermal decomposition of chrysotile asbestos in view of safe recycling of the transformation product. *Journal of Hazardous Materials*, **156**, 260–266.

Gualtieri, A.F., Giacobbe, C., and Viti, C. (2012) The dehydroxylation of serpentine group minerals. *American Mineralogist*, **97**, 666–680.

Huang, T.-H. (1953) Serpentine-fused phosphate, citric solubility and glass content correlation. *Journal of Agricultural and Food Chemistry*, **1**, 62–67.

Kim, D.-J. and Chung, H.-S. (2003) Synthesis and characterization of ZSM-5 zeolite from serpentine. *Applied Clay Science*, **24**, 69–77.

Li, W.-J., Huang, Z.-H., Liu, Y.-G., Fang, M.-H., Ouyang, X., and Huang, S.-F. (2012) Phase behavior of serpentine mineral by carbothermal reduction nitridation. *Applied Clay Science* **57**, 86–90.

Li, Z.-H., Dai, Y.-N., and Xue, H.-S. (2005) Thermodynamical analysis and experimental test of magnesia by vacuum carbothermic reduction. *Nonferrous Metals*, **57**, 56–59.

Lin, P.-C., Huang, C.-W., Hsiao, C.-T., and Teng, H. (2008) Magnesium hydroxide extracted from a magnesium-rich mineral for $CO_2$ sequestration in a gas–solid system. *Environmental Science & Technology*, **42**, 2748–2752.

Lou, V.L.K., Mitchell, T.E., and Heuer, A.H. (1985) Review-graphical displays of the thermodynamics of high-temperature gas-solid reactions and their application to oxidation of metals and evaporation of oxides. *Journal of the American Ceramic Society*, **68**, 49–58.

Lyubimov, D.N., Dolgopolov, K.N., Kozakov, A.T., and Nikolskii, A.V. (2011) Improvement of performance of lubricating materials with additives of clayey minerals. *Journal of Friction and Wear*, **32**, 442–451.

Mazzoni, A.D. and Aglietti, E.F. (1998) SiC-$Si_3N_4$ bonded materials by the nitridation of SiC and talc. *Ceramics International*, **24**, 327–332.

Mendelovici, E., Frost, R.L., and Kloprogge, J.T. (2001) Modification of chrysotile surface by organosilanes: An IR-photoacoustic spectroscopy study. *Journal of Colloid and Interface Science*, **238**, 273–278.

Murphy, W.J., and Ross, R.A. (1977) A comparative study of thermal effects on surface and structural parameters of natural Californian and Quebec chrysotile asbestos up to 700 degrees C. *Clays and Clay Minerals*, **25**, 78–89.

Nishikawa, K., Takahashi, K., Karjalainen, A., Wen, C.-P., Furuya, S., Hoshuyama, T., Todoroki, M., Kiyomoto, Y., Wilson, D., Higashi, T., Ohtaki, M., Pan, G. W., and Wagner, G. (2008) Recent mortality from pleural mesothelioma, historical patterns of asbestos use, and adoption of bans: A global assessment. *Environmental Health Perspectives*, **116**, 1675–1680.

Papirer, J.H., Dovergne, G., Siffert, B., and Leroy, P. (1976) Surface modification of chrysotile asbestos under the influence of aluminium trichlorid. *Clays and Clay Minerals*, **24**, 101–102.

Porcu, M., Orr, R., Cincotti, A., and Cao, G. (2005) Self-propagating reactions for environmental protection: Treatment of wastes containing asbestos. *Industrial & Engineering Chemistry Research*, **44**, 85–91.

Pronost, J., Beaudoin, G., Lemieux, J.M., Hebert, R., Constantin, M., Marcouiller, S., Klein, M., Duchesne, J., Molson, J.W., Larachi, F., and Maldague, X. (2012) $CO_2$-depleted warm air venting from chrysotile milling waste (Thetford Mines, Canada): Evidence for in-situ carbon capture from the atmosphere. *Geology*, **40**, 275–278.

Qi, X.-W., Lu, L., Jia, Z.-N., Yang, Y.-L., and Liu, H.-R. (2012) Comparative tribological properties of magnesium hexasilicate and serpentine powder as lubricating oil

additives under high temperature. *Tribology International*, **49**, 53–57.

Schulze, R.K., Hill, M.A., Field, R.D., Papin, P.A., Hanrahan, R.J., and Byler, D.D. (2004) Characterization of carbonated serpentine using XPS and TEM. *Energy Conversion and Management*, **45**, 3169–3179.

Valentine, R., Chang, M.J., Hart, R.W., Finch, G.L., and Fisher, G.L. (1983) Thermal modification of chrysotile asbestos: evidence for decreased cytotoxicity. *Environmental Health Perspectives*, **51**, 357–368.

Wang, L.-J., Lu, A.-H., Wang, C.-Q., Zheng, X.-S., Zhao, D.-J., and Liu, R. (2006) Nano-fibriform production of silica from natural chrysotile. *Journal of Colloid and Interface Science*, **295**, 436–439.

Wypych, F., Adad, L.B., Mattoso, N., Marangon, A.A.S., and Schreiner, W.H. (2005) Synthesis and characterization of disordered layered silica obtained by selective leaching of octahedral sheets from chrysotile and phlogopite structures. *Journal of Colloid and Interface Science*, **283**, 107–112.

Zaremba, T. and Peszko, M. (2008) Investigation of the thermal modification of asbestos wastes for potential use in ceramic formulation. *Journal of Thermal Analysis and Calorimetry*, **92**, 873–877.

Zaremba, T., Krząkała, A., Piotrowski, J., and Garczorz, D. (2010) Study on the thermal decomposition of chrysotile asbestos. *Journal of Thermal Analysis and Calorimetry*, **101**, 479–485.

(*Received 10 July 2012; revised 11 February 2013; Ms. 689; AE: W.F. Jaynes*)